Doctoral theses at NTNU, 2022:276

Arturo A. Arosemena

Turbulent flows of generalized Newtonian fluids: mechanics and structural coherence

Doctoral thesis

NTNU
Norwegian University of Science and Technology
Thesis for the Degree of
Philosophiae Doctor
Faculty of Natural Sciences
Department of Chemical Engineering

NTNU
Norwegian University of
Science and Technology

Arturo A. Arosemena

Turbulent flows of generalized Newtonian fluids: mechanics and structural coherence

Thesis for the Degree of Philosophiae Doctor

Trondheim, September 2022

Norwegian University of Science and Technology
Faculty of Natural Sciences
Department of Chemical Engineering

NTNU
Norwegian University of
Science and Technology

NTNU
Norwegian University of Science and Technology

Thesis for the Degree of Philosophiae Doctor

Faculty of Natural Sciences
Department of Chemical Engineering

ISBN 978-82-326-6412-2 (printed ver.)
ISBN 978-82-326-6781-9 (electronic ver.)
ISSN 1503-8181 (printed ver.)
ISSN 2703-8084 (online ver.)

Doctoral theses at NTNU, 2022:276

Printed by NTNU Grafisk senter

Abstract

Most flows are turbulent in nature, yet fluids exhibit a plethora of inherent responses to applied stress. Fluids that respond in a linear manner, such as water and air, are labelled as Newtonian, whereas the majority of them that do not are often called non-Newtonian. Some of these fluids show instantaneous deformation in directions perpendicular to the applied stress, others present elastic recovery, or yield-stress (plasticity), and some even flow more easily under increasing shear stress. The latter, a type of shear-dependent rheology known as shear-thinning or pseudoplastic behaviour, is one of the most common non-Newtonian fluid behaviours in numerous industrial settings. Consequently, the understanding of turbulent flows of these fluids; i.e., those exhibiting shear-dependent rheology, is fairly important for a good number of engineers and scientists.

The present thesis is concerned with the investigation of turbulent flows corresponding to generalized Newtonian (GN) fluids. The aim is to study the mean-flow properties, and the features of some coherent structures; more specifically, turbulent vortices. For this purpose, the numerical simulations of two distinct flows are considered: turbulent channel flow, and turbulent flow in a baffled stirred tank with a Rushton-type impeller. Here, a GN fluid refers to an idealization of a real fluid presenting shear-dependent rheology as its most characteristic rheological feature. GN fluids are modelled through a so-called constitutive equation, where the response to stress is made proportional to it through a material function (apparent shear viscosity) depending on the rate of deformation. In this work, the Carreau model is selected to incorporate the GN fluid rheology into the momentum equation.

Key accomplishments of this thesis include: (i) the displaying of drag reducing features in turbulent channel flow for a slight-to-moderate degree of shear-thinning, even in the absence of other non-Newtonian behaviours (e.g., extensional thickening, or elastic effects); (ii) the discovery of qualitative similarities between turbulent pipes and turbulent channels of GN fluids, which hints to the possibility of having a universal near-wall behaviour for these internal flows even after complex effects are introduced; (iii) the analysis of quasi-

streamwise vortices, and of the near-wall self-sustaining process in turbulent channel flow of a shear-thinning fluid; (iv) the presentation of the mean momentum balance analysis (see, e.g., Klewicki, 2013) for turbulent channel flow of GN fluids; (v) the study of turbulent vortices in a baffled stirred tank with (potential) important implications for dispersed systems; among other findings.

Keywords: Turbulent flows, numerical simulations, mean-flow properties, coherent structures.

Preface

> *Our own experience provides the basic material for our imagination, whose range is therefore limited. It will not help to try to imagine that one has webbing on one's arms, which enables one to fly around at dusk and dawn catching insects in one's mouth; that one has very poor vision, and perceives the surrounding world by a system of reflected high-frequency sound signals; and that one spends the day hanging upside down by one's feet in an attic. In so far as I can imagine this (which is not very far), it tells me only what it would be like for me to behave as a bat behaves. But that is not the question. I want to know what it is like for a bat to be a bat.*
>
> *Nagel (1974).*

The present thesis is submitted to the Norwegian University of Science and Technology (NTNU) for partial fulfilment of the requirements for the degree of philosophiae doctor. The doctoral work spanned from August 2018 to May 2022. Most of it (ca. 3.5 years) has been performed in the Environmental Engineering and Reactor Technology Group at the Department of Chemical Engineering. The remaining part of the work (ca. 05. years) has been carried out at the Department of Chemistry and Chemical Engineering, Chalmers University of Technology (Gothenburg, SE). The work has been supervised by Prof. Jannike Solsvik, and co-supervised by Profs. Helge I. Andersson, and Ronnie Andersson. The thesis is an article-based one, consisting of four chapters (either motivational, explanatory, or synoptic in nature), and four research papers (listed next, and collected at the end of the document). Most research, in connection to this thesis, has been economically supported by the Research Council of Norway (RCN, grant no. 274398). Additional funding (1 year) has been provided by the Department of Chemical Engineering in connection with teaching duties.

Paper I. Turbulent channel flow of generalized Newtonian fluids at a low Reynolds number.

Arturo A. Arosemena, Helge I. Andersson, and Jannike Solsvik.
J. Fluid Mech. **908**, A43 (2021).

Contributions: All authors contributed to the conceptualization of the work. A. A. A. performed the numerical experiments, computed the different statistics during post-processing, and wrote the draft. H. I. A. and J. S. supervised the work, and reviewed the final draft. All authors contributed to editing the manuscript.

Paper II. Effects of shear-thinning rheology on near-wall turbulent structures.

Arturo A. Arosemena, Ronnie Andersson, Helge I. Andersson, and Jannike Solsvik.
J. Fluid Mech. **925**, A37 (2021).

Contributions: A. A. A., R. A. and J. S. conceptualized the work. A. A. A. computed the different statistics, and wrote the draft. R. A., H. I. A. and J. S. supervised the work, and reviewed the final draft. All authors contributed to editing the manuscript.

Paper III. Velocity–vorticity correlations and the four-layer regime in turbulent channel flow of generalized Newtonian fluids.

Arturo A. Arosemena and Jannike Solsvik.
Eur. J. Mech. B Fluids **91**, 1–8 (2022).

Contributions: A. A. A. conceptualized the work, computed the different statistics, and wrote the draft. J. S. supervised the work, and reviewed the final draft. Both authors contributed to editing the manuscript.

Paper IV. Characterization of vortical structures in a stirred tank.

Arturo A. Arosemena, Haider Ali, and Jannike Solsvik.
Phys. Fluids **34**, 5.0083843 (2022).

Contributions: A. A. A. and J. S. conceptualized the work. H. A. performed the numerical simulation, and wrote the section describing the numerical experiments. A. A. A. computed the different statistics, and wrote the remaining part of the draft. J. S. supervised the work, and reviewed the final draft. All authors contributed to editing the manuscript.

Trondheim, 31.05.2022.
Arturo A. Arosemena.

Acknowledgements

In life, a fair amount of events take place, and some are more significant than others simply because what they represent. A PhD education, for instance, marks the end of our formal training in academia. Moreover, I am of the opinion that after a PhD, most researchers are humbled by the realization that we know pretty much nothing about pretty much everything. Perhaps, this is the most valuable lesson. Continue learning is the only way forward if one wants to 'see a bit through the smoke', so to speak. Moving away from this opinion/reflection, it is a fact that my work would not be possible without the assistance of certain people and organizations. I am deeply grateful to all of you, and I am going to proceed with some punctual and personal acknowledgments. If I have not mentioned someone in particular, which may have had an impact in my work, I apologize beforehand. Please know that I also thank you.

First of all, I would like to thank my supervisors. I am deeply grateful for your mentorship. Jannike, thank you for the opportunity to work in this project, for backing my ideas, for checking my manuscripts, for being patient with me, and for always be willing to help. I have no complaints. It is difficult to teach, start your own group, and to supervise several PhD candidates, all at the same time. You manage to do it and do it well. Helge, thank you for always paying attention to my work, for helping me correcting many mistakes in my writings, and for your guidance during our first peer-review. The blow to my psyche after some initial comments from the referees was pretty much mended thanks to you. Also, it is incredible to me how you manage to follow my ideas, even when I am not able to explain them well. In such cases, you have helped me to clarify them. I am very grateful to you for this. Ronnie, thank you for receiving me in Chalmers, for your patience, and for taking the time to discuss our work on a weekly basis despite your many other duties. I hope we can work together once again at some point in the future.

Also, I would like to thank the professors, researchers, and other PhD candidates within the Reactor Technology group at IKP, and within the Thermo Fluids group at EPT, whom have interacted with me during the last four years. You have made my stay at NTNU more interesting, and altogether more enjoy-

able. A special thanks go to my office mates, initially Canberk and now Davide.

Last but certainly not least, I thank my family and friends for their support. I am forever indebted to my grandmother, Lelys, and my mother, Mitzy, for raising me. Mum, without doubt, you are the best person I know. Thank you for your devotion, unconditional support and love, and for showing me, what good parenthood actually looks like. Despite the distance and lack of constant communication, I am sure that not a day goes by without you sending me your care. Finally, I would like to thank my wife, Angelica, for accompanying me and for sacrificing so much for us. You are a joy to the eyes and soul.

Financial support for this work was provided by the Department of Chemical Engineering at NTNU, and by the Research Council of Norway through the FRINATEK project: 'Fundamental investigation of non-Newtonian fluid flow in bioprocessing', grant no. 274398. Numerical simulations were performed on resources provided Sigma2, part of the Norwegian Competence Centre for HPC, through grant no. NN9646K and no. NN9771K. I am also quite grateful to NTNU and its IT division for the resources provided in the local cluster, IDUN.

Contents

Nomenclature

The following nomenclature, mentioned in more than one chapter of this thesis, is listed here for convenience. In the appended articles, the nomenclature may be different, but it is always clearly defined therein.

Abbreviations

3D	Three-dimensional.
DNS	Direct numerical simulations.
GN	Generalized Newtonian.
LES	Large-eddy simulations.
NS	Navier–Stokes.
PDF	Probability density function.

Greek letters

α	Flow index; see equation (1.3).
$\dot{\gamma}$	Strain rate.
Λ	Time constant; see equation (1.3).
μ	Fluid dynamic viscosity/apparent viscosity.
μ_0	Zero-shear-rate-viscosity; see equation (1.3).
μ_∞	Infinite-shear-rate-viscosity; see equation (1.3).
μ_c	Characteristic viscosity. In this work, it is taken as the nominal value of μ at the wall, μ_w, for the channel flow.
ρ	Fluid density.

$\overline{\tau_w}$	Total mean shear stress at the wall; see equation (1.9).
$\overline{\tau_{xy}}$	Total mean shear stress; see equation (1.10).

Other symbols

$(\,)^+$	Property in 'inner', or 'wall' units.
b	Exponent in Carreau-Yasuda fluid model; see equation (1.3).
$\mathcal{H} = y/h$	Wall-normal coordinate, y, in 'outer' units.
h	Channel half-height. More generally, outer-length scale in a wall-bounded flow.
$\ell = \mu_c/(\rho u_\tau)$	Viscous, or inner-length scale in a wall-bounded flow.
$Re_\tau = h/\ell$	Frictional Reynolds number.
u_τ	Friction velocity; see equation (1.11).

Chapter 1

Introduction

> *. . . theory is what gives meaning to observation. . . Tomorrow, it may be wrong. Even so, it deserves to be regarded as one of the better things of which man is capable.*
>
> *Lumley (1992).*

Observation and critical thinking have led humanity to prosper for the last thousands of years. Our inherent curiosity and ingenuity have allowed us to create wonders. Nonetheless, our discoveries and technological advances pall when considering all still unknown to us. Fluid flow phenomena is plagued with examples. For instance, we use different devices to transport through air and water, yet during this process, we waste enormous amounts of energy, create noise and pollute the environment. Moreover, in certain branches of fluids dynamics the lack of knowledge is more pronounced than in others. In terms of flow regimes, consider turbulent against laminar flow or in terms of fluid properties, consider Newtonian versus non-Newtonian behaviour.

The primary aim of the present thesis is to improve–even if only slightly and with several limitations–our basic understanding about the mechanics and possible coherence of turbulent flows of Newtonian and shear-dependent viscosity fluids; the later, a type of non-Newtonian rheology.

1.1 Background

1.1.1 Turbulence

Flows perceived as 'smooth' are known as laminar flows whereas their opposite (chaotic or irregular) as turbulent flows. Of course, there are some flows in transition where turbulent spots are somewhat intermittent within ordered,

Figure 1.1: *The Yellow River Breaches its Course* by Ma Yuan.

laminar regions. Most flows in nature and technological applications are turbulent whilst laminar ones occur only as fairly rare exceptions (Monin & Yaglom, 1971, p. 2). 'Turbulent' are the various motions of the air and water in our surroundings. From typical wind gusts in the earth's atmosphere, cumulus clouds and water currents below the surface of the oceans, to more dangerous geophysical events such as tropical cyclones (hurricanes and typhoons), tsunamis and extreme storm waves (also called rogue or killer waves). In engineering applications, examples of turbulent flow include both external flows around aircraft, automobiles, building and sea vessels, and internal flows in pipelines, combustion engines and chemical reactors. In the latter example, turbulence can be crucial for mixing (molecular diffusion) and homogenization (macromixing or stirring) of fluid mixtures, and for influencing the chemical reactions rates in liquids or gases.

The previous paragraph highlights the ubiquitous nature of turbulent flows and their technological importance but does not clarify the actual meaning nor origin of the word 'turbulence'. From a historical point of view, humans have probably observed and documented turbulence as a distinct regime for centuries. Paintings from all over the world constitute evidence of such awareness. Representative examples are *The Yellow River Breaches its Course* (ca. 1222) by Ma Yuan (see figure 1.1), *The Great Wave off Kanagawa* (ca. 1830–1832) by Katsushika Hokusai and *Starry Night* (1889) by Vincent Van Gogh. Also, related to art, the work of Leonardo da Vinci (1452–1519) is often referenced when tracing back the origin of the study of turbulence physics. In particular, because of his depictions of wake flows and the usage of the word *turbolenza* in his writings. However, it is known that Leonardo employed this word rather ambiguously and in occasions, with a meaning that is not according to its modern usage in fluids mechanics (Marusic & Broomhall, 2021).

In a scientific context, studies about turbulence probably began at the very beginning of the nineteenth century with observations about what French engineers called *eaux courantes* or open-channel flows (Darrigol, 2005, p. 219). In 1822, just after proposing his equations for viscous-fluid motion, Claude-Louis Navier made some distinction between 'linear' and 'nonlinear' flows and, a decade or so later, Adhémar Barré de Saint-Venant opposed 'regular' to 'tumultuous' flows. Afterwards, studies about pressure drops in pipes gained more popularity and by the 1860s, the experiments of hydraulic engineers like Gotthilf Hagen and Henry Darcy made clear that the character of the flow in very narrow pipes was potentially different from that in large pipes (Eckert, 2021). Nevertheless, during the nineteen century and regarding precise characterization of transition to turbulence in pipe flows, the work of Osborne Reynolds is likely the most influential. Reynolds (1883) is remembered for the experimental apparatus and his interpretation of dye-streak visualization results but, actually, it is Reynolds publication from 1895 which is the most noteworthy. Reynolds (1895) contributions consisted in: (i) clarification of the nondimensional parameter, mentioned in his previous paper, which is responsible for the transition from laminar regime to turbulence in incompressible flow (later called Reynolds number by Sommerfeld, 1908), (ii) decomposition of the flow into average and fluctuating parts (nowadays called Reynolds decomposition), leading to the averaged momentum equations, and (iii) the deduction of the turbulent kinetic energy equation on which Reynolds observed that the terms comprising products of Reynolds stress and mean velocity gradient represented a transfer of kinetic energy from the mean flow to turbulence (Jackson & Launder, 2007). An interesting and to some extent paradoxical fact is that the Reynolds decomposition led to the Reynolds stress tensor, and to the so-called closure problem in turbulence which was initially tackled using eddy-viscosity models based on Joseph Boussinesq hypothesis for the mixing in thin shear layers. The hypothesis was proposed in 1872 by Boussinesq, and published in 1877, several years before Reynolds (1895). Boussinesq (1877) is also remarkable because of the recognition of higher momentum transfer in what he denoted as 'tumultuous movements'. The phrase being a clear trace of Saint-Venant influence in Boussinesq work.

To conclude this brief summary about the start of turbulence studies, it is relevant to point out that neither Boussinesq nor Reynolds have used the word 'turbulence' in their publications. Aside 'tumultuous movements', Boussinesq used phrases such as 'eddy agitations' and 'liquid eddy theory' whereas Reynolds employed others such as 'sinuous paths', 'sinuous motion' and 'irregular eddies' (Schmitt, 2007). The introduction of the phrase 'turbulent flow' and the abstract concept of turbulence to the literature of fluid mechanics is attrib-

uted to Willian Thomson, known as Lord Kelvin (Davidson *et al.*, 2011, p. xi). From an etymological point of view, 'turbulent' appears to come from the Latin words *turba* meaning turmoil, stir or its complement *turbulentus* meaning full of stir. On the other hand, 'turbulence' appears to come from the Latin word *turbulentia* meaning perturbation or trouble.

The preceding discussion makes clear that it is difficult to precisely define turbulence. A more fruitful endeavour is perhaps to simply point out some of the major qualitative features of turbulent flows. These are:

- Irregularity or apparent stochastic/random nature. Turbulent flows exhibit chaotic fluctuations in time and space. The fluctuations in space are three-dimensional and thereby, turbulence is also rotational.
- A wide range of scales. Turbulent flows are characterized for swirling-like flow patterns of different sizes. For instance, in atmospheric flows, relevant scales range from hundreds of kms to parts of a mm (Tsinober, 2013, p. 7).
- High diffusivity. Turbulent flows are strongly diffusive which causes rapid mixing and enhancement transport of momentum, energy and mass.
- Large Reynolds numbers. Turbulent flows take place when the ratio of nonlinear inertia to viscous forces is large, i.e., at high Reynolds numbers.
- Dissipation of kinetic energy into heat. Viscous shear stresses perform deformation work, increasing the internal energy, at the expenses of kinetic energy of the turbulence (Tennekes & Lumley, 1972, p. 3). For sustaining turbulent flows, a continuous supply of energy is required.
- Unpredictability. Small changes in initial conditions produce large changes to the subsequent motions (Davidson, 2015, p. 12).

The above list is based on our current understanding of turbulence and may change with time. For instance, ideas such as coherent structures, the inverse cascade process, the footprint of the initial conditions in asymptotic (mature) turbulence, and the usefulness of two dimensional turbulence as a first approximation when studying large-scale motions in the atmosphere and oceans, were at some point controversial to say the least. Moreover, the list is not all-inclusive and is only intended as a summary of some of the most important and general features of all turbulent flows. Certain classes or families of turbulent flows have their own additional features. Such features have been addressed (to some degree) by numerous researchers including physicists, mathematicians and engineers during the twenty century and close to the first quarter of the twenty-first century. In fact, with respect to studies about turbulence and turbulent flows, the existing literature is quite overwhelming; in the search engine *Semantic Scholar*, the word 'turbulence' and phrases such as 'turbulent channel flow' and 'turbulent boundary layer' lead to about 476 000, 350 000 and 325 000 results,

respectively.

Considering the amount of publications related to turbulence and even when limiting ourselves to particular families of flows for a type of fluid, it seems unrealistic to provide a comprehensive assessment of previous contributions. The following subsections, specifically 1.1.3-1.1.4, only review some of the most important studies for the present thesis. For a systematic but concise description of key developments in turbulence research, before the advent of massive computations (roughly up to mid-1970s), the epilogue of Davidson *et al.* (2011) is recommended.

1.1.2 Generalized Newtonian (GN) fluids

Similar to the laminar-turbulent dichotomy in case of flow regime, fluids are classified as Newtonian and non-Newtonian. Newtonian fluids are those flowing regularly according to Newton linear law of friction; i.e., fluids where the response (rate of deformation with time) to the applied stress is linear. Non-Newtonian are the remaining, complex, majority of fluids. The recent review of Ewoldt & Saengow (2022) about designing complex fluids starts with: 'To be Newtonian is restrictive; to be non-Newtonian is everything else'. The phrase conveys this significant fact; most fluids in industry and everyday life are non-Newtonian. Typical examples are polymer solutions, drilling fluids, fresh concrete, honey, ketchup, toothpaste and biological fluids such as blood or saliva. Of course, this fact (majority of fluids being non-Newtonian) does not diminish the importance of Newtonian fluids and the study of their rheology; i.e., deformation and flow. Ultimately water and air, the most important fluids for humanity, exhibit Newtonian behaviour.

The continuum-level aspects of a fluid, whether Newtonian or not, depends on its microscopic structure. For instance, in case of polymer solutions, the rheological properties and resulting macroscopic behaviour are dependent on the molecular architecture of the constituent molecules (e.g., molecular weight, chain branching, and electrical charge distribution), the polydispersity of the solution, and the interactions between solute and solvent (Bird & Wiest, 1995). A further complication is that different microscopic configurations may lead to similar rheological features. There are even handbooks about rheological modifiers (e.g., polymers, particles, and droplets) for given solvents in the literature; see e.g., Ash & Ash (2006). Nonetheless, in the present thesis, the molecular approach is considered out of scope and a 'material agnostic' approach is taken. Basically, attention is paid to the macroscopic rheological behaviour of the fluid and not to its microscopic composition.

Under the idealization of fluids as continuous media, non-Newtonian rheological response to stress is incorporated into the momentum equation by

means of a so-called constitutive equation. The idea is to use a fundamental relationship which expresses the stress tensor in terms of various kinematic tensors (Bird & Wiest, 1995). In principle, the issue is similar to the closure problem in turbulence where–depending of the type of flow and which effects are to be captured–a particular model is used for the turbulent or Reynolds stress. Naturally in the case of closures for non-Newtonian fluid behaviour, the deciding factor is(are) the dominant rheological feature(s). Real fluids show a spectrum of responses to both shear and normal stresses, while non-Newtonian models include only the most important ones for a given flow under consideration. C. W. Macosko (Macosko, 1994, p. 4) remarked four key phenomena in rheology: (i) viscoelasticity, (ii) shear-thinning, (iii) shear normal stresses, and (iv) extensional thickening. Viscoelasticity is the concurrence of both viscous (either Newtonian or not) and elastic (either linear or not) effects in a material subjected to deformation. Shear-thinning describes a non-Newtonian fluid behaviour where the apparent viscosity decreases with flow strength (either stress or strain rate). 'Shear normal stresses' is the terminology used to describe the occurrence of normal stress differences in a fluid under simple shear. The dramatic 'Weissenberg effect', in which a fluid climbs up a rotating rod, occurs because of such inequality of normal stresses. Finally, extensional thickening refers to the increase of extensional viscosity (also known as Trouton viscosity) with flow strength in a fluid subject to elongation and/or shear. Any proposed constitutive equation should attempt to describe these four important rheological responses. In such endeavour of being as much comprehensive as possible, the 8-constant Oldroyd model (Oldroyd, 1958) is perhaps the most successful. Nevertheless, the 8-constant Oldroyd model has been rarely implemented. Generally speaking, the utility of the constitutive relations in hydrodynamic problem solving has been inversely proportional to the complexity of the relation (Bird, 1976).

Though the four key phenomena are important, shear-thinning is probably the most important one for many engineering applications (Bird *et al.*, 1987, pp. 106–107). To illustrate, consider a common problem in the petroleum industry. During the transportation of waxy crude oil and gas condensate mixtures in subsea pipelines, as soon as the temperature is lower than the wax appearance temperature, paraffin crystals start to precipitate in the crude oil (Pedersen & Rønningsen, 2000). These precipitations bring about a number of interconnected challenges, such as reduction of the effective pipe diameter, variations of pressure drop in the pipeline, and the appearance of non-Newtonian behaviour in the suspension. Regarding the latter, a volume fraction of wax particles of even a few tenths of a percent causes pronounced shear-thinning behaviour (Rønningsen, 2012). The importance and wide-spread occurrence of shear-thinning

phenomenon is seen as well from the non-Newtonian examples mentioned in the introductory paragraph to this section. Most of them are known to exhibit some degree of shear-thinning. In the following lines, the discussion is centred around shear-thinning and related phenomena.

The recognition of different rheological behaviours has led not only to numerous models but also to classification schemes beyond the Newtonian–non-Newtonian fluid distinction. Such schemes are convenient for grouping rheological features albeit, at the same time, they are quite arbitrary and to some extent confusing when doing systematic reading of the available literature. For example, when considering fluid categories according to their main response in simple shear flow, some authors broadly classify fluids as time-dependent and time-independent fluids (see e.g., Ionescu *et al.*, 2020) whereas others recognize viscoelasticity as an additional category (see e.g., Chhabra & Richardson, 2008; Irgens, 2014, p. 5 and p. 8, respectively). Nevertheless, none of the two classification schemes cover effects such as differences of normal stresses in shear, for instance. Moreover, although the mentioned key phenomena are perhaps the most important ones, these are to date only a fraction of all observed rheological phenomena. A more broad yet still arbitrary and not all-inclusive organization for macroscopic rheological behaviour of fluids, could be based upon the four key phenomena. Furthermore, rheological phenomena commonly listed in the time-dependent and time-independent fluid categories (e.g. thixotropy and shear thickening), in a sense, are all related to the shear-thinning phenomenon (Ewoldt & Saengow, 2022). The following rheological behaviours can be grouped in the category of 'related to shear-thinning phenomenon':

- Shear-thickening. It is the opposite behaviour to shear-thinning; i.e., an increase of viscosity with flow strength. Morris (2020) is recommended for a review on recent developments and current issues.
- Yield stress. It is, basically, shear-thinning behaviour to the extreme. That is, solid-like-to-fluid transition at a particular critical stress or range of stresses (Ewoldt & Saengow, 2022).
- Thixotropy. It refers to reversible, time-dependent, shear-thinning behaviour; i.e., decrease of viscosity with time at high flow strength and subsequent recovery with time at low flow strength (Larson & Wei, 2019). The opposite phenomenon from thixotropy is called anti-thixotropy or rheophexy; i.e., reversible, time-dependent increase in viscosity (Mewis & Wagner, 2009).

Figure 1.2 shows the difference between Newtonian, shear-thinning, and the other phenomena grouped as related to shear-thinning behaviour.

Returning to the topic of constitutive equations and considering the responses illustrated in figure 1.2, it seems generalizing Newton's law of friction

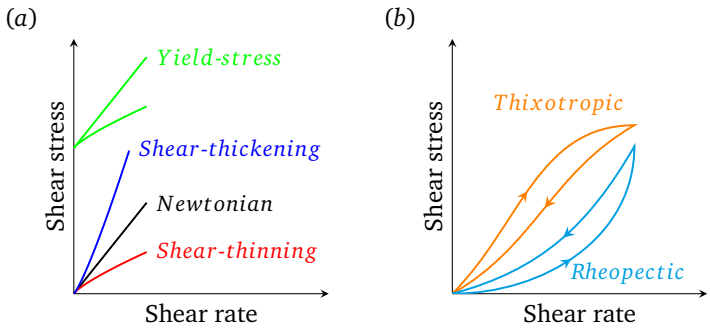

Figure 1.2: Illustration of response to simple shear for: (*a*) Newtonian, shear-dependent and yield-stress rheological behaviours and (*b*) time-dependent rheological behaviours related to shear-thinning.

is the simplest approach to account for shear-thinning/thickening fluid behaviour. The empiricism consists into changing the proportionality constant (dynamic viscosity) to a material function (apparent viscosity) depending on the rate of deformation. Under such rationale, one can write

$$\tau_{ij}^{\mathrm{GN}} = 2\mu \mathrm{S}_{ij}, \tag{1.1}$$

where, τ_{ij}^{GN} is the viscous stress tensor, $\mu = \mu(\dot{\gamma})$ is the apparent dynamic viscosity solely depending on the strain rate $\dot{\gamma} = \left(2\mathrm{S}_{ij}\mathrm{S}_{ji}\right)^{1/2}$, and $\mathrm{S}_{ij} = \left(\partial u_i/\partial x_j + \partial u_j/\partial x_i\right)/2$ is the strain rate tensor. Here, u_i denotes the velocity component in the i direction. Also, when index notation is used, subscript i (or any other subscript) takes the value 1, 2 or 3 to represent the component in the x, y or z direction of the Cartesian coordinate system, respectively; e.g., $(x_1, x_2, x_3) = (x, y, z)$ and $(u_1, u_2, u_3) = (u, v, w)$. Equation (1.1) is the constitutive equation for time-independent, purely viscous (inelastic and without a yield-stress) fluids known as generalized Newtonian or GN fluids. It is stressed that GN fluids are only an idealization of real fluids presenting shear-dependent viscosity as their most characteristic rheological feature. In addition, from a reverse viewpoint and since constant viscosity can be interpreted as a viscosity function whose value is the same for every $\dot{\gamma}$-value, Newtonian fluids can also be viewed as a particularisation of GN fluids.

Many models have been proposed for $\mu(\dot{\gamma})$; the most widely used are:

- Power-law model (de Waele, 1923; Ostwald, 1925). In this model, the apparent viscosity is described with a function that is proportional to some power of $\dot{\gamma}$; i.e.,

$$\mu(\dot{\gamma}) = \mathcal{M}\dot{\gamma}^{\alpha-1}. \tag{1.2}$$

The power-law model has two parameters to be fitted experimentally: (i) $\mathcal{M}\,[\mathrm{Pa}\cdot\mathrm{s}^{\alpha}]$ known as the consistency index and (ii) $\alpha\,[-]$ known as the power-law or flow index. $\mathcal{M}$ is related to the magnitude of the viscosity. On the other hand, α controls the macroscopic rheological behaviour. When $\alpha = 1$ Newtonian behaviour is recovered. If $\alpha < 1$ the fluid is said to be shear-thinning, whereas if $\alpha > 1$ the fluid is said to shear-thickening. The power-law model has two bad features (Bird, 1976): (i) it gives unrealistic values for the viscosity at low and high values of $\dot{\gamma}$ and (ii) no characteristic time, useful to characterize the fluidity of the material, can be constructed from $\mathcal{M}$ and α.

- Carreau-Yasuda model (Carreau, 1968; Yasuda, 1979). The model corrects the undesirable features of the power-law fitting, and reads

$$\mu = \mu_{\infty} + (\mu_0 - \mu_{\infty})\left[1 + (\Lambda\dot{\gamma})^b\right]^{(\alpha-1)/b}. \tag{1.3}$$

The Carreau-Yasuda model is more complex since it has five parameters to be fitted experimentally (Morrison, 2001, p. 231): (i) $\mu_{\infty}\,[\mathrm{Pa}\cdot\mathrm{s}]$ known as the infinite-shear-rate-viscosity; i.e., asymptotic value attained as $\dot{\gamma}$ gets large, (ii) $\mu_0\,[\mathrm{Pa}\cdot\mathrm{s}]$ known as the zero-shear-rate-viscosity; i.e., constant value approached as $\dot{\gamma}$ gets small, (iii) $\Lambda\,[\mathrm{s}]$ is a time constant for the fluid and determines the shear rate at which the plateau for μ_0/μ_{∞} ends/begins, (iv) $b\,[-]$ is an exponent that affects the shape of the transition between zero-shear-rate plateau and the power-law-like region of the viscosity rheogram, and (v) $\alpha\,[-]$ is still the power-law index. With $b = 2$, equation (1.3) is known as the Carreau model which describes viscosity data well enough for most engineering applications (Bird, 1976).

Figure 1.3 displays two viscosity profiles for 'normal whole blood' (Cho & Kensey, 1991); one corresponding to power-law and the other to the Carreau model. From this figure, one can note some of the aforementioned features of the two models. Other models such as the Eyring (Ree *et al.*, 1959) or Spriggs (Spriggs, 1965) models have been used but most studies have concentrated on the power-law or the Carreau models (Macosko, 1994, p. 87).

1.1.3 Wall-bounded shear flows of GN fluids

Wall-bounded shear flows refer to turbulent flows bounded (at least in part) by one or more solid surfaces (Pope, 2000, p. 264), and in which the mean velocity is predominantly one-dimensional in nature (Davidson, 2015, p. 105). This family includes both internal and external flows, such as those mentioned at the start of subsection 1.1.1. Therefore, the study and understanding of wall-bounded turbulent flows is of enormous technological importance. For instance,

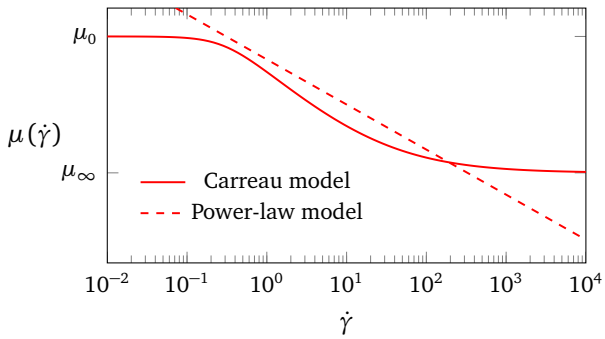

Figure 1.3: Comparison of viscosities calculated using the power-law and Carreau models for blood. Parameters for the two models as given in Cho & Kensey (1991).

about half the energy spent in transporting fluids through pipes and channels, or moving vehicles through air and water, is dissipated by turbulence in the immediate vicinity of walls (Jiménez, 2012). Furthermore, as highlighted in subsection 1.1.1, scientific work about turbulence probably began with observations about pipe flow (a type of turbulent shear flow limited by walls), and in certain aspects, wall-turbulence is more accessible than other problems in turbulence. Let us think about Kolmogorov's theory of locally isotropic turbulence (Kolmogorov, 1941*a*,*b*); i.e, turbulence where all statistics are invariant under translations, rotations and reflections of the spatial coordinate system and shifts in time. The theory follows Richardson's phenomenology of an energy cascade (see Richardson, 1922, p. 66), where energy is transferred from the largest scales to the smallest ones through a self-similar 'inertial' cascade (see e.g., schematic representation in Jiménez, 2004, p. 596), until it is dissipated by viscosity. Kolmogorov's theory of the small scales has been quite successful in predicting an energy spectrum which closely approximates the experimental observations, not only for isotropic turbulence but for small-scale turbulence in general (Jiménez, 2013). Nevertheless, this theory does not answer a fundamental question: *how energy enters the cascade in a first place?*. Conversely in shear flows, the source of energy is clear (gradient of the average/mean velocity), and energy enters turbulence through the interaction of that source with the transverse velocity fluctuations (Jiménez, 2013).

Our discussion about wall-bounded turbulence starts with the so-called classical theory found in most textbooks (see e.g., Monin & Yaglom, 1971; Tennekes & Lumley, 1972; Pope, 2000; Davidson, 2015). The theory concerns canonical wall-bounded turbulent flows (smooth pipes, channels and constant-pressure boundary layers), and in what follows, it is presented for the simplest case of

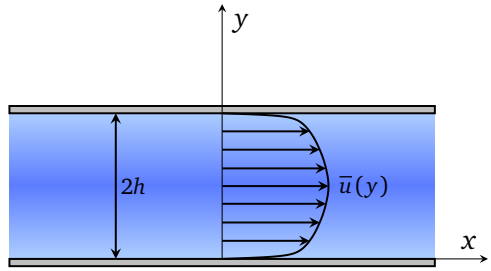

Figure 1.4: Turbulent plane channel flow.

a fully developed plane turbulent channel flow. The initial focus is on central issues such as the balance of mean forces, mean velocity profiles and scaling.

Consider turbulent flow through a rectangular smooth duct of height $2h$ which is unidirectional driven by a pressure gradient. The duct is extremely long ($L/h \gg 1$) and wide ($W/h \gg 1$); a plane channel, and it is at rest with respect to the Cartesian coordinate system. The streamwise, wall-normal, and spanwise directions are denoted by x, y and z, respectively. Hence, with the exception of the pressure that decreases from entrance to exit, derivatives of mean quantities with respect to x are assumed to be zero. All derivatives with respect to z are also assumed to be zero. Moreover, the mean flow is considered: (i) stationary and (ii) to be in the $x-y$ plane since it is driven in the x direction. A sketch of the turbulent plane channel flow is shown in figure 1.4. The only non-zero mean velocity is the streamwise component, $\overline{u}(y)$, since continuity requires the y component to be zero everywhere if it is zero at the impermeable, non-slip walls. Then, for an incompressible GN fluid at constant temperature, the relevant equations are the x and y mean-momentum equations which read

$$0 = \frac{\mathrm{d}\overline{\tau^{\mathrm{R}}_{xy}}}{\mathrm{d}y} - \frac{\partial \overline{p}}{\partial x} + \frac{\mathrm{d}\overline{\tau^{\mathrm{GN}}_{xy}}}{\mathrm{d}y}, \tag{1.4}$$

and

$$0 = \frac{\mathrm{d}\overline{\tau^{\mathrm{R}}_{yy}}}{\mathrm{d}y} - \frac{\partial \overline{p}}{\partial y} + \frac{\mathrm{d}\overline{\tau^{\mathrm{GN}}_{yy}}}{\mathrm{d}y}. \tag{1.5}$$

These equations are obtained by introducing the Reynolds decomposition into the Navier–Stokes equations, and then averaging in the homogeneous directions and time. Here, $\overline{\tau^{\mathrm{R}}_{ij}} = -\rho\overline{u'_i u'_j}$ is the turbulent stress or so-called Reynolds stress tensor, $\overline{(\,)}$ and $(\,)'$ are used to indicate the mean (averaged in time and homogeneous directions) and fluctuating parts of a scalar, vector or tensor field, respectively, ρ is GN fluid density, and $\overline{p}$ is the mean pressure.

Integration of equation (1.5), from the wall ($y = 0$) to a position y in the channel, yields

$$\overline{p}(x, y) = \overline{\tau_{yy}}(y) - \overline{\tau^{\mathrm{GN}}_{yy_w}} + \overline{p_w}(x), \tag{1.6}$$

where, $\overline{\tau_{yy}} = \overline{\tau^{\mathrm{R}}_{yy}} + \overline{\tau^{\mathrm{GN}}_{yy}}$. Since $v' = 0$ at $y = 0$, $\overline{\tau^{\mathrm{R}}_{yy}}$ is zero at the wall. Also, $\overline{\tau^{\mathrm{GN}}_{yy_w}} = \overline{\tau^{\mathrm{GN}}_{yy}}(y = 0)$, and $\overline{p_w} = \overline{p}(x, y = 0)$. Because $\overline{\tau_{yy}}$ is independent of x and $\overline{\tau^{\mathrm{GN}}_{yy_w}}$ is a constant, it follows that $\partial\overline{p}/\partial x = \mathrm{d}\overline{p_w}/\mathrm{d}x$. In consequence, equation (1.4) can be re written as

$$\frac{\mathrm{d}\overline{p_w}(x)}{\mathrm{d}x} = \frac{\mathrm{d}\overline{\tau_{xy}}(y)}{\mathrm{d}y} = \text{constant}, \tag{1.7}$$

where the total mean shear stress, $\overline{\tau_{xy}}(y) = \overline{\tau^{\mathrm{R}}_{xy}} + \overline{\tau^{\mathrm{GN}}_{xy}}$. For this flow there is no mean acceleration, so equation (1.7) amounts to a balance of mean forces: the axial normal stress gradient is balanced by the cross-stream shear-stress gradient (Pope, 2000, p. 267). Once again, integrating from the wall ($y = 0$) to a position y in the channel, results in

$$\overline{\tau_{xy}}(y) - \overline{\tau_w} = \frac{\mathrm{d}\overline{p_w}}{\mathrm{d}x} y. \tag{1.8}$$

At the centre of the channel ($y = h$), $\overline{\tau_{xy}}$ must be zero due to symmetry reasons. Hence, if $y = h$, equation (1.8) simplifies to

$$\frac{\mathrm{d}\overline{p_w}}{\mathrm{d}x} = -\frac{\overline{\tau_w}}{h}, \tag{1.9}$$

which is the aforementioned constant. Finally, considering result (1.9), equation (1.8) recasts to

$$\overline{\tau_{xy}}(y) = \overline{\tau_w}\left(1 - \frac{y}{h}\right). \tag{1.10}$$

Thus, for a given constant (negative) mean pressure gradient, channel half-height and regardless of the type of fluid (e.g., Newtonian or shear-dependent), equation (1.10) gives the total mean shear stress profile for the plane channel. The importance of the mean shear stress (and more specifically of $\overline{\tau_w}$) is not to be overlooked. From a practical point of view, a closed channel is but a carrier that allows the transport of fluid from one location to another. For this purpose, one can connect the channel to the discharge of another carrier; directly imposing a flow rate. Alternatively, a mechanical device (e.g., a pump) can be used to increase the fluid pressure at the channel's entrance. However, as seen from equation (1.9), the increase in pressure should be large enough such that the resulting pressure gradient balanced out the resistance exerted by the enclosing walls. In other words, $\overline{\tau_w}$ is the skin friction; i.e., the resistance to flow due

to viscous effects (recall that $u_i' = 0$ at $y = 0$). Based on $\overline{\tau_w}$, it is also customary to define different skin-friction coefficients such as $c_f = \overline{\tau_w}/\left(0.5\rho\overline{u_c}^2\right)$ and $C_f = \overline{\tau_w}/\left(0.5\rho\overline{u_b}^2\right)$. Here, $\overline{u_c} = \overline{u}(y = h)$ is the mean velocity at the channel centre, and $\overline{u_b} = \int_0^h \overline{u}(y)\,\mathrm{d}y/h$ is the bulk velocity. It can be seen that the mean velocity profile is required for calculating either of these reference velocities. Furthermore, $\overline{u_c}$, $\overline{u_b}$, and $\overline{u}(y)$ in general, may be used in flow rate estimations. Hence, the determination of the mean velocity profile is quite important as well.

In principle, solving equation (1.10) would yield the mean velocity profile, yet to solve this equation we need to know the distribution for the turbulent shear stress. The situation is even more complicated for shear-dependent rheology, since we also need the distributions for $\overline{\mu}$ and $2\overline{\mu' S_{xy}'}$; the later arising due to viscosity fluctuations. At this point, one possibility is to introduced closures for the different terms (e.g., mixing length theory for $\overline{\tau_{xy}^{\mathrm{R}}}$). Another possibility would be to use dimensional analysis and asymptotic observations. Considering that both $\overline{\tau_{ij}^{\mathrm{R}}}$ and $\overline{\tau_{ij}^{\mathrm{GN}}}$ contribute to the total mean shear stress, it is reasonable to expect that these contributions are not always of the same order-of-magnitude. Moreover, the boundary conditions already hinted to a flow subdivision of at least two regions with their corresponding sets of scaling parameters. The non-slip condition at the wall give rise to a viscous-dominated region of characteristic length $\ell \ll h$, whereas far away from it, there is another region with characteristic length h where inertial effects are dominant. As the ratio $Re_\tau = h/\ell$ increases; the so-called frictional Reynolds number, the behaviour of these two regions is expected to be more and more distinct. Therefore, treating the flow in a piece-wise fashion, we have (at least) an inner-layer region where $y/h \ll 1$, and an outer-layer region where $y/\ell \gg 1$. Of course, if the length-scale ratio Re_τ is large enough, it should be possible to encounter an overlap region where both conditions hold simultaneously (Tennekes & Lumley, 1972, p. 147).

For the inner-layer region ($y/h \ll 1$), equation (1.10) may be re written as

$$-\rho\overline{u'v'} + \overline{\mu}\frac{\mathrm{d}\overline{u}}{\mathrm{d}y} + \overline{\mu'\left(\frac{\partial u'}{\partial y} + \frac{\partial v'}{\partial x}\right)} \approx \overline{\tau_w} \equiv \rho u_\tau^2, \tag{1.11}$$

where, u_τ is a friction velocity based on $\overline{\tau_w}$ and ρ. Taking u_τ and μ_c as characteristic velocity and viscosity, leads us to a characteristic viscous-length $\ell = \mu_c/(\rho u_\tau)$. For this dimensional group, and because in the plane channel $\overline{u}$ is a function of y only, the solution has the functional form

$$\frac{\overline{u}}{u_\tau} = f\left(y/\ell\right), \quad y/h \ll 1. \tag{1.12}$$

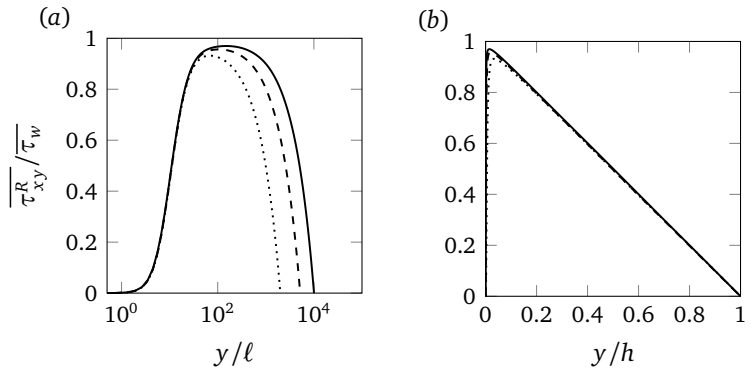

Figure 1.5: Distribution of $-\overline{u'v'}/u_\tau^2$ for turbulent channel flow of a Newtonian fluid against: (*a*) y/ℓ and (*b*) y/h. Dotted, dashed, and continuous lines styles correspond to $Re_\tau \approx 2000$ (Hoyas & Jiménez, 2006), 5200 (Lee & Moser, 2015), and 10000 (Hoyas *et al.*, 2022), respectively.

The same is expected for any other statistical turbulence quantity (e.g., $\overline{u'v'}/u_\tau^2 = f_2(y/\ell)$ as seen in figure 1.5 (*a*), $\overline{\mu}/\mu_c = f_3(y/\ell)$, and so on). For shear-dependent viscosity (as for many other types of non-Newtonian rheology), there is no consensus about the characteristic viscosity. For Newtonian rheology, μ_c is simply the dynamic viscosity at a given temperature. Equation (1.11) is known as the law of the wall and was postulated by Prandtl (1925) for fluids with constant viscosity. Also, normalized quantities based on the dimensional group corresponding to the inner-layer region are often called inner or wall units, and are denoted by the superscript +. For example, $y^+ = y/\ell$ and $\overline{u^+} = \overline{u}/u_\tau$.

On the other hand, for the outer-layer region ($y/\ell \gg 1$), towards the channel centre and where viscous effects are fairly negligible; see figure 1.5 (*b*), equation (1.10) simplifies to

$$-\frac{\overline{u'v'}}{u_\tau^2} \approx \left(1 - \frac{y}{h}\right). \tag{1.13}$$

Thus, u_τ and h appear to be the relevant characteristic velocity and length for the outer-layer region. In consequence, we would expect functional forms of the type $g(y/h)$ such as equation (1.13). In case of the mean velocity profile, it is customary to express its departure from the centreline value as

$$\frac{\overline{u_c} - \overline{u}}{u_\tau} = F(y/h), \quad y/\ell \gg 1. \tag{1.14}$$

This expression is due to von Kármán (1930) and it is known as the velocity defect law.

Now, let us consider the overlap region (also known as the inertial sublayer), where $\mathcal{H} = y/h \ll 1$ and $y^+ \gg 1$ hold simultaneously. Here, equation (1.10) results in

$$-\frac{\overline{u'v'}}{u_\tau^2} \approx 1 \equiv \text{constant}, \tag{1.15}$$

which is consistent with the assumption of having descriptions of the type $g\left(y^+\right)$ and $G(\mathcal{H})$ that are valid at the same time. Following the approach of Millikan (1938), and matching the wall-normal gradients of equations (1.12) and (1.14), we obtain

$$\frac{u_\tau}{\ell}\frac{\mathrm{d}f\left(y^+\right)}{\mathrm{d}y^+} = -\frac{u_\tau}{h}\frac{\mathrm{d}F(\mathcal{H})}{\mathrm{d}\mathcal{H}}. \tag{1.16}$$

Multiplying by y/u_τ, this becomes

$$y^+\frac{\mathrm{d}f\left(y^+\right)}{\mathrm{d}y^+} = -\mathcal{H}\frac{\mathrm{d}F(\mathcal{H})}{\mathrm{d}\mathcal{H}} = \text{constant} \equiv \frac{1}{\kappa}. \tag{1.17}$$

On the integration, and subsequent substitution into (1.12) and (1.14), we find

$$\frac{\overline{u}}{u_\tau} = \frac{1}{\kappa}\ln y^+ + A, \quad \frac{\overline{u_c} - \overline{u}}{u_\tau} = -\frac{1}{\kappa}\ln y^+ + B, \quad \ell \ll y \ll h. \tag{1.18}$$

This is the log-law of the wall, κ is known as the von Kármán constant, and A, B are the additive constants. At present, there is considerable evidence that these constants are probably flow-dependent (see, e.g., Nagib & Chauhan, 2008; Marusic *et al.*, 2010; Smits *et al.*, 2011). Nevertheless, in case of Newtonian fluids, most of the reported values for κ and A are generally within 5% of 0.41 and 5.2, respectively (Pope, 2000, p. 274). The log-law is extremely popular since it has proved to be an excellent fit to the experimental data, but it has its detractors (Davidson, 2015, p. 125). Some researchers have proposed the use of a power-law with Re_τ-dependent coefficients for the overlap region (see, e.g., Buschmann & el Hak, 2003). In this regards, recently, Oberlack *et al.* (2022) claimed to have shown that the profile of $\overline{u}$ in the overlap region (there, $400 \lesssim y^+ \lesssim 2500$) is indeed logarithmic. In summary, equations (1.12), (1.14) and (1.18) are the mean velocity distributions in the limit of $Re_\tau \to \infty$, for the classical two-layer region description with a single overlap. The start of the inner-layer region and up to $y^+ \approx 5$ is often referred to as the viscous sublayer, and there $\overline{u} \approx y^+$. This thin-layer is observed as well in turbulent wall-bounded flow of shear-dependent fluids (Singh *et al.*, 2018). The region between viscous sublayer and the log-law region is called buffer layer. The start of the log-law is not very distinct, but it seems to be somewhere in the interval $30 \lesssim y^+ \lesssim 400$.

The same can be said about the end of the log-law, which seems to be within the interval $0.1 \lesssim \mathcal{H} \lesssim 0.25$.

The two sets of parameters corresponding to the classical inner-/outer-layer description have not been entirely successful in the scaling of wall-bounded turbulence statistics (see, e.g., section about raw statistical quantities in Spalart & Abe, 2021). These scaling failures have led to corrections of the classical description and to empirical scaling of some quantities based on Re_τ (see, e.g., Luchini, 2017, 2018; Spalart & Abe, 2021), and to alternative approaches such as a three-layers region description with two overlap layers (e.g., Afzal & Bush, 1985; Sreenivasan & Sahay, 1997), and a four-layer region description (Wei *et al.*, 2005). On a personal level, the latter is found particularly appealing since the starting point of the analysis is the mean differential statement of dynamics (Klewicki, 2013); i.e., equation (1.4) instead of equation (1.10). This is the actual governing equation (momentum) of the problem we attempt to solve (turbulent flow field). Furthermore, the ideas of Wei *et al.* (2005) can be extrapolated to explore different effects in the canonical wall-bounded flows (see e.g., White *et al.*, 2018; Wei, 2018), and to improve our understanding of more complex flows (see e.g., Wei, 2020).

Up to this point and broadening the arguments of the classical theory to include shear-dependent rheology, we have outlined some central issues about wall-bounded turbulent flows. However, we have yet to address another matter of importance: *how is the shear-dependency of the viscosity affecting these central issues?*. Of course, we should consider which fluids are to be compared in a first place. For instance, in polymeric solutions, some authors are of the opinion that the polymeric solution is to be compared to the pure solvent (Lumley, 1969) whereas others have taken as a benchmark fluid, a hypothetical Newtonian fluid having about the same shear viscosity as the polymeric solution at the wall (e.g., Draad *et al.*, 1998; Warholic *et al.*, 1999; Ptasinski *et al.*, 2001). In our opinion, since viscous effects are known to be particularly important in the regions of high mean shear near the wall ($y^+ \lesssim 50$, see definition of the 'viscous wall region' in Pope, 2000, pp. 270–271), it does seem reasonable to compare Newtonian and shear-dependent fluids having about the same shear viscosity at the wall, and under the same operational conditions (same flow rate or streamwise pressure gradient). In what remains of the subsection, we will highlight some differences between a shear-thinning fluid and a corresponding Newtonian benchmark fluid, in terms of frictional drag, mean velocity distribution, and mean shear stress. The discussion about the differences between a shear-thickening fluid and its Newtonian benchmark fluid are omitted since as previously remarked, this is simply the opposite behaviour to shear-thinning.

As commented earlier, it is customary to present the skin friction in a nondi-

mensional form; e.g., C_f. From a physical point of view, C_f is the ratio between skin friction and a measure of the mean fluid kinetic energy per unit volume. In consequence, a(an) decrease(increase) of C_f implies a(an) decrease(increase) of the skin friction drag respect to the measure of available mean kinetic energy. Thus, C_f can be used to define a decrease or increase in the level of drag with respect to a benchmark case. Assuming shear-thinning rheology results in drag reduction (DR), we defined the level of DR as (Gyr & Bewersdorff, 1995, p. 9)

$$\mathrm{DR}\% = \frac{C_{f,N} - C_{f,P}}{C_{f,N}} \times 100\%. \tag{1.19}$$

Here, the subscripts 'N' and 'P' stand for Newtonian and pseudoplastic (another name used to describe shear-thinning behaviour) fluid cases, respectively. When comparing fluids at the same $\overline{\tau_w}$, equation (1.19) can be rewritten as

$$\mathrm{DR}\% = \left[1 - \left(\frac{\overline{u_{b,N}}}{\overline{u_{b,P}}}\right)^2\right] \times 100\%, \tag{1.20}$$

which is to be a positive percentage amount in case of drag reduction. In consequence, we expect $\overline{u_{b,P}} > \overline{u_{b,N}}$. Likewise, in case of a given flow rate, *DR* is reflected in $\overline{\tau_{w,P}} < \overline{\tau_{w,N}}$. The fact that the bulk velocity is larger for a given $\overline{\tau_w}$, implies an enhancement of $\overline{u}$ towards the core of the wall-bounded flow when comparing a shear-thinning fluid case with the corresponding Newtonian fluid benchmark. Moreover, assuming logarithmic behaviour occurs in a overlap region and the same ℓ is used in the scaling, an upshifted log-law profile is expected for such shear-thinning fluid case. On the other hand, with respect to the mean shear stress and for the same $\overline{\tau_w}$, there should be a redistribution in the contributions of $\overline{\tau^{\mathrm{R}}_{xy}}$ and $\overline{\tau^{\mathrm{GN}}_{xy}}$. In case of a shear-thinning fluid, because of the local increase in viscosity as we move from the wall and due to larger wall-normal streamwise velocity gradients, we can expect $\overline{\tau^{\mathrm{GN}}_{xy,P}} > \overline{\tau^{\mathrm{GN}}_{xy,N}}$, and therefore $\overline{\tau^{\mathrm{R}}_{xy,P}} < \overline{\tau^{\mathrm{R}}_{xy,N}}$, in regions where viscous effects cannot be neglected. Another point to remark is that for shear-dependent rheology, $\overline{\tau^{\mathrm{GN}}_{xy}}$ may be split into a contribution due to mean quantities and another based on the correlation between the fluctuations in viscosity and the fluctuations in the shear rate. That is

$$\overline{\tau^{\mathrm{GN}}_{xy}} = \overline{\tau^{\mathrm{N}}_{xy}} + \overline{\tau^{\mathrm{NN}}_{xy}}, \tag{1.21}$$

where, $\overline{\tau^{\mathrm{N}}_{xy}} = 2\overline{\mu}\overline{S_{xy}}$ and $\overline{\tau^{\mathrm{NN}}_{xy}} = 2\overline{\mu' S'_{xy}}$. The latter term being nonzero since $\mu \neq$ constant. Here, it is reasonable to ponder how large is this new nonlinear contribution with respect to the traditional viscous term, i.e., $\overline{\tau^{\mathrm{N}}_{xy}}$. For a shear-thinning fluid case, $\overline{\tau^{\mathrm{NN}}_{xy}}$ and $\overline{\tau^{\mathrm{N}}_{xy}}$ are of opposite sign and at most, $\overline{\tau^{\mathrm{NN}}_{xy}}/\overline{\tau^{\mathrm{N}}_{xy}} \approx$

$\alpha-1$ (Collins, 1990, pp. 59–61). Naturally, this is still constrained to $\overline{\tau_{xy}^{\mathrm{GN}}} = \overline{\tau_w}$ at the wall, thus for $\alpha < 1$, the ratio is smaller in magnitude than $\alpha - 1$.

Finally, in regards to wall-bounded flows of GN fluids, there is still much more that can be discussed, e.g., turbulence intensities, budgets for the Reynolds stresses, intermittency, anisotropy, Reynolds number effects, or the similarities and differences between the canonical flows, among many other interesting topics. Even so, we stop here with our briefing since the subsection is meant for outlining only some of the most fundamental aspects that can be discussed without relying too much on experimental and numerical data of previous studies.

1.1.4 Coherent structures and their identification

In subsection 1.1.3, we considered some key aspects about the classical mean-field theory of wall-bounded turbulence. From a practical perspective, such approach is possibly the most useful. Indeed, it is customary to design and select engineering devices using estimations based on relevant flow statistics rather than on individual realizations of the flow. Nonetheless, the traditional view has an important drawback; it provides limited insight into the flow dynamics. This has brought forth a complementary approach where one hopes that at least part of the dynamics can be described in terms of a relatively small number of more elementary processes than the full Navier–Stokes (NS) equations (Jiménez, 2018). The basic idea is that there are regions of space and time (significantly larger than the smallest local scales) within which the flow field has a characteristic coherent pattern (Pope, 2000, p. 322). These patterns, known as coherent structures (CS) or organized motions, make important contributions to the statistics of the flow (Marusic & Adrian, 2012). In consequence, beyond our desire to find order in apparent disorder (Hussain, 1986), the study of CS is also technologically driven; we hope to understand these structures in order to modify them and achieve engineering goals such as, reduction of drag in pipes and enhancement of mixing in chemical reactors. It is worth commenting that the structural view probably started with Theodorsen (1952, 1955), who proposed a horseshoe vortex as the central structural element (Lozano-Durán, 2015, p.11); see figure (1.6). Interestingly, Theodorsen ideas about the importance of horseshoe vortices in turbulence initially received a lukewarm reception from the community (Adrian, 2007) and were even very much opposed by some groups (see Lumley & Davis, 2003, p. 6). At higher Reynolds numbers, horseshoes are known as hairpins vortices (see, e.g., Head & Bandyopadhyay, 1981).

Efforts to isolate organized motion usually proceed in two ways (Cantwell, 1981): (i) inferences based on statistics and construction of entities repres-

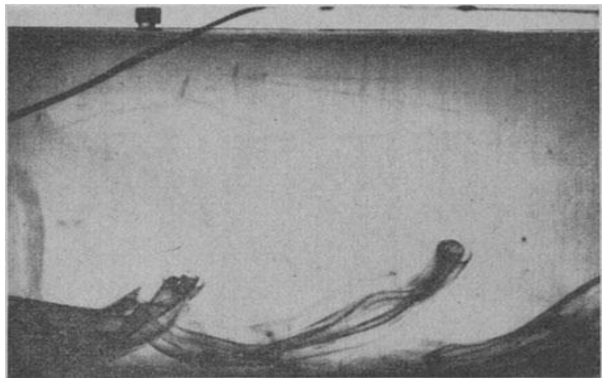

Figure 1.6: Structure labelled as horseshoe vortex by Theodorsen (1955). From Theodorsen (1955), copyright ©1955 Springer Fachmedien Wiesbaden.

enting the most probable state of the flow, which are not necessarily observable instantaneously or individually (Hussain, 1986), and (ii) identification of instantaneous flow structures. Naturally, both descriptions may be related; a strong instantaneous event occurring often enough should leave traces in a related statistical representation. Moreover, statistics are also required for the characterization of the structures identified instantaneously. These connections between statistical representations and actual structures are (unfortunately) often reflected in the terminology used when discussing CS. For instance, some works use 'eddies' to denote a statistical construct, whereas others for denoting large-scale motions visualized instantaneously, or simply as a synonym for vortices. To avoid potential misunderstandings, the term eddy(ies) is left for inferences about statistics and corresponding stochastic constructs. In what follows, some of the most well-known coherent motions in wall-bounded turbulence are introduced.

Wall-bounded flows are inhomogeneous and anisotropic, and as seen before, the wall segregates them into layers that are studied separately (Jiménez, 2012). Up to the upper edge of the buffer layer, the dominant structural features are streaks (low- and high- speed regions of streamwise velocity) and quasi-streamwise vortices/rolls involved in a self-sustaining process (Robinson, 1991; Panton, 2001; Jiménez, 2013). The streaks carry turbulent kinetic energy whereas the vortices, organize both the dissipation and the momentum transfer (Jiménez, 2013); one can consider a vortex with an orientation other than wall normal as a 'pump' that transport momentum across the mean velocity gradient (Robinson, 1991). In regards to the self-sustaining or regenerative process, the consensus is that the rolls cause the streaks by 'pumping' away fluid from the wall (Blackwelder & Eckelmann, 1979) however, there is still some degree

of uncertainty about how the streaks generate the rolls. A compelling possibility is that newborn streaks undergo meandering motion, breakdown and the perturbations created by the disrupted streaks generate the rolls through nonlinear interactions (see, e.g., Hamilton *et al.*, 1995; Jiménez & Pinelli, 1999; Schoppa & Hussain, 2002). Recent evidence (Lozano-Durán *et al.*, 2021) seems to suggest that among the various possible mechanisms leading to the breakdown of the streaks, non-modal transient growth (Schoppa & Hussain, 2002) is sufficient for sustaining realistic wall turbulence.

It is hypothesized that a similar but more disorganized dynamical scenario to the one describe above occurs away from the wall (see, e.g., Flores & Jiménez, 2010; Cossu & Hwang, 2017; Lozano-Durán *et al.*, 2020). The energy-containing structures are still streak, although internally turbulent ones of much larger size than in the buffer layer as studied by Sillero (2014), whereas the momentum transfer related structures are not the individual vortices any longer (Jiménez, 2013). The role of organizing the Reynolds stresses is taken by vortex clusters (del Álamo *et al.*, 2006) and tangential Reynolds-stress structures (Lozano-Durán *et al.*, 2012), which are three-dimensional (3D) analogues of the sweeps and ejections in the classical quadrant analysis (Wallace *et al.*, 1972). All these structures (large streaks, vortex clusters and 3D Reynolds-stress events) may be separated into attached and detached (background) families based on their minimum distance from the wall (see del Álamo *et al.*, 2006), and are self-similar in the log-law region. When considering a statistical construct based on neighbouring attached sweep-ejection pairs of similar size, the underlying composite structure consists of a sweep, an ejection to one side of it, and a vortex cluster in-between (see Lozano-Durán, 2015, sec. 3.6.1). The composite structure sits in the interface between low- and high-velocity streaks and it is compatible with a single streamwise large-scale roller (Jiménez, 2013, 2018). These self-similar attached streaks/rollers in the log-law region are consistent with Townsend's attached-eddy model (Townsend, 1976, pp. 152–154). For a recent review about attached-eddy models of wall-turbulence, Marusic & Monty (2019) is suggested. It is worth commenting that organized packets of hairpins have been shown to exist in the log-law region (Adrian, 2007), although they tend to be more common at relatively low Reynolds numbers and become disorganized as the Reynolds number increases (Jiménez, 2018). Additionally, regarding statistical descriptions outside the inner-layer, Jiménez (2013) remarked that the so-called large-scale motions (LSM, Adrian, 2007; Smits *et al.*, 2011) are probably the aforementioned composite structures. There are also very-large-scale motions (VLSM, Kim & Kim, 1999) or superstructures (Hutchins & Marusic, 2007*a*) which are even larger than the LSM. The LSM and VLSM descriptions may be particularly relevant at high Reynolds numbers,

where they have been associated with a significant amount of turbulent kinetic energy and tangential Reynolds stress (Guala *et al.*, 2006; Balakumar & Adrian, 2007). These motions have an influence in the inner-layer region (Hoyas & Jiménez, 2006; Hutchins & Marusic, 2007*b*). The clearest manifestation of such influence is, perhaps, the known scaling failures of some statistics as mentioned in subsection 1.1.3.

In general, advances in the study of CS in wall-bounded turbulence has benefited from three modern developments (see Jiménez, 2018): (i) linear approximations coming from stability analyses of transitional flows (see, e.g., Schmid & Henningson, 2001; Schmid, 2007), (ii) computation of nonturbulent nonlinear solutions of the NS equations (see, e.g., Kawahara *et al.*, 2012; Graham & Floryan, 2021), and (iii) direct numerical simulations (DNS) of wall-bounded turbulent flows. Approaches (i) and (ii) have been useful in shading light on the interactions between structures; i.e., the mechanisms of self-sustainment of turbulence, whereas approach (iii), in principle, has allowed us to capture all the flow complexities. Initially, DNS were restricted to low Reynolds numbers (Kim *et al.*, 1987), but with more powerful computers, current simulations (Oberlack *et al.*, 2022) are fairly closer to the largest well-resolved experimental results (Samie *et al.*, 2018). The main disadvantages of DNS are the computational time and the requirement for enough storage to save large amounts of data, in case dynamical analyses are of interest. Nonetheless, once stored, the spatially resolved sequences of 3D flow fields can be interrogated forwards and backwards in time to potentially answer 'any' question (Jiménez, 2018). As a result, DNS seem particularly appealing for studying structural coherence, yet precisely, *how do we approach CS identification?*

A classical approach to CS identification consists into isolating individually connected regions by thresholding some intense property (Jiménez, 2018). The considered property should be either relevant for what we aim to study (e.g., energy content, or momentum), or alternatively, an indicator for a particular type of CS already associated with our aim. Moreover, it would be even better if the considered property is quadratic and not linear (e.g., enstrophy vs. vorticity magnitude for vortex detection). The probability density function (PDF) of any quantity is made more intermittent by representing it in terms of a higher power of its variable, and it is more easy to threshold a more intermittent property, for which high intensity is more localized (Jiménez, 2018). Subsequently, the next point to address is how to select the threshold for isolating the CS. If the threshold is too low, most of the property of interest is captured but it is almost impossible to distinguish the CS individually. Conversely, for a very high threshold, only a few very intense structures accounting for a small fraction of the property of interest are detected. The percolation transition between these

two limits is typically sharp and may be used to define a threshold that includes a significant fraction of the property of interest while still segmenting the flow into individual structures (Jiménez, 2018). This systematic way of choosing a threshold was introduced by Moisy & Jiménez (2004) and has been successfully implemented for analysing CS in wall-bounded turbulence by del Álamo *et al.* (2006); Lozano-Durán *et al.* (2012); Sillero (2014), among others. It is important to remark that a threshold based on the percolation transition is only one among many possible threshold choices (Jiménez, 2018). Furthermore, the percolation transition results into a range of thresholds spanning about a decade and the selection of a given threshold within that range should be accompanied by a sensitivity analysis of the obtained results.

Finally, although the structures mentioned thus far have been reported for wall-bounded flows of Newtonian fluids, it is reasonable to anticipate the same same near-wall structures and interactions for shear-dependent rheology, just that with some degree of modification. For instance, assuming shear-thinning viscosity yields drag reduction when compared to a Newtonian base case, one can expect enhancement of the energy-containing structures and suppression of the momentum-transfer related ones. Recall that for a given $\overline{\tau_w}$, $\overline{u_{b,P}} > \overline{u_{b,N}}$ and $\overline{\tau^{\mathrm{R}}_{xy,P}} < \overline{\tau^{\mathrm{R}}_{xy,N}}$; see subsection 1.1.3.

1.2 Aims

The objective of this thesis is to improve our understanding in terms of the mechanics, and possible structural coherence of turbulent flows of Newtonian and shear-dependent viscosity fluids. Here, 'mechanics' is short for 'statistical fluid mechanics', and refers to the traditional approach of studying the flow statistics (e.g., means, standard deviations, correlations, and so on). Conversely, 'structural coherence' is referring to the study of CS (e.g., streaks, or quasi-streamwise vortices); i.e., their identification and characterization. In this regard, particular attention is paid to vortical structures. Vortices are quite relevant in chemical engineering (e.g., consider their role in mixing, or their interactions with fluid particles in turbulent dispersions). Also, the research is focused (slightly) more towards comparing the results of Newtonian and shear-thinning fluids. The latter is, perhaps, the most common type of time-independent non-Newtonian behaviour (Chhabra & Richardson, 2008, p. 6).

To accomplish the above, first, numerical simulations of turbulent channel flow of GN fluids at a target Re_τ are considered. Such configuration is selected not only for its technological importance, but also, because it has been extensively studied for Newtonian fluid rheology. In essence, the idea is to explore what changes (or not) in the canonical channel flow if the working fluid

presents even a slight-to-moderate degree of shear-dependent viscosity as its main rheological feature. Next, a further step in complexity is taken by considering the numerical simulations of turbulent flow of GN fluids in a baffled-stirred tank; a device commonly used in numerous industries for chemical and biochemical processes. The analyses in the stirred tank are limited to the study of vortical structures. The investigation of turbulent statistics in the agitated vessel is being continued elsewhere.

Altogether, this work aims to contribute to the exiting literature on shear-dependent viscosity fluids, turbulent channel flows, and stirred tank reactors.

1.3 Outline of thesis

Beyond this section, the thesis is organized into three more chapters. Chapter 2 briefly describes the numerical methodology and experiments. Chapter 3 provides a summary of each research article, with synopses of the main findings. Finally, chapter 4 concludes the thesis, remarking as well some limitations of this work and providing some suggestions for future ones. The research articles (papers I – IV) are included in full (as displayed in the journals) at the end of the thesis.

Chapter 2

Numerical simulations

> *The principal role of computers in fluid dynamics should be to give physical insight into dynamics, not to generate "realistic" flows or to extol the minor virtues of one numerical scheme over another.*
>
> *Orszag & Israeli (1974).*

The interest in the computation of turbulent flows probably started with V. Bjerknes in 1912 who hinted at the possibility of numerical weather forecasting (Hunt, 1998, p. xxi) but more concretely with Richardson (1922) who proposed the use of finite differences for discretizing the equations of weather prediction. At that time, computing was performed by individuals with the aid of slide rules and calculating machines, and Richardson fantasized with the idea of thousands of them in a large hall under coordination of a chief forecaster acting like an orchestra conductor (Richardson, 1922, p. 219). Nowadays, computing is performed by efficient electronic machines working in parallel within a network, and numerical methodologies for problem solving of turbulent flows consist of either Reynolds-averaged Navier–Stokes (RANS) equations modelling, or fully time-dependent simulations such as DNS and large-eddy simulations (LES). In this thesis, DNS and LES are implemented for simulating turbulent flows of GN fluids. In the following, some practical details about setting-up DNS and LES are outlined, and the considered numerical experiments are briefly explained.

2.1 DNS of turbulent channel flow of GN fluids

In DNS, the NS equations are numerically solved for all the scales of motions with initial and boundary conditions appropriate for the flow under consideration, and with each simulation producing a single realization (Pope, 2000, p.

344). Turbulence statistics are then computed on the fly, or afterwards based on collected flow fields. Details such as: grid resolution, domain size, time stepping, simulation time, number of stored flow fields (if they are to be collected for post-processing) and frequency of their storage, are some of the most common aspects to keep in mind while doing DNS. These aspects are closely related with the disadvantages mentioned for DNS in subsection 1.1.4; i.e., computational cost and storage requirement. The determination of the latter is perhaps more straightforward than the determination of the former. In case flow fields are to be collected, to an approximation, the storage requirement is given by the product of: (i) the total number of data points (in space and time) to be saved, (ii) the total number of components of the fields to be saved (e.g., velocity and pressure fields), and (iii) the amount of `bytes` (B) that are necessary to save each component in, e.g., a `.dat` or a `.ascii` file. For instance, considering 250×10^9 data points, the three velocity components and pressure to be saved, and about 8 B per component, results in 8 TB of data.

Now, let us explore the computational cost for DNS of a wall-bounded flow, such as turbulent channel flow (see figure 1.4). To an approximation, the required computational time $\left(T_{\text{comp}}\right)$ is given by

$$T_{\text{comp}} = \text{FLOP of simulation}\left(\frac{1}{\text{FLOP/s of machine}}\right), \tag{2.1}$$

where, FLOP stands for 'floating-point-operations', and T_{comp} is the ratio between the total number of computer operations required for the simulation to the theoretical peak FLOP/s of the used machine. Today, a standard computer node has CPU- and GPU-capabilities of (at least) about 1 GFLOP/s and 1 TFLOP/s, respectively, whereas massive HPC-systems have capabilities of (at least) about 1 PFLOP/s. On the other hand, the number of required computer operations depends on the total number of data points and the number of FLOP per datapoint which varies from computer code to computer code. The total number of data points $\left(N_{xyzt}\right)$ is given by

$$N_{xyzt} = N_x N_y N_z N_t, \tag{2.2}$$

where,

$$N_x = \frac{L_x}{\Delta x} \sim \frac{\mathcal{A}h}{\mathcal{D}\ell} \equiv \left(\frac{\mathcal{A}}{\mathcal{D}}\right) Re_\tau, \tag{2.3}$$

$$N_y = \frac{L_y}{\Delta y} \sim \frac{2h}{\mathcal{D}\ell} \equiv \left(\frac{2}{\mathcal{D}}\right) Re_\tau, \tag{2.4}$$

$$N_z = \frac{L_z}{\Delta z} \sim \frac{\mathcal{B}h}{\mathcal{D}\ell} \equiv \left(\frac{\mathcal{B}}{\mathcal{D}}\right) Re_\tau, \tag{2.5}$$

and

$$N_t = \frac{T_{\text{sim}}}{\Delta t} \sim \frac{T_{\text{sim}}}{\eta/u_\tau} \sim \frac{T_{\text{sim}}}{h/u_\tau} Re_\tau^{3/4} \equiv \mathcal{C} Re_\tau^{3/4}. \tag{2.6}$$

Here, L_x, L_y and L_z, and $\Delta x, \Delta y$ and Δz are the computational domain and grid resolution in the x-, y- and z-direction, respectively. T_{sim} and Δt represent simulation time and time stepping, respectively, and η is the Kolmogorov's length scale. $\mathcal{A}, \mathcal{B}, \mathcal{C}$ and $\mathcal{D}$ are constants larger than 1. Therefore,

$$N_{xyzt} \sim \frac{2\mathcal{A}\mathcal{B}\mathcal{C}}{\mathcal{D}^3} Re_\tau^{15/4}. \tag{2.7}$$

Assuming 1×10^4 FLOP per data-point are required, which is about 10 times the number of operations per data-point in DNS of homogeneous isotropic turbulence (Pope, 2000, p. 348), and that $2\mathcal{A}\mathcal{B}\mathcal{C}/\mathcal{D}^3 \approx 500$, close to 8.9×10^{17} FLOP are needed for $Re_\tau \approx 1000$. For a 1 GFLOP/s computer, this results in ≈ 28 years, whilst for a 1 TFLOP/s computer, in ≈ 10 days. In case of a 1 PFLOP/s cluster, computing time reduces to ≈ 15 minutes.

Next, let us discuss the constants appearing in expression (2.7). In principle, $\mathcal{A}$ and $\mathcal{B}$ should be $\gg 1$ such that the simulated duct flow approaches ideal plane channel flow. Periodic boundary conditions are imposed in the streamwise and spanwise directions. The period is the size of the computational box, and we would like it to be as large as possible to avoid unphysical behaviour related to periodicity near the boundaries. In practice, computational capabilities are limited and thus, the computational domain is set as large as it is feasible. Regarding this point, two questions come to mind: *how large should be the computational box to properly reproduce one-point turbulence statistics?*; i.e., the so-called minimal flow units (Jiménez & Moin, 1991) and, *how large is to be the computational domain to capture the largest scales in the flow?*. It has been found that $\mathcal{A} \approx 500/Re_\tau$ and $\mathcal{B} \approx 100/Re_\tau$ seem to be sufficient for reproducing one-point statistics up to the upper-edge of the buffer layer (Jiménez & Moin, 1991; Jiménez, 2013), whereas $\mathcal{A} \approx 6$ and $\mathcal{B} \approx 3$ seem to define the box size resulting in correct one-point statistics in the log-law region (Flores & Jiménez, 2010) and perhaps even at all wall-normal distances (Lozano-Durán & Jiménez, 2014). Meanwhile, the other question is still somewhat open. Considering the existence of very-large but narrow velocity structures, e.g. up to $10 - 20h$ long in the outer-layer region, it does seem reasonable to use a box size with $\mathcal{A} \approx 25$ and $\mathcal{B} \approx 9.5$ just like Hoyas & Jiménez (2006) as the standard computational box for simulations. Nonetheless, even for the relatively low $Re_\tau \approx 550$ in a very-large box ($\mathcal{A} \approx 190$ and $\mathcal{B} \approx 19$), only about 80% of the streamwise kinetic energy at $y/h = 1$ is captured by a closed contour in the corresponding premultiplied two-dimensional spectrum (Lozano-Durán &

Parameter	N180/D180	P180
L_x/h	12.57	18.85
L_y/h	2.00	2.00
L_z/h	6.28	7.85
$T_A/(h/u_\tau)$	30.00	30.00
Δx^+	9.88	14.81
Δy^+_{min}	0.22	0.22
Δy^+_{max}	4.62	4.62
Δz^+	4.94	6.17
$\Delta t/(h/u_\tau)$	0.20	0.20

Table 2.1: Parameters of the DNS. D180 and P180 refer to the shear-thickening and shear-thinning fluid cases whilst N180 refers to the base Newtonian case. All cases at $Re_\tau = 180$.

Jiménez, 2014). With respect to the constant $\mathcal{C}$, it should be $\gg 1$ as well. Actually, the simulation time comprises an initialization time (T_S), and an averaging time (T_A). T_S is a transient period where the flow evolves from the initial conditions, and depends on how the simulation is initialized (e.g., from a laminar field with superimposed small perturbations, or from another turbulent flow field). T_A is the time required for the convergence of turbulence statistics, starting after T_S, and once the instantaneous flow fields are representative states of the turbulent channel flow (e.g., once equation (1.10) starts to be approximately fulfilled). Typically only T_A is reported, and estimations of the computational cost are based on it rather than on the total simulation time. For proper convergence of the statistics corresponding to structures of size λ, T_A is to be proportional to their characteristic period, λ/u_τ, and inversely proportional to the number of structures that can occupy the computational domain, $L_x L_z/\lambda^2$ (del Álamo, 2005, p. 27). Hence,

$$T_A \sim \frac{\lambda/u_\tau}{L_x L_z/\lambda^2} \equiv \frac{\lambda^3}{u_\tau L_x L_z}. \tag{2.8}$$

For example, in case of the largest structures being of size $3L_x/4$, where $L_z = L_x/2$ and $L_x = 25h$, $T_A/(h/u_\tau) \approx 21$. From equation (2.8), one can also note that a lower T_A is required for larger computational boxes. Finally, $\mathcal{D} \sim \mathcal{O}(\eta)$. In practice, $\eta \sim \Delta y < \Delta z < \Delta x$. Moreover, although $\Delta t \sim \eta/u_\tau$, due to the implemented numerical scheme, we may require an even lower time stepping for numerical stability considerations.

The previous discussion allows one to realize that the setup of the different parameters in DNS requires care and, although it is a somewhat technical matter, it is not trivial at all. Here, DNS of incompressible, turbulent flow of GN

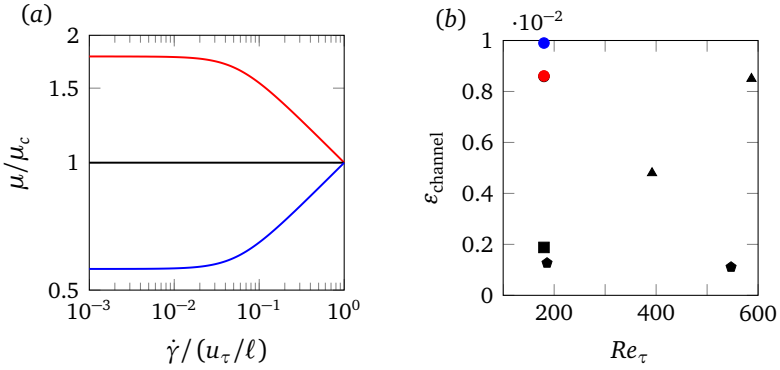

Figure 2.1: Viscosity rheogram and error indicator for the considered cases: (*a*) normalized viscosity, μ/μ_c, against normalized strain-rate, $\dot{\gamma}/(u_\tau/\ell)$, in a log-log plot for the considered GN fluids and (*b*) error indicator for the channel flow simulations, $\varepsilon_{\text{channel}}$ as defined in Vinuesa *et al.* (2016). In (*a*), black, blue and red line styles are used for cases N180, D180 and P180, respectively. Also, μ_c is the nominal viscosity at maximum strain rate. In (*b*), markers ●, ● and ● represent cases N180, D180 and P180, respectively, whereas ■, ▲ and ⬟ correspond to Kim *et al.* (1987), Moser *et al.* (1999) and del Álamo & Jiménez (2003), respectively. Note that marker ● overlaps ●.

fluids between two long and wide parallel plates at a distance $2h$ are considered. The geometrical configuration of the duct is intended as an approximation to plane channel as described in subsection 1.1.3. The flow is driven by a constant pressure gradient, physical non-slip and impermeability boundary conditions are imposed at the walls, and periodicity is set in the directions parallel to the wall. Table 2.1 summarizes the parameters of the different numerical experiments. Three cases are studied: (i) N180, (ii) D180, and (iii) P180 corresponding to Newtonian, slight shear-thickening, and slight shear-thinning behaviours at a $Re_\tau = 180$, respectively. The Carreau model, equation (1.3) with $b = 2$, was selected to incorporate the shear-dependent viscosity in cases D180 and P180. See figure 2.1(*a*) and table 2.2. Figure 2.1(*b*), displaying the root-mean-square norm of the difference between computed $\overline{\tau_{xy}}/\overline{\tau_w}$ and $1-y/h$, $\varepsilon_{\text{channel}}$ as defined in Vinuesa *et al.* (2016), is given as an overall indicator of the error in the simulations. Details about the implemented code for performing the DNS and the reasons for selecting the parameters shown in table 2.1 are given in subsection 2.2 of paper I. In the remaining part of this subsection, let us discuss the considerations behind the selected value for Re_τ, and the rheological behaviour of cases D180 and P180.

In experiments of wall-bounded flows, choosing suitable Reynolds numbers is imperative. Not only because it determines the flow regime, but also the sep-

Parameter	D180	P180
μ_∞/μ_0	0.001	0.001
μ_0/μ_c	0.561	1.782
$\Lambda/(h/u_\tau)$	0.100	0.100
α	1.200	0.800

Table 2.2: Carreau model parameters for shear-dependent GN fluids considered in the DNS. D180 and P180 refer to the shear-thickening and shear-thinning fluid cases at $Re_\tau = 180$. The characteristic viscosity, μ_c, is taken as μ_w which is the constant dynamic viscosity of the Newtonian base case; i.e., $\mu_w = \mu \equiv \rho u_\tau h/Re_\tau = 1/180\,[\mathrm{Pa}\cdot\mathrm{s}]$.

aration between turbulent scales. In fact, since $Re_\tau = h/\ell$, it is not surprising that criteria for the existence of the log-law region are based upon a minimal Re_τ-value. As commented in subsection 1.1.3, the start/end of the log-lag region is not very distinct. Even so, it is perhaps safe to assume that the log-law exits and holds from $y^+ \approx 150$ to $\mathcal{H} \approx 0.15$; i.e. at no less than $Re_\tau \approx 1000$, and it is only appreciably wide if Re_τ is substantially higher (Vela-Martín *et al.*, 2021). Therefore, it does seem appropriate to consider a $Re_\tau \gtrsim 1000$ when carrying-out DNS of wall-bounded flows of Newtonian fluids and, probably, of GN fluids in general. Nevertheless, *what about the computational cost?*. Aside the cost associated with N_{xyzt}, it is good to keep in mind that the implementation of any constitutive equation accounting for non-Newtonian behaviour is accompanied by an increase in the number of FLOP per data-point. Furthermore, the resources available to us may also impose additional restrictions: *is our code running in a parallel or serial manner?*, *is it CPU- or GPU-based?*, and even in the ideal case of a GPU-based code running in parallel, where CPUs are only used for intercommunication between computer nodes, *what are the number of GPU/CPU-hours allocated to us?*. Most industrialized countries have powerful HPC-capabilities, however these resources are always in high demand by different groups in all kind of disciplines. These restrictions and the general grow of the computational cost (due to the increase of FLOP per data-point with the implemented constitutive equations) are likely the reasons why most numerical simulations of non-Newtonian fluids are performed at fairly low Re_τ. For instance, most DNS of channel flow of viscoelastic fluids are at $Re_\tau = \mathcal{O}\left(10^2\right)$ (Xi, 2019), with some rare attempts at higher Re_τ (Thais *et al.*, 2013; Pereira *et al.*, 2017). In case of DNS of wall-bounded flows where the fluid viscosity is purely shear-dependent, $Re_\tau = 750$ for pipe flow is probably the largest achieved to date (Singh *et al.*, 2018). Here, due restrictions imposed by the available resources, a frictional Reynolds number matching the one used in the seminal work of Kim *et al.* (1987) is selected.

Regarding the parameters of the Carreau model–once again equation (1.3) with $b = 2$–in cases D180 and P180 (see table 2.2), their selection is made bearing in mind two key points: (i) the cases should exhibit a noticeable yet slight degree of shear-dependency in terms of their viscosity such that, even for such a low Re_τ and in case $\alpha < 1$, the flow remains fully turbulent, and (ii) the fluids should have the same nominal shear viscosity at the wall as the Newtonian case for comparison purposes. Point (i) is achieved by setting Λ and α. The shear-dependency of the profiles is made 'noticeable' by taking a small enough time constant, such that the power-law-like region covers a significant range of strain rate values. Meanwhile, a 'slight' degree of shear-thinning/thickening behaviour is attained by choosing a power-law index not much lower/larger than 1. On the other hand, key point (ii) is achieved by setting μ_0. For given Λ, b and α, equation (1.3) would have two unassigned parameter; μ_∞ and μ_0. However, by definition, μ_∞ is much lower/larger than μ_0 for shear-thinning/thickening fluid behaviour. Assuming μ_∞ is of no consequence for the considered range of $\dot{\gamma}$; i.e. μ_∞ is much lower/larger than μ_w for P180/D180, allows us to find a value for μ_0 for the desired nominal shear viscosity at the wall. It is emphasized that the assigned value to the ratio μ_∞/μ_0 in the simulations, as shown in table 2.2, it is only used for convenience. In reality, μ_0 and μ_∞ are usually within one or two orders of magnitude and, of course, this ratio is larger than 1 for shear-thickening fluids.

2.2 LES of turbulent flow of GN fluids in a baffled tank stirred by a Rushton turbine

In LES, the largest energy-containing scales are fully resolved, whilst the smallest, more isotropic ones, are modelled. In consequence, LES are a sort of in-between DNS and traditional turbulence modelling. The success of LES rests on the fact that, at least on average, the energy and the information mostly travel from the largest to the smallest scales (Davidson, 2015, p. 398); i.e., in a so-called direct cascade. Moreover, LES are quite appealing for many applications where the transfer of, e.g., momentum, heat and chemical pollutants are seemly dominated by the largest scales (Davidson, 2015, p. 399), yet the complexity of the flow and/or the geometry involved make it too expensive for DNS. In general, computational cost and storage capabilities are still issues in LES, though considerably less so than in DNS due to loosening in grid resolutions and time stepping constrains.

For this thesis, LES of turbulent flow of GN fluids in a baffled-stirred tank are considered. A schematic representation of the stirred vessel is shown in figure 2.2, whereas most of the parameters of the simulations are summarized

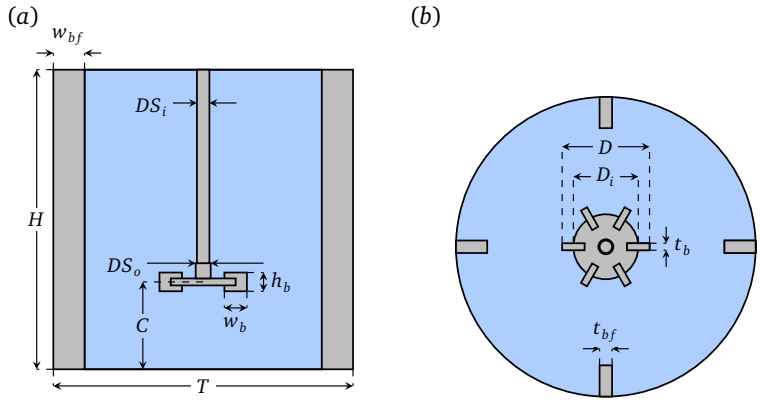

Figure 2.2: Geometrical configuration of the stirred tank considered in the LES: (*a*) cross-sectional view and (*b*) top view.

in table 2.3. The tank diameter, T, is set to 24 [cm], and operates at 600 or 800 revolutions per minute (rpm). The working fluid has $\rho = 1 \times 10^3 \left[\mathrm{kg/m^3}\right]$ and it is either water with $\mu = 1 \times 10^{-3}\,[\mathrm{Pa \cdot s}]$, or 0.2 wt% carboxymethyl cellulose (CMC) solution displaying shear-thinning behaviour. The rheology of the CMC 0.2% solution is taken into account through the Carreau model with $\mu_0 = 97.40 \times 10^{-3}\,[\mathrm{Pa \cdot s}]$, $\mu_\infty = 14.80 \times 10^{-3}\,[\mathrm{Pa \cdot s}]$, $\Lambda = 0.2815\,[\mathrm{s}]$, and $\alpha = 0.6892$. See figure 2.3. Further details about the simulations and the implemented numerical procedure are given in subsection II of paper IV.

The flow fields obtained from the LES are then used as input data for the investigation of vortical structures (larger than the dissipative scales) in the agitated vessel. The vortical structures are identified through a fully frame invariant version of an Eulerian local region-type method (see Epps, 2017), which also considers that the stirred flow is inhomogeneous in all spatial directions. Here, the final objective is to explore some characteristic aspects of the identified vortices; e.g., their size, number density, and shape.

It is worth pointing out that the numerical experiments for these LES are designed with different aims in mind, not all of them relevant for the present thesis; e.g., exploring scaled-up effects once a larger tank size is considered, or drawing comparisons with laboratory-based measurements. Therefore, instead of the Reynolds number, the experiments for the LES are conceived for a matching rotational speed of the impeller; an easy to control operational condition in the laboratory even for different working GN fluids.

Parameter	W600/C600	W800/C800
H/T	1.000	1.000
C/T	0.292	0.292
D/T	0.292	0.292
D_i/T	0.217	0.217
h_b/T	0.063	0.063
t_b/T	0.008	0.008
w_b/T	0.075	0.075
DS_i/T	0.042	0.042
DS_o/T	0.050	0.050
t_{bf}/T	0.042	0.042
w_{bf}/T	0.104	0.104
$T_A/\left(T/u_{\text{tip}}\right)$	3.115	4.154
$\Delta t/\left(T/u_{\text{tip}}\right)$	1.833×10^{-3}	2.444×10^{-3}
$Re_{\text{mix}} = \rho N D^2/\mu_a$	$49.000/1.144 \times 10^3$	$65.333/1.616 \times 10^3$

Table 2.3: Parameters of the LES. W600/C600 and W800/C800 refer to water/CMC 02.% case where the tank operates at 600 [rpm] and 800 [rpm], respectively. T denotes the tank diameter and u_{tip} represents the tip speed of the impeller. Re_{mix} is a mixing Reynolds number based on the impeller rotational speed N, the impeller diameter D, and μ_a for an average strain rate according to the Metzner–Otto correlation for a Rushton-type stirrer; see Metzner & Otto (1957).

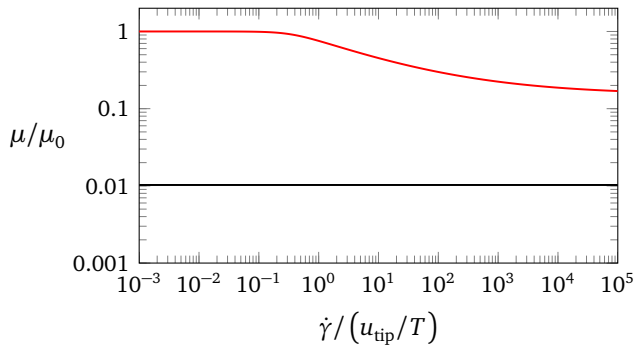

Figure 2.3: Normalized viscosity, μ/μ_0, against $\dot{\gamma}/\left(u_{\text{tip}}/T\right)$ for the GN fluids considered in the LES. Black and red line styles are used to represent the profiles corresponding to water and CMC 0.2%. Here, $\mu_0 = 97.40 \times 10^{-3}$ [Pa · s] and $u_{\text{tip}}/T = 10$ [1/s].

Chapter 3

Summaries of papers

> *Turbulence research, in common with other sciences at some point in their development, has changed from a subject driven by the need for good data, to one driven by the need for new ideas.*
>
> *Jiménez (2018).*

In this part of the thesis, summaries of the attached papers are given. The idea is to provide an accessible (for readership with a background in turbulence) and concise (ca. 250–500 words) overview of each research article with a synopsis of the corresponding main findings. In general terms, papers I and III are about statistical fluid mechanics of turbulent channel flow of GN fluids. On the other hand, papers II and IV are about structural coherence. The latter in a stirred tank reactor operating under turbulent flow conditions and with GN fluids. The former in turbulent channel flow of GN fluids. Also, papers I – III are based upon the DNS briefly explained in section 2.1, whereas paper IV is based on the LES outlined in section 2.2.

Paper I

In paper I, the governing equations (conservation of mass and momentum) are introduced, and the procedure followed to perform the DNS is outlined. To our knowledge, these DNS of turbulent channel flow of GN fluids are the first reported in a peer-reviewed journal. The paper also presents the averaged governing equations, and the Reynolds stress budgets equations. The latter are shown in terms of production, transport, and dissipation rates; akin to how the budgets are traditionally displayed for Newtonian fluids (see, e.g. Mansour *et al.*, 1988). Subsequently and based on the collected flow fields, several typical turbulence statistics are computed, presented and examined for each case. These include first (expectation), second and higher order central moments of the velocity field, and

the mean shear stress profiles. In addition, a quadrant analysis (Wallace *et al.*, 1972) is carried out, the Reynolds stress budgets are discussed, and anisotropy invariant maps (Lumley & Newman, 1977; Antonia *et al.*, 1991) are reported.

In terms of findings, the paper revealed that shear-thinning rheology (opposite trends observed with shear-thickening) leads to several features associated with the so-called low-drag-reduction regime (LDR, see Warholic *et al.*, 1999). Compared to the Newtonian benchmark case: (i) there is an increase in bulk velocity, (ii) the streamwise turbulence intensity is enhanced, whilst the cross-sectional ones are suppressed and overall, there is a higher degree of anisotropy, and (iii) the Reynolds shear stress, as well as the production rate of turbulent kinetic energy, decreases. The findings are consistent with those reported for DNS of turbulent pipe flow of GN fluids (Gavrilov & Rudyak, 2016; Singh *et al.*, 2017, 2018), and for turbulent channel flow of viscoelastic fluids at the LDR; albeit with some characteristic differences in the latter case. In contrast to a viscoelastic fluid (see, e.g. Dimitropoulos *et al.*, 2001; Ptasinski *et al.*, 2003) and with shear-thinning: (i) the new mean shear stress component opposes the traditional mean viscous shear stress, and (ii) compared to the Newtonian base case, there is an increase in the peak of the traditional mean viscous dissipation rate (in absolute magnitude) at the channel wall.

Altogether, the effect of having shear-thinning fluid behaviour (and of a strain-rate-dependent rheology in general) is found particularly important within the inner-layer region. Furthermore, we are of the opinion that similar to other drag-reducing flows, the changes in the turbulence statistics are connected to changes in the dominant near-wall structures.

Paper II

Paper II is an extension of paper I, and focuses on changes in the near-wall structures with strain-rate-dependent rheology compared to the benchmark case; specifically with shear-thinning behaviour. The paper starts presenting the profiles for mean velocity and Reynolds shear stress. These are practical indicators for grasping the underlying changes in the structural features. An/A increase/decrease in mean velocity/Reynolds shear stress with shear-thinning possibly implies an enhancement/suppression of the dominant energy carrier structures/momentum transfer organizing structures; i.e., velocity streaks/quasi-streamwise vortices in the vicinity of the wall. Afterwards, the paper proceeds to present and discuss statistical evidence about the effects of the fluid rheology over the quasi-streamwise vortices. Part of the findings are grounded directly on flow-

field-based statistics, such as two-point correlations and vorticity intensities, and part on statistics of the instantaneous, 3D vortical structures. The structures are identified by thresholding the Q-criterion (Hunt *et al.*, 1988), which is normalized by its standard deviation to account for inhomogeneities in the flow (Nagaosa & Handler, 2003). The effects over the velocity streaks are found in previous publications (see, e.g., Singh *et al.*, 2017, 2018), yet are also given as an appendix in paper II for completeness. Finally, towards the end of the paper and in the spirit of De Angelis *et al.* (2002), the correlations between each velocity component and each involved viscous force, one related to the mean viscosity and the other to the fluctuations in viscosity for the shear-thinning case, are examined. Here, the aim is to gain insight into the potential disruption of the near-wall self-sustaining process (see, e.g., Hamilton *et al.*, 1995; Jiménez & Pinelli, 1999) with shear-thinning behaviour.

Considering the collective evidence and in comparison with the benchmark case, paper II shows that quasi-streamwise vortices appear to depart from the wall, diminish in population and strength, and grow in size with shear-thinning rheology. More specifically, the vortical structures are still comprised of wall-attached and wall-detached families (del Álamo *et al.*, 2006), and those wall-attached seem to maintain about the same shape regardless of the fluid rheology. However, the ones confined to the region where viscous effects are thought important appear more elongated and thus, larger in size for the drag-reducing fluid case. Furthermore, with respect to the regenerative cycle near the wall, its character does seem to remain unchanged. Near-wall vortices cause the velocity streaks and their instability, for instance, result in the formation of the quasi-streamwise vortices. The difference is that with shear-thinning rheology, the viscosity increases as we move away from the wall, and a new force arises due to viscosity fluctuations. These two factors appear to be leading to less energetic streamwise-oriented vortices and more stable and thicker streaks, respectively.

Paper III

Paper III is another extension of paper I, and for the most part considers: (i) the relative contributions of the vortex-stretching and advective transport terms (Tennekes & Lumley, 1972, p. 80) to the wall-normal gradient of the Reynolds shear stress, and (ii) the identification and extension of regions where viscous effects are important from a mean dynamics perspective (Klewicki, 2013). Point (ii) is addressed by considering the wall-normal distribution of the stress gradients in the Reynolds-averaged

streamwise momentum equation for the turbulent channel.

Overall, the article coveys how points (i) and (ii) differ for the different GN fluid cases. Paper III reveals that both velocity–vorticity products are affected by the strain-rate-dependent rheology. It is found that compared to the Newtonian case and with, e.g., shear-thinning behaviour: (a) the peak in the advective transport term in the very near wall region (considered related to the outward motion of the sublayer streaks, see Klewicki *et al.*, 1994) is suppressed, and (b) there is an general attenuation of the vortex-stretching term (associated with a change-of-scale effect, see Tennekes & Lumley, 1972, p. 80). From a physical perspective, (a) potentially implies the velocity streaks are more stable, whilst (b) implies a decrease in the range of turbulent scales. On the other hand, the mean momentum balance analysis revealed that a four-layer structure (Wei *et al.*, 2005) persists for all GN fluid cases, albeit with the starting point and extension of some layers being affected by the strain-rate-dependent rheology. For instance, in case of shear-thinning fluid behaviour and compared to the benchmark case, the upper bound of the intermediate layers is further away from the wall. This suggests an extension of the region, where as a whole, viscous effects are still important. Moreover, the trend is found strikingly similar to the one seen with an increase of frictional Reynolds number in wall-bounded flows of Newtonian fluids (see, e.g., Klewicki *et al.*, 2012; Chin *et al.*, 2014). The finding hints that the strain-rate-dependent rheology should be taken into account for the scaling of the intermediate layers. A scaling factor, on an empirical basis, is proposed.

Paper IV

Paper IV may be considered as a 'leap' in complexity from the others since it involves a highly three-dimensional flow which is fully inhomogeneous, though it has some connection to paper II. That is, it also concerns the study of vortical structures for both, Newtonian and shear-thinning fluids. The paper begins with a brief account about what has been studied in previous stirred-tank-investigations (not only those referring to vortical structures) for readership not familiar with the topic. Next, paper IV proceeds to describe the numerical experiments, the implemented procedure for the simulations, and the methodology used for identifying the instantaneous, 3D structures. Essentially, the vortex identification is performed using a material objective (i.e., observer-independent) version of the Q-criterion. The criterion, as other Eulerian local region-type methods (see, e.g., Epps, 2017), can be objectivized by considering a net version

of the velocity gradient tensor (Liu *et al.*, 2019; Haller, 2021). In addition, and as in paper II, the objectivized criterion is normalized by its standard deviation to account for the inhomogeneities in the flow. Afterwards, for the identified vortices, paper IV presents and discusses statistics (e.g., cumulative distribution functions, or PDFs) in connection to aspects such as: size, number density, shape, distribution and organization in space, and correlation with the kinetic energy due to turbulence and the periodic passage of the blades. To our knowledge, some of these aspects have been rarely investigated or have not been addressed at all for turbulent flow in a stirred tank. The paper finalizes with a summary of our main findings, and some potential implications for liquid–liquid and gas–liquid dispersed systems. It is worth commenting that the article also explores the influence of changing the rotational speed of the tank, and the rheology of the working fluid. However, due to disparity in the resulting Reynolds numbers, the latter is difficult to set apart from possible Reynolds numbers effects. As displayed in table 2.3, for a given rotational speed of the tank, the mixing Reynolds number is one order of magnitude larger for the Newtonian fluid than for the shear-thinning one.

In general, together with other findings, paper IV revealed: (i) the number density of the smallest identified structures (about an order of magnitude less than the tank diameter) is the largest in the impeller region and the ones adjacent to it; specifically, towards the radial discharge and the lower circulation loop (see, e.g., Chhabra & Richardson, 2008, p. 404), (ii) for the same tank regions, vortices having similar size seem to be organized in pairs, and the probability of encountering several pairs nearby is rather high, and (iii) tube-like structures are as probably to appear as spherical blobs if not more so; the likelihood of finding sphere-like structures is larger only in the most energetic regions of the tank.

Chapter 4

Conclusion and outlook

> *We have learned a lot by studying pipes, boundary layers, and channels, and there are still gaps in our knowledge... I would suggest, in fact, that we may have reached a point of diminishing returns in studying canonical flows. It may be more fruitful to begin to test our knowledge of wall-bounded flows by examining more complicated flows. We might ask the question "Do we have enough insight into the structure of wall-bounded flows to manipulate the energetic motions and reduce drag, or enhance heat transfer?" Or, "What fundamental understanding might we gain by such experiments?"*
>
> *Smits (2020).*

The present thesis has the goal of improving our understanding about turbulent flows of Newtonian and shear-dependent viscosity fluids, particularly those with shear-thinning behaviour. Towards this end, the following contributions are highlighted:

- For turbulent channel flow, it has been shown that even a slight to moderate degree of shear-thinning results in drag-reducing features regardless of any other rheological behaviour (e.g., extensional thickening, or elastic effects).
- Considering the results of Gavrilov & Rudyak (2016); Singh *et al.* (2017, 2018), several qualitative similarities have been found for internal wall-bounded flows (pipes and channels), when considering a particular type of GN fluid. This hints to the possibility of having universal near-wall behaviour for channel and pipe flows, even when more complex effects are introduced.
- For turbulent channel flow, it has been revealed that the character of the near-wall self-sustaining process, reported for Newtonian fluids, remains

unchanged with shear-thinning rheology. Vortices in the vicinity of the wall still cause the streaks, and the 'breakdowns' of velocity streaks (for instance) result in the formation of the quasi-streamwise vortices. The difference is that with shear-thinning rheology, the near-wall momentum transfer organizing structures appear to be suppressed whilst the energetic structures are seemly enhanced.

- Through a mean momentum balance analysis (Klewicki, 2013) for channel flow, it has been displayed that the overall region where viscous effects are important may, indeed, vary with the type of fluid rheology. Furthermore, the findings strongly suggest that proper scaling at the intermediate layers in turbulent channel flow, and possibly in wall-bounded flows in general, should take into account the shear-dependent viscosity in case of shear-thinning/thickening fluids.
- For the more complex turbulent flow in a stirred tank reactor, it has been shown that vortical structures mostly appear in sphere-like or tube-like forms. In case of shear-thinning fluid rheology, they also tend more towards ribbon-like shapes (see Moisy & Jiménez, 2004, for the terminology). These observations contrast with some common views about turbulent vortices in stirred tank reactors. For instance, in theoretical models for breakup and coalescence of fluid particles (see, e.g., Liao & Lucas, 2009, 2010; Solsvik *et al.*, 2013, for reviews of these models), it is common to represent the turbulent vortices interacting with the drops or bubbles as spherical structures.

At this juncture, it would be wise to point out two important limitations of this work (probably more exist, yet to be foreseen). First, the performed turbulent channel flow simulations are at a fairly low frictional Reynolds number. As commented in chapter 2, a substantially high value for the frictional Reynolds number is required when studying all regions in wall-bounded flows. Second, for both the channel flow and the stirred-tank-flow simulations, the non-Newtonian rheology is implemented through a constitutive equation where the viscosity solely depends on the second invariant of the strain rate tensor. A long-standing criticism for this approach (see, e.g., Oliveira & Pinho, 1998) is that since a turbulent flow is 3D, and considering GN fluids may be seen as particularisation of Reiner–Rivlin fluids (see, e.g. Macosko, 1994, pp. 83–84), the viscosity should also be function of the third invariant of the strain rate tensor. Of course, this reasoning somewhat weakens when recalling that such particularisation is only possible after discarding the second normal stress coefficient in the Reiner–Rivlin fluid equation. Nevertheless, it is certainly a possibility that using a more complex constitutive equation may depict shear-dependent viscosity behaviour in a more realistic manner. To date, we still cannot reproduce

all experimental observations of rheological complexity for the viscous stress, lacking even important phenomenology (Ewoldt & Saengow, 2022).

Finally, on a personal note, I would like to conclude this work with some suggestions for future investigations. The following tentative topics and research questions come to mind:

- Simulations of turbulent wall-bounded flows of GN fluids at higher frictional Reynolds numbers. *In case of moderate shear-dependent behaviour, how high should be the Reynolds number for studying the low-lag region?; what are the characteristics of coherent structures such as vortex clusters and 3D-quadrant events?; what can be said about the scaling of intermediate layers in terms of Reynolds number and shear-dependency?; altogether, how similar or different is the turbulence in a wall-bounded flow for shear-dependent fluids compared to Newtonian ones?, and is it possible to gain new insight about canonical wall-bounded flows?*.
- Simulations of turbulent wall-bounded flows of shear-thinning fluids in a more complex setup. *What about introducing competing drag-reducing mechanisms of different nature?, e.g. using riblet-mounted surfaces; what about considering a multiphase scenario?, e.g. adding small solid or fluid particles, or considering a free surface; what about introducing rotational, thermal, or magnetic effects?; what about the introduction of obstacles or changes in geometry?; e.g. effect of changing the aspect ratio of a duct with secondary flow, or a sudden contraction of the geometry; what about combinations of any of the prior?*.
- Simulations of turbulent wall-bounded flows of shear-thinning fluids with related phenomena, and other key phenomena. *How does the turbulent flow change in case of thixotropy?; how does it change with shear normal stresses, viscoelasticity, extensional thickening, or combinations of these phenomena?; what constitutive equation reproduces the largest number of key phenomena without exponentially increasing the number of floating point operations to be performed?; what numerical scheme(s) may be implemented to solve such equation in a manner that the overall computational cost is significantly reduced?*.
- Turbulence modelling of turbulent wall-bounded flows of GN fluids. *Despite the constant increase of computational capabilities, from an applied perspective, is it worth to invest in the turbulence modelling of these flows?; if so, what model(s) should we invest in and what kind of information is required?; would it be possible to use the fitted models in more complex flows?*
- High-fidelity simulations of turbulent flows in stirred tank reactors working with GN fluids at matching Reynolds number. *Is the mixing Reynolds*

number the most appropriate for characterizing turbulence in stirred tanks?; what is the isolated effect of changing the GN rheology on the turbulence of a stirred tank reactor operating at a given Reynolds number?; how does the turbulent flow changes when introducing further complexities?, e.g., perturbation devices, electric currents, chemical reactions, microorganisms, or mass and heat transfer in general.

A curious situation in research, compared to engineering or design, is that one ends up with further questions rather than answers. For most of us, this makes our day-to-day quite engaging and entertaining. Continuous learning is certainly pleasing.

Bibliography

ADRIAN, R. J. 2007 Hairpin vortex organization in wall turbulence. *Phys. Fluids* **19**, 041301.

AFZAL, N. & BUSH, W. B. 1985 A three-layer asymptotic analysis of turbulent channel flow. *Proc. Indian Acad. Sci. (Math. Sci.)* **94**, 135–148.

ANTONIA, R. A., KIM, J. & BROWNE, L. W. B. 1991 Some characteristics of small-scale turbulence in a turbulent duct flow. *J. Fluid Mech.* **233**, 369–388.

ASH, M. & ASH, I. 2006 *Handbook of rheology modifiers*. Endicott, NY: Synapse Inf. Resour.

BALAKUMAR, B. J. & ADRIAN, R. J. 2007 Large- and very-large-scale motions in channel and boundary-layer flows. *Philos. Trans. R. Soc. A* **365**, 665–681.

BIRD, R. B. 1976 Useful non-Newtonian models. *Annu. Rev. Fluid Mech.* **8**, 13–34.

BIRD, R. B., ARMSTRONG, R. C. & HASSAGER, O. 1987 *Dynamics of polymeric liquids, vol. 1: fluid mechanics*. Wiley.

BIRD, R. B. & WIEST, J. M. 1995 Constitutive equations for polymeric liquids. *Annu. Rev. Fluid Mech.* **27**, 169–193.

BLACKWELDER, R. F. & ECKELMANN, H. 1979 Streamwise vortices associated with the bursting phenomenon. *J. Fluid Mech.* **94**, 577–594.

BOUSSINESQ, J. 1877 Essai sur la théorie des eaux courantes. *Mem. de l'Académie des Sciences* **23**.

BUSCHMANN, M. H. & EL HAK, M. GAD 2003 Debate concerning the mean-velocity profile of a turbulent boundary layer. *AIAA J.* **41**, 565–572.

CANTWELL, B. J. 1981 Organized motion in turbulent flow. *Annu. Rev. Fluid Mech.* **13**, 457–515.

CARREAU, P. J. 1968 Rheological equations from molecular network theories. PhD thesis, UW, Madison.

CHHABRA, R. P. & RICHARDSON, J. F. 2008 *Non-Newtonian flow and applied rheology*. Butterworth-Heinemann.

CHIN, C., PHILIP, J., KLEWICKI, J., OOI, A. & MARUSIC, I. 2014 Reynolds-number-dependent turbulent inertia and onset of log region in pipe flows. *J. Fluid Mech.* **757**, 747–769.

CHO, Y. I. & KENSEY, K. R. 1991 Effects of the non-Newtonian viscosity of blood on flows in a diseased arterial vessel. part 1: Steady flows. *Biorheology* **28**, 241–262.

COLLINS, P. J. 1990 Prediction of turbulent flow of inelastic shear-thinning fluids in ducts and mixing vessels. PhD thesis, ICL, London.

COSSU, C. & HWANG, Y. 2017 Self-sustaining processes at all scales in wall-bounded turbulent shear flows. *Philos. Trans. R. Soc. A* **375**, 20160088.

DARRIGOL, O. 2005 *Worlds of flow: a history of hydrodynamics from the Bernoullis to Prandtl*. OUP.

DAVIDSON, P. A. 2015 *Turbulence: an introduction for scientists and engineers*. OUP.

DAVIDSON, P. A., KANEDA, Y., MOFFATT, K. & SREENIVASAN, K. R. 2011 *A voyage through turbulence*. CUP.

DE ANGELIS, E., CASCIOLA, C.M. & PIVA, R. 2002 DNS of wall turbulence: dilute polymers and self-sustaining mechanisms. *Comput. Fluids* **31**, 495–507.

DEL ÁLAMO, J. C. 2005 La organización a gran escala de canales turbulentos. PhD thesis, UPM, Madrid.

DEL ÁLAMO, J. C. & JIMÉNEZ, J. 2003 Spectra of the very large anisotropic scales in turbulent channels. *Phys. Fluids* **15**, L41–L44.

DEL ÁLAMO, J. C., JIMÉNEZ, J., ZANDONADE, P. & MOSER, R. D. 2006 Self-similar vortex clusters in the turbulent logarithmic region. *J. Fluid Mech.* **561**, 329–358.

DIMITROPOULOS, C. D., SURESHKUMAR, R., BERIS, A. N. & HANDLER, R. A. 2001 Budgets of Reynolds stress, kinetic energy and streamwise enstrophy in viscoelastic turbulent channel flow. *Phys. Fluids* **13**, 1016.

DRAAD, A. A., KUIKEN, G. D. C. & NIEUWSTADT, F. T. M. 1998 Laminar-turbulent transition in pipe flow for Newtonian and non-Newtonian fluids. *J. Fluid Mech.* **377**, 267–312.

ECKERT, M. 2021 Pipe flow: a gateway to turbulence. *Arch. Hist. Exact Sci.* **75**, 249–282.

EPPS, B. P. 2017 Review of vortex identification methods. In *55th AIAA aerospace sciences meeting*. Grapevine, TX, USA.

EWOLDT, R. H. & SAENGOW, C. 2022 Designing complex fluids. *Annu. Rev. Fluid Mech.* **54**, 413–441.

FLORES, O. & JIMÉNEZ, J. 2010 Hierarchy of minimal flow units in the logarithmic layer. *Phys. Fluids* **22**, 071704.

GAVRILOV, A. A. & RUDYAK, V. YA. 2016 Direct numerical simulation of the turbulent flows of power-law fluids in a circular pipe. *Thermophys. Aeromech.* **23**, 473–486.

GRAHAM, M. D. & FLORYAN, D. 2021 Exact coherent states and the nonlinear dynamics of wall-bounded turbulent flows. *Annu. Rev. Fluid Mech.* **53**, 227–253.

GUALA, M., HOMMEMA, S. E. & ADRIAN, R. J. 2006 Large-scale and very-large-scale motions in turbulent pipe flow. *J. Fluid Mech.* **554**, 521–542.

GYR, A. & BEWERSDORFF, H.-W. 1995 *Drag reduction of turbulent flows by additives*. Springer.

HALLER, G. 2021 Can vortex criteria be objectivized? *J. Fluid Mech.* **908**, A25.

HAMILTON, J. M., KIM, J. & WALEFFE, F. 1995 Regeneration mechanisms of near-wall turbulence structures. *J. Fluid Mech.* **287**, 317–348.

HEAD, M. R. & BANDYOPADHYAY, P. R. 1981 New aspects of turbulent boundary-layer structure. *J. Fluid Mech.* **107**, 297–338.

HOYAS, S. & JIMÉNEZ, J. 2006 Scaling of velocity luctuations in turbulent channels up to $Re_\tau = 2000$. *Phys. Fluids* **18**, 011702.

HOYAS, S., OBERLACK, M., KRAHEBERGER, S., ALCÁNTARA-ÁVILA, F. & LAUX, J. 2022 Wall turbulence at high friction Reynolds numbers. *Phys. Rev. Fluids* **7**, 014602.

HUNT, J.C.R. 1998 Lewis Fry Richardson and his contributions to mathematics, meteorology, and models of conflict. *Annu. Rev. Fluid Mech.* **30**, xiii–xxxvi.

HUNT, J. C. R., WRAY, A. A. & MOIN, P. 1988 Eddies, streams and convergence zones in turbulent flows. *Center Turbul. Res., Proc. Summer Prog.* pp. 193–208.

HUSSAIN, A. K. M. FAZLE 1986 Coherent structures and turbulence. *J. Fluid Mech.* **173**, 303–356.

HUTCHINS, N. & MARUSIC, I. 2007*a* Evidence of very long meandering features in the logarithmic region of turbulent boundary layers. *J. Fluid Mech.* **579**, 1–28.

HUTCHINS, N. & MARUSIC, I. 2007*b* Large-scale influences in near-wall turbulence. *Philos. Trans. R. Soc. A* **365**, 647–664.

IONESCU, C. M., BIRS, I. R., COPOT, D., MURESAN, C. I. & CAPONETTO, R. 2020 Mathematical modelling with experimental validation of viscoelastic properties in non-Newtonian fluids. *Phil. Trans. R. Soc. A* **378**, 20190284.

IRGENS, F. 2014 *Rheology and non-Newtonian fluids*. Springer.

JACKSON, D. & LAUNDER, B. 2007 Osborne Reynolds and the publication of his papers on turbulent flow. *Annu. Rev. Fluid Mech.* **39**, 19–35.

JIMÉNEZ, J. & MOIN, P. 1991 The minimal flow unit in near-wall turbulence. *J. Fluid Mech.* **225**, 213–240.

JIMÉNEZ, J. 2004 The contributions of A. N. Kolmogorov to the theory of turbulence. *Arbor* **178**, 589–606.

JIMÉNEZ, J. 2012 Cascades in wall-bounded turbulence. *Annu. Rev. Fluid Mech.* **44**, 27–45.

JIMÉNEZ, J. 2013 Near-wall turbulence. *Phys. Fluids* **25**, 101302.

JIMÉNEZ, J. 2018 Coherent structures in wall-bounded turbulence. *J. Fluid Mech.* **842**, P1.

JIMÉNEZ, J. & PINELLI, A. 1999 The autonomous cycle of near-wall turbulence. *J. Fluid Mech.* **389**, 355–359.

KAWAHARA, G., UHLMANN, M. & VAN VEEN, L. 2012 The significance of simple invariant solutions in turbulent flows. *Annu. Rev. Fluid Mech.* **44**, 203–225.

KIM, J., MOIN, P. & MOSER, R. 1987 Turbulence statistics in fully developed channel flow at low Reynolds number. *J. Fluid Mech.* **177**, 133–166.

KIM, K. C. & KIM, R. J. 1999 Very large-scale motion in the outer layer. *Phys. Fluids* **11**, 417–422.

KLEWICKI, J., CHIN, C., BLACKBURN, H. M., OOI, A. & MARUSIC, I. 2012 Emergence of the four layer dynamical regime in turbulent pipe flow. *Phys. Fluids* **24**, 045107.

KLEWICKI, J. C. 2013 Self-similar mean dynamics in turbulent wall flows. *J. Fluid Mech.* **718**, 596–621.

KLEWICKI, J. C., MURRAY, J. & FALCO, R. E. 1994 Vortical motion contributions to stress transport in turbulent boundary layers. *Phys. Fluids* **6**, 277–286.

KOLMOGOROV, A. N. 1941*a* Dissipation of energy in isotropic turbulence. *Dokl. Akad. Nauk. SSSR* **32**, 19–21.

KOLMOGOROV, A. N. 1941*b* The local structure of turbulence in incompressible viscous fluids at very large reynolds number. *Dokl. Akad. Nauk. SSSR* **30**, 299–303.

VON KÁRMÁN, T. 1930 Mechanische ahnlichkeit und turbulenz. In *3rd. Int. Congr. Applied Mechanics*, pp. 85–93. Stockholm, SE.

LARSON, R. G. & WEI, Y. 2019 A review of thixotropy and its rheological modeling. *J. Rheol.* **63**, 477–501.

LEE, M. & MOSER, R. D. 2015 Direct numerical simulation of turbulent channel flow up to $Re_\tau = 5200$. *J. Fluid Mech.* **774**, 395–415.

LIAO, Y. & LUCAS, D. 2009 A literature review of theoretical models for drop and bubble breakup in turbulent dispersions. *Chem. Eng. Sci.* **64**, 3389–3406.

LIAO, Y. & LUCAS, D. 2010 A literature review on mechanisms and models for the coalescence process of fluid particles. *Chem. Eng. Sci.* **65**, 2851–2864.

LIU, J., GAO, Y. & LIU, C. 2019 An objective version of the Rortex vector for vortex identification. *Phys. Fluids* **31**, 065112.

LOZANO-DURÁN, A. 2015 Time-resolved evolution of coherent structures in turbulent channels. PhD thesis, UPM, Madrid.

LOZANO-DURÁN, A., BAE, H. J. & ENCINAR, M. P. 2020 Causality of energy-containing eddies in wall turbulence. *J. Fluid Mech.* **882**, A2.

LOZANO-DURÁN, A., CONSTANTINOU, N. C., NIKOLAIDIS, M.-A. & KARP, M. 2021 Cause-and-effect of linear mechanisms sustaining wall turbulence. *J. Fluid Mech.* **914**, A8.

LOZANO-DURÁN, A., FLORES, O. & JIMÉNEZ, J. 2012 The three-dimensional structure of momentum transfer in turbulent channels. *J. Fluid Mech.* **694**, 100–130.

LOZANO-DURÁN, A. & JIMÉNEZ, J. 2014 Effect of the computational domain on direct simulations of turbulent channels up to $Re_\tau = 4200$. *Phys. Fluids* **26**, 011702.

LUCHINI, P. 2017 Universality of the turbulent velocity profile. *Phys. Rev. Lett.* **118**, 224501.

LUCHINI, P. 2018 Structure and interpolation of the turbulent velocity profile in parallel flow. *Eur. J. Mech. B* **71**, 15–34.

LUMLEY, J. L. 1969 Drag reduction by additives. *Annu. Rev. Fluid Mech.* **1**, 367–384.

LUMLEY, J. L. 1992 Some comments on turbulence. *Phys. Fluids A* **4**, 203–211.

LUMLEY, J. L. & DAVIS, S. H. 2003 Stanley Corrsin: 1920–1986. *Annu. Rev. Fluid Mech.* **35**, 1–10.

LUMLEY, J. L. & NEWMAN, G. R. 1977 The return to isotropy of homogeneous turbulence. *J. Fluid Mech.* **82**, 161–178.

MACOSKO, C. W. 1994 *Rheology principles, measurements, and applications*. Wiley-VCH.

MANSOUR, N. N., KIM, J. & MOIN, P. 1988 Reynolds-stress and dissipation-rate budgets in a turbulent channel flow. *J. Fluid Mech.* **194**, 15–44.

MARUSIC, I. & ADRIAN, R. J. 2012 The eddies and scales of wall turbulence. In *Ten chapters in turbulence* (ed. P. A. Davidson, Y. Kaneda & K. R. Sreenivasan), pp. 176–220. CUP.

MARUSIC, I. & BROOMHALL, S. 2021 Leonardo da Vinci and fluid mechanics. *Annu. Rev. Fluid Mech.* **53**, 1–25.

MARUSIC, I., MCKEON, B. J., MONKEWITZ, P. A., NAGIB, H. M., SMITS, A. J. & SREENIVASAN, K. R. 2010 Wall-bounded turbulent flows at high Reynolds numbers: recent advances and key issues. *Phys. Fluids* **22**, 065103.

MARUSIC, I. & MONTY, J. P. 2019 Attached eddy model of wall turbulence. *Annu. Rev. Fluid Mech.* **51**, 49–74.

METZNER, A. B. & OTTO, R. E. 1957 Agitation of non-Newtonian fluids. *AIChE J.* **3**, 3–10.

MEWIS, J. & WAGNER, N. J. 2009 Thixotropy. *Adv. Colloid Interface Sci.* **147–148**, 214–227.

MILLIKAN, C. B. 1938 A critical discussion of turbulent flows in channels and circular tubes. In *5th. Int. Congr. Applied Mechanics*, pp. 386–392. Cambridge, MA, USA.

MOISY, F. & JIMÉNEZ, J. 2004 Geometry and clustering of intense structures in isotropic turbulence. *J. Fluid Mech.* **513**, 111–133.

MONIN, A. S. & YAGLOM, A. M. 1971 *Statistical fluid mechanics, vol. I: mechanics of turbulence*. MIT Press.

MORRIS, J. F. 2020 Shear thickening of concentrated suspensions: Recent developments and relation to other phenomena. *Annu. Rev. Fluid Mech.* **52**, 121–144.

MORRISON, F. A. 2001 *Understanding rheology*. OUP.

MOSER, R. D., KIM, J. & MANSOUR, N. N. 1999 Direct numerical simulation of turbulent channel flow up to $Re_\tau = 590$. *Phys. Fluids* **11**, 943–945.

NAGAOSA, R. & HANDLER, R. A. 2003 Statistical analysis of coherent vortices near a free surface in a fully developed turbulence. *Phys. Fluids* **15**, 375–394.

NAGEL, T. 1974 What is it like to be a bat? *Phil. Rev.* **83**, 435–450.

NAGIB, H. M. & CHAUHAN, K. A. 2008 Variations of von Kármán coefficient in canonical flows. *Phys. Fluids* **20**, 101518.

OBERLACK, M., HOYAS, S., KRAHEBERGER, S. V., ALCÁNTARA-ÁVILA, F., & LAUX, J. 2022 Turbulence statistics of arbitrary moments of wall-bounded shear flows: A symmetry approach. *Phys. Rev. Lett.* **128**, 024502.

OLDROYD, J. G. 1958 Non-Newtonian effects in steady motion of some idealized elasticoviscous fluids. *Proc. Roy. Soc. London Ser. A* **245**, 278–297.

OLIVEIRA, P. J. & PINHO, F. T. 1998 A qualitative assessment of the role of a viscosity depending on the third invariant of the rate-of-deformation tensor upon turbulent non-Newtonian flow. *J. Non-Newtonian Fluid Mech.* **78**, 1–25.

ORSZAG, S. A. & ISRAELI, M. 1974 Numerical simulation of viscous incompressible flows. *Annu. Rev. Fluid Mech.* **6**, 281–318.

OSTWALD, W. 1925 Ueber die geschwindigkeitsfunktion der viskosität disperser systeme. i. *Kolloid Z.* **36**, 99–117.

PANTON, R. L. 2001 Overview of the self-sustaining mechanisms of wall turbulence. *Prog. Aerosp. Sci.* **37**, 341–385.

PEDERSEN, K. S. & RØNNINGSEN, H. P. 2000 Effect of precipitated wax on viscosity–a model for predicting non-Newtonian viscosity of crude oils. *Energy Fuels* **14**, 43–51.

PEREIRA, A. S., MOMPEAN, G., THAIS, L. & THOMPSON, R. L. 2017 Statistics and tensor analysis of polymer coil–stretch mechanism in turbulent drag reducing channel flow. *J. Fluid Mech.* **824**, 135–173.

POPE, S. B. 2000 *Turbulent flows*. CUP.

PRANDTL, L. 1925 Bericht über untersuchungen zur ausgebildeten turbulenz. *Z. Angew. Math. Mech.* **5**, 136–139.

PTASINSKI, P. K., BOERSMA, B. J., NIEUWSTADT, F. T. M., HULSEN, M. A., BRULE, B. H. A. A. VAN DER & HUNT, J. C. R. 2003 Turbulent channel flow near maximum drag reduction: simulations, experiments and mechanisms. *J. Fluid Mech.* **490**, 251–291.

PTASINSKI, P. K., NIEUWSTADT, F. T. M., BRULE, B. H. A. A. VAN DEN & HULSEN, M. A. 2001 Experiments in turbulent pipe flow with polymer additives at maximum drag reduction. *Flow Turbul. Combust.* **66**, 159–182.

REE, F. H., REE, T. & EYRING, H. 1959 Relaxation theory of transport problems in condensed systems. *Ind. Eng. Chem.* **50**, 1036–1040.

REYNOLDS, O. 1883 An experimental investigation of the circumstances which determine whether the motion of water in parallel channels shall be direct or sinuous and of the law of resistance in parallel channels. *Philos. Trans. R. Soc. A* **174**, 935–982.

REYNOLDS, O. 1895 On the dynamical theory of incompressible viscous fluids and the determination of the criterion. *Philos. Trans. R. Soc. A* **186**, 123–164.

RICHARDSON, L. F. 1922 *Weather prediction by numerical process*. CUP.

ROBINSON, S. K. 1991 Coherent motions in the turbulent boundary layer. *Annu. Rev. Fluid Mech.* **23**, 601–639.

RØNNINGSEN, H. P. 2012 Rheology of petroleum fluids. *Ann. Trans. Nord. Rheo. Soc.* **20**, 11–18.

SAMIE, M., MARUSIC, I., HUTCHINS, N., FU, M., FAN, Y., HULTMARK, M. & SMITS, A. 2018 Fully resolved measurements of turbulent boundary layer flows up to $Re_\tau = 20000$. *J. Fluid Mech.* **851**, 391–415.

SCHMID, P. J. 2007 Nonmodal stability theory. *Annu. Rev. Fluid Mech.* **39**, 129–162.

SCHMID, P. J. & HENNINGSON, D. S. 2001 *Stability and transition in shear flows*. Springer.

SCHMITT, F. G. 2007 About Boussinesq's turbulent viscosity hypothesis: historical remarks and a direct evaluation of its validity. *C. R. Mécanique* **335** (9), 617–627.

SCHOPPA, W. & HUSSAIN, F. 2002 Coherent structure generation in near-wall turbulence. *J. Fluid Mech.* **453**, 57–108.

SILLERO, J. A. 2014 High Reynolds numbers turbulent boundary layers. PhD thesis, UPM, Madrid.

SINGH, J., RUDMAN, M. & BLACKBURN, H. M. 2017 The influence of shear-dependent rheology on turbulent pipe flow. *J. Fluid Mech.* **822**, 848–879.

SINGH, J., RUDMAN, M. & BLACKBURN, H. M. 2018 Reynolds number effects in pipe flow turbulence of generalized Newtonian fluids. *Phys. Rev. Fluids* **3**, 094607.

SMITS, A. J. 2020 Some observations on Reynolds number scaling in wall-bounded flows. *Phys. Rev. Fluids* **5**, 110514.

SMITS, A. J., MCKEON, B. J. & MARUSIC, I. 2011 High-Reynolds number wall turbulence. *Annu. Rev. Fluid Mech.* **43**, 53–75.

SOLSVIK, J., TANGEN, S. & JAKOBSEN, H. A. 2013 On the constitutive equations for fluid particle breakage. *Rev. Chem. Eng.* **29**, 241–356.

SOMMERFELD, A. 1908 Ein beitrag zur hydrodynamischen erklärung der turbulenten flüssigkeitsbewegung. In *Int. Congr. Math. 4th*, , vol. 3, pp. 116–124. Rome, IT.

SPALART, P. R. & ABE, H. 2021 Empirical scaling laws for wall-bounded turbulence deduced from direct numerical simulations. *Phys. Rev. Fluids* **6**, 044604.

SPRIGGS, T. W. 1965 A four-constant model for viscoelastic fluids. *Chem. Eng. Sci.* **20**, 931–940.

SREENIVASAN, K. R. & SAHAY, A. 1997 The persistence of viscous effects in the overlap region, and the mean velocity in turbulent pipe and channel flows. In *Self-sustaining mechanisms of wall turbulence* (ed. R. Panton), pp. 253–272. Computational Mechanics Publications.

TENNEKES, H. & LUMLEY, J. L. 1972 *A first course in turbulence*. MIT Press.

THAIS, L., GATSKI, T. B. & MOMPEAN, G. 2013 Analysis of polymer drag reduction mechanisms from energy budgets. *Int. J. Heat Fluid Flow* **43**, 52–61.

THEODORSEN, T. 1952 Mechanism of turbulence. In *2nd Midwestern Conf. of Fluid Mechanics*. Columbus, OH, USA.

THEODORSEN, T. 1955 The structure of turbulence. In *50 Jahre Grenzschichtforschung* (ed. H. Görtler & W. Tollmien), pp. 55–62. Springer.

TOWNSEND, A. A. 1976 *The structure of turbulent shear flow*. CUP.

TSINOBER, A. 2013 *The essence of turbulence as a physical phenomenon: with emphasis on issues of paradigmatic nature*. Springer.

VELA-MARTÍN, A., ENCINAR, M. P., GARCÍA-GUTIÉRREZ, A. & JIMÉNEZ, J. 2021 A low-storage method consistent with second-order statistics for time-resolved databases of turbulent channel flow up to $Re_\tau = 5300$. *J. Comput. Sci.* **56**, 101476.

VINUESA, R., PRUS, C., SCHLATTER, P. & NAGIB, H. M. 2016 Convergence of numerical simulations of turbulent wall-bounded flows and mean cross-flow structure of rectangular ducts. *Meccanica* **51**, 3025–3042.

DE WAELE, A. 1923 Viscometry and plastometry. *J. Oil Color Chem. Assoc.* **6**, 33–88.

WALLACE, J. M., ECKELMANN, H. & BRODKEY, R. S. 1972 The wall region in turbulent shear flow. *J. Fluid Mech.* **54**, 39–48.

WARHOLIC, M. D., MASSAH, H. & HANRATTY, T. J. 1999 Influence of drag-reducing polymers on a turbulence: effects of Reynolds number, concentration and mixing. *Exp. Fluids* **27**, 461–472.

WEI, T. 2018 Multiscaling analysis of the mean thermal energy balance equation in fully developed turbulent channel flow. *Phys. Rev. Fluids* **3**, 094608.

WEI, T. 2020 Properties of the mean momentum balance in turbulent Taylor–Couette flow. *J. Fluid Mech.* **891**, A10.

WEI, T., FIFE, P., KLEWICKI, J. & MCMURTY, P. 2005 Properties of the mean momentum balance in turbulent boundary layer, pipe and channel flows. *J. Fluid Mech.* **522**, 303–327.

WHITE, C. M., DUBIEF, Y. & KLEWICKI, J. 2018 Properties of the mean momentum balance in polymer drag-reduced channel flow. *J. Fluid Mech.* **834**, 409–433.

XI, L. 2019 Turbulent drag reduction by polymer additives: fundamentals and recent advances. *Phys. Fluids* **31**, 121302.

YASUDA, K. 1979 Investigation of the analogies between viscometric and linear viscoelastic properties of polystyrene fluids. PhD thesis, MIT, Cambridge.

Paper I

Turbulent channel flow of generalized Newtonian fluids at a low Reynolds number

Arturo A. Arosemena, Helge I. Andersson, and Jannike Solsvik

J. Fluid Mech. **908**, A43 (2021)

J. Fluid Mech. (2021), *vol*. 908, A43. © The Author(s), 2020.

Published by Cambridge University Press

doi:10.1017/jfm.2020.903

Turbulent channel flow of generalized Newtonian fluids at a low Reynolds number

Arturo A. Arosemena[1],†, Helge I. Andersson[2] and Jannike Solsvik[1],†

[1]Department of Chemical Engineering, Norwegian University of Science and Technology (NTNU), 7491 Trondheim, Norway

[2]Department of Energy and Process Engineering, Norwegian University of Science and Technology (NTNU), 7491 Trondheim, Norway

(Received 23 December 2019; revised 4 September 2020; accepted 15 October 2020)

Several studies concerning the turbulent pipe flow of generalized Newtonian (GN) fluids may be found in the literature, but not for channel flow, although that has been extensively studied for other types of non-Newtonian fluids, such as those with viscoelastic effects. Direct numerical simulations corresponding to statistically converged turbulent channel flow of GN fluids at a low frictional Reynolds number have been performed. The shear-dependent viscosity is introduced through the Carreau fluid model, and results corresponding to the Newtonian fluid case are compared to those of moderate shear-thickening and shear-thinning fluid behaviour. The different statistics studied reveal that shear-dependent fluid rheology appears mainly to affect the flow within the inner layer region and with shear-thinning behaviour; suppressing near-wall structures such as quasi-streamwise vortices and low-speed streaks, inhibiting turbulence generating events and leading to different drag reduction features. These include: enhancement of streamwise turbulence intensity and suppression of the other cross-sectional intensities, decrease of the Reynolds shear stress (leading to a lessening in turbulent production), decrease in energy redistribution between individual components of the Reynolds stress tensor through the velocity–pressure gradient term and overall increase in turbulence anisotropy at both small and large scales. In particular, it is noted that at the channel centre ‘rod-like’ turbulence states, a known low-Reynolds-number behaviour, are more clearly seen with shear-thinning fluid rheology.

Key words: turbulence simulation

1. Introduction

Shear-dominated wall-bounded turbulent flows such as in pipes, channels and boundary layers are of utmost importance. Approximately 25 % of the energy used in industry is destined to transport fluids through pipes and channels, or to propel vehicles in air or water, and approximately a quarter of that energy is irreversibly dissipated near walls

† Email addresses for correspondence: arturo.arosemena@ntnu.no, jannike.solsvik@ntnu.no

(Jiménez 2013). Furthermore, in many industrial settings, such as bioreactors in biochemical plants or the drilling machines used in petroleum extraction, the transported fluid is non-Newtonian. A non-Newtonian fluid has non-uniform viscosity, which may depend on shear stress history and/or strain rate in a nonlinear manner, and it is typically classified within three main groups (see e.g. Irgens 2014): (i) time-independent fluids, in which fluid viscosity is not a function of time, (ii) time-dependent fluids and (iii) viscoelastic fluids consisting of materials with partial elastic recovery but also with viscous features.

The interest in non-Newtonian flows has increased since Toms (1948) reported frictional drag reductions in turbulent pipe flows due to a small amount of polymer additives. The first explanation of the drag reduction phenomenon may be attributed to Lumley (1969, 1973). He reasoned that the expansion of molecules, mainly within the buffer layer, leads to an increase in effective viscosity, the dampening of small eddies, the reduction of the Reynolds shear stress, the thickening of the sublayer and the consequent drag reduction. Results reported by Achia & Thompson (1977) also supported the idea about stretched molecules leading to less 'bursting' (Kline *et al.* 1967) and thus less turbulent kinetic energy production and subsequent drag reduction. The other explanation for frictional drag reduction, put forward by Tabor & de Gennes (1986), attributes the decrease in drag to the elasticity of the polymer additives and argues that the increase in effective viscosity is rather small and therefore negligible.

Many studies (e.g. Den Toonder *et al.* 1997; De Angelis, Casciola & Piva 2002; Min *et al.* 2003*b*; Ptasinski *et al.* 2003; Escudier, Nickson & Poole 2009; Shahmardi *et al.* 2019) have been committed to understand variations of drag in turbulent pipes, ducts and channels of polymeric solutions where viscoelastic effects are important. However, for a wide range of materials, the non-Newtonian rheology is mostly strain-rate-dependent and viscoelastic effects may be neglected (Rudman *et al.* 2004). Generalized Newtonian (GN) fluids are a class of time-independent, purely viscous, non-Newtonian fluids commonly encountered in numerous engineering and commercial applications, e.g. fluids in bioreactors displaying shear-thinning behaviour, drilling fluids, cosmetics or food products. In a GN fluid, the stress tensor due to viscous effects, $\tau_{ij,vis}$, is given by

$$\tau_{ij,vis} = 2\mu S_{ij}, \tag{1.1}$$

where $\mu = \mu(\dot{\gamma})$ is the apparent dynamic viscosity, which solely depends on the strain rate $\dot{\gamma} = (2S_{ij}S_{ji})^{1/2}$, and S_{ij} is the strain-rate tensor. Note as well that certain materials flow like a GN fluid once a certain yield-stress value is exceeded. Such materials are called time-independent yield-stress or viscoplastic fluids.

Experimental studies about turbulent flows of GN fluids have primarily focused on friction factor measurements and one-point statistics. Metzner & Reed (1955) and Dodge & Metzner (1959) proposed correlations for the Fanning friction factor based on an alternative definition for the Reynolds number. Park *et al.* (1989) reported an increase in the mean velocity and axial turbulence intensities and a decrease in the tangential intensities, in pipe flows, caused by shear-thinning behaviour in GN fluids. Pinho & Whitelaw (1990) and Pereira & Pinho (1994) additionally reported a suppression of the radial turbulence intensities and a delay in transition from laminar to turbulent flow due to shear thinning. Rudman & Blackburn (2003) presented similar findings and also compared turbulent flows of GN fluids with those of yield-stress fluids. In Rudman & Blackburn (2003) it is recognized that even a small amount of elasticity may importantly affect the results.

Experimental issues such as the difficulty in removing unwanted plastic and viscoelastic effects from solutions with polymer additives and the necessity of specialized equipment to study non-Newtonian fluids, which are mostly not optically transparent (Gavrilov & Rudyak 2016*a*), have motivated a growing interest in numerical studies. Direct numerical simulation (DNS) is particularly appealing because it does not require closures for turbulence modelling and allows us to include/exclude plastic and elastic effects from the employed rheological model. Nonetheless, despite their industrial relevance and the advantages of direct simulations, few DNS studies about turbulent flows of GN fluids are available in the literature.

Rudman & Blackburn (2003), Rudman *et al.* (2004) and Rudman & Blackburn (2006) presented the first group of DNS studies for turbulent flows of GN and yield-stress fluids. In agreement with the experimental investigations for turbulent pipe flows, an increase in the mean axial velocity, delay in transition to turbulence, suppression of radial and tangential turbulence intensities and enhancement of the axial intensity with shear thinning were noted. Also, the decrease in the root-mean-square (r.m.s.) values of the axial vorticity fluctuations and reduced turbulence production with shear-thinning behaviour were documented. Gavrilov & Rudyak (2016*a*) showed similar results but in addition reported an increase in turbulent kinetic energy with increasing shear thinning and, motivated by the work of Escudier *et al.* (2009), studied for the first time large-scale anisotropy of a purely viscous GN fluid flow through anisotropy-invariant maps (Lumley & Newman 1977) of the Reynolds stress anisotropy tensor. Here the noted increase in anisotropy near the wall with shear thinning is attributed to a suppression of the mechanism of redistribution of fluctuation energy between individual components of the Reynolds stress tensor, but the corresponding budgets, showing such decrease in energy redistribution, are not actually presented. Also, small-scale anisotropy (see e.g. Antonia, Kim & Browne 1991; Yeung & Brasseur 1991), equally important for realizable turbulence, is not studied.

More recently, Singh, Rudman & Blackburn (2017*b*) considered the influence of increasing shear-thinning behaviour of GN fluids, in turbulent pipes flows, on first- and second-order statistics. In the same publication and likely motivated by the work of Ptasinski *et al.* (2003), the mean and turbulent kinetic energy budgets are presented for the first time. However, the individual budgets of the second moments of the velocity fluctuations are not shown. The budgets for the Reynolds stresses not only allow us to understand how the different terms contribute to the corresponding stresses, and to the overall turbulent kinetic energy, but also are necessary to directly evaluate closure models for turbulence. Singh *et al.* (2017*b*), based on the joint probability distributions of the axial and wall-normal velocity fluctuations at some wall-normal positions, suggested as well that shear-thinning rheology suppresses contributions from ‘sweeps’ and ‘ejections’ (Wallace, Eckelmann & Brodkey 1972) to the Reynolds shear stress. Nonetheless, in the publication, the cause for the variation with rheology in the contributions from those physical events is not explained.

Singh, Rudman & Blackburn (2017*a*), on the other hand, studied the effect of yield stress on a turbulent pipe flow of a GN fluid. Here, it is found that the effect of increasing the yield stress is similar to an increase in shear-thinning behaviour, with the important difference that the new stress, arising due to fluctuations in viscosity, increases as the pipe’s core is approached. Subsequently, Singh, Rudman & Blackburn (2018) considered Reynolds-number effects on a turbulent pipe flow of a GN fluid. In this investigation, up to a moderate frictional Reynolds number, it is reported that rheological effects are still present. In the paper, it is also noted that the mean viscosity profile appears to be

Reynolds-number-independent. Finally, with respect to recent DNS studies of turbulent flows of GN fluids, Zheng *et al.* (2019) compared finite-volume-scheme-based predictions obtained using OpenFOAM, for low-order statistics in a turbulent pipe flow, with high-order spectral-element DNS code results. The study reported that turbulence statistics predicted by OpenFOAM for shear-thinning fluids usually differ by less than 10 %.

In addition, direct simulations of GN fluid flow based on lattice Boltzmann methods have been performed as well, e.g. Gabbanelli, Drazer & Koplik (2005), Yoshino *et al.* (2007), Wang & Ho (2011) and more recently Chen & Shu (2020). However, those studies are generally limited to the laminar flow regime.

Other non-DNS numerical studies are based either on large-eddy simulations or on solving the time-averaged governing equations with some closure for the Reynolds stress tensor and the correlation term appearing with non-Newtonian rheology. Consider, for instance, Malin (1997), Cruz & Pinho (2003), Sungkorn, Derksen & Khinast (2012), Ohta & Miyashita (2014), Gnambode *et al.* (2015) and Gavrilov & Rudyak (2016*b*).

In this work, results from DNS of statistically converged turbulent channel flow corresponding to GN fluids, at a low Reynolds number, are presented and qualitatively compared to those of turbulent channel flow of viscoelastic fluids and another canonical flow of GN fluids such as turbulent pipe flow. In the results sections, aside from examining first- and second-order statistics of GN fluid flows, physical motions contributing to the turbulence production are considered in detail to comprehend how changes with rheology, in dominating fluctuations and their large intermittent values, cause variations in the shear stress budget and more specifically in the Reynolds shear stress. Also, all relevant non-zero Reynolds stress budgets for turbulent channel flow of GN fluids are presented for the first time, allowing us, for example, to better understand the decrease/increase in energy redistributed from streamwise fluctuations with shear thinning/shear thickening. Furthermore, not only large-scale but also small-scale anisotropy of turbulent GN fluid flow is appraised and, finally, at the end of the paper, the different reported drag-reducing features with shear-thinning behaviour are discussed in light of variations noted in the near-wall structures, i.e. quasi-streamwise vortices and velocity streaks.

2. Formulation

2.1. *Governing equations and characteristic scales*

Consider the equations, in a Cartesian coordinate system and index notation, governing mass and momentum conservation in the absence of external forces for a GN fluid, i.e.

$$\frac{\partial u_i}{\partial x_i} = 0, \tag{2.1}$$

$$\frac{\partial u_i}{\partial t} + \frac{\partial (u_i u_j)}{\partial x_j} = \frac{1}{\rho}\frac{\partial}{\partial x_j}(-p\delta_{ij} + 2\mu S_{ij}), \tag{2.2}$$

where streamwise, wall-normal and spanwise directions are denoted by $\boldsymbol{x} = (x_1, x_2, x_3) = (x, y, z)$, the corresponding instantaneous velocity field by $\boldsymbol{u} = (u_1, u_2, u_3) = (u, v, w)$ and the pressure by p. Here t denotes time, ρ is the density of the incompressible, isothermal GN fluid, δ_{ij} is the Kronecker delta and $S_{ij} = (\partial u_i/\partial x_j + \partial u_j/\partial x_i)/2$ is the aforementioned strain-rate tensor.

For GN fluids, shear-thinning and shear-thickening behaviours may be reproduced through different rheological models (constitutive equations to relate apparent viscosity

and strain rate) such as the power-law (PL) or the Carreau fluid models. In both models, certain parameters are to be specified based on experimental data obtained from a rheogram. Regarding particularities of such models, for example, PL is simpler but leads to non-physical results at large and low shear-rate values whilst the Carreau fluid model may be considered a truncated power-law introduced to avoid this issue. The apparent viscosity for the Carreau fluid model (see e.g. Irgens 2014) is given by

$$\mu = \mu_\infty + (\mu_0 - \mu_\infty)[1 + (\Lambda\dot{\gamma})^2]^{(\alpha-1)/2}, \tag{2.3}$$

where μ_∞ and μ_0 are the 'infinite' and 'zero' shear-rate viscosities, respectively, Λ is a time constant and α is the flow index, which for shear thinning is to be less than unity and for shear thickening more than unity.

Considering a characteristic velocity U_c, viscosity μ_c, length L_c, time L_c/U_c and stress ρU_c^2 for the flow, (2.1)–(2.3) can be rewritten in non-dimensional form as

$$\frac{\partial u_i}{\partial x_i} = 0, \tag{2.4}$$

$$\frac{\partial u_i}{\partial t} + \frac{\partial (u_i u_j)}{\partial x_j} = \frac{\partial}{\partial x_j}\left(-p\delta_{ij} + \frac{2\beta}{Re} S_{ij}\right), \tag{2.5}$$

$$\beta = \frac{\mu_\infty}{\mu_c} + \left(\frac{\mu_0}{\mu_c} - \frac{\mu_\infty}{\mu_c}\right)[1 + (\Lambda\dot{\gamma})^2]^{(\alpha-1)/2}, \tag{2.6}$$

where $Re = \rho U_c L_c/\mu_c$ is the Reynolds number and $\beta = \mu/\mu_c$ is the viscosity ratio between the apparent fluid viscosity and the characteristic viscosity. Observe that, for simplicity, the same notation as in (2.1)–(2.3) has been used in (2.4)–(2.6).

For wall-bounded shear flows, typically $U_c = u_\tau$ and $L_c = h$ in the outer layer and $L_c = \mu_c/(\rho u_\tau)$ in the inner layer; see for instance Pope (2000). Here u_τ and h refer to the wall friction velocity and the outer length scale, respectively. Regarding the characteristic viscosity, its selection is not clear and is open to debate within the scientific community (see e.g. Rudman *et al.* 2004). Here, as in Pinho & Whitelaw (1990), Ptasinski *et al.* (2003) and Singh *et al.* (2017*a*), the nominal wall viscosity μ_w is taken as characteristic viscosity, i.e. $\mu_c = \mu_w$. The complete set of governing equations for a GN fluid is given by (2.4) and (2.5) and a constitutive equation for the apparent viscosity such as (2.6). It is worth mentioning that $\alpha = 1$, in the aforementioned constitutive equation, allows us to recover Newtonian fluid behaviour.

2.1.1. *Averaged governing equations*

Introducing the Reynolds decomposition, i.e. splitting the variables into an ensemble average $\bar{(\,)}$ and a fluctuating component $(\,)'$, as $u_i = \bar{u}_i + u_i'$, $p = \bar{p} + p'$, $\beta = \bar{\beta} + \beta'$ and $S_{ij} = \bar{S}_{ij} + S_{ij}'$, into (2.4) and (2.5) and taking the average leads to

$$\frac{\partial \bar{u}_i}{\partial x_i} = 0, \tag{2.7}$$

$$Re\left[\frac{\partial \bar{u}_i}{\partial t} + \frac{\partial (\bar{u}_i \bar{u}_j)}{\partial x_j}\right] = -Re\frac{\partial \bar{p}}{\partial x_i} + \frac{\partial}{\partial x_j}\left(2\bar{\beta}\bar{S}_{ij} + 2\overline{\beta' S_{ij}'} - \overline{u_i' u_j'}\right), \tag{2.8}$$

where, in comparison with the Reynolds-averaged Navier–Stokes equations for a Newtonian fluid, a new non-Newtonian term $(2\overline{\beta' S_{ij}'})$ arises. This new viscous stress,

denoted as 'turbulent viscous stress' in Singh *et al.* (2017*b*), due to fluctuations in viscosity, is analogous to the recognized polymer stress in Ptasinski *et al.* (2001, 2003). Therefore, the total mean shear stress $\bar{\tau} = \bar{\tau}_{12}$ for a GN fluid is given by

$$\bar{\tau} = 2\bar{\beta}\bar{S}_{12} + 2\overline{\beta' S'_{12}} - \overline{u'_1 u'_2}. \tag{2.9}$$

Since in a GN fluid the viscosity depends on the velocity gradient, through the strain rate, its fluctuating part is not expected to vanish at the wall ($(\cdot)|_w$). Thus, $\bar{\tau}|_w = 2(\bar{\beta}\bar{S}_{12} + \overline{\beta' S'_{12}})|_w$.

2.1.2. *Reynolds stress budget equations*

The transport equation for the correlation of the velocity fluctuations, $\overline{u'_i u'_k}$, corresponding to a GN fluid is deduced in a similar manner as it is deduced for a Newtonian fluid. Thus, the added products $(u'_i \mathrm{D}(u'_k)/\mathrm{D}t + u'_k \mathrm{D}(u'_i)/\mathrm{D}t)$ are time-averaged. Here $\mathrm{D}(\,)/\mathrm{D}t = \partial(\,)/\partial t + \bar{u}_j \partial(\,)/\partial x_j$ is the material time derivative.

The transport equation for the velocity correlation, see for instance Pinho (2003) or appendix A, in non-dimensional form is given by

$$\begin{aligned}
Re\frac{\mathrm{D}}{\mathrm{D}t}\left(\overline{u'_i u'_k}\right) = {} & Re\left[-\overline{u'_i u'_j}\frac{\partial \overline{u_k}}{\partial x_j} - \overline{u'_k u'_j}\frac{\partial \overline{u_i}}{\partial x_j} - \frac{\partial}{\partial x_j}\left(\overline{u'_i u'_j u'_k}\right)\right] + \bar{\beta}\frac{\partial^2}{\partial x_j \partial x_j}\left(\overline{u'_i u'_k}\right) \\
& - Re\overline{\left(u'_i \frac{\partial p'}{\partial x_k} + u'_k \frac{\partial p'}{\partial x_i}\right)} - 2\bar{\beta}\overline{\frac{\partial u'_i}{\partial x_j}\frac{\partial u'_k}{\partial x_j}} \\
& + \left(\frac{\partial \bar{\beta}}{\partial x_j}\right)\left[\frac{\partial}{\partial x_j}\left(\overline{u'_i u'_k}\right) + \overline{u'_i \frac{\partial u'_j}{\partial x_k}} + \overline{u'_k \frac{\partial u'_j}{\partial x_i}}\right] \\
& + \overline{\left(\frac{\partial \beta'}{\partial x_j}\right)\left[\frac{\partial}{\partial x_j}\left(u'_i u'_k\right) + u'_i \frac{\partial u'_j}{\partial x_k} + u'_k \frac{\partial u'_j}{\partial x_i}\right]} + \overline{\beta' \frac{\partial^2}{\partial x_j \partial x_j}\left(u'_i u'_k\right)} \\
& - 2\overline{\beta' \frac{\partial u'_i}{\partial x_j}\frac{\partial u'_k}{\partial x_j}} + \overline{\left(\frac{\partial \beta'}{\partial x_j}\right)\left[u'_i\left(\frac{\partial \overline{u_k}}{\partial x_j} + \frac{\partial \overline{u_j}}{\partial x_k}\right) + u'_k\left(\frac{\partial \overline{u_i}}{\partial x_j} + \frac{\partial \overline{u_j}}{\partial x_i}\right)\right]} \\
& + \overline{\beta'\left[\frac{\partial^2}{\partial x_j \partial x_j}\left(u'_i \overline{u_k}\right) + \frac{\partial^2}{\partial x_j \partial x_j}\left(\overline{u_i} u'_k\right)\right]} \\
& - 2\overline{\beta'\left[\frac{\partial u'_i}{\partial x_j}\frac{\partial \overline{u_k}}{\partial x_j} + \frac{\partial \overline{u_i}}{\partial x_j}\frac{\partial u'_k}{\partial x_j}\right]} - \overline{\beta'\left[\overline{u_k}\frac{\partial^2 u'_i}{\partial x_j \partial x_j} + \overline{u_i}\frac{\partial^2 u'_k}{\partial x_j \partial x_j}\right]}.
\end{aligned} \tag{2.10}$$

As can be seen from (2.10), several new terms have arisen due to the non-Newtonian rheology. To facilitate the later discussion, the new terms are labelled as follows:

(i)

$$P_{ik} = -Re\left[\overline{u'_i u'_j}\frac{\partial \overline{u_k}}{\partial x_j} + \overline{u'_k u'_j}\frac{\partial \overline{u_i}}{\partial x_j}\right] \quad \Longrightarrow \quad \text{total production rate}, \tag{2.11}$$

(ii)

$$TT_{ik} = -Re\frac{\partial}{\partial x_j}\left(\overline{u'_i u'_j u'_k}\right) \quad \Longrightarrow \quad \text{turbulent transport rate}, \tag{2.12}$$

(iii)

$$MD_{ik} = \bar{\beta}\frac{\partial^2}{\partial x_j \partial x_j}\left(\overline{u_i' u_k'}\right) \quad \Longrightarrow \quad \text{mean viscous diffusion rate,} \tag{2.13}$$

(iv)

$$\Pi_{ik} = -Re\overline{\left(u_i'\frac{\partial p'}{\partial x_k} + u_k'\frac{\partial p'}{\partial x_i}\right)} \quad \Longrightarrow \quad \text{velocity–pressure gradient transport rate,} \tag{2.14}$$

(v)

$$M\epsilon_{ik} = 2\bar{\beta}\overline{\frac{\partial u_i'}{\partial x_j}\frac{\partial u_k'}{\partial x_j}} \quad \Longrightarrow \quad \text{mean viscous dissipation rate,} \tag{2.15}$$

(vi)

$$Mv_{ik} = \left(\frac{\partial \bar{\beta}}{\partial x_j}\right)\left[\frac{\partial}{\partial x_j}\left(\overline{u_i' u_k'}\right) + \overline{u_i'\frac{\partial u_j'}{\partial x_k}} + \overline{u_k'\frac{\partial u_j'}{\partial x_i}}\right]$$
$$\Longrightarrow \quad \text{mean viscosity gradient transport rate,} \tag{2.16}$$

(vii)

$$Tv_{ik} = \overline{\left(\frac{\partial \beta'}{\partial x_j}\right)\left[\frac{\partial}{\partial x_j}\left(u_i' u_k'\right) + u_i'\frac{\partial u_j'}{\partial x_k} + u_k'\frac{\partial u_j'}{\partial x_i}\right]}$$
$$\Longrightarrow \quad \text{turbulent viscosity gradient transport rate,} \tag{2.17}$$

(viii)

$$TD_{ik} = \overline{\beta'\frac{\partial^2}{\partial x_j \partial x_j}\left(u_i' u_k'\right)} \quad \Longrightarrow \quad \text{turbulent viscous diffusion rate,} \tag{2.18}$$

(ix)

$$T\epsilon_{ik} = 2\overline{\beta'\frac{\partial u_i'}{\partial x_j}\frac{\partial u_k'}{\partial x_j}} \quad \Longrightarrow \quad \text{turbulent viscous dissipation rate,} \tag{2.19}$$

(x)

$$\widetilde{Tv}_{ik} = \overline{\left(\frac{\partial \beta'}{\partial x_j}\right)\left[u_i'\left(\frac{\partial \overline{u_k}}{\partial x_j} + \frac{\partial \overline{u_j}}{\partial x_k}\right) + u_k'\left(\frac{\partial \overline{u_i}}{\partial x_j} + \frac{\partial \overline{u_j}}{\partial x_i}\right)\right]}$$
$$\Longrightarrow \quad \text{turbulent viscosity gradient transport rate related to mean flow,} \tag{2.20}$$

(xi)

$$\widetilde{TD}_{ik} = \overline{\beta'\left[\frac{\partial^2}{\partial x_j \partial x_j}\left(u_i'\overline{u_k}\right) + \frac{\partial^2}{\partial x_j \partial x_j}\left(\overline{u_i} u_k'\right) - \overline{u_k}\frac{\partial^2 u_i'}{\partial x_j \partial x_j} - \overline{u_i}\frac{\partial^2 u_k'}{\partial x_j \partial x_j}\right]}$$
$$\Longrightarrow \quad \text{turbulent viscous diffusion rate related to mean flow, and} \tag{2.21}$$

(xii)

$$\widetilde{T\epsilon}_{ik} = 2\beta' \overline{\left[\frac{\partial u_i'}{\partial x_j} \frac{\partial \overline{u_k}}{\partial x_j} + \frac{\partial \overline{u_i}}{\partial x_j} \frac{\partial u_k'}{\partial x_j} \right]}$$

$$\Longrightarrow \quad \text{turbulent viscous dissipation rate related to mean flow.} \tag{2.22}$$

The overall equation is recast as

$$B_{ik} = P_{ik} + T_{ik} - \epsilon_{ik}, \tag{2.23}$$

where total dissipation ϵ_{ik} and transport T_{ik} rates, contributing to budget $B_{ik} = Re\, \mathrm{D}(\overline{u_i' u_k'})/\mathrm{D}t$, are given by

$$\epsilon_{ik} = M\epsilon_{ik} + T\epsilon_{ik} + \widetilde{T\epsilon}_{ik} \tag{2.24}$$

and

$$T_{ik} = TT_{ik} + MD_{ik} + \Pi_{ik} + Mv_{ik} + Tv_{ik} + TD_{ik} + \widetilde{Tv}_{ik} + \widetilde{TD}_{ik}, \tag{2.25}$$

respectively. The transport equation for the turbulent kinetic energy is found by taking the summation of the diagonal components of (2.23) and dividing the resulting expression by 2. Also, the transport equation for the velocity correlation $\overline{u_i' u_k'}$ corresponding to a Newtonian fluid may be recovered from (2.23) by considering constant viscosity.

It is worth pointing out that, in the following sections, the results are presented in inner (viscous) units unless otherwise specified. Consequently, all variables are non-dimensionalized with $\mu_c = \mu_w$, $L_c = (\mu_w/\rho)/u_\tau$ and $U_c = u_\tau$ and are identified as $\{\}^+$ quantities.

2.2. *Numerical set-up, computational domain and grid resolution*

Direct numerical simulations of a statistically converged plane turbulent channel flow of GN fluids at a low frictional Reynolds number, $Re_\tau = \rho u_\tau h/\mu_w$, have been performed. A turbulent channel flow is statistically stationary and homogeneous in the spanwise and streamwise directions. Since the flow is restricted by the channel walls, non-slip and impermeability boundary conditions are imposed at the walls. In the homogeneous directions, periodic boundary conditions may be employed if the domain is large enough to contain the largest structures in the flow.

DNS requires resolution of all spatial and temporal scales within the flow. Typically, a domain is considered sufficiently large if two-point correlations of the turbulent fluctuations decay close to zero at a separation of half the period in the homogeneous directions (see Moin & Mahesh 1998). Regarding the grid resolution for DNS, it should be fine enough to capture the smallest scales in proximity to the wall. Generally, the resolution is $O(\eta)$, η being the Kolmogorov length scale. In Kim, Moin & Moser (1987) and Moser, Kim & Mansour (1999), the grid resolution is considered adequate if there is an evident scale separation, i.e. energy density at high wavenumbers is several decades lower than the one at low wavenumbers and if no energy pile-up is happening at the smallest scales.

The numerical simulations have been carried out using a finite-volume method on a collocated grid. Central differencing is used for the spatial discretization whilst the Crank–Nicolson scheme is employed for the discretization in time. The numerical procedure is based on an implicit, two-time-step advancement technique where the Poisson equation for the pressure is solved with an efficient multigrid method (see Emvin 1997). For more details regarding the numerical procedure and the FORTRAN 77 code,

GN fluid case	L_x/h	L_z/h	Δx^+	Δy^+_{min}	Δy^+_{max}	Δz^+	μ_∞/μ_0	μ_0/μ_w	$\Lambda(U_c/L_c)$	α
P180	6π	2.5π	14.81	0.22	4.62	6.17	1×10^{-3}	1.782	0.1	0.8
N180	4π	2π	9.88	0.22	4.62	4.94	—	1	—	1.0
D180	4π	2π	9.88	0.22	4.62	4.94	1×10^{-3}	0.561	0.1	1.2

TABLE 1. Parameters of the simulation. Here L_x and L_z are the periodic streamwise and spanwise dimensions of the computational domain, $L_y = 2h$ is the domain in the wall-normal direction, Δx^+ and Δz^+ are the constant grid spacings in inner units corresponding to the streamwise and spanwise directions whilst Δy^+_{min} and Δy^+_{max} are the minimum and maximum grid spacings in inner units corresponding to the wall-normal direction. P180 and D180 refer to the shear thinning or pseudo-plastic and shear thickening or dilatant fluid cases whilst N180 refers to the base Newtonian case.

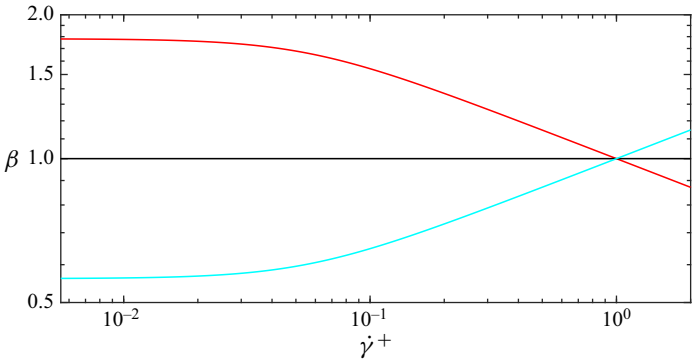

FIGURE 1. Viscosity rheogram. The flow index α is equal to 0.8 and to 1.2 for cases P180 and D180, respectively, whilst $\Lambda(U_c/L_c) = 0.1$ for both non-Newtonian cases. The profiles corresponding to P180 and D180 are identified by red and cyan colours, respectively.

called CALC-LES, see, for instance, Davidson & Peng (2003) and Davidson (2018). The GN fluid rheology has been incorporated into the code through the Carreau fluid model and the simulation parameters are summarized in table 1. A viscosity rheogram, β versus $\dot{\gamma}^+$, is also shown in figure 1. For all GN fluid cases, a target $Re_\tau = 180$ is considered. For cases N180 and D180, a computational box as in Kim *et al.* (1987) is used. For case P180, a larger computational domain is employed since structures of larger size than those in the Newtonian case are expected. See, for instance, Rudman & Blackburn (2006) and Singh *et al.* (2017*b*).

Synthetic turbulence (Davidson 2007) has been used to initialize case N180, whilst the simulations for the non-Newtonian cases have been initialized using a flow field corresponding to the Newtonian case at the same target Re_τ and the initial transients have been discarded. Statistically steady state is considered to have been achieved once a linear profile for $\bar{\tau}$ is observed (Vinuesa *et al.* 2016). The initial transient time is over 200 convective time units, and 150 flow fields saved every ≈ 0.2 eddy turnover times have been considered to compute the statistics.

With respect to the computational domain, for all cases, the two-point correlations between turbulent fluctuations, i.e. $R_{ij} = \overline{u_i'(\boldsymbol{x}, t)u_j'(\boldsymbol{x} + \boldsymbol{r}, t)}/\overline{u_i'(\boldsymbol{x}, t)u_j'(\boldsymbol{x}, t)}$, where $\boldsymbol{r}$ is the separation vector between the two points, appear to be decreasing with increasing

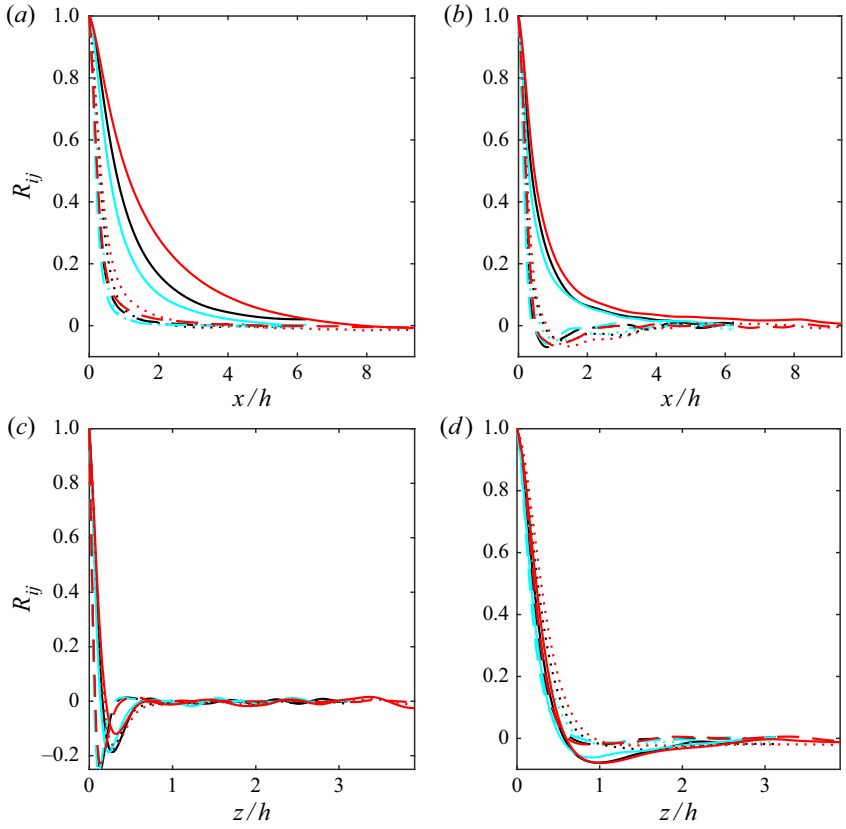

FIGURE 2. Normalized two-point correlations R_{ij}: streamwise separation at (*a*) $y^+ \approx 5.07$ and (*b*) $y^+ \approx 154.96$, spanwise separation at (*c*) $y^+ \approx 5.07$ and (*d*) $y^+ \approx 154.96$. Line styles '——', '- - -' and '· · ·' are used to identify R_{11}, R_{22} and R_{33}, respectively. Profiles corresponding to P180, N180 and D180 are identified by red, black and cyan colours, respectively.

separation in the homogeneous directions and the employed domains are deemed adequate; see figure 2. Note that, since the two-point correlations are related to the integral length scales, as expected, more elongated/larger structures are present in case P180 and finer structures in case D180 when compared with the Newtonian base case. Such observation is further supported by the instantaneous flow structures shown in figure 3. As can be seen, longer low-speed streamwise velocity streaks are observed for the shear-thinning case. Figure 3 also suggests that, for all fluid cases, the turbulent flow regime is achieved despite the low frictional Reynolds number used for the simulations.

To check the grid resolution, pre-multiplied one-dimensional spectral energy densities based on the presented two-point correlations are considered; see figure 4. Here, for all cases, an evident energy drop-off is occurring as the wavenumber increases and the maximum value in the different spectral energy densities is expected close to the wavenumbers corresponding to the respective integral length scales. For instance, the maximum in the pre-multiplied energy spectrum based on the two-point correlation for u' is expected at a wavenumber corresponding to the longitudinal integral length scale. Note as well that the pre-multiplied spectra corresponding to case P180, when compared to the results from cases N180 and D180 for the same number of modes, are presenting lower maximum amplitudes due to the increase in the computational domain for that case.

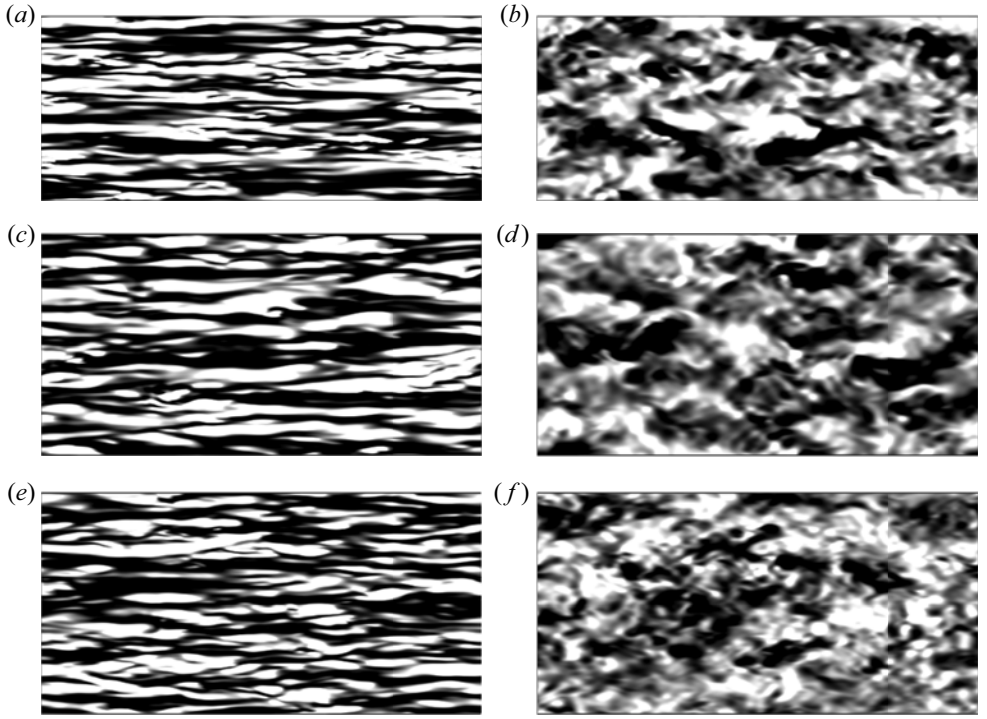

FIGURE 3. Contours of instantaneous streamwise velocity fluctuations normalized by frictional velocity at $y^+ \approx 5.07$ (*a*,*c*,*e*) and $y^+ \approx 154.96$ (*b*,*d*,*f*): (*a*,*b*) P180, (*c*,*d*) N180 and (*e*,*f*) D180. White and black represent positive and negative fluctuations, respectively.

In addition, whilst considering the computational resolution, a length scale based on the mean viscosity and the total dissipation rate has been computed; see figure 5. For the Newtonian case, this is the Kolmogorov length scale. For cases P180 and D180, since Kolmogorov's first similarity hypothesis (see e.g. Pope 2000) is stated for constant viscosity, such length scale $\tilde{\eta} = (\bar{\mu}/\rho)^{3/4}/\epsilon_k^{1/4}$, where $\epsilon_k = (\epsilon_{11} + \epsilon_{22} + \epsilon_{33})/2$ is the total mean dissipation rate (see Bradshaw & Perot (1993) and Bradshaw (1995) for a note about true dissipation), is analogous to η in the regions with minor variation in the mean viscosity profile, i.e. in the near-wall region and close to the channel's centre (see § 3.1). As seen from figure 5, for N180, $\Delta y^+_{min} < \eta^+$ in the near-wall region and $\Delta y^+_{max} \approx O(\eta^+)$ at the channel's centre. Similar trends are noted for the non-Newtonian fluid cases when comparing the wall-normal grid resolution with $\tilde{\eta}^+$.

Based on the energy drop-off previously noted and on the η^+ and $\tilde{\eta}^+$ values, the computational resolution appears to be adequate for the different cases. Also, a verification with published data for the Newtonian case is presented in appendix B.

3. Results

3.1. *Low-order statistics*

The mean (averaged in time and in homogeneous directions) streamwise velocity profile $\bar{u}^+$ and its diagnosis function $y^+ \mathrm{d}\bar{u}^+/\mathrm{d}y^+$ are presented in figure 6. In the same figure,

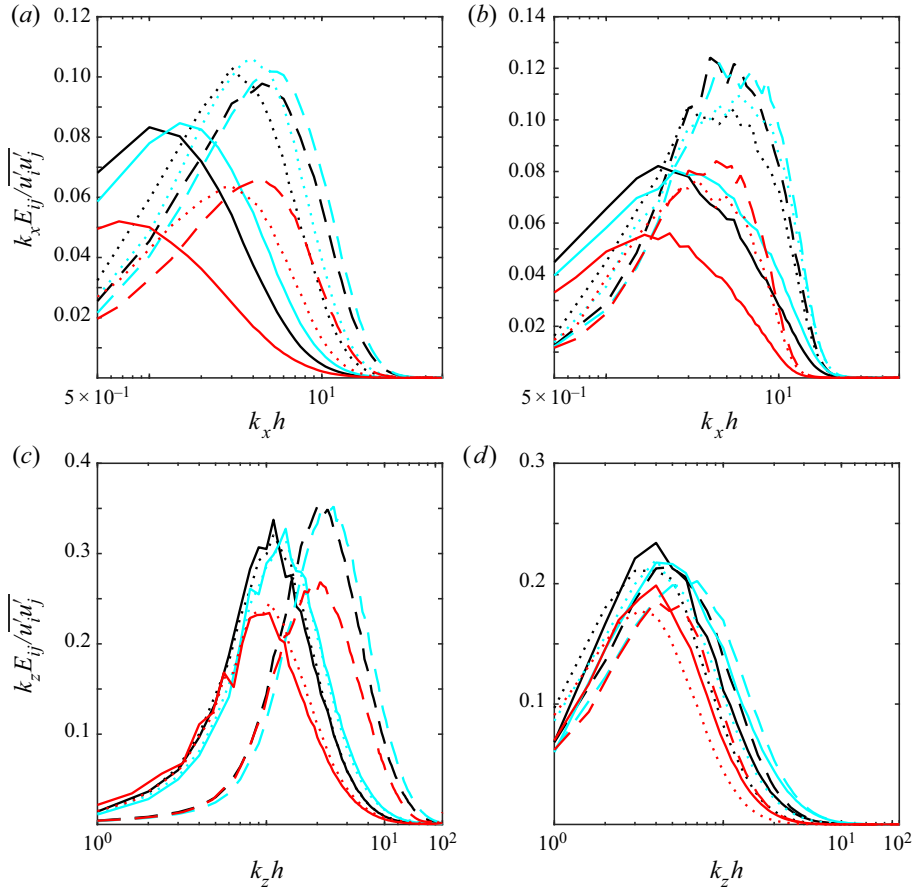

FIGURE 4. Pre-multiplied one-dimensional spectral energy density: against normalized streamwise wavenumber $k_x h$ at (*a*) $y^+ \approx 5.07$ and (*b*) $y^+ \approx 154.96$, and against normalized spanwise wavenumber $k_z h$ at (*c*) $y^+ \approx 5.07$ and (*d*) $y^+ \approx 154.96$. Line styles '——', '- - -' and '· · ·' are used to identify results corresponding to E_{11}, E_{22} and E_{33} spectral energy densities, respectively. Profiles corresponding to P180, N180 and D180 are identified by red, black and cyan colours, respectively.

the mean viscosity profile $\bar{\mu}^+ = \bar{\beta}$ and an analogous quantity to the diagnosis but for the mean viscosity, $y^+ \mathrm{d}\bar{\beta}/\mathrm{d}y^+$, are presented as well.

To discuss variations against the wall-normal coordinate y^+, the classical flow-region subdivision based on case N180 is considered: there is an inner region, comprising a viscous sublayer ($y^+ \lesssim 5$); a buffer region ($5 \lesssim y^+ \lesssim 55$); a quite limited – if it exists at all – log region ($55 \lesssim y^+ \lesssim 62$); and a remaining outer region. Within the viscous sublayer, for all cases, $\bar{u}^+ \approx y^+$ and for $y^+ \lesssim 10$, minor deviation for the non-Newtonian cases is noted in $\bar{u}^+$ and $\bar{\beta}$ when compared to case N180. For $y^+ \gtrsim 10$, $\bar{u}^+$ increases with decreasing flow index α, and a larger bulk velocity, implying a lower friction factor for a common driving pressure gradient, is observed. Also, as evidenced by the diagnosis function, the starting point of the log region and the corresponding $y^+ \mathrm{d}\bar{u}^+/\mathrm{d}y^+ \approx 1/\kappa$, where κ is the von Kármán constant, increase with decreasing flow index.

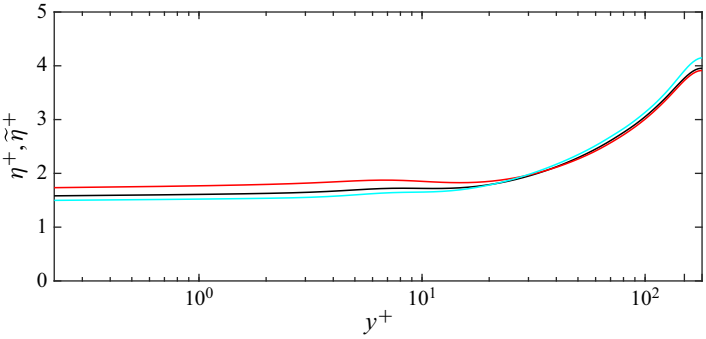

FIGURE 5. Kolmogorov's length scale η^+ and analogous length scale $\tilde{\eta}^+$, for the non-Newtonian cases, against y^+. Profiles corresponding to P180, N180 and D180 are identified by red, black and cyan colours, respectively.

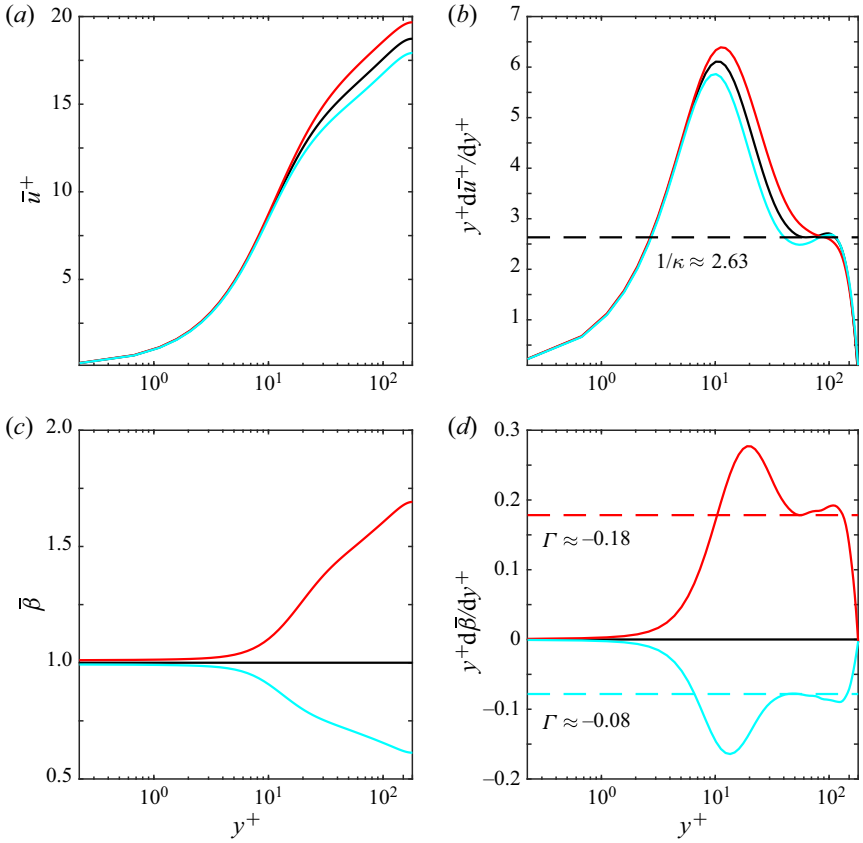

FIGURE 6. First-order statistics: (*a*) $\bar{u}^+$, (*b*) $y^+ \mathrm{d}\bar{u}^+/\mathrm{d}y^+$, (*c*) $\bar{\beta}$ and (*d*) $y^+ \mathrm{d}\bar{\beta}/\mathrm{d}y^+$ versus y^+. Profiles corresponding to P180, N180 and D180 are identified by red, black and cyan colours, respectively.

Regarding $\bar{\beta}$, for $y^+ \gtrsim 10$, it deviates rapidly from the corresponding constant Newtonian value, as expected. Since $\bar{\beta}$ appears to behave in a log manner within a certain y^+ range, an analogous diagnosis function based on $\bar{\beta}$ has been considered. On a first

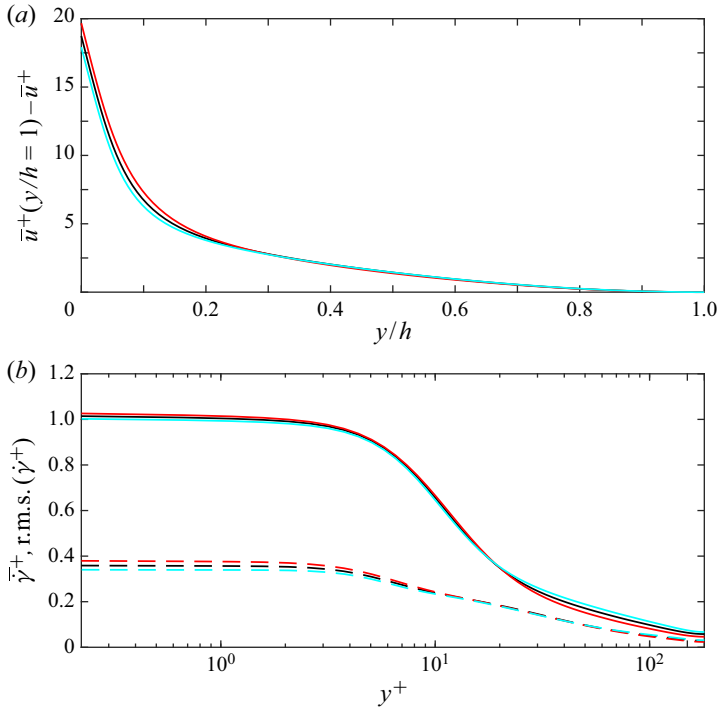

FIGURE 7. (*a*) Velocity defect profile against y/h and (*b*) low-order statistics corresponding to the strain rate against y^+; '——' mean strain rate $\bar{\dot{\gamma}}^+$ and '- - -' r.m.s. values of strain-rate fluctuations r.m.s.$(\dot{\gamma}^+)$. Profiles corresponding to P180, N180 and D180 are identified by red, black and cyan colours, respectively.

impression, such a log region in the mean viscosity ($y^+ \mathrm{d}\bar{\beta}/\mathrm{d}y^+ \approx \Gamma$) indeed occurs but different slopes Γ for cases P180 and D180 are observed; see figure 6(*d*).

For the outer layer region, the velocity defect profile $\bar{u}^+(y/h=1) - \bar{u}^+$ shown in figure 7(*a*) is apprised. From the velocity defect profile, it is clear that larger mean centreline velocity values are observed with decreasing flow index. Also, it appears that, in the outer layer region ($y^+ \gtrsim 62$ or $y/h \gtrsim 0.35$), all curves collapse. Such behaviour suggests independence of the velocity defect profile in the outer region and that differences in the mean velocity profiles between the different cases (P180, N180 and D180) are most likely due to differences in the flow within the inner region. This observation has also been made by Singh *et al.* (2018).

Distribution in the i direction ($i = 1, 2, 3$) of the r.m.s. values of the velocity fluctuations and the vorticity fluctuations, i.e. r.m.s.$(u_i^+) = \overline{(u_i')^2}^{1/2}/u_\tau$ and r.m.s.$(\omega_i^+) = \overline{(\omega_i')^2}^{1/2}[\mu_w/(\rho u_\tau^2)]$, respectively, is presented in figure 8. The r.m.s. values corresponding to fluctuations in viscosity r.m.s.$(\beta) = \overline{(\mu')^2}^{1/2}/\mu_w$ are also shown in figure 8. The r.m.s. values for the velocity fluctuations appear to be affected by the rheology mainly outside the viscous sublayer. The streamwise turbulence intensity increases with decreasing flow index whilst the opposite is observed in the spanwise and wall-normal turbulence intensities for the same trend. The wall-normal position at which a peak in the streamwise turbulence intensity appears moves slightly from the wall with decreasing flow index.

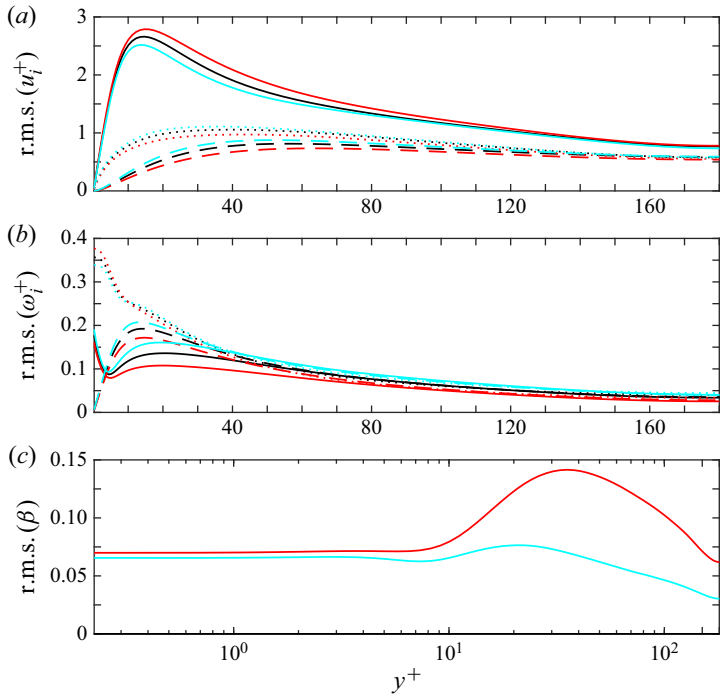

FIGURE 8. Second-order statistics: (*a*) turbulence intensities r.m.s.(u_i^+), (*b*) r.m.s. values of vorticity fluctuations r.m.s.(ω_i^+) and (*c*) r.m.s. value of viscosity fluctuations r.m.s.(β). In (*a*,*b*) line styles '——', '- - -' and '· · ·' are used to identify r.m.s. values based on x, y and z velocity and vorticity fluctuation components. Profiles corresponding to P180, N180 and D180 are identified by red, black and cyan colours, respectively.

With respect to the r.m.s. values of the vorticity fluctuations, in the near-wall region, there is an increase in the spanwise component whilst a decrease is observed for the other two components with decreasing flow index. Thus, we anticipate an increase in the magnitude of the mean viscous dissipation since, for homogeneous turbulence, the enstrophy is approximately equal to the ratio between mean viscous dissipation rate and mean kinematic viscosity. At a wall-normal position within the buffer region ($y^+ \approx 10$), the opposite is then observed for the r.m.s. values of the spanwise vorticity fluctuation, i.e. the r.m.s. value decreases with shear thinning. Moreover, after such a point, the r.m.s. values of all vorticity fluctuations appear to decrease with decreasing flow index.

It is interesting to note that the presented results suggest an overall increase in the anisotropy of the velocity and vorticity correlation tensors, $\overline{u_i' u_k'}$ and $\overline{\omega_i' \omega_k'}$, with shear thinning (see § 3.5).

Regarding the r.m.s. values corresponding to fluctuations in viscosity, similar to the mean viscosity profile, the distribution appears to be approximately constant in the viscous sublayer and then it starts to increase with y^+ up to a certain value within the inner region. After such a wall-normal position, the r.m.s. values of the viscosity fluctuations start to decrease more rapidly. Here, the plateau in $\bar{\beta}$ and r.m.s.(β) within the viscous sublayer is likely due to small variations in the mean strain rate and its r.m.s. values, respectively (see figure 7*b*). Note that, altogether, r.m.s.(β) is larger for case P180, suggesting larger

fluctuations from $\bar{\beta}$ with shear thinning. It is also noted that the peak in r.m.s.(β) moves from the wall with shear thinning.

Finally, it is worth pointing out some qualitative similarities with channel flow of viscoelastic fluids, which is another type of drag-reducing fluid. Compared to the Newtonian case and as with shear thinning, there is a noticeable increase in the mean streamwise velocity with viscoelasticity. Also for $Re_\tau < 1000$, a minimal – if any – presence of a log-law region is observed (Thais, Gatski & Mompean 2012). With respect to the turbulence intensities, compared to the Newtonian case and as with shear thinning, Ptasinski *et al.* (2003) and Min, Choi & Yoo (2003*a*) reported an enhancement of the streamwise turbulence intensity and a decrease of the wall-normal and spanwise turbulence intensities with viscoelasticity and in the case of small drag reduction (SDR) regime (see Warholic, Massah & Hanratty 1999). In contrast, the same publications reported a decrease in all turbulence intensities with viscoelasticity for the large drag reduction (LDR) regime. On the other hand, regarding low-order statistics reported for other canonical flows of GN fluids, it is worth mentioning that Singh *et al.* (2017*b*) showed similar trends with shear thinning for pipe flow. For $\alpha < 1$, there is an increase in the mean axial velocity, mean viscosity and axial turbulence intensity whereas both radial and azimuthal turbulence intensities decrease.

3.2. *Mean shear stress budget*

For a statistically stationary fully developed flow of an incompressible GN fluid, the total mean shear stress $\bar{\tau}^+$ (see § 2.1.1) is given by

$$\bar{\tau}^+ = \bar{\tau}^+_{vis} + \bar{\tau}^+_{tur} + \bar{\tau}^+_{GN}, \tag{3.1}$$

where $\bar{\tau}^+_{vis} = \bar{\beta}\mathrm{d}\bar{u}^+/\mathrm{d}y^+$, $\bar{\tau}^+_{tur} = -\overline{u'v'}/u_\tau^2$ and $\bar{\tau}^+_{GN} = \overline{2\beta' S'_{12}}^+$ are the viscous stress, the turbulent or Reynolds shear stress and the new stress due to fluctuation in viscosity, respectively. Owing to the constant pressure gradient driving the flow, the total mean shear stress is linear, i.e. $\bar{\tau}^+ = 1 - y^+/Re_\tau$.

The different contributions to the total mean shear rate are shown in figure 9. As can be seen, the mean viscous stress increases in the shear-thinning case. Since $\bar{\tau}^+_{vis}$ depends on $\bar{\beta}$ and $\mathrm{d}\bar{u}^+/\mathrm{d}y^+$, its increase can be discussed considering figure 6(*b*,*c*). For $y^+ \lesssim 10$, there is minor variation in the mean viscosity and in the mean streamwise velocity gradient. Thus, the increase in $\bar{\tau}^+_{vis}$ for the shear-thinning case is attributed to a small increase in both quantities. For $y^+ > 10$, outside the viscous sublayer, the increase in the mean viscous stress is mostly due to $\bar{\beta}$, which quite significantly increases in the shear-thinning case due to the higher 'zero' shear-rate viscosity (see viscosity rheogram, figure 1). In the near-wall region where the turbulent stress is close to zero, the decrease/increase in the viscous stress component due to shear thickening/shear thinning is compensated by the new stress component. Note that the sign of $\bar{\tau}^+_{GN}$ depends on the sign of $\alpha - 1$. Outside the viscous sublayer, the new stress starts to decrease and the viscous stress is then compensated by the turbulent stress component. Thus, for example, an increase in the viscous stress due to shear thinning is compensated by a decrease in the Reynolds shear stress. It is also interesting to note that $\bar{\tau}^+_{tur}$, for all cases, appear to collapse in the outer region, suggesting that the cross-correlation $\overline{u'v'}/u_\tau^2$ is independent of the rheology in that region.

Finally, it is worth contrasting the mean shear stress budget corresponding to the shear-thinning fluid with the budget of a drag-reducing polymer solution, i.e. a

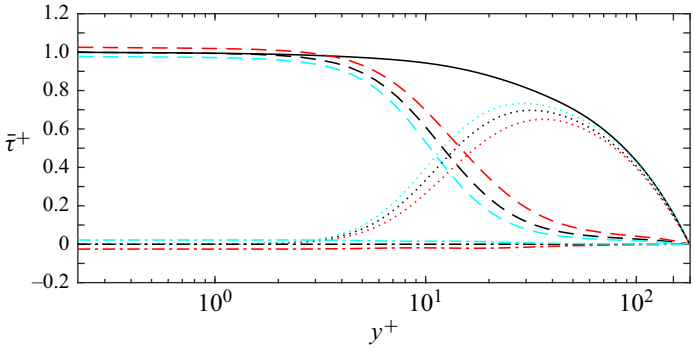

FIGURE 9. Mean shear stress budget. Line styles '——', '- - -', '· · ·' and '- · -' are used to identify $\bar{\tau}^+$, $\bar{\tau}^+_{vis}$, $\bar{\tau}^+_{tur}$ and $\bar{\tau}^+_{GN}$, respectively. Profiles corresponding to P180, N180 and D180 are identified by red, black and cyan colours, respectively.

viscoelastic fluid. Compared to the Newtonian case and as with shear thinning, there is a significant overall reduction in the Reynolds shear stress with polymer additives (Min *et al.* 2003*a*; Ptasinski *et al.* 2003). In addition, Ptasinski *et al.* (2003) reported that the polymer stress, arising due to viscoelastic effects, is always positive but relatively small and mainly important near to the wall for SDR, whereas for LDR, this contribution is large and important across the whole channel. Note that, in contrast, the analogous $\bar{\tau}^+_{GN}$ is always negative for shear thinning and mainly important close to the wall. On the other hand, regarding Reynolds stress budgets reported for other canonical flows of GN fluids, Singh *et al.* (2017*b*) presented similar trends with shear thinning for pipe flow. For $\alpha < 1$, the mean viscous stress slightly increases near the wall and more noticeably in the buffer layer region whereas the Reynolds shear stress decreases for all y^+ and a new negative stress arises in the total mean stress balance.

3.3. *Quadrant analysis*

To improve our understanding of the generation of Reynolds shear stress and the related production of turbulent kinetic energy, a quadrant analysis (Wallace *et al.* 1972) is carried out. Contributions to the cross-correlation $-\overline{u'v'}$ are classified according to the sign of the velocity fluctuations into four categories or quadrants: Q1 ($u' > 0,\ v' > 0$), Q2 ($u' < 0,\ v' > 0$), Q3 ($u' < 0,\ v' < 0$) and Q4 ($u' > 0,\ v' < 0$), and each of the quadrant motions is associated with a physical event: positive production of turbulent kinetic energy arises due to low-speed fluid moving from the wall (Q2 events) and high-speed fluid moving towards the wall (Q4 events). Such motions have been visualized, see for instance Kline *et al.* (1967) and Corino & Brodkey (1969), and denoted as ejection and sweep events, respectively. Q1 and Q3 motions, which correspond to high-speed fluid reflected outwards from the wall and low-speed fluid deflected towards the wall, account for negative production of turbulent kinetic energy, and in the absence of a better terminology may be called outwards and wallwards interactions (Wallace 2016).

The quadrant-conditioned contributions to the Reynolds shear stress are presented in figure 10 for the different cases. In the following discussion, changes in quadrant event contributions with shear thinning are also considered in light of variation with decreasing

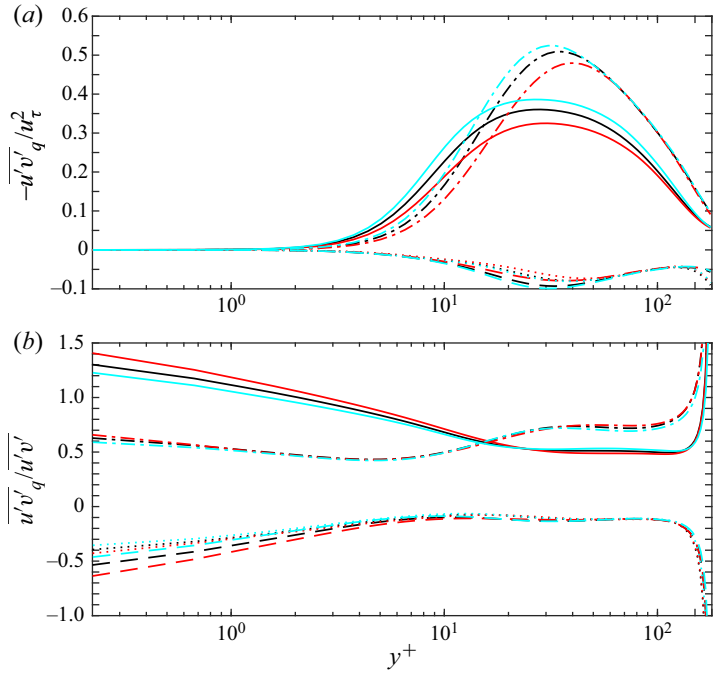

FIGURE 10. Quadrant contributions to $-\overline{u'v'}/u_\tau^2$: (*a*) non-fractional $-\overline{u'v'}_q/u_\tau^2$ and (*b*) fractional $\overline{u'v'}_q/\overline{u'v'}$ contributions. The subscript q refers to quadrant-conditioned averages. Line styles '- - -', '- · -', '· · ·' and '——' are used for Q1, Q2, Q3 and Q4 contributions, respectively. Profiles corresponding to P180, N180 and D180 are identified by red, black and cyan colours, respectively.

flow index in the skewness and flatness profiles corresponding to the velocity fluctuations. The profiles are shown in figure 11.

From the non-fractional contributions to $-\overline{u'v'}/u_\tau^2$, a decrease in contributions from all quadrants' events with shear thinning is observed. This trend is consistent with the perceived decrease in Reynolds shear stress with shear thinning seen in § 3.2. Also, from the non-fractional contributions, it is noted that the wall-normal position at which contributions from sweep and ejection events coincide has moved slightly from the wall for the shear-thinning case. A similar behaviour – with shear thinning – is then expected for the peaks corresponding to maximum production and maximum turbulent kinetic energy (see § 3.4).

Observing the fractional quadrant contributions, it is noticed that, for all fluid cases, sweep events appear to dominate in the very near-wall region whilst ejection events contribute more to $-\overline{u'v'}/u_\tau^2$ after the y^+ position where the contributions due to Q2 and Q4 motions are approximately the same. Within the viscous sublayer where quite large intermittency is present, a more pronounced increase in the fractional Q1 contribution is observed for the shear-thinning case. Such an increase, mainly compensated by fractional contributions due to Q4 events, is expected since the correlation between $u' > 0$ and $v' > 0$ appears to vary little with rheology (see non-fractional contribution profiles) and the overall Reynolds shear stress is decreasing with shear thinning even within such a very near-wall region. As reflected in the normalized skewness profiles,

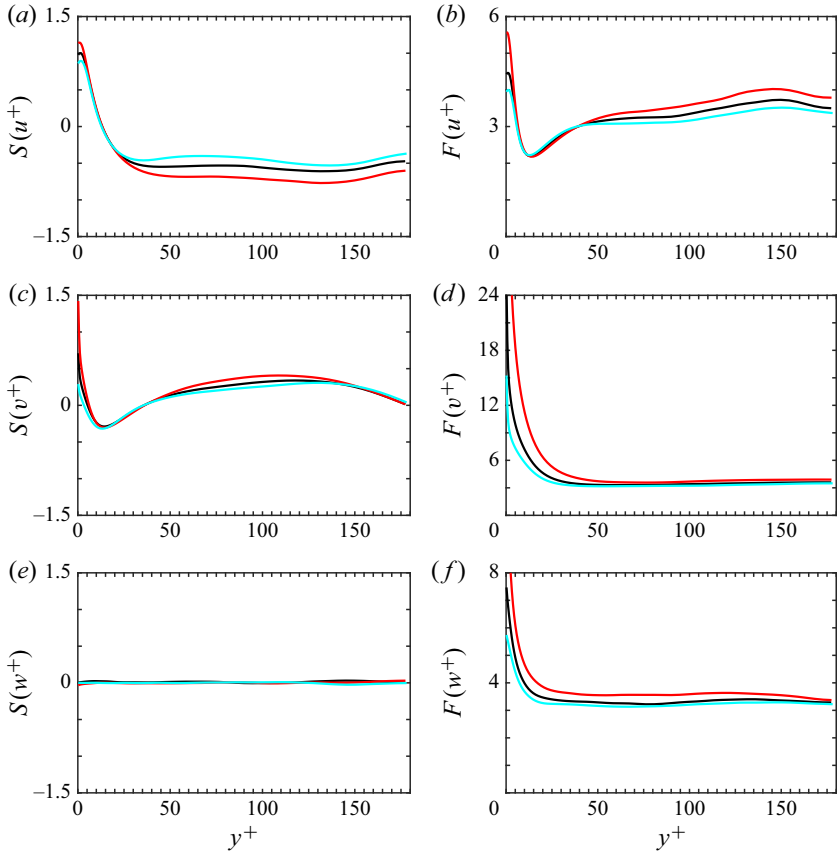

FIGURE 11. Skewness S and flatness F profiles of velocity fluctuations: (*a*) $S(u^+) = \overline{(u')^3}/(\overline{u'u'})^{3/2}$, (*b*) $F(u^+) = \overline{(u')^4}/(\overline{u'u'})^2$, (*c*) $S(v^+) = \overline{(v')^3}/(\overline{v'v'})^{3/2}$, (*d*) $F(v^+) = \overline{(v')^4}/(\overline{v'v'})^2$, (*e*) $S(w^+) = \overline{(w')^3}/(\overline{w'w'})^{3/2}$ and (*f*) $F(w^+) = \overline{(w')^4}/(\overline{w'w'})^2$. Profiles corresponding to P180, N180 and D180 are identified by red, black and cyan colours, respectively.

large positive streamwise and wall-normal velocity fluctuations appear to dominate more with shear thinning and, as shown in the non-fractional contributions, lead to a decrease in contributions from Q2 and Q4 events, which decreases the overall Reynolds shear stress.

Outside the viscous sublayer but before the wall-normal position where Q2 and Q4 contributions are approximately the same, there is little variation in the non-fractional contributions due to Q1 and Q3 events with rheology. The decrease in contribution from sweep and ejection events, together causing the decrease in $-\overline{u'v'}/u_\tau^2$, appears to be related to the appearance of more dominant large positive streamwise fluctuation and less dominant negative wall-normal fluctuations with shear thinning, as reflected in the normalized skewness profiles. After the point with equal contributions from Q2 and Q4 events but before a position $y^+ \approx 30$–35 where ejection events dominate due to large intermittent $v' > 0$ values for all GN fluids, the decrease in Reynolds shear stress with shear thinning appears to be linked to a slight increase in dominant $u' > 0$ and $v' < 0$ signals.

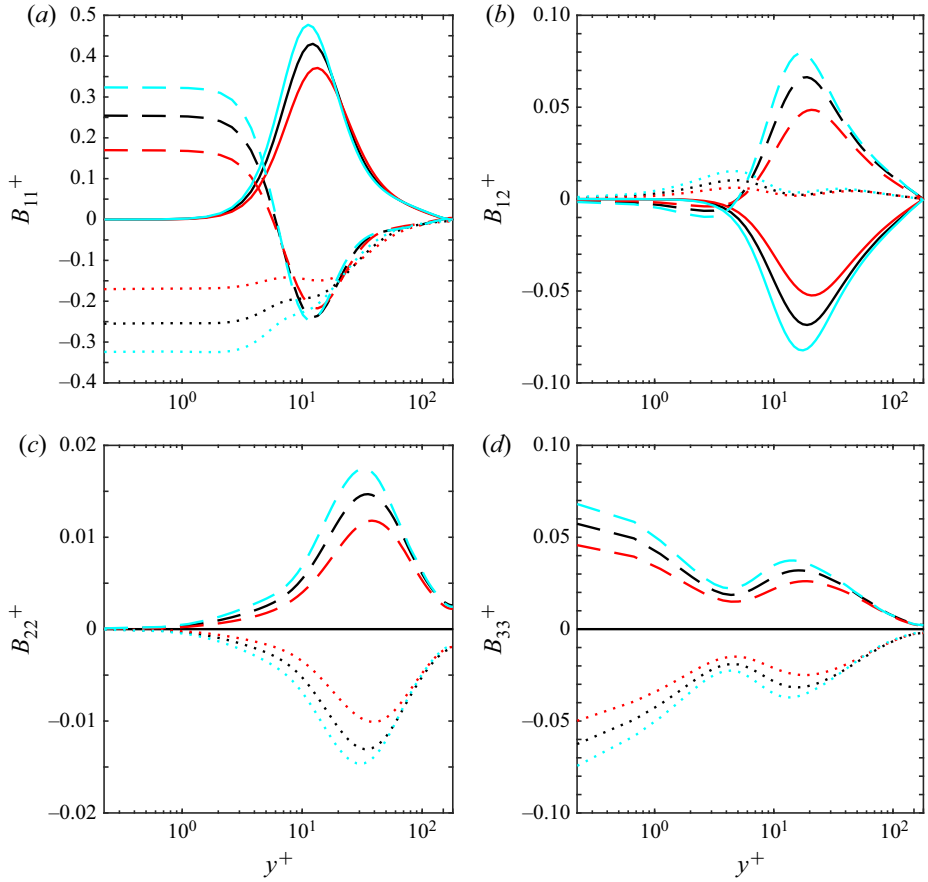

FIGURE 12. Reynolds stress budgets: (*a*) B_{11}^+, (*b*) B_{12}^+, (*c*) B_{22}^+ and (*d*) B_{33}^+. The line styles '——', '- - -' and '· · ·' are used to identify P_{ik}^+, T_{ik}^+ and $-\epsilon_{ik}^+$, respectively. Profiles corresponding to P180, N180 and D180 are identified by red, black and cyan colours, respectively.

Finally, after the position $y^+ \approx 30$–35, non-fractional contributions due to Q1, Q2 and Q3 events almost do not vary with rheology, and the observed decrease in $-\overline{u'v'}/u_\tau^2$ for the shear-thinning case is attributed to a decrease in the contribution from sweep events with shear thinning. Here, such behaviour is likely to be due to more dominant $u' < 0$ and $v' > 0$ signals with decreasing flow index, as reflected in the corresponding normalized skewness profiles.

3.4. *Reynolds stress budgets*

The Reynolds stress budgets, corresponding to the equations presented in § 2.1.2, are considered. The total production, transport and dissipation rates corresponding to budgets B_{ik}^+ of the relevant non-zero stresses in a fully developed turbulent channel flow, for the different GN fluid cases, are shown in figure 12. The turbulent kinetic energy budget B_k^+ and the turbulent kinetic energy profile $k^+ = \overline{u_i'u_i'}/(2u_\tau^2)$ are presented in figure 13.

For all cases, and as expected, the interaction between $-\overline{u'v'}/u_\tau^2$ and mean shear causes a production rate in budget B_{11}^+. Since the mean velocity gradients increase with shear

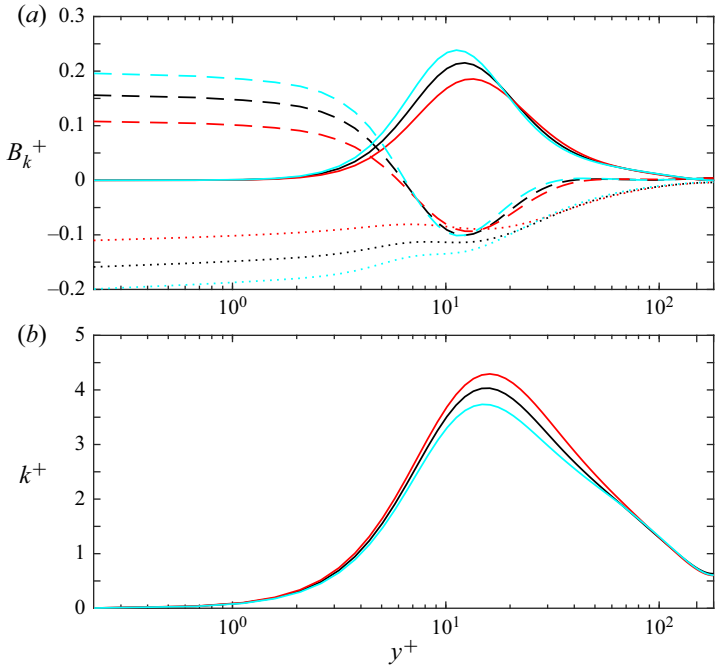

FIGURE 13. Plots of (*a*) B_k^+ and (*b*) k^+. In panel (*a*), the line styles '——', '- - -' and '· · ·' are used to identify P_k^+, T_k^+ and $-\epsilon_k^+$, respectively. Profiles corresponding to P180, N180 and D180 are identified by red, black and cyan colours, respectively.

thinning (see $\bar{u}^+$ profile in § 3.1), the decrease in P_{11}^+, in its near-peak region, is attributed to the observed decrease in Reynolds shear stress with decreasing flow index (see $\bar{\tau}_{tur}^+$ in § 3.2). Note as well that, as commented in § 3.3, the peak in production at $y^+ \approx 12$ for the Newtonian case has moved slightly from the wall with shear thinning. In budget B_{11}^+, the energy from the production region is then distributed through T_{11}^+ towards and away from the wall. At the wall, a good portion of the transported energy from the maximum production region is then dissipated at a rate ϵ_{11}^+. Everywhere P_{11}^+ is balanced by $T_{11}^+ - \epsilon_{11}^+$. Note that, consistently with the decrease in the production rate with shear thinning, the amount of energy that is irreversibly dissipated decreases with decreasing flow index.

Since budgets B_{22}^+ and B_{33}^+ do not contain a production term, their source is energy being redistributed from budget B_{11}^+. Here, an apparent decrease in redistribution of energy from B_{11}^+ to B_{22}^+ and B_{33}^+, reflected in the decrease of T_{11}^+, T_{22}^+ and T_{33}^+, is occurring with decreasing flow index. This observation is consistent with the noticed increase in streamwise turbulence intensity and the decrease in the spanwise and wall-normal intensities with shear thinning, seen in § 3.1.

For budget B_{12}^+, the interaction between wall-normal turbulence intensities and mean shear yields production. Owing to the aforementioned decrease in the wall-normal intensities with decreasing flow index, there is a decrease in the production rate P_{12}^+ with shear thinning. This observation is consistent with the noted decrease in Reynolds shear stress with decreasing flow index. As for the B_{11}^+ budget, the source from the production region is transported towards and away from the wall through T_{12}^+. However, different

from that budget, little of that source (even less so for the shear-thinning fluid case) is 'dissipated' at a rate ϵ_{12}^{+} and mostly is balanced by T_{12}^{+}.

The balance of the turbulent kinetic energy budget B_k^{+} is based on the terms appearing in B_{11}^{+}, B_{22}^{+} and B_{33}^{+}, where budget B_{11}^{+} with turbulent production dominates over the others. Thus, the balance of B_k^{+} and the corresponding observations are similar to those made for budget B_{11}^{+}. It is interesting to note that most variations in the terms of B_k^{+} with rheology appear to be restricted to the inner layer region. Also, with respect to the total dissipation rate, since from the r.m.s. values of the vorticity fluctuations (see § 3.1) an increase in the magnitude of the mean viscous dissipation rate is expected with shear thinning, the overall decrease in the magnitude of ϵ_k^{+} appears to be due to the non-Newtonian terms contributing to it.

Regarding k^{+}, as expected, there is an increase with shear thinning and, similar to the production rate, its peak has moved slightly from the wall with decreasing flow index. The increase in turbulent kinetic energy may be explained by considering the deficit in redistribution of energy from budget B_{11}^{+} to B_{22}^{+} and B_{33}^{+} with shear thinning, since it causes the observed increase in anisotropy between the turbulence intensities. The profile of k^{+} may also be understood while examining the total production and dissipation rates. Within the region where production exceeds dissipation and the transport rate T_k^{+} is negative, there is an increase in how much P_k^{+} exceeds $-\epsilon_k^{+}$ with decreasing flow index. This is reflected by an increase in the turbulent kinetic energy profile within the same region.

Contributions from the different terms in (2.23) to total transport and dissipation rates for budgets B_{11}^{+}, B_{12}^{+} and B_k^{+} are shown in figures 14–16. Contributions to budgets corresponding to the other diagonal components of $\overline{u_i' u_k'}$, i.e. B_{22}^{+} and B_{33}^{+}, are presented in appendix C.

For the transport rate T_{11}^{+}, the traditional terms Π_{11}^{+}, TT_{11}^{+} and MD_{11}^{+} contribute the most. The velocity–pressure gradient term Π_{11}^{+} notably decreases in magnitude with decreasing flow index. This behaviour is to be expected since redistribution of energy to budgets B_{22}^{+} and B_{33}^{+} decreases with shear thinning. The mean viscous diffusion MD_{11}^{+}, which constitutes the largest contribution to T_{11}^{+}, appears to be mainly affected by rheology within the viscous sublayer and increases with decreasing flow index. Since the mean viscosity varies little for $y^{+} \lesssim 10$, such an increase is attributed to an increase of diffusion of $\overline{u'u'}/u_\tau^2$ with shear thinning. The turbulent transport TT_{11}^{+}, on the other hand, is mainly affected outside the viscous sublayer but within the inner layer region by rheology. Here TT_{11}^{+} mostly decreases in magnitude with decreasing flow index.

The non-Newtonian transport term mainly affecting T_{11}^{+} within the viscous sublayer is $\widetilde{TD}_{11}^{+}$. Since, in the very near-wall region, the fluctuations in viscosity are rather small (see the r.m.s.(β) profile in § 3.1), the diffusion of $u'\bar{u}/u_\tau^2$ is considered the reason for the large magnitude in $\widetilde{TD}_{11}^{+}$ within this region. Also, the turbulent viscous diffusion rate related to mean flow decreases the total transport rate T_{11}^{+} with shear thinning. Other transport terms such as TD_{11}^{+}, Tv_{11}^{+} and Mv_{11}^{+} related to fluctuation in viscosity, their gradients and gradients in the mean viscosity either decrease or increase with rheology at different wall-normal positions but almost do not affect the total transport rate. The remaining transport term $\widetilde{Tv}_{11}^{+}$ increases with decreasing flow index and appears to be mainly relevant in the inner region outside the viscous sublayer. In this region both gradients of fluctuations in viscosity and advected gradients of the mean streamwise velocity are expected to contribute to $\widetilde{Tv}_{11}^{+}$.

For the total dissipation rate ϵ_{11}^{+}, $M\epsilon_{11}^{+}$ and $\widetilde{T\epsilon}_{11}^{+}$ appear to contribute the most. The mean viscosity increases with decreasing flow index; however, at the wall and in the

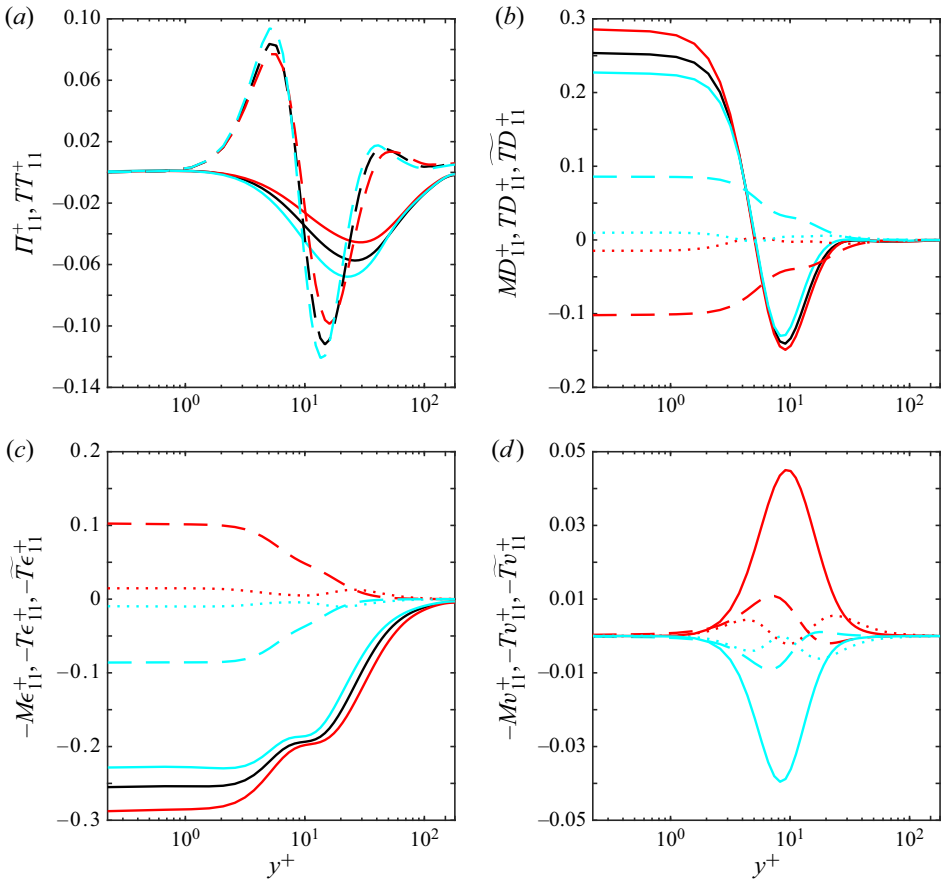

FIGURE 14. Contributions to T_{11}^+ and $-\epsilon_{11}^+$ in budget B_{11}^+: (*a*) line styles '——' and '- - -' are used for Π_{11}^+ and TT_{11}^+; (*b*) line styles '——', '- - -' and '· · ·' are used for MD_{11}^+, $\widetilde{TD}_{11}^+$ and TD_{11}^+; (*c*) line styles '——', '- - -' and '· · ·' are used for $-M\epsilon_{11}^+$, $-\widetilde{T}\epsilon_{11}^+$ and $-T\epsilon_{11}^+$; and (*d*) line styles '——', '- - -' and '· · ·' are used for $\widetilde{T}v_{11}^+$, Mv_{11}^+ and Tv_{11}^+. Profiles corresponding to P180, N180 and D180 are identified by red, black and cyan colours, respectively.

very near-wall region, the mean viscosity is almost unaffected by rheology. Therefore, the increase of magnitude in $M\epsilon_{11}^+$ with shear thinning is mainly attributed to an increase in the autocorrelation of streamwise velocity fluctuation gradients. This observation is consistent with the increase in the r.m.s. values of the spanwise vorticity fluctuations at the wall and very near it with shear thinning (see § 3.1). Outside the viscous sublayer and mainly for $y^+ \gtrsim 10$, the mean viscosity starts to increase in a more noticeable manner with decreasing flow index, and contributes more to the increase in magnitude of the mean viscous dissipation rate within that region.

The non-Newtonian dissipation rate $\widetilde{T}\epsilon_{11}^+$ increases in magnitude with decreasing flow index and mainly affects ϵ_{11}^+ in the inner region, specially within the viscous sublayer. In the vicinity of the wall, the fluctuations in viscosity are fairly small and the large magnitude observed for $\widetilde{T}\epsilon_{11}^+$ is attributed to the correlation between mean streamwise velocity gradients and streamwise velocity fluctuation gradients. Note that the decrease in

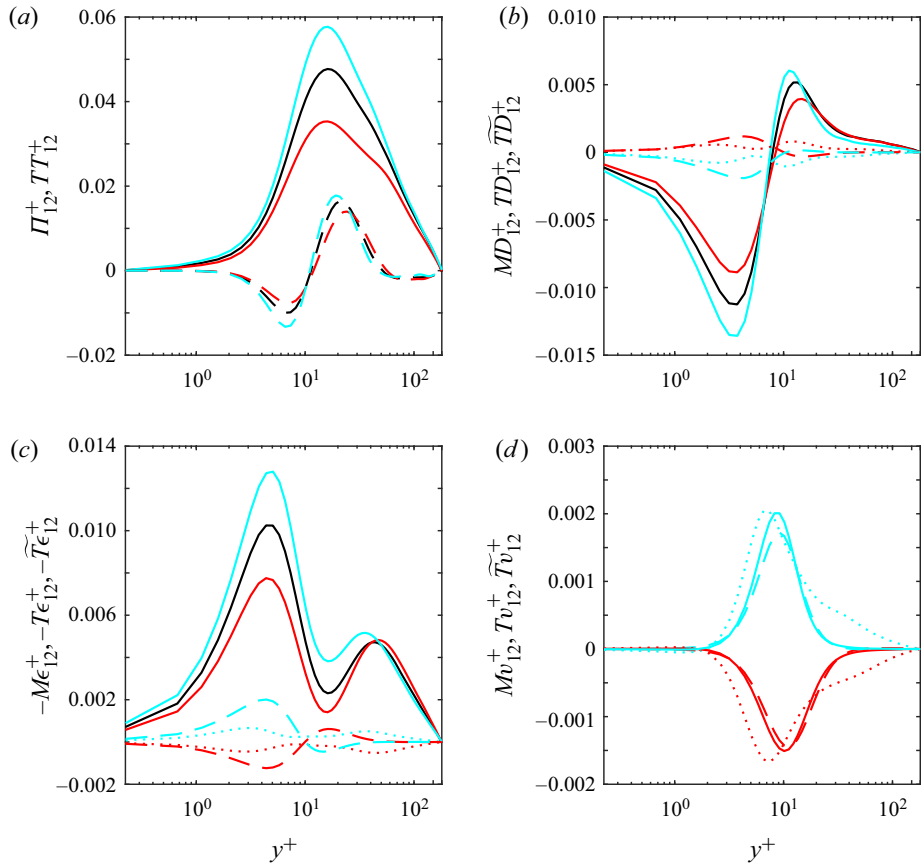

FIGURE 15. Contributions to T_{12}^+ and $-\epsilon_{12}^+$ in budget B_{12}^+: (*a*) line styles '——' and '- - -' are used for Π_{12}^+ and TT_{12}^+; (*b*) line styles '——', '- - -' and '· · ·' are used for MD_{12}^+, $\widetilde{TD}_{12}^+$ and TD_{12}^+; (*c*) line styles '——', '- - -' and '· · ·' are used for $-M\epsilon_{12}^+$, $-\widetilde{T}\epsilon_{12}^+$ and $-T\epsilon_{12}^+$; and (*d*) line styles '——', '- - -' and '· · ·' are used for $\widetilde{T}v_{12}^+$, Mv_{12}^+ and Tv_{12}^+. Profiles corresponding to P180, N180 and D180 are identified by red, black and cyan colours, respectively.

the magnitude of ϵ_{11}^+ at the wall with shear thinning is mainly attributed to dissipation at rate $\widetilde{T}\epsilon_{11}^+$, since the magnitude of $M\epsilon_{11}^+$ is increasing with decreasing flow index. The other non-Newtonian dissipation rate $T\epsilon_{11}^+$ also causes the decrease in the magnitude of the total dissipation rate ϵ_{11}^+ with shear thinning. Nonetheless, compared to $\widetilde{T}\epsilon_{11}^+$, it is smaller in magnitude. The dissipation rate $T\epsilon_{11}^+$ arises due to interactions between fluctuations in viscosity and squared streamwise velocity fluctuation gradients.

For the transport rate T_{12}^+, the important terms appear to be the velocity–pressure gradient term and the turbulent transport rate. Most of the production P_{12}^+ is balanced by Π_{12}^+ and TT_{12}^+. Within the inner region, the mean viscous diffusion rate appears to contribute in no significant manner to the rate T_{12}^+ and, even less so, other non-zero transport terms associated to the non-Newtonian rheology.

The total 'dissipation' rate ϵ_{12}^+ is quite low and it is mainly due to the mean viscous 'dissipation' rate $M\epsilon_{12}^+$. The rate $T\epsilon_{12}^+$ presents the opposite sign to $M\epsilon_{12}^+$ for the same

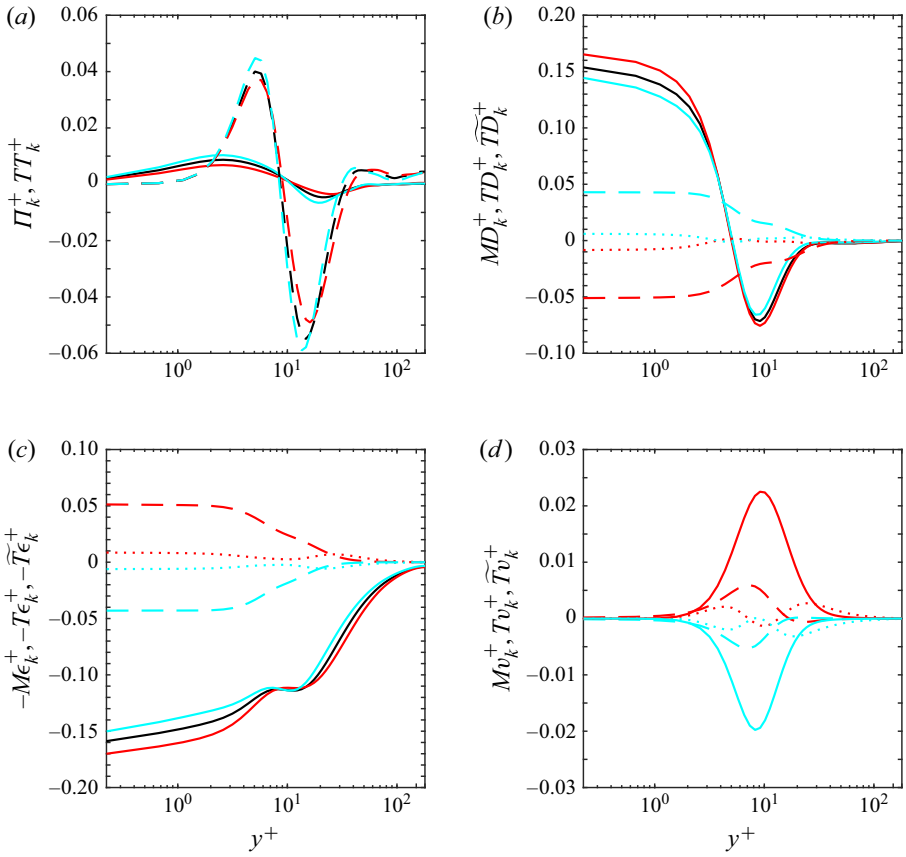

FIGURE 16. Contributions to T_k^+ and $-\epsilon_k^+$ in budget B_k^+: (*a*) line styles '——' and '- - -' are used for Π_k^+ and TT_k^+; (*b*) line styles '——', '- - -' and '· · ·' are used for MD_k^+, $\widetilde{TD}_k^+$ and TD_k^+; (*c*) line styles '——', '- - -' and '· · ·' are used for $-M\epsilon_k^+$, $-\widetilde{T\epsilon}_k^+$ and $-T\epsilon_k^+$; and (*d*) line styles '——', '- - -' and '· · ·' are used for $\widetilde{Tv}_k^+$, Mv_k^+ and Tv_k^+. Profiles corresponding to P180, N180 and D180 are identified by red, black and cyan colours, respectively.

non-Newtonian fluid case, whilst the rate $\widetilde{T\epsilon}_{12}^+$ either increases or decreases the total rate ϵ_{12}^+, depending on which part of the inner region is being considered. Nonetheless, none of the 'dissipation' rates appearing with non-Newtonian rheology contribute considerably to the total rate ϵ_{12}^+.

Regarding the terms contributing to the total transport and dissipation rates in budget B_k^+, the observed trends with rheology are the same as those noted for T_{11}^+ and ϵ_{11}^+, since the terms in budget B_{11}^+ contribute the most to the turbulent kinetic energy budget. The profile of rate Π_k^+ is, of course, different from the profile of the velocity–pressure gradient term in budget B_{11}^+, but the trend of a decrease in magnitude with shear thinning, due to less energy being redistributed, is the same.

Also, it is worth mentioning some similarities found with the budgets reported for another type of drag-reducing fluid, namely a viscoelastic fluid. For the channel flow of a viscoelastic fluid, Dimitropoulos *et al.* (2001) showed that the most significant changes

in budget B_k^+ relative to Newtonian values are observed in the turbulence production, mean viscous dissipation and turbulence transport rates. Compared to the Newtonian case and as with shear thinning, there is a decrease in the production term and in the absolute peak values for the turbulent transport term with viscoelasticity. In addition, opposite to the behaviour seen for shear thinning, Dimitropoulos *et al.* (2001) reported a decrease in the mean viscous dissipation with shear thinning. The paper also shows that viscoelastic terms, contributing to B_k^+, are relatively small when compared to the production, mean diffusion or mean viscous dissipation rates. Regarding the individual budgets, Dimitropoulos *et al.* (2001) revealed that viscoelastic effects are most pronounced in the velocity–pressure gradient term. Compared to the Newtonian case and as with shear thinning, in the budget B_{11}^+, the rate Π_{11}^+ is reduced with viscoelasticity, in particular close to the region of maximum production. The paper also reported a significant reduction in rate Π_{12}^+ of budget B_{12}^+. Note that figure 15(*a*) shows a similar behaviour with shear thinning. On the other hand, regarding budgets reported for other canonical flows of GN fluids, Singh *et al.* (2017*b*) presented the budget B_k^+ for pipe flow and reported similar trends with shear thinning. For $\alpha < 1$, there is a decrease of turbulence production in the buffer layer region, whereas the magnitude of the turbulence transport and mean viscous dissipation rates increase in the near-wall region. Also for shear thinning, in pipe flow, the magnitude of the total dissipation rate is decreased due to contributions from the non-Newtonian terms. It is worth commenting that an apparent inner region dependence on the flow index for the budget B_k^+ is also reported by Singh *et al.* (2017*b*) for pipe flow.

In summary, some of the most relevant findings are as follows.

(i) Rheological variations affecting the Reynolds shear stress and the mean shear lead to shear-dependent changes in the production rate P_{11}^+ and therefore also in P_k^+.
(ii) With shear thinning, the decrease in P_{11}^+ is reflected by a decrease in the amount of energy redistributed through Π_{11}^+ to budgets B_{22}^+ and B_{33}^+.
(iii) Such decrease in energy redistribution with decreasing flow index results in an increase of large-scale turbulence anisotropic behaviour (see figure 8*a*).
(iv) The lessening of production with shear thinning also leads to a decrease in the total dissipation rate ϵ_{11}^+ and consequently in ϵ_k^+.
(v) Since the mean dissipation rates $M\epsilon_{11}^+$ and $M\epsilon_k^+$ actually increase with decreasing flow index, the noted decrease in the corresponding total dissipation is attributed to the non-Newtonian contributions, in particular to $\widetilde{T\epsilon}_{11}^+$ and $\widetilde{T\epsilon}_k^+$, respectively.
(vi) Finally, note that, for all budgets, the terms associated with non-Newtonian rheology appear to be mainly important within the inner layer region.

3.5. *Invariant analysis*

All turbulent flows of practical interest are anisotropic, and drag-reducing fluids are known to have an even higher degree of anisotropy compared to Newtonian fluids (Escudier *et al.* 2009). The analysis of invariants corresponding to relevant tensors are typically performed to determine their degree of anisotropy and to identify realizable states of turbulence. To study the anisotropic behaviour of turbulence in GN fluids, for both large- and small-scale motions, an invariant analysis is presented. Any symmetric tensor σ_{ik}, such as the strain-rate tensor or the Reynolds stress tensor, may be decomposed into an isotropic

and a traceless deviatoric part. The non-dimensional anisotropy tensor a_{ik} is then given by

$$a_{ik} = \frac{\sigma_{ik}}{\sigma_{jj}} - \frac{1}{3}\delta_{ik} \tag{3.2}$$

and since the anisotropy tensor is traceless ($a_{ii} = 0$), the relevant non-zero invariants are

$$-II_a = \tfrac{1}{2}a_{ik}a_{ki}, \quad III_a = \tfrac{1}{3}a_{ik}a_{kj}a_{ji}, \tag{3.3a,b}$$

which are denoted as the second and third invariants of a_{ik}, respectively.

Lumley & Newman (1977) introduced an anisotropy invariant map (AIM) consisting of a $-II$ versus III plot to investigate the anisotropy of the Reynolds stress tensor. Such a map, nowadays called the Lumley triangle, was originally based on the invariants of b_{ik}, the Reynolds stress anisotropy tensor, defined by

$$b_{ik} = \frac{\overline{u_i'u_k'}}{\overline{u_j'u_j'}} - \frac{1}{3}\delta_{ik}. \tag{3.4}$$

Analogous AIMs have been used to study small-scale anisotropy by considering quantities such as the dissipation rate and the vorticity correlation tensor, see for instance Mansour, Kim & Moin (1988), Antonia *et al.* (1991) and Barri & Andersson (2010). Here, the anisotropy tensors corresponding to the vorticity correlation and the total dissipation rate are given by

$$c_{ik} = \frac{\overline{\omega_i'\omega_k'}}{\overline{\omega_j'\omega_j'}} - \frac{1}{3}\delta_{ik} \tag{3.5}$$

and

$$d_{ik} = \frac{\epsilon_{ik}}{\epsilon_{jj}} - \frac{1}{3}\delta_{ik}, \tag{3.6}$$

respectively. Additionally, an anisotropy tensor e_{ik}, for the mean viscous dissipation only, may be given by

$$e_{ik} = \frac{M\epsilon_{ik}}{M\epsilon_{jj}} - \frac{1}{3}\delta_{ik}. \tag{3.7}$$

In all the mentioned AIMs, realizable turbulent states are constrained within certain limiting values; see figure 17. At the origin, $-II_a = III_a = 0$, all elements of a non-dimensional anisotropy tensor a_{ik} vanish and three-component isotropic turbulence (3C-IT) is found. If one diagonal component of a_{ik} is void of the corresponding property (energy or enstrophy, for example), e.g. $a_{11} = -1/3$, and the two other diagonal components are equal, e.g. $a_{22} = a_{33} = 1/6$, then two-component isotropic turbulence (2C-IT) is encountered. Finally, one-component (1C) turbulence corresponds to a situation where all of the corresponding property is within a diagonal component, e.g. $a_{11} = 2/3$.

In the $-II_a$ versus III_a plot, the origin is connected to the 1C and 2C-IT points through the relationship $III_a = \pm 2(-II_a/3)^{3/2}$ marking all cases of axisymmetric turbulence (i.e. two diagonal components of a_{ik} are equal and all off-diagonal components have vanished). The 2C-IT and 1C points, meanwhile, are connected by the line $-II_a = 3III_a + 1/9$ where two-component (2C) states reside. With the aim of adding physical context to the limiting states in the Lumley triangle, consider, for example, axisymmetric

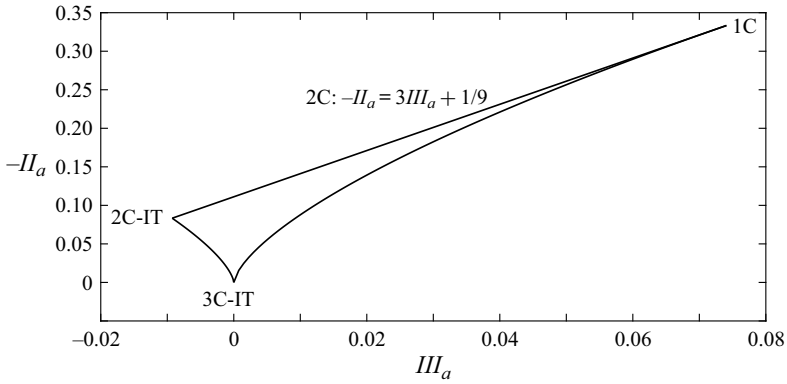

FIGURE 17. Limiting states in anisotropy invariant map.

deformation created by passing initially isotropic turbulence through a hypothetical slip-free axisymmetric nozzle or diffuser (see the same example as in Hanjalić & Launder (2011)). If the streamwise strain rate is $\partial\bar{u}/\partial x$ and the symmetry axis corresponds to the spanwise z axis, then continuity and axisymmetry considerations lead to $-0.5\partial\bar{u}/\partial x = 0.5\partial\bar{v}/\partial y = \partial\bar{w}/\partial z$. In a similar manner, the stress field will remain axisymmetric through the contraction/expansion, i.e. $b_{22} = b_{33} = -b_{11}/2$ and thus the resulting invariants are $II_b = 3b_{11}^2/4$ and $III_b = b_{11}^3/4$. Eliminating b_{11} then yields the previous relationship $III_b = \pm 2(-II_b/3)^{3/2}$; marking all cases of axisymmetric turbulence. The positive region (right-hand side in Lumley triangle) corresponds to axisymmetric expansion, which in the limit results in the 1C state, i.e. $\overline{v'v'} = \overline{w'w'} = 0$. On the other hand, the negative region corresponds to axisymmetric contraction and in the extreme limit results in the 2C isotropic turbulence state, i.e. $\overline{u'u'} = 0$.

The Lumley triangles for the different defined anisotropy tensors are presented in figure 18. In the same figure, the corresponding turbulence triangles (Choi & Lumley 2001) are shown as well. The map $\zeta^2 = -II/3$ versus $\xi^3 = III/2$ is used to emphasize the region in the proximity of the isotropic state. As noted by Emory & Iaccarino (2014), the Lumley triangle appears to provide more insight while studying states near the 1C and 2C limiting states whilst the turbulence triangle stretches the lower left quadrant of the Lumley triangle and focuses on the regions near the 2C-IT and 3C-IT limits.

For all GN fluids, the considered invariants vary from the 2C state limit in the vicinity of the wall to nearly isotropic at the channel's centre. Near the wall, the wall-normal diagonal component of the considered symmetric tensors are negligible, e.g. $\overline{v'v'} \approx \overline{\omega_2'\omega_2'} \approx 0$, and, as y^+ increases, the data transition from the upper boundary to the right-hand boundary of the Lumley triangle. With shear thinning, in comparison to the Newtonian case, a larger maximum value for $-II$ is observed on the anisotropy invariant maps corresponding to b_{ik}, c_{ik} and d_{ik}. In the AIMs, the movement of the data towards the 1C limit with shear thinning is attributed to the deficit in energy redistribution from budget B_{11}^+ to budgets B_{22}^+ and B_{33}^+, mentioned in § 3.4. In the case of the Reynolds stress tensor, for instance, near-wall behaviour (see figure 19) displays the expected increase in the streamwise component $\overline{u'u'}/u_\tau^2$ and the decrease of the wall-normal and spanwise components with shear thinning. Such increase of $\overline{u'u'}/u_\tau^2$, with decreasing flow index, is reflected in the Lumley triangle

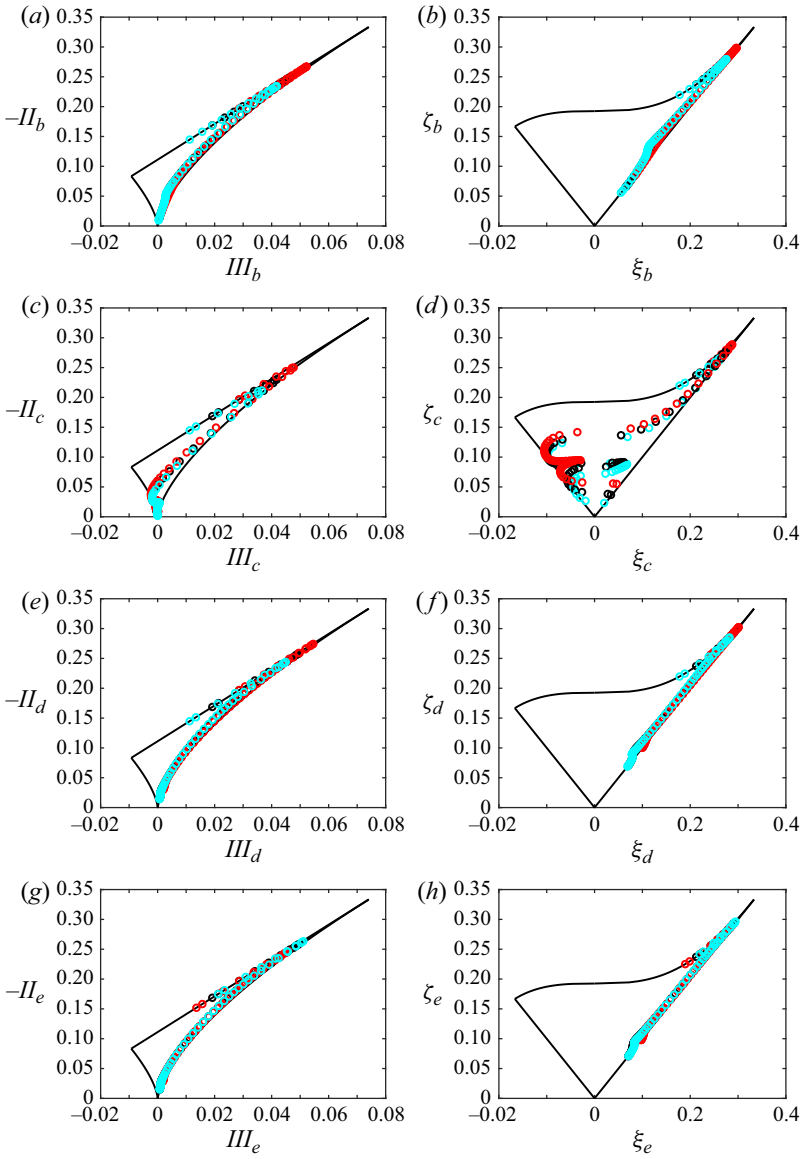

FIGURE 18. AIMs: (*a*) Lumley triangle for b_{ik}, (*b*) turbulence triangle for b_{ik}, (*c*) Lumley triangle for c_{ik}, (*d*) turbulence triangle for c_{ik}, (*e*) Lumley triangle for d_{ik}, (*f*) turbulence triangle for d_{ik}, (*g*) Lumley triangle for e_{ik} and (*h*) turbulence triangle for e_{ik}. Profiles corresponding to P180, N180 and D180 are identified by red, black and cyan colours, respectively.

with near-wall 2C states closer to the 1C point. In a similar manner, the increase in $\overline{\omega_3'\omega_3'}$ and in the magnitude of $M\epsilon_{11}$ with shear thinning yield the observed movement of the data towards the 1C limit in the respective AIMs.

Opposite to the mean dissipation, the data of the total dissipation in the vicinity of the wall do not approach states closer to the 1C limit with decreasing flow index. Owing to the non-Newtonian terms contributing to the total dissipation rate, there is a decrease in

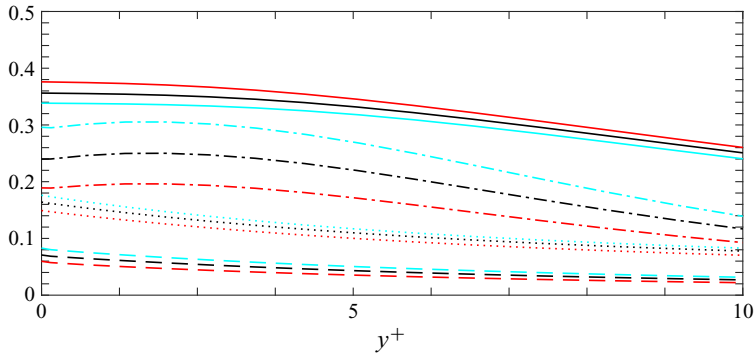

FIGURE 19. Near-wall behaviour for correlation of velocity fluctuations. Line styles '——', '- - -', '· · ·' and '- · -' represent $(\overline{u'u'}^{1/2}/u_\tau)/y^+$, $10(\overline{v'v'}^{1/2}/u_\tau)/y^{+2}$, $(\overline{w'w'}^{1/2}/u_\tau)/y^+$ and $350(-\overline{u'v'}/u_\tau^2)/y^{+3}$, respectively. Profiles corresponding to P180, N180 and D180 are identified by red, black and cyan colours, respectively.

the magnitude of ϵ_{11}^+ with shear thinning (as seen in § 3.4) causing the observed behaviour in the corresponding Lumley triangle.

For all GN fluids, after the location of the maximum in the different AIMs, the transition to anisotropic states occurs closer to the axisymmetric limit where $III > 0$ takes place because one diagonal component is larger than the other two. Consider, for example, the streamwise component of the Reynolds stress in comparison with the other lateral components (see turbulence intensity profiles in § 3.1). Note that an actual axisymmetric state only occurs once the off-diagonal components of the corresponding anisotropy tensor are zero (e.g. $b_{12} = \overline{u'v'} = 0$ at the channel's centre).

As seen from the turbulence triangles, the data corresponding to b_{ik}, c_{ik}, d_{ik} and e_{ik} move closer to the axisymmetric limiting states with shear thinning. This observation is consistent with the decrease in the off-diagonal components corresponding to the different anisotropy tensors with shear thinning. See, for instance, the variation of the Reynolds shear stress with shear thinning in § 3.2. It is also observed that there is no appreciable difference in the turbulence triangles describing the mean viscous dissipation rate anisotropy and the total dissipation rate anisotropy in proximity to the axisymmetric limit. This behaviour is consistent with the observed decrease in the non-Newtonian terms contributing to ϵ_{11}^+ in the outer layer region.

To complement the anisotropy analysis, the Lumley flatness (Lumley 1979) $\mathcal{F} = 1 + 27III + 9II$ and the axisymmetric parameter (Lee & Reynolds 1985) $\mathcal{A} = III/[2(-II/3)^{3/2}]$ are shown in figure 20. The Lumley flatness allows one to easily distinguish between 2C line states ($\mathcal{F} = 0$) and 3C-IT ($\mathcal{F} = 1$). Meanwhile, the axisymmetric parameter is a compact way to quantify axisymmetric modes: $\mathcal{A} = -1$ corresponds to axisymmetric states where $III < 0$ and the correlation tensor (e.g. $\overline{u_i'u_k'}$ or $\overline{\omega_i'\omega_k'}$) has a smaller diagonal component than the other two equal ones; whilst $\mathcal{A} = 1$ corresponds to axisymmetric states where $III > 0$ and the correlation tensor has one larger diagonal component than the other two equal ones. Here terminology such as 'rod-like' or 'cigar-shaped' turbulence and 'disk-like' or 'pancake-shaped' turbulence is used while considering $\mathcal{A} = 1$ and $\mathcal{A} = -1$ states of the vorticity correlation anisotropy tensor, respectively. Alternative terminology is omitted here to avoid misunderstanding;

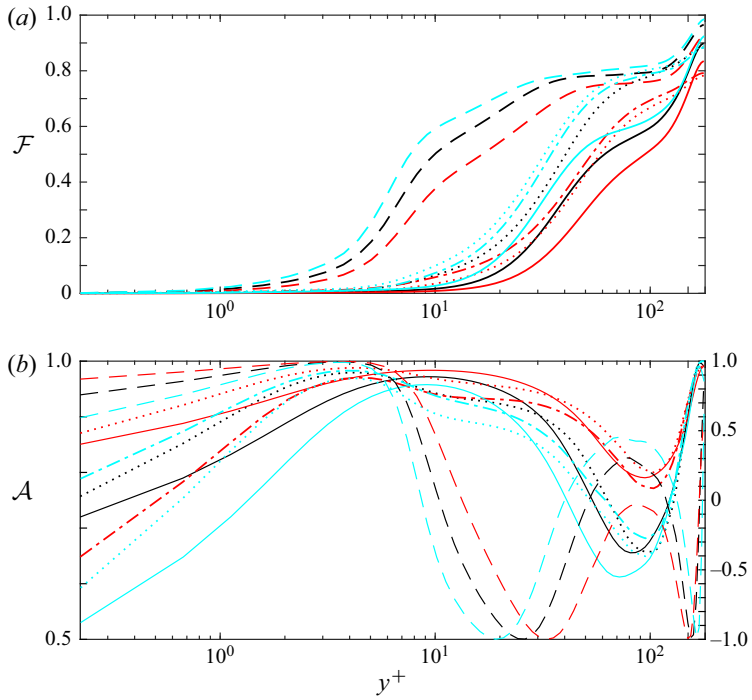

FIGURE 20. Lumley's flatness and axisymmetric parameter: (*a*) line styles '——', '- - -', '· · ·' and '- · -' are used for $\mathcal{F}_b$, $\mathcal{F}_c$, $\mathcal{F}_d$ and $\mathcal{F}_e$; and (*b*) line styles '——', '- - -', '· · ·' and '- · -' are used for $\mathcal{A}_b$, $\mathcal{A}_c$ (right axis), $\mathcal{A}_d$ and $\mathcal{A}_e$. Profiles corresponding to P180, N180 and D180 are identified by red, black and cyan colours, respectively.

see, for instance, Simonsen & Krogstad (2005) where it is clarified that notation used for the axisymmetric states refers to the shape of the symmetrical second-order tensor with zero trace σ_{ik} under study, e.g. the Reynolds stress tensor or the vorticity correlation tensor.

With the exception of the very near-wall behaviour in the total dissipation rate, the overall increase in anisotropy with decreasing flow index at the channel's centre and elsewhere is reflected by larger $-II$ values in the AIMs and consequently lower Lumley flatness. For all GN fluids, the profiles corresponding to the axisymmetric parameters show that, close to the end of the viscous sublayer, i.e. before the buffer layer region, the state $\mathcal{A} = 1$ is approached. This observation is consistent with the noticed transition from the upper boundary to the right-hand boundary in the AIMs. After the maximum value of $-II$ is achieved on the respective maps, $\mathcal{A}_b$, $\mathcal{A}_d$ and $\mathcal{A}_e$ remain relatively close to the $\mathcal{A} = 1$ state (especially as the flow index decreases) although there is a localized decrease in the axisymmetric parameters, most noticeable for $\mathcal{A}_b$, in the outer layer. This behaviour is observed on the respective turbulence triangles as a sudden but short deviation from the near-right boundary region towards the centre of the map, more clearly seen for increasing flow index.

With respect to the $\mathcal{A}_c$ scalar, an apparent change from a cigar-shaped axisymmetric state, at the end of the viscous sublayer, to a disk-like state ($III_c < 0,\ \mathcal{A}_c = -1$), within the buffer region, is noticed. The wall-normal position at which the pancake-shaped axisymmetric mode is observed appears to move slightly away from the wall with

shear thinning. After such point, it is difficult to point out a trend in $\mathcal{A}_c$ since oscillations at different y^+ positions are noted. Nonetheless, states closer to disk-like turbulence appear to be more frequent, especially with decreasing flow index. Interestingly enough, close to the channel's centre, rod-like states are suddenly approached. This observation is consistent with the presented ζ versus ξ map and the slight dominance of the spanwise vorticity autocorrelation $\overline{\omega_3'\omega_3'}$ over $\overline{\omega_1'\omega_1'}$ and $\overline{\omega_2'\omega_2'}$ near the channel's centre as seen in § 3.1.

4. Discussion and final remarks

Direct numerical simulations for statistically converged turbulent channel flow of GN fluids at a low Reynolds number have been performed. A GN fluid presents time-independent rheology and is free of plastic effects. In the simulation, GN fluid rheology has been incorporated through a relatively simple constitutive equation, the Carreau fluid model. To investigate the difference between Newtonian and shear-dependent fluid behaviour, the flow index α is varied. Here, when a trend is associated to shear thinning $\alpha < 1$, the opposite trend is associated to shear thickening $\alpha > 1$. Note that the selected rheological model is likely to be of no consequence since, for the same rheology characterization at large strain rates, quite similar statistics are expected even if a different rheological model is implemented (see e.g. Singh, Rudman & Blackburn 2016).

Through different statistics and analyses, it is found that shear-dependent fluid rheology seems to affect the channel flow mainly within the inner layer region. As we move further away from the viscous sublayer, the monotonic increase in the apparent fluid viscosity for $\alpha < 1$ leads to drag reduction. For a constant driving pressure gradient, a decrease in the friction factor with decreasing flow index is reflected by an increase in the mean streamwise velocity for $y^+ \gtrsim 10$ and in consequence higher mean bulk velocity $\int_0^{h^+} \bar{u}^+ \,\mathrm{d}y^+/h^+$ and flow rate. The diagnosis function also reveals that the limited log region starts further away from the wall and with a slightly larger slope with shear-thinning fluid rheology. This thickening of the buffer layer is consistent with the observed increase in streamwise turbulence intensity and the shift in its peak value for $\alpha < 1$.

The previous well-known drag-reducing-related characteristics are attributed to changes in the near-wall structures within the buffer layer region for shear-thinning fluid rheology. Quasi-streamwise vortices (rolls) are suppressed; as figure 8(*b*) shows, shear-thinning effects reduce the intensity of the streamwise vorticity fluctuations and also move the location of the local minimum and maximum values towards the channel's centre. These two extrema locations correspond to the average locations of the edge and centre, respectively, of the near-wall rolls (Moser & Moin 1984). Hence, the quasi-streamwise vortical structures not only decrease in intensity but also grow in size and depart from the wall.

The suppression of the near-wall streamwise rolls is accompanied by variations in the high- and low-speed fluid alternating regions (streaks) in the spanwise direction. It is recognized that there is an interaction between the rolls and the mean spanwise vorticity which induces low-speed streamwise streaks (see e.g. § 4.2.6 in Davidson 2015). These streaks eventually begin to oscillate and lift away from the wall during the so-called burst process. Each burst contains one or more ejections of low-speed fluid resulting from the same streak instability (Luchik & Tiederman 1987). Since burst or ejection events occur in a quasi-periodic manner, particular attention is paid to statistical quantities such as the average time between bursts and average spanwise spacing of the near-wall streaks.

As seen in figure 2(*c*), for $\alpha < 1$, the location of the minimum in the two-point correlation of the streamwise fluctuating velocity occurs at a larger spanwise separation, and a similar trend (not shown here) was found at other wall-normal positions within the buffer layer region. Note that the location of this minimum is the mean distance between a high-speed and a low-speed streak; thus the average streak spacing is twice such distance (Moser & Moin 1984). Since, for shear-thinning fluid rheology, a larger average streak spacing is found, a larger average time between bursts is expected and, in consequence, there is an inhibition of the related turbulence generating event. As revealed by the quadrant analysis, the decrease in Reynolds shear stress – leading to a reduction in the production of turbulent kinetic energy – arises due to a decrease from all positive production events but, within the buffer layer, especially due to a diminishing in contributions from ejection events.

Another common characteristic of drag-reducing flow, such as the decrease in the spanwise and wall-normal turbulence intensities, is explained from the Reynolds stress budgets. In connection to the decrease in turbulence production with shear thinning, there is a decrease in the velocity–pressure gradient terms, which are commonly split into a pressure–transport term and an energy redistributive pressure–strain rate term. Thus, since the velocity–pressure gradient terms play a dominant role in the redistribution of energy from streamwise to wall-normal and spanwise directions, their decrease leads to the observed trends for the turbulent intensities and consequently to an increase in anisotropy at the largest scales with $\alpha < 1$. The budgets also show that, although the magnitude of the mean viscous dissipation $M\epsilon_k^+$ increases with shear thinning, the overall dissipation rate ϵ_k^+ decreases in magnitude since there is less energy available for irreversible dissipation at the wall; hence the importance of the non-Newtonian terms, in particular the turbulent viscous dissipation rate related to the mean flow, whilst studying the total dissipation in GN fluids.

Turbulence anisotropy variations at both large and small scales due to the non-Newtonian rheology are studied through anisotropy invariant maps. The presented analysis reveals an overall increase in anisotropy for the Reynolds stress, vorticity correlation and mean viscous dissipation with shear thinning. In contrast to the mean viscous dissipation, in the near-wall region, the anisotropy of the total dissipation rate decreases with shear thinning due to non-Newtonian effects. On the other hand, regarding the data closer to the axisymmetric limits, as one moves from the wall towards the channel's centre, states closer to the axisymmetric limit where $III > 0$ are seen for the Reynolds stress budgets and the dissipation rates. In the case of vorticity correlation, states between rod-like and disk-like turbulence are seen in the direction of the channel's centre. Here, states closer to disk-like or pancake-shaped turbulence appear to be preferred, especially with decreasing flow index. Finally, at the channel's centre, rod-like turbulence is approached. This observation is consistent with the slight dominance of the spanwise vorticity correlation over the other two components for all GN fluid cases. Anisotropy at the smallest scales is a recognized behaviour at low Reynolds numbers (Andersson, Zhao & Variano 2015) and appears to be even more noticeable with shear thinning.

Acknowledgements

This work was supported by the Research Council of Norway (RCN, Grant No. 274398). The authors are grateful for computer resources provided by Sigma2 (Grant No. NN9646K) and by local cluster, IDUN, at NTNU.

Declaration of interests

The authors report no conflict of interest.

Appendix A. Transport equation corresponding to $\overline{u_i'u_k'}$ for channel flow of a GN fluid

This appendix contains the derivation of the transport equation for the correlation of the velocity fluctuations, $\overline{u_i'u_k'}$, corresponding to a GN fluid, and it is deduced in a similar manner as it is deduced for a Newtonian fluid. Start out from the averaged momentum conservation equation for a GN fluid, which reads

$$\frac{\mathrm{D}\overline{u_i}}{\mathrm{D}t} = -\frac{1}{\rho}\frac{\partial \bar{p}}{\partial x_i} + \frac{1}{\rho}\frac{\partial}{\partial x_j}\left(2\bar{\mu}\overline{S_{ij}} + 2\overline{\mu' S_{ij}'}\right) + \frac{\partial}{\partial x_j}\left(-\overline{u_i'u_j'}\right). \tag{A 1}$$

Subtracting (A 1) from the transport equation for the instantaneous velocity component u_i, i.e.

$$\begin{aligned}&\frac{\partial}{\partial t}\left(\overline{u_i} + u_i'\right) + \left(\overline{u_j} + u_j'\right)\frac{\partial}{\partial x_j}\left(\overline{u_i} + u_i'\right)\\ &\quad = -\frac{1}{\rho}\frac{\partial}{\partial x_i}\left(\bar{p} + p'\right) + \frac{1}{\rho}\frac{\partial}{\partial x_j}\left[2\left(\bar{\mu} + \mu'\right)\left(\overline{S_{ij}} + S_{ij}'\right)\right]\end{aligned} \tag{A 2}$$

yields a transport equation for the fluctuating velocity component u_i'. Thus

$$\begin{aligned}&\frac{\partial u_i'}{\partial t} + \overline{u_j}\frac{\partial u_i'}{\partial x_j} + u_j'\frac{\partial \overline{u_i}}{\partial x_j} + u_j'\frac{\partial u_i'}{\partial x_j}\\ &\quad = -\frac{1}{\rho}\frac{\partial p'}{\partial x_i} + \frac{1}{\rho}\frac{\partial}{\partial x_j}\left(2\bar{\mu}S_{ij}' + 2\mu'\overline{S_{ij}} + 2\mu' S_{ij}' - 2\overline{\mu' S_{ij}'}\right) + \frac{\partial}{\partial x_j}\left(\overline{u_i'u_j'}\right).\end{aligned} \tag{A 3}$$

In a similar manner, an equation for the other fluctuating velocity component u_k' is obtained

$$\begin{aligned}&\frac{\partial u_k'}{\partial t} + \overline{u_j}\frac{\partial u_k'}{\partial x_j} + u_j'\frac{\partial \overline{u_k}}{\partial x_j} + u_j'\frac{\partial u_k'}{\partial x_j}\\ &\quad = -\frac{1}{\rho}\frac{\partial p'}{\partial x_k} + \frac{1}{\rho}\frac{\partial}{\partial x_j}\left(2\bar{\mu}S_{kj}' + 2\mu'\overline{S_{kj}} + 2\mu' S_{kj}' - 2\overline{\mu' S_{kj}'}\right) + \frac{\partial}{\partial x_j}\left(\overline{u_k'u_j'}\right).\end{aligned} \tag{A 4}$$

Multiplying (A 3) by u_k', (A 4) by u_i' and adding the products yields a transport equation for $\overline{u_i'u_k'}$ once the resulting equation has been averaged. In consequence, the transport equation for $\overline{u_i'u_k'}$ reads

$$\begin{aligned}\frac{\mathrm{D}}{\mathrm{D}t}\left(\overline{u_i'u_k'}\right) = &-\overline{u_i'u_j'}\frac{\partial \overline{u_k}}{\partial x_j} - \overline{u_k'u_j'}\frac{\partial \overline{u_i}}{\partial x_j} - \frac{\partial}{\partial x_j}\left(\overline{u_i'u_j'u_k'}\right) + \frac{\bar{\mu}}{\rho}\frac{\partial^2}{\partial x_j \partial x_j}\left(\overline{u_i'u_k'}\right)\\ &- \frac{1}{\rho}\overline{\left(u_i'\frac{\partial p'}{\partial x_k} + u_k'\frac{\partial p'}{\partial x_i}\right)} - \frac{1}{\rho}\left(2\bar{\mu}\right)\overline{\frac{\partial u_i'}{\partial x_j}\frac{\partial u_k'}{\partial x_j}}\end{aligned}$$

$$+\frac{1}{\rho}\left(\frac{\partial\bar{\mu}}{\partial x_j}\right)\left[\frac{\partial}{\partial x_j}\left(\overline{u_i'u_k'}\right)+\overline{u_i'\frac{\partial u_j'}{\partial x_k}}+\overline{u_k'\frac{\partial u_j'}{\partial x_i}}\right]$$
$$+\frac{1}{\rho}\overline{\left(\frac{\partial\mu'}{\partial x_j}\right)\left[\frac{\partial}{\partial x_j}\left(u_i'u_k'\right)+u_i'\frac{\partial u_j'}{\partial x_k}+u_k'\frac{\partial u_j'}{\partial x_i}\right]}$$
$$+\frac{1}{\rho}\overline{\left(\frac{\partial\mu'}{\partial x_j}\right)\left[u_i'\left(\frac{\partial\overline{u_k}}{\partial x_j}+\frac{\partial\overline{u_j}}{\partial x_k}\right)+u_k'\left(\frac{\partial\overline{u_i}}{\partial x_j}+\frac{\partial\overline{u_j}}{\partial x_i}\right)\right]}$$
$$+\frac{1}{\rho}\overline{\mu'\frac{\partial^2}{\partial x_j\partial x_j}\left(u_i'u_k'\right)}-\frac{1}{\rho}(2)\,\overline{\mu'\frac{\partial u_i'}{\partial x_j}\frac{\partial u_k'}{\partial x_j}}+\frac{1}{\rho}\overline{\left(\mu'u_i'\frac{\partial^2\overline{u_k}}{\partial x_j\partial x_j}+\mu'u_k'\frac{\partial^2\overline{u_i}}{\partial x_j\partial x_j}\right)}. \tag{A 5}$$

In (A 5), the last two terms may be rewritten as

$$\frac{1}{\rho}\overline{\left(\mu'u_i'\frac{\partial^2\overline{u_k}}{\partial x_j\partial x_j}+\mu'u_k'\frac{\partial^2\overline{u_i}}{\partial x_j\partial x_j}\right)}=\frac{1}{\rho}\overline{(\mu')\left[\frac{\partial^2}{\partial x_j\partial x_j}\left(u_i'\overline{u_k}\right)+\frac{\partial^2}{\partial x_j\partial x_j}\left(\overline{u_i}u_k'\right)\right]}$$
$$+\frac{1}{\rho}(-2)\,\overline{\mu'\left[\frac{\partial u_i'}{\partial x_j}\frac{\partial\overline{u_k}}{\partial x_j}+\frac{\partial\overline{u_i}}{\partial x_j}\frac{\partial u_k'}{\partial x_j}\right]}$$
$$-\frac{1}{\rho}\overline{(\mu')\left[\overline{u_k}\frac{\partial^2u_i'}{\partial x_j\partial x_j}+\overline{u_i}\frac{\partial^2u_k'}{\partial x_j\partial x_j}\right]} \tag{A 6}$$

and, finally, (A 5) may be reformulated as

$$\frac{\mathrm{D}}{\mathrm{D}t}\left(\overline{u_i'u_k'}\right)=-\overline{u_i'u_j'}\frac{\partial\overline{u_k}}{\partial x_j}-\overline{u_k'u_j'}\frac{\partial\overline{u_i}}{\partial x_j}-\frac{\partial}{\partial x_j}\left(\overline{u_i'u_j'u_k'}\right)+\frac{\bar{\mu}}{\rho}\frac{\partial^2}{\partial x_j\partial x_j}\left(\overline{u_i'u_k'}\right)$$
$$-\frac{1}{\rho}\overline{\left(u_i'\frac{\partial p'}{\partial x_k}+u_k'\frac{\partial p'}{\partial x_i}\right)}-\frac{1}{\rho}(2\bar{\mu})\,\overline{\frac{\partial u_i'}{\partial x_j}\frac{\partial u_k'}{\partial x_j}}$$
$$+\frac{1}{\rho}\left(\frac{\partial\bar{\mu}}{\partial x_j}\right)\left[\frac{\partial}{\partial x_j}\left(\overline{u_i'u_k'}\right)+\overline{u_i'\frac{\partial u_j'}{\partial x_k}}+\overline{u_k'\frac{\partial u_j'}{\partial x_i}}\right]$$
$$+\frac{1}{\rho}\overline{\left(\frac{\partial\mu'}{\partial x_j}\right)\left[\frac{\partial}{\partial x_j}\left(u_i'u_k'\right)+u_i'\frac{\partial u_j'}{\partial x_k}+u_k'\frac{\partial u_j'}{\partial x_i}\right]}$$
$$+\frac{1}{\rho}\overline{\left(\frac{\partial\mu'}{\partial x_j}\right)\left[u_i'\left(\frac{\partial\overline{u_k}}{\partial x_j}+\frac{\partial\overline{u_j}}{\partial x_k}\right)+u_k'\left(\frac{\partial\overline{u_i}}{\partial x_j}+\frac{\partial\overline{u_j}}{\partial x_i}\right)\right]}$$
$$+\frac{1}{\rho}\overline{\mu'\frac{\partial^2}{\partial x_j\partial x_j}\left(u_i'u_k'\right)}-\frac{1}{\rho}(2)\,\overline{\mu'\frac{\partial u_i'}{\partial x_j}\frac{\partial u_k'}{\partial x_j}}$$
$$+\frac{1}{\rho}\overline{(\mu')\left[\frac{\partial^2}{\partial x_j\partial x_j}\left(u_i'\overline{u_k}\right)+\frac{\partial^2}{\partial x_j\partial x_j}\left(\overline{u_i}u_k'\right)\right]}$$
$$+\frac{1}{\rho}(-2)\,\overline{\mu'\left[\frac{\partial u_i'}{\partial x_j}\frac{\partial\overline{u_k}}{\partial x_j}+\frac{\partial\overline{u_i}}{\partial x_j}\frac{\partial u_k'}{\partial x_j}\right]}-\frac{1}{\rho}\overline{(\mu')\left[\overline{u_k}\frac{\partial^2u_i'}{\partial x_j\partial x_j}+\overline{u_i}\frac{\partial^2u_k'}{\partial x_j\partial x_j}\right]}. \tag{A 7}$$

Note that (2.10) is the non-dimensionalized form of (A 7).

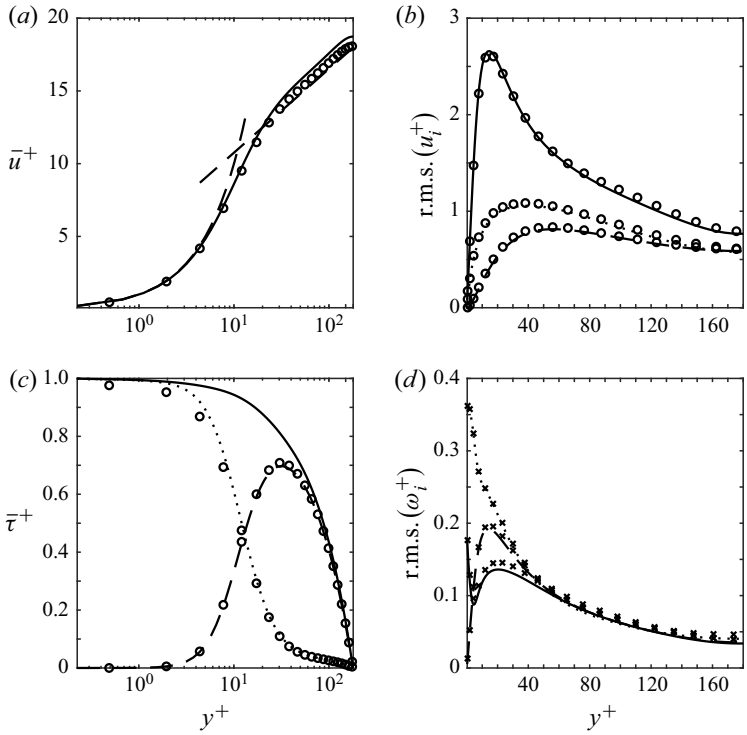

FIGURE 21. Verification for case N180: (*a*) mean (averaged in time and in homogeneous directions) streamwise velocity profile $\bar{u}^+$, (*b*) turbulence intensities r.m.s.(u_i^+), (*c*) shear stress profiles $\bar{\tau}^+$ (lines '——' total stress, '· · ·' viscous stress and '- - -' turbulent stress) and (*d*) r.m.s. values of vorticity fluctuations r.m.s.(ω_i^+). In (*b*,*d*), the x, y and z components are denoted by '——', '- - -' and '· · ·', respectively. Results from Kim *et al.* (1987) and Moser *et al.* (1999) are identified by '○' and '×' markers, respectively.

Appendix B. Verification

The results corresponding to case N180 shown in figure 21 agree with those reported by Kim *et al.* (1987) and Moser *et al.* (1999). Contributions to the turbulent kinetic energy budget in figures 13(*a*) and 16(*a–c*) and the η^+ profile presented in figure 5 also appear to agree qualitatively with the profiles reported by Mansour *et al.* (1988) and Antonia *et al.* (1991), respectively.

Observed trends for non-Newtonian results presented in § 3 agree with those reported in previous studies, e.g. Rudman & Blackburn (2006), Gavrilov & Rudyak (2016*a*) and Singh *et al.* (2017*b*), for turbulent pipe flows.

Appendix C. Contributions to budgets B_{22}^+ and B_{33}^+

Contributions from the different terms in (2.23) to total transport and dissipation rates for budgets B_{22}^+ and B_{33}^+ are shown in figures 22 and 23. For transport rate T_{22}^+, the velocity–pressure gradient, the turbulent transport and the mean viscous diffusion rates contribute the most. The rate Π_{22}^+, which is the source of energy for budget B_{22}^+, decreases with decreasing flow index as expected. Similar to the production rate P_{11}^+ in budget B_{11}^+, the

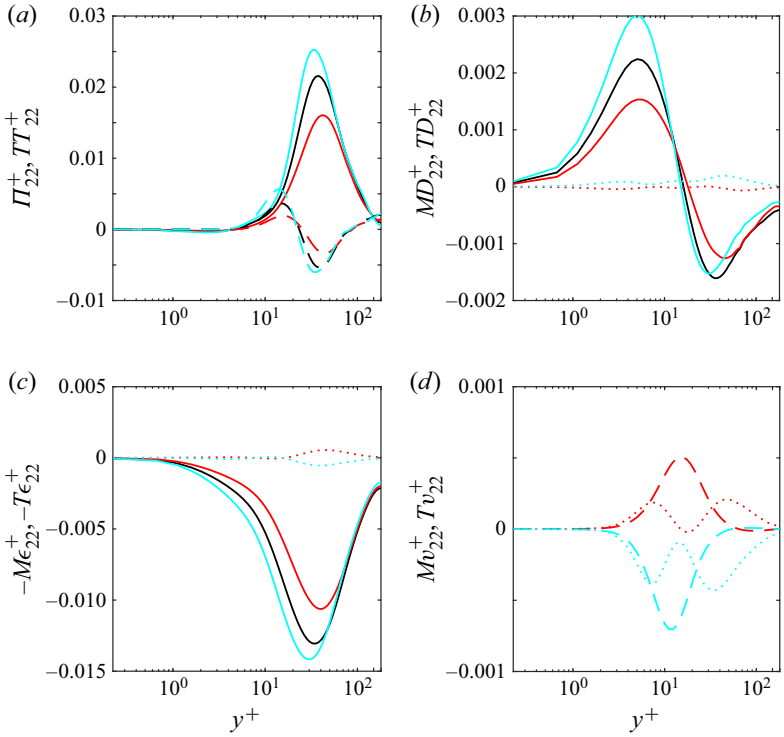

FIGURE 22. Contributions to T_{22}^+ and $-\epsilon_{22}^+$ in budget B_{22}^+: (*a*) line styles '——' and '- - -' are used for Π_{22}^+ and TT_{22}^+; (*b*) line styles '——' and '· · ·' are used for MD_{22}^+ and TD_{22}^+; (*c*) line styles '——' and '· · ·' are used for $-M\epsilon_{22}^+$ and $-T\epsilon_{22}^+$; and (*d*) line styles '- - -' and '· · ·' are used for Mv_{22}^+ and Tv_{22}^+. Profiles corresponding to P180, N180 and D180 are identified by red, black and cyan colours, respectively.

energy in Π_{22}^+ is transported towards and away from the wall, mainly through the turbulent transport rate. Since there is less energy to be distributed with shear thinning, within the inner region, the magnitudes of TT_{22}^+ and MD_{22}^+ decrease with shear thinning as well. With respect to the non-Newtonian terms, the transport rate TD_{22}^+ decreases with decreasing flow index whilst Mv_{22}^+ and Tv_{22}^+ increase. However, these terms are rather small and do not contribute significantly to the total transport rate.

The total dissipation rate ϵ_{22}^+ balancing T_{22}^+ is mainly due to the mean viscous dissipation rate $M\epsilon_{22}^+$, which presents the same trends of Π_{22}^+ with rheology, i.e. it decreases in magnitude with decreasing flow index. The other non-zero contribution to rate ϵ_{22}^+, although fairly low in magnitude, is $T\epsilon_{22}^+$. This non-Newtonian dissipation rate increases in magnitude with shear thinning.

For transport rate T_{33}^+, mainly the pressure–velocity gradient term and the mean viscous diffusion (especially very close to the wall) are important. As for budget B_{22}^+, less energy is redistributed from budget B_{11}^+ with decreasing flow index. The magnitudes of Π_{33}^+ and consequently of TT_{33}^+ and MD_{33}^+ decrease with shear thinning. Other non-zero transport terms, associated with the non-Newtonian rheology, do not contribute much to rate T_{33}^+.

As for $T\epsilon_{22}^+$, the mean viscous dissipation rate contributes the most to the total rate $T\epsilon_{33}^+$ and decreases in magnitude with shear thinning since there is less energy that may be

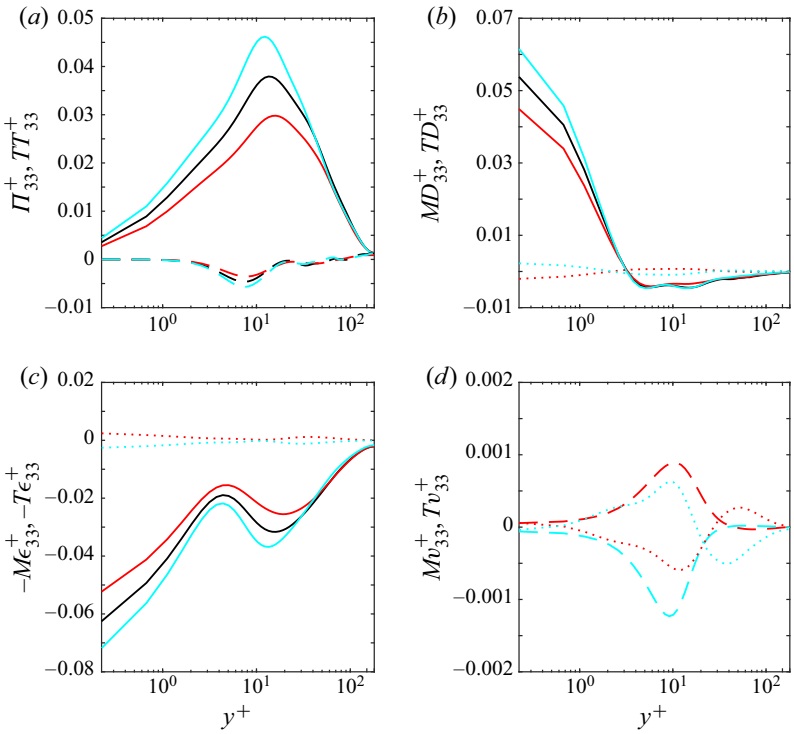

FIGURE 23. Contributions to T_{33}^+ and $-\epsilon_{33}^+$ in budget B_{33}^+: (*a*) line styles '——' and '- - -' are used for Π_{33}^+ and TT_{33}^+; (*b*) line styles '——' and '· · ·' are used for MD_{33}^+ and TD_{33}^+; (*c*) line styles '——' and '· · ·' are used for $-M\epsilon_{33}^+$ and $-T\epsilon_{33}^+$; and (*d*) line styles '- - -' and '· · ·' are used for Mv_{33}^+ and Tv_{33}^+. Profiles corresponding to P180, N180 and D180 are identified by red, black and cyan colours, respectively.

dissipated. The other non-zero dissipation rate $T\epsilon_{33}^+$ is small in comparison to $M\epsilon_{33}^+$ and shows the opposite behaviour with decreasing flow index.

REFERENCES

ACHIA, B. U. & THOMPSON, D. W. 1977 Structure of the turbulent boundary in drag-reducing pipe flow. *J. Fluid Mech.* **81**, 439–464.

ANDERSSON, H. I., ZHAO, L. & VARIANO, E. A. 2015 On the anisotropic vorticity in turbulent channel flows. *Trans. ASME: J. Fluids Engng* **137**, 084503.

ANTONIA, R. A., KIM, J. & BROWNE, L. W. B. 1991 Some characteristics of small-scale turbulence in a turbulent duct flow. *J. Fluid Mech.* **233**, 369–388.

BARRI, M. & ANDERSSON, H. I. 2010 Computer experiments on rapidly rotating plane Couette flow. *Commun. Comput. Phys.* **7**, 683–717.

BRADSHAW, P. 1995 Addendum to "A note on turbulent energy dissipation in the viscous wall region". *Phys. Fluids* A **7**, 2297.

BRADSHAW, P. & PEROT, J. B. 1993 A note on turbulent energy dissipation in the viscous wall region. *Phys. Fluids* A **5**, 3305–3306.

CHEN, Z. & SHU, C. 2020 Simplified lattice Boltzmann method for non-Newtonian power-law fluid flows. *Intl J. Numer. Meth. Fluids* **92**, 38–54.

CHOI, K.-S. & LUMLEY, J. L. 2001 The return to isotropy of homogeneous turbulence. *J. Fluid Mech.* **436**, 59–84.

CORINO, E. R. & BRODKEY, R. S. 1969 A visual investigation of the wall region in turbulent flow. *J. Fluid Mech.* **37**, 1–30.

CRUZ, D. O. A. & PINHO, F. T. 2003 Turbulent pipe flow predictions with a low Reynolds number $k-\varepsilon$ model for drag reducing fluids. *J. Non-Newtonian Fluid Mech.* **114**, 109–148.

DAVIDSON, L. 2007 Using isotropic synthetic fluctuations as inlet boundary conditions for unsteady simulations. *Adv. Appl. Fluid Mech.* **1** (1), 1–35.

DAVIDSON, L. 2018 CALC-LES: a Fortran code for LES and hybrid LES-RANS. *Tech. Rep.* Chalmers University of Technology.

DAVIDSON, L. & PENG, S.-H. 2003 Hybrid LES-RANS: a one-equation SGS model combined with a $k-\omega$ for predicting recirculating flows. *Intl J. Numer. Meth. Fluids* **43** (9), 1003–1018.

DAVIDSON, P. A. 2015 *Turbulence: An Introduction for Scientists and Engineers*. Oxford University Press.

DE ANGELIS, E., CASCIOLA, C. M. & PIVA, R. 2002 DNS of wall turbulence: dilute polymers and self-sustaining mechanisms. *Comput. Fluids* **31**, 495–507.

DEN TOONDER, J. M. J., HULSEN, M. A., KUIKEN, G. D. C. & NIEUWSTADT, F. T. M. 1997 Drag reduction by polymer additives in a turbulent pipe flow: numerical and laboratory experiments. *J. Fluid Mech.* **337**, 193–231.

DIMITROPOULOS, C. D., SURESHKUMAR, R., BERIS, A. N. & HANDLER, R. A. 2001 Budgets of Reynolds stress, kinetic energy and streamwise enstrophy in viscoelastic turbulent channel flow. *Phys. Fluids* **13**, 1016–1027.

DODGE, D. W. & METZNER, A. B. 1959 Turbulent flow of non-Newtonian systems. *AIChE J.* **5**, 189–204.

EMORY, M. & IACCARINO, G. 2014 Visualizing turbulence anisotropy in the spatial domain with componentality contours. In *Annual Research Briefs 2014*, pp. 123–138. Center for Turbulence Research, Stanford University.

EMVIN, P. 1997 The full multigrid method applied to turbulent flow in ventilated enclosures using structured and unstructured grids. PhD thesis, Chalmers University of Technology, Gothenburg.

ESCUDIER, M. P., NICKSON, A. K. & POOLE, R. J. 2009 Turbulent flow of viscoelastic shear-thinning liquids through a rectangular duct: quantification of turbulence anisotropy. *J. Non-Newtonian Fluid Mech.* **160**, 2–10.

GABBANELLI, S., DRAZER, G. & KOPLIK, J. 2005 Lattice Boltzmann method for non-Newtonian (power-law) fluids. *Phys. Rev.* E **72**, 046312.

GAVRILOV, A. A. & RUDYAK, V. Y. 2016*a* Direct numerical simulation of the turbulent flows of power-law fluids in a circular pipe. *Thermophys. Aeromech.* **23**, 473–486.

GAVRILOV, A. A. & RUDYAK, V. Y. 2016*b* Reynolds-averaged modeling of turbulent flows of power-law fluids. *J. Non-Newtonian Fluid Mech.* **227**, 45–55.

GNAMBODE, P. S., ORLANDI, P., OULD-ROUISS, M. & NICOLAS, X. 2015 Large–Eddy simulation of turbulent pipe flow of power-law fluids. *Intl J. Heat Fluid Flow* **54**, 196–210.

HANJALIĆ, K. & LAUNDER, B. 2011 *Modelling Turbulence in Engineering and the Environment: Second-Moment Routes to Closure*. Cambridge University Press.

IRGENS, F. 2014 *Rheology and Non-Newtonian fluids*. Springer.

JIMÉNEZ, J. 2013 Near-wall turbulence. *Phys. Fluids* **25**, 101302.

KIM, J., MOIN, P. & MOSER, R. 1987 Turbulence statistics in fully developed channel flow at low Reynolds number. *J. Fluid Mech.* **177**, 133–166.

KLINE, S. J., REYNOLDS, W. C., SCHRAUB, F. A. & RUNSTADLER, P. W. 1967 The structure of turbulent boundary layers. *J. Fluid Mech.* **30**, 741–773.

LEE, M. J. & REYNOLDS, W. C. 1985 Numerical experiments on the structure of homogeneous turbulence. *Tech. Rep.* Stanford University.

LUCHIK, T. S. & TIEDERMAN, W. G. 1987 Timescale and structure of ejections and bursts in turbulent channel flows. *J. Fluid Mech.* **174**, 529–552.

LUMLEY, J. L. 1969 Drag reduction by additives. *Annu. Rev. Fluid Mech.* **1**, 367–384.

LUMLEY, J. L. 1973 Drag reduction in turbulent flow by polymer additives. *J. Polym. Sci.* **7**, 263–290.

LUMLEY, J. L. 1979 Computational modeling of turbulent flows. In *Advances in Applied Mechanics* (ed. Chia-Shun Yih). Elsevier.

LUMLEY, J. L. & NEWMAN, G. R. 1977 The return to isotropy of homogeneous turbulence. *J. Fluid Mech.* **82**, 161–178.

MALIN, M. R. 1997 Turbulent pipe flow of power-law fluids. *Intl Commun. Heat Mass Transfer* **24**, 977–988.

MANSOUR, N. N., KIM, J. & MOIN, P. 1988 Reynolds-stress and dissipation-rate budgets in a turbulent channel flow. *J. Fluid Mech.* **194**, 15–44.

METZNER, A. B. & REED, J. C. 1955 Flow of non-Newtonian fluids–correlation of the laminar, transition, and turbulent-flow regions. *AIChE J.* **1**, 434–444.

MIN, T., CHOI, H. & YOO, J. Y. 2003*a* Maximum drag reduction in a turbulent channel flow by polymer additives. *J. Fluid Mech.* **492**, 91–100.

MIN, T., YOO, J. Y., CHOI, H. & JOSEPH, D. D. 2003*b* Drag reduction by polymer additives in a turbulent channel flow. *J. Fluid Mech.* **486**, 213–238.

MOIN, P. & MAHESH, K. 1998 Direct numerical simulation: a tool in turbulence research. *Annu. Rev. Fluid Mech.* **30**, 539–578.

MOSER, R. D., KIM, J. & MANSOUR, N. N. 1999 Direct numerical simulation of turbulent channel flow up to $Re_\tau = 590$. *Phys. Fluids* **11**, 943–945.

MOSER, R. D. & MOIN, P. 1984 Direct numerical simulation of curved turbulent channel flow. *Tech. Rep.* NASA TM 85974. Stanford University.

OHTA, T. & MIYASHITA, M. 2014 DNS and LES with an extended Smagorinsky model for wall turbulence in non-Newtonian viscous fluids. *J. Non-Newtonian Fluid Mech.* **206**, 29–39.

PARK, J. T., MANNHEIMER, R. J., GRIMLEY, T. A. & MORROW, T. B. 1989 Pipe flow measurements of a transparent non-Newtonian slurry. *Trans. ASME: J. Fluids Engng* **11**, 331–336.

PEREIRA, A. S. & PINHO, F. T. 1994 Turbulent pipe flow characteristics of low molecular weight polymer solutions. *J. Non-Newtonian Fluid Mech.* **55**, 321–344.

PINHO, F. T. 2003 A GNF framework for turbulent flow models of drag reducing fluids and proposal for a $k - \varepsilon$ type closure. *J. Non-Newtonian Fluid Mech.* **114**, 149–184.

PINHO, F. T. & WHITELAW, J. H. 1990 Flow of non-Newtonian fluids in a pipe. *J. Non-Newtonian Fluid Mech.* **34**, 129–144.

POPE, S. B. 2000 *Turbulent Flows*. Cambridge University Press.

PTASINSKI, P. K., BOERSMA, B. J., NIEUWSTADT, F. T. M., HULSEN, M. A., VAN DER BRULE, B. H. A. A. & HUNT, J. C. R. 2003 Turbulent channel flow near maximum drag reduction: simulations, experiments and mechanisms. *J. Fluid Mech.* **490**, 251–291.

PTASINSKI, P. K., NIEUWSTADT, F. T. M., VAN DER BRULE, B. H. A. A. & HULSEN, M. A. 2001 Experiments in turbulent pipe flow with polymer additives at maximum drag reduction. *Flow Turbul. Combust.* **66**, 159–182.

RUDMAN, M. & BLACKBURN, H. M. 2003 Turbulent pipe flow of non-Newtonian fluids. In *Computational Fluid Dynamics 2002* (ed. S. W. Armfield, P. Morgan & K. Srinivas), pp. 687–692. Springer.

RUDMAN, M. & BLACKBURN, H. M. 2006 Direct numerical simulation of turbulent non-Newtonian flow using a spectral element method. *Appl. Math. Model.* **30**, 1229–1248.

RUDMAN, M., BLACKBURN, H. M., GRAHAM, L. J. W. & PULLUM, L. 2004 Turbulent pipe flow of shear-thinning fluids. *J. Non-Newtonian Fluid Mech.* **118**, 33–48.

SHAHMARDI, A., ZADE, S., ARDEKANI, M. N., POOLE, R. J., LUNDELL, F., ROSTI, M. E. & BRANDT, L. 2019 Turbulent duct flow with polymers. *J. Fluid Mech.* **859**, 1057–1083.

SIMONSEN, A. J. & KROGSTAD, P.-Å. 2005 Turbulent stress invariant analysis: clarification of existing terminology. *Phys. Fluids* **17**, 088103.

SINGH, J., RUDMAN, M. & BLACKBURN, H. M. 2016 The rheology dependent region in turbulent pipe flow of a Generalised Newtonian fluid. In *20th Australasian Fluid Mechanics Conference (AFMC)*. Australasian Fluid Mechanics Society.

SINGH, J., RUDMAN, M. & BLACKBURN, H. M. 2017*a* The effect of yield stress on pipe flow turbulence for generalised Newtonian fluids. *J. Non-Newtonian Fluid Mech.* **249**, 53–62.

SINGH, J., RUDMAN, M. & BLACKBURN, H. M. 2017*b* The influence of shear-dependent rheology on turbulent pipe flow. *J. Fluid Mech.* **822**, 848–879.

SINGH, J., RUDMAN, M. & BLACKBURN, H. M. 2018 Reynolds number effects in pipe flow turbulence of generalized Newtonian fluids. *Phys. Rev. Fluids* **3**, 094607.

SUNGKORN, R., DERKSEN, J. J. & KHINAST, J. G. 2012 Modeling of aerated stirred tanks with shear-thinning power law liquids. *Intl J. Heat Fluid Flow* **36**, 153–166.

TABOR, M. & DE GENNES, P. G. 1986 A cascade theory of drag reduction. *Europhys. Lett.* **2**, 519–522.

THAIS, L., GATSKI, T. B. & MOMPEAN, G. 2012 Some dynamical features of the turbulent flow of a viscoelastic fluid for reduced drag. *J. Turbul.* **13**, N19.

TOMS, B. A. 1948 Some observations on the flow of linear polymer solutions through straight tubes at large Reynolds numbers. In *Proceedings of the International Congress on Rheology*, pp. 135–141. North Holland.

VINUESA, R., PRUS, C., SCHLATTER, P. & NAGIB, H. M. 2016 Convergence of numerical simulations of turbulent wall-bounded flows and mean cross-flow structure of rectangular ducts. *Meccanica* **51**, 3025–3042.

WALLACE, J. M. 2016 Quadrant analysis in turbulence research: history and evolution. *Annu. Rev. Fluid Mech.* **48**, 131–158.

WALLACE, J. M., ECKELMANN, H. & BRODKEY, R. S. 1972 The wall region in turbulent shear flow. *J. Fluid Mech.* **54**, 39–48.

WANG, C.-H. & HO, J.-R. 2011 A lattice Boltzmann approach for the non-Newtonian effect in the blood flow. *Comput. Maths Applics.* **62**, 75–86.

WARHOLIC, M. D., MASSAH, H. & HANRATTY, T. J. 1999 Influence of drag-reducing polymers on turbulence: effects of Reynolds number, concentration and mixing. *Exp. Fluids* **27**, 461–472.

YEUNG, P. K. & BRASSEUR, J. G. 1991 The response of isotropic turbulence to isotropic and anisotropic forcing at the large scales. *Phys. Fluids* A **3**, 884–897.

YOSHINO, M., HOTTA, Y., HIROZANE, T. & ENDO, M. 2007 A numerical method for incompressible non-Newtonian fluid flows based on the lattice Boltzmann method. *J. Non-Newtonian Fluid Mech.* **147**, 69–78.

ZHENG, E. Z., RUDMAN, M., SINGH, J. & KUANG, S. B. 2019 Direct numerical simulation of turbulent non-Newtonian flow using OpenFOAM. *Appl. Math. Model.* **72**, 50–67.

Paper II

Effects of shear-thinning rheology on near-wall turbulent structures

Arturo A. Arosemena, Ronnie Andersson, Helge I. Andersson, and Jannike Solsvik

J. Fluid Mech. **925**, A37 (2021)

J. Fluid Mech. (2021), *vol*. 925, A37, doi:10.1017/jfm.2021.657

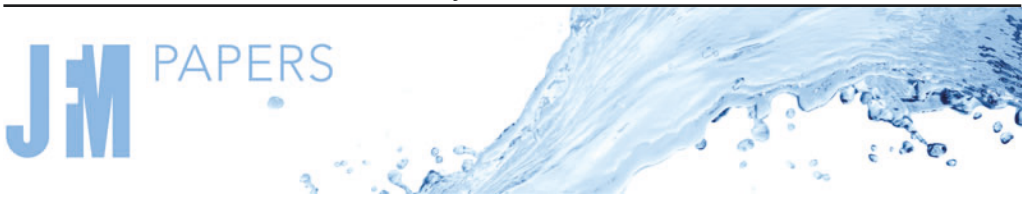

Effects of shear-thinning rheology on near-wall turbulent structures

Arturo A. Arosemena[1],†, Ronnie Andersson[2], Helge I. Andersson[3] and Jannike Solsvik[1],†

[1]Department of Chemical Engineering, Norwegian University of Science and Technology (NTNU), NO-7491 Trondheim, Norway

[2]Department of Chemistry and Chemical Engineering, Chalmers University of Technology, SE-41296 Gothenburg, Sweden

[3]Department of Energy and Process Engineering, Norwegian University of Science and Technology (NTNU), NO-7491 Trondheim, Norway

(Received 30 December 2020; revised 31 May 2021; accepted 15 July 2021)

Turbulent channel flow simulation of a shear-thinning fluid is considered – see Arosemena *et al.* (*J. Fluid Mech.*, vol. 908, 2021, p. A43) – and compared with a Newtonian base case to reveal the effects of the shear-dependent rheology on the near-wall structures. Analyses of different flow statistics revealed that, for the shear-thinning fluid case, the streamwise vortices appear to grow in size, depart from the wall and present a lessening in their intensity. Information regarding variations in the quasi-longitudinal vortices is also obtained from three-dimensional structures identified through a normalized Q-criterion. With shear-thinning rheology, it is shown that the structures are comprised of wall-attached and -detached families which are taller than for a Newtonian fluid. Also, for a given height, the structures appear to be longer, with approximately the same width and overall larger volume for the shear-thinning fluid case; albeit their fractal dimension remains the same when compared to the Newtonian base case. Moreover, it is observed that the number density of vortical structures decreases with shear-thinning fluid behaviour. These observations, in conjunction with the known changes to the longitudinal velocity structures which appear to be less streaky, more spanwise separated and thickened with shear-thinning rheology, strongly suggest that the near-wall self-sustaining process has been disrupted. As we move slightly away from the wall and with shear-thinning behaviour, the local increase in viscosity seems to lead to less energetic vortices whereas the streaks are provided with an additional source of energy due to fluctuations in viscosity.

Key words: rheology, turbulent boundary layers

† Email addresses for correspondence: arturo.arosemena@ntnu.no, jannike.solsvik@ntnu.no

1. Introduction

Turbulence is ever present in nature and in numerous man-made processes. Wall-bounded turbulent flows, in particular, are extremely important for technological applications. Close to 25 % of the energy used in industry is destined to transport fluids in pipes and channels, or to propel vehicles through air or water, and approximately a quarter of that energy is irreversibly dissipated by turbulence in regions close to walls (Jiménez 2013). Moreover, in several industrial settings, the transported fluid is non-Newtonian. A non-Newtonian fluid exhibits non-constant viscosity which may depend on shear stress and/or strain rate history in a nonlinear manner and can be classified within three main groups (Irgens 2014): (i) time-independent fluids, which are further divided into viscoplastic/yield-stress fluids and purely viscous fluids, (ii) time-dependent fluids and (iii) viscoelastic fluids consisting of materials with both elastic and viscous effects.

Considering the previous context, this work focuses on purely viscous fluids and is an extension of the turbulent channel flow study of Arosemena, Andersson & Solsvik (2021). Our aim is to explore the changes on the near-wall turbulent structures, in particular the quasi-streamwise vortices, due to shear-thinning fluid behaviour; a non-Newtonian rheology exhibiting drag-reducing features.

1.1. *Rheological drag reduction in generalized Newtonian fluids*

Although elastic effects are present in several drag-reducing fluids, within a given range of particle concentration and for certain polymer solutions such effects are negligible; e.g. consider the variations of the elastic recovery index (Durán *et al.* 2000) in solutions with a concentration of less than 2.5 wt% of carboxymethyl cellulose reported by Benchabane & Bekkour (2008). Generalized Newtonian (GN) fluids are a type of time-independent, purely viscous fluids which stress tensor due to viscous effects, $\tau_{ij_{vis}}$, is given by

$$\tau_{ij_{vis}} = 2\mu S_{ij}, \tag{1.1}$$

where $\mu = \mu(\dot{\gamma})$ is the apparent dynamic viscosity solely depending on the strain rate $\dot{\gamma} = (2S_{ij}S_{ji})^{1/2}$ and S_{ij} is the strain rate tensor. GN fluids are commonly encountered in various industrial and commercial applications and those of non-Newtonian nature are classified into pseudoplastic/shear-thinning and dilatant/shear-thickening fluids based on the observed trend in their apparent viscosity with increasing strain rate. Regarding the shear-thinning fluids, they exhibit decreasing apparent viscosity with increasing strain rate and are frequently found in bioreactors, in drilling activities within the petroleum industry and are used as additives in cosmetic and food products. Polymer solutions with shear-thinning behaviour such as those with concentrations of carboxymethyl cellulose, xanthan gum and polyacrylamide, are also commonly used for turbulent flow experiments of drag-reducing non-Newtonian fluids (Escudier *et al.* 2001).

Many experimental (Park *et al.* 1989; Pinho & Whitelaw 1990; Pereira 1994) and numerical (Rudman & Blackburn 2003, 2006; Gavrilov & Rudyak 2016) studies have reported features common to the low drag reduction (LDR) regime (Warholic, Massah & Hanratty 1999), such as enhancement of streamwise turbulence intensity and suppression of other cross-sectional intensities, decrease in Reynolds shear stress and overall reduction of turbulent production with shear-thinning fluid behaviour. More recently, and based on observations of the Reynolds stress budgets and to the overall turbulent kinetic energy, for turbulent pipe (Singh, Rudman & Blackburn 2017) and channel (Arosemena *et al.* 2021) flows, strain-rate-dependent rheology has been found to be mainly important within the inner layer region. This remark is supported as well by the Singh, Rudman &

Blackburn (2016) results where, for a fixed GN fluid rheology within the inner layer region, no significant differences are observed in the mean-flow and first-order statistics even if different apparent fluid viscosity profiles are attained outside the inner layer. Singh, Rudman & Blackburn (2018) also reported small contributions from viscosity fluctuation terms to the mean shear stress budget, mean flow and turbulent kinetic energy budget up to moderate frictional Reynolds numbers, $Re_\tau = 323$–750. Arosemena *et al.* (2021) further reasoned that observed drag-reducing features with shear-thinning behaviour are likely related to important changes to the near-wall turbulent structures and, in consequence, to the self-sustaining process occurring near the wall.

1.2. *Near-wall self-sustaining process*

The inner region of wall-bounded turbulent shear flows has been extensively investigated and remarkable well-organized coherent structures have been found. In the vicinity to the wall, where shear dominates, flow visualizations by Kline *et al.* (1967) in boundary layers and by Corino & Brodkey (1969) in pipes revealed regions of low- and high-speed fluid ('streaks') staggered in the spanwise direction. Such streaks undergo a series of dynamical processes leading to production of turbulence; during an intermittent, quasi-cyclical process, outward ejections of low-speed fluid and inrush of high-speed fluid towards the wall occur (Wallace, Eckelmann & Brodkey 1972; Willmarth & Lu 1972). The other important near-wall structures consist of quasi-streamwise vortices or rolls. The streaks contain most of the turbulent kinetic energy and the vortices both organize the energy dissipation and the momentum transfer (Jiménez 2013).

A recurring topic in the study of near-wall structures is the regeneration cycle involving the streaks and vortices. While it is generally accepted that the quasi-streamwise vortices cause the streaks by advection of the mean velocity gradient (Blackwelder & Eckelmann 1979) and with independence from the presence of the wall (Lee, Kim & Moin 1990), there is still uncertainty regarding what causes the rolls. Explanations for the regeneration cycle of near-wall vortical structures can be grouped within two main categories (Schoppa & Hussain 2002): (i) parent–offspring regeneration (see for instance Brooke & Hanratty (1993) in the case of roll-up of near-wall streamwise vorticity sheets and Zhou *et al.* (1999) for quasi-streamwise vortex generation from hairpin-shaped vortical structures) and (ii) instability-based generation (see for instance Swearingen & Blackwelder 1987; Robinson 1991; Jiménez 1994 or Hamilton, Kim & Waleffe 1995 for velocity streak instability-based generation). Jiménez & Pinelli (1999) showed that disturbing the streaks in a region where the wall-normal coordinate – in inner viscous/wall units – is less than 60 but greater than 20 inhibits the formation of streamwise vortices and suggested that a regeneration cycle based on streaks instabilities dominates over other mechanisms for the generation of rolls. Jiménez & Pinelli (1999) additionally showed that near-wall turbulence is autonomous in the sense that streaks and vortices do not decay even after the outer flow is artificially removed. On the other hand, Schoppa & Hussain (2002) argued that most buffer streaks are too weak to be unstable to the inflectional mechanism described by Jiménez & Pinelli (1999) and proposed an alternative explanation for the streaks instability based on (linear) transient growth of secondary perturbations. Hence, it seems there is no unanimous agreement in how the near-wall vortical structures are produced, albeit the idea of the regeneration of rolls due to the instability of the streaks, leading to their breakdown, is consistent between multiple authors (see also Hoepffner, Brandt & Henningson (2005) and more recently, Cossu *et al.* (2011)).

Despite the shortcomings in our understanding regarding the near-wall vortex dynamics, we do know that any drag-reducing strategy is based on disturbing the turbulence

regeneration cycle (Karniadakis & Choi 2003). Drag reduction can be achieved by decreasing the intensity of the quasi-streamwise vortices or by weakening their interaction with the near-wall flow (Tardu 1995) and the use of riblets (Choi, Moin & Kim 1993; García-Mayoral & Jiménez 2011) and polymer additives (several studies, e.g. Ptasinski *et al.* 2003; Dubief *et al.* 2004; Kim *et al.* 2007; Li & Graham 2007; Kim & Sureshkumar 2013) are within the few successful strategies that actually disrupt the self-sustained regeneration cycle. In polymer solutions, known effects of viscoelasticity on the wall turbulence are the reduction in the strength and numbers of the quasi-streamwise vortices and a reduction in the spanwise meandering and thickening of the streaks (Kim *et al.* 2007; White & Mungal 2008). The self-sustained cycle is seemly disrupted by the polymers which oppose the motion of the vortices (Dubief *et al.* 2005; Kim *et al.* 2007), take energy from them and release it into the streaks (Dubief *et al.* 2004, 2005). In contrast to studies about polymer solutions accounting for viscoelastic effects, works related to drag-reducing GN fluids have not directly addressed probable mechanisms leading to disruption of the self-sustaining process in the absence of elastic effects and, in general, less attention has been given to the phenomenological changes in the near-wall turbulence structures; for instance, observations about structures are limited to instantaneous contours of the streamwise streaks, two-point velocity correlations and integral length scales (see e.g. Rudman & Blackburn 2006, Singh *et al.* 2017, Arosemena *et al.* 2021 or alternatively Appendix A) whereas findings about the quasi-streamwise vortices are not often reported.

1.3. *Methods for vortex identification and the Q-criterion*

The identification of three-dimensional structures involves connecting fluid regions where a certain condition for a quantity of interest is fulfilled. In the case of vortical structures, the identification methods can be broadly classified as Lagrangian or Eulerian, the last being the most common type of vortex identification method (Epps 2017). Several (well-known) Eulerian identification methods such as Q-criterion (Hunt, Wray & Moin 1988), the discriminant Δ-criterion (Chong, Perry & Cantwell 1990), the λ_2-criterion (Jeong & Hussain 1995) or the more recent omega method (Liu *et al.* 2016) are based on conditions related to either the eigenvalues or the invariants corresponding to the velocity gradient tensor, $\boldsymbol{D} = D_{ij}$. The characteristic equation of D_{ij} is given by (see e.g. Zhou *et al.* 1999)

$$\xi_i^3 + P\xi_i^2 + Q\xi_i + R = 0, \tag{1.2}$$

where ξ_i are the eigenvalues of D_{ij} and P, Q and R are the first, second and third invariants of the velocity gradient tensor, respectively. Hence

$$P = -\mathrm{tr}(\boldsymbol{D}), \quad Q = \tfrac{1}{2}[P^2 - \mathrm{tr}(\boldsymbol{DD})], \quad \text{and} \quad R = -\det(\boldsymbol{D}). \tag{1.3a–c}$$

Here, tr is the trace of the tensor quantity and det is the absolute value of the determinant. For an incompressible fluid, $P = 0$ and the second invariant of D_{ij} simplifies to

$$\begin{aligned} Q &= -\tfrac{1}{2}(D_{ij}D_{ji}) \\ &= \tfrac{1}{2}(\Omega_{ij}\Omega_{ij} - S_{ij}S_{ij}), \end{aligned} \tag{1.4}$$

since $D_{ij} = S_{ij} + \Omega_{ij}$, i.e. the sum of its symmetric and antisymmetric parts, respectively. Here, S_{ij} is the aforementioned strain rate tensor and Ω_{ij} is the rotation rate tensor.

In the present work, the Q-criterion is considered to identify vortical structures which, as noted by Chakraborty, Balachandar & Adrian (2005), represents a local measure of the excess of rotation relative to the strain rate. Chakraborty *et al.* (2005) also observed

remarkably similar vortical structures when comparing the Q-criterion to other local identification methods based on point-wise values of the velocity gradient tensor. This observation strongly suggests that the choice of a particular method for identifying the structures does not significantly impact the results. Ideally, a vortex is a connected fluid region with $Q \geq 0$. However, similar to other methods, a non-zero threshold value is to be selected for the identification of individual structures; otherwise a 'sponge-like' object, occupying a significant part of the total domain, will be observed. Another difficulty when detecting structures in inhomogeneous flows is the necessity of non-constant threshold values for proper visualization. For a channel flow which is inhomogeneous in the wall-normal direction, different thresholds may be required at different wall-normal positions. Nagaosa & Handler (2003) showed that the probability density function (p.d.f.) of the Q-values normalized by its standard deviation is homogeneous everywhere except in the viscous sublayer and, based on this result, proposed that the threshold values should vary in the wall-normal direction according to the standard deviation of the Q-values.

In this study, vortical structures are identified by the Q-criterion, i.e. $Q \geq Q_{thresh}$; where $Q_{thresh} \geq 0$ is required to account for the statistical wall-normal dependency of the channel flow. Further details regarding the identification method, and the statistical information obtained as a result of it, are provided in § 3.2.

1.4. *Outline*

The paper is organized as follows. Section 2 summarizes the numerical experiments considered for the study, § 3 presents evidence of the changes to the quasi-streamwise vortices due to shear-thinning rheology compared with a Newtonian base case, § 4 explains probable reasons for the modification of the near-wall self-sustaining process and, finally, § 5 shows a summary of the main findings and drawn conclusions. Readers not familiar with the changes to the velocity streaks due to shear-thinning rheology are also encouraged to glance through Appendix A.

2. The numerical experiments

The data to be analysed are taken from channel flow simulations of GN fluids at a target $Re_\tau = \rho u_\tau h/\mu_w = 180$ (Arosemena *et al.* 2021). Here, ρ is the fluid density, $u_\tau = (\bar{\tau}_w/\rho)^{1/2}$ is the frictional velocity defined in terms of the shear stress at the wall $\bar{\tau}_w$, h is the channel half-width and μ_w is the nominal wall viscosity (Draad, Kuiken & Nieuwstadt 1998; Ptasinski *et al.* 2001). The code, called CALC-LES (Davidson & Peng 2003; Davidson 2020), solves the incompressible form of the momentum and continuity equations through a finite volume method on a collocated grid, using central differencing approximations in space and the Crank–Nicolson scheme in time. The numerical procedure is based on an implicit, two-time stepping technique where Poisson's equation for the pressure is solved with an efficient multigrid method; see Emvin (1997). To incorporate the GN fluid rheology, the apparent fluid viscosity is modelled through the Carreau fluid model, i.e.

$$\mu = \mu_\infty + (\mu_0 - \mu_\infty)[1 + (\Lambda\dot{\gamma})^2]^{(\alpha-1)/2}, \tag{2.1}$$

where μ_∞ and μ_0 are the 'infinite' and 'zero' shear rate viscosities, respectively, Λ is a time constant and α is the flow index which for shear thinning is to be less than unity. Note that Newtonian fluid behaviour is recovered for $\alpha = 1$. Also, within the iterative process of the two-step time-advancement technique, the viscosity is handled

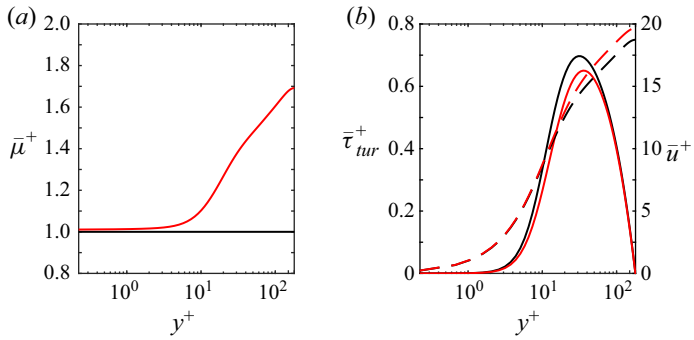

Figure 1. Mean viscosity, Reynolds shear stress and velocity profiles: (*a*) $\bar{\mu}^+$ and (*b*) $\bar{\tau}^+_{tur}, \bar{u}^+$. In (*a*), $\mu_\infty/\mu_0 = 1 \times 10^{-3}$, $\mu_0^+ \approx 1.782$, $\Lambda^+ = 0.1$ and α is set to 0.8 and to 1 for cases P180 and N180, respectively. In (*b*), profiles corresponding to $\bar{\tau}^+_{tur}$ and $\bar{u}^+$ are indicated by the line styles '——' and '- - -', respectively. Line colours as explained in table 1.

in a manner similar to how the turbulent viscosity is handled for a hybrid large eddy simulation–Reynolds-averaged Navier–Stokes (LES–RANS) model; see e.g. Davidson & Peng (2003). In the simulations, the flow is driven by a constant pressure gradient and, for a given flow index, the different parameters in the Carreau model are fixed to achieve the nominal wall viscosity corresponding to the target frictional Reynolds number. To properly solve the different turbulent scales, a large enough computational domain and a fine enough spatial grid are considered. Regarding the boundary conditions, the top and bottom are physical (no-slip, impermeable) walls and periodicity is set in the streamwise and spanwise directions of the computational box.

Table 1 summarizes the computational set-up for the Newtonian (N180) and pseudoplastic/shear-thinning (P180) fluid cases. Meanwhile, figure 1(*a*) shows the attained mean (averaged over time and the spatially homogeneous directions) dynamic viscosity for case P180. Note that, for the shear-thinning fluid case, the viscosity at the channel centre is indeed noticeably larger than its nominal wall value; $\mu_0/\mu_w \approx 1.782$. On the other hand, $\mu_w \gg \mu_\infty$ and, in consequence, the 'infinite' shear rate viscosity is asymptotically attained at strain rate values much larger than the ones reached here for case P180. It is also remarked that, at the given flow conditions and within the region where viscous effects are particularly dominant, the increase of local viscosity with shear-thinning behaviour is (on average) less than 50 % of the value at the wall. Such increase is comparable to what has been reported in previous studies (see viscosity rheograms in e.g. Rudman *et al.* 2004; Gavrilov & Rudyak 2016; Singh *et al.* 2018). It is worth mentioning as well that the use of different values for the flow index is not expected to change the observed trends with shear-thinning rheology. Consider, for instance, Singh *et al.* (2017) where consistent trends, such as a continuous increase in the mean velocity profile and a decrease in the Reynolds shear stress, are observed with decreasing flow index, i.e. increasing shear-thinning fluid behaviour.

Hereafter, we denote the streamwise (or longitudinal), wall-normal and spanwise (or lateral) coordinates by x, y and z, respectively, and the corresponding velocity and vorticity components by u, v, w and $\omega_x, \omega_y, \omega_z$, respectively. Most variables and parameters, denoted by '+' superscript, are given in 'wall' units using $\mu_w, u_\tau, (\mu_w/\rho)/u_\tau, (\mu_w/\rho)/u_\tau^2$ and ρu_τ^2 as characteristic viscosity, velocity, length, time and stress, respectively. Here, t indicates time, and mean and fluctuating variables are identified by $\overline{(\,)}$ and $(\,)'$, respectively. On the other hand, when index notation is used, suffix i (or any other

GN fluid case	Line/marker colour	$\rho U_b 2h/\mu_w$	L_x/h	L_z/h	Δx^+	Δy^+_{min}	Δy^+_{max}	Δz^+	N_f	t_f^+
N180	Black	5692	4π	2π	9.88	0.22	4.62	4.94	150	5400
P180	Red	5993	6π	2.5π	14.81	0.22	4.62	6.17	150	5400

Table 1. Parameters of the simulations. Here, U_b is the bulk flow velocity, L_x and L_z are the periodic streamwise and spanwise lengths of the computational box, Δx^+ and Δz^+ are the constant grid spacings in the x and z directions, respectively, whilst Δy^+_{min} and Δy^+_{max} are the minimum and maximum grid spacing in the wall-normal direction; N_f is the number of collected flow fields and t_f^+ is the time span over which the fields are collected, after discarding the initial transients. The rheological parameters for cases N180 and P180 are given in the caption of figure 1.

suffix) takes the value 1, 2 or 3 to represent the x, y or z component, respectively, and – unless otherwise specified – repeated indices imply summation from x to z. Also, root-mean-squared values are denoted by rms( ).

In this paper, the majority of the analysis and discussion are limited to the viscous wall region $y^+ \lesssim 50$ (Pope 2000). In a canonical flow of Newtonian fluids, while considering variations with the wall-normal coordinate, it is common to consider a flow-region subdivision: there is an inner layer region; comprised of a viscous sublayer ($y^+ \lesssim 5$), a buffer layer region ($5 \lesssim y^+ \lesssim 55$), a quite limited – if at all exiting for such a low Re_τ – log-law region ($55 \lesssim y^+ \lesssim 62$) and a remaining outer region. Here, the y^+-ranges for the buffer and log-law layers are assigned based on the wall-normal position at which the limited, logarithmic-law behaviour for the mean velocity, in case N180, is observed. The viscous wall region is within the inner layer and it is where viscous contributions to the total shear stress are significant and viscous effects are important to the overall mean dynamics.

3. Near-wall turbulent structures

The analysis of structures corresponding to a GN drag-reducing fluid case allows us to understand the effects of variations of local viscosity on the channel flow without considering elastic effects. Furthermore, for several important materials, the non-Newtonian rheology is primarily of shear-thinning nature and viscoelastic effects are negligible (Rudman *et al.* 2004). On this point, it is important to note that, although we are interested in near-wall structural changes with shear-thinning behaviour, this does not diminish the importance of flow statistics. Information about coherent structures can be inferred from statistical quantities since an event should occur often enough for it to be relevant to the overall dynamics (Jiménez 2013). Of course, the previous statement does not imply that rare but intense events are unimportant.

We will start our discussion with the computation of quite a noticeable drag-reducing feature; the percentage amount of drag reduction, DR%, defined as (see for instance Gyr & Bewersdorff 1995)

$$\mathrm{DR}\% = \frac{C_{f,N} - C_{f,P}}{C_{f,N}} \times 100\,\%, \tag{3.1}$$

where the friction coefficient $C_f = \bar{\tau}_w/(\rho U_b^2/2) = 2u_\tau^2/U_b^2$ or, alternatively, $C_f = 2(Re_\tau/Re_b)^2$ in terms of the bulk-based Reynolds number $Re_b = \rho U_b h/\mu_w$. The subscripts 'N' and 'P' denote the Newtonian and pseudoplastic/shear-thinning fluid

cases, respectively. Thus, for the parameters corresponding to the GN fluid flow cases summarized in table 1, the amount of drag reduction is approximately

$$\begin{aligned} \mathrm{DR}\% &= \left[1 - \left(\frac{Re_{b,N}}{Re_{b,P}}\right)^2\right] \times 100\,\% \\ &\approx 10\,\%. \end{aligned} \tag{3.2}$$

Due to shear-thinning behaviour, along with the amount of drag reduction, there is a perceptible decrease in the Reynolds shear stress, i.e. $\bar{\tau}^+_{tur} = -\overline{u'v'}/u^2_\tau$, and an increase in the mean velocity profile, $\bar{u}^+$, as seen in figure 1(*b*). The decrease in $\bar{\tau}^+_{tur}$ implies an overall suppression of turbulent production but furthermore, it represents a clear statistic indicative of the weakening of near-wall vortices. On the other hand, the enhancement of $\bar{u}^+$ with the considered shear-dependent rheology is self-evident; recall that $U^+_b = \int_0^{h^+} \bar{u}^+ \,\mathrm{d}y^+/h^+$, nonetheless, it is interesting to note that, for case P180 and as seen from figure 1(*b*), the starting point of the apparent log-law region seems to move (slightly) further away from the wall. This observation suggests that, with shear-thinning behaviour, there is a modest thickening of the buffer layer and a probable extension of the overall region where viscous effects are important to the mean dynamics. Moreover, the change in the $\bar{u}^+$ profile also suggests potential variations in the near-wall velocity structures with shear-thinning rheology.

The following subsections address the changes in quasi-streamwise vortices with shear-thinning rheology considering evidence both from the flow statistics and from identified three-dimensional vortical structures. For observations regarding the changes in the velocity streaks due to shear-thinning behaviour, consider for instance Singh *et al.* (2017) and Arosemena *et al.* (2021), or alternatively, Appendix A.

3.1. *Effects on quasi-streamwise vortices: evidence from flow statistics*

In wall-bounded turbulent flow of Newtonian fluids, the quasi-streamwise vortices are highly elongated structures which are slightly inclined from the wall (Jeong *et al.* 1997). Several vortices are associated with each velocity streak, with a longitudinal spacing of order $\lambda^+_x \approx 300$–400 (Jiménez & Moin 1991; Jiménez, Álamo & Flores 2004) and there is no clear evidence that the near-wall region is dominated by pairs of counter-rotating streamwise vortices (Bakewell & Lumley 1967) although there is a tendency for vortices with opposite sign to stack on top of each other (Jiménez & Moin 1991).

Statistical evidence about quasi-streamwise vortical structures, in the viscous wall region, can be inferred by analysing the streamwise and spanwise coherence of v' and w' through the two-point correlations of these fluctuating velocity components, i.e. $R_{ij}(y, \boldsymbol{r}) = \overline{u'_i(\boldsymbol{x}, t)u'_j(\boldsymbol{x}+\boldsymbol{r}, t)}/\overline{u'_i(\boldsymbol{x}, t)u'_j(\boldsymbol{x}, t)}$; where $\boldsymbol{x} = (x, y, z)$ and $\boldsymbol{r}$ is the separation vector between the two points. Figures 2 and 3 show R_{22} and R_{33} for separations in the longitudinal direction δx^+ and in the spanwise direction δz^+, respectively, at $y^+ \approx 5, 30$ and 50. The position of a minimum in the R_{22} and R_{33} correlations with spanwise separation is related to the average diameter d^+_{av} of a vortex and to the mean spanwise spacing between pairs of counter-rotating vortices, respectively (Moser & Moin 1984). Figure 3(*a*) reveals that, outside the sublayer, $R_{22}(\delta z^+)$ decays more slowly and larger d^+_{av} values are attained with shear-thinning rheology. On the other hand, a minimum in $R_{33}(\delta z^+)$ is only observed in the very near-wall region and not for $y^+ \gtrsim 20$; see figure 3(*b*). Thus, pairs of counter-rotating rolls with centre at the same wall-normal position do

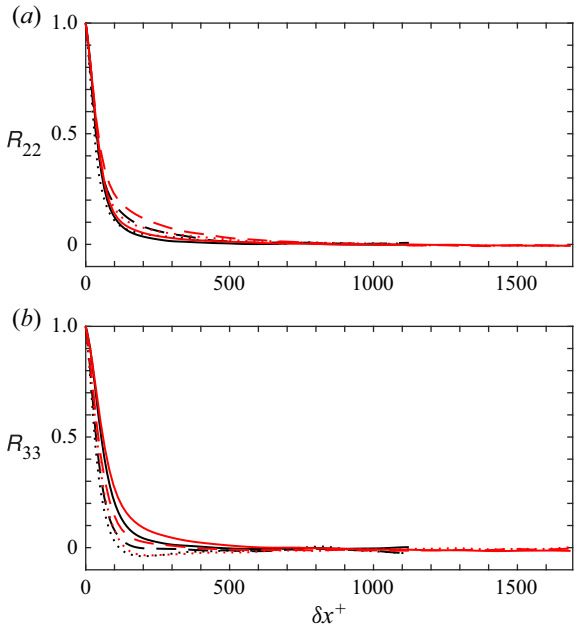

Figure 2. Normalized two-point correlations with streamwise separation δx^+: (*a*) R_{22} and (*b*) R_{33}. Line styles '——', '- - -' and '· · ·' are used to identify correlations at $y^+ \approx 5$, 30 and 50, respectively. Line colours as explained in table 1.

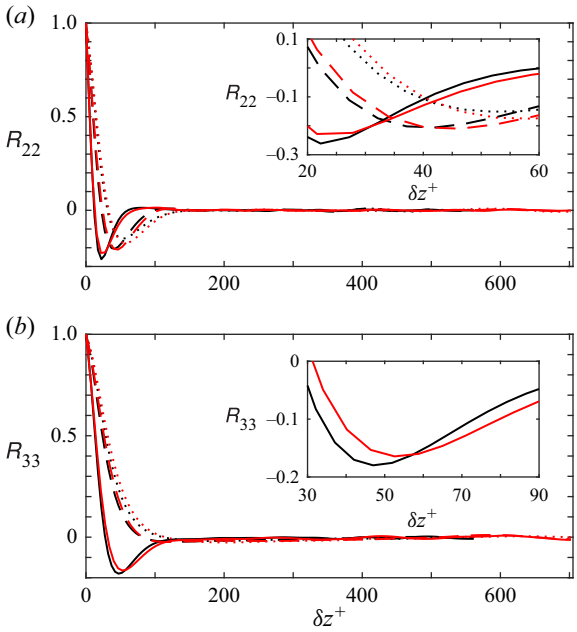

Figure 3. Normalized two-point correlations with spanwise separation δz^+: (*a*) R_{22} and (*b*) R_{33}. Line styles '——', '- - -' and '· · ·' are used to identify correlations at $y^+ \approx 5$, 30 and 50, respectively. Line colours as explained in table 1.

not appear to be a dominant feature within the viscous wall region. Furthermore, such a configuration is even less probable with shear-thinning fluid behaviour since the average vortex diameter keeps increasing as we move further away from the wall, as

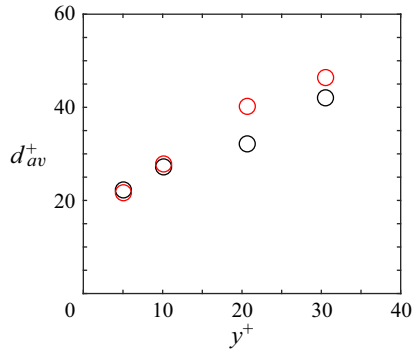

Figure 4. Average distance across a vortex, d^+_{av}. Marker colours as explained in table 1.

seen in figure 4. Regarding longitudinal coherence of v' and w' which is related to the average spacing in the x-direction between vortical structures, figure 2(*a*,*b*) reveals longer streamwise coherence with shear-thinning rheology, although there is no clear statistical evidence of an increase in the mean streamwise spacing between rolls as the wall-normal position increases.

The average diameter of near-wall vortices can also be estimated by considering the profile of the standard deviation corresponding to the longitudinal vorticity component, i.e. $\mathrm{rms}(\omega_x^+) = \mathrm{rms}(\omega_x'^+)$ shown in figure 5(*a*). The wall-normal positions of the local minimum and maximum away from the wall in the $\mathrm{rms}(\omega_x'^+)$ profile correspond to the average locations of the edge and centre, respectively, of the quasi-streamwise rolls (Moser & Moin 1984). As seen in figure 5(*a*), the mean locations corresponding to the edge and centre of the quasi-streamwise vortices have moved slightly further away from the wall with shear-thinning rheology. In consequence, on average, the vortices grow in size and depart away from the wall with shear-thinning fluid behaviour. Note that, overall, the mean diameter is approximately 30 wall units and it is comparable to the estimates seen in figure 4. With respect to the other large value in the $\mathrm{rms}(\omega_x'^+)$ profile, it occurs at the wall because of the no-slip boundary condition. Figure 5(*a*) also allows us to notice a general decrease in the intensity of the streamwise and wall-normal vorticities with the non-Newtonian rheology. Regarding the $\mathrm{rms}(\omega_z'^+)$ profile, we observe a similar trend with shear-thinning fluid behaviour for $y^+ > 10$. However, note that, close to the sublayer region, there is an overall increase in the spanwise vorticity intensity with shear-thinning rheology. This behaviour is explained in the context of the vorticity transport in the vicinity to the wall, which is discussed below.

Since we are interested in the changes experienced by the near-wall vortices with shear-thinning rheology and in the overall self-sustaining cycle of such structures, it is worth considering and discussing the characteristics of the vorticity field close to the wall. The transport equation for the instantaneous vorticity field, obtained by applying the operator 'curl' to the momentum equation for an incompressible GN fluid, is given by

$$\frac{\mathrm{D}}{\mathrm{D}t}(\bar{\omega}_i + \omega_i') = (\bar{\omega}_j + \omega_j')\frac{\partial}{\partial x_j}(\bar{u}_i + u_i') + \varepsilon_{ijk}\frac{\partial}{\partial x_j}\left(\frac{1}{\rho}\frac{\partial \tau_{kl\,vis}}{\partial x_l}\right). \tag{3.3}$$

Here, $\mathrm{D}(\,)/\mathrm{D}t = \partial(\,)/\partial t + (\bar{u}_j + u_j')\partial(\,)/\partial x_j$ is the material time derivative and ε_{ijk} is the alternation or Levi-Civita tensor. In (3.3), the first term on the right-hand side represents the vorticity production terms P_{ω_i} whilst the last term accounts for diffusion of vorticity

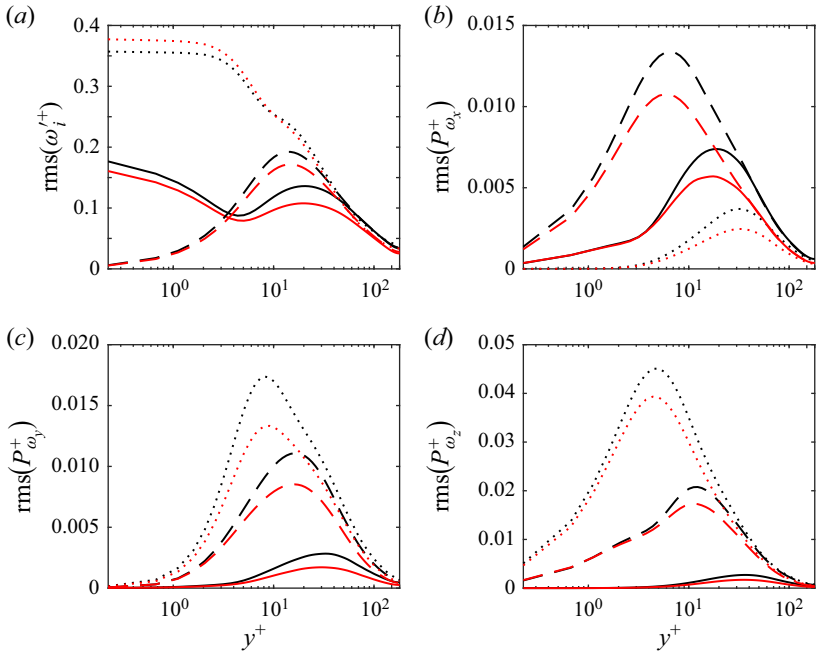

Figure 5. Vorticity intensities and root-mean-squared values corresponding to production terms of the vorticity components: (*a*) rms($\omega_i'^+$), (*b*) rms($P^+_{\omega_x}$), (*c*) rms($P^+_{\omega_y}$) and (*d*) rms($P^+_{\omega_z}$). In (*a*), standard deviations corresponding to x, y and z vorticity components are indicated by the line styles '——', '- - -' and '· · ·', respectively. In (*b–d*), root-mean-squared profiles of production terms due to effects over x, y and z vorticity components are indicated by the line styles '——', '- - -' and '· · ·', respectively. Line colours as explained in table 1.

due to viscous effects. Note that, in a fully developed turbulent channel, the mean vorticity is simply the lateral component, i.e. $\bar{\omega}_z = -\partial\bar{u}/\partial y$. In consequence, the production of the x, y and z vorticity components are given by

$$\begin{aligned} P_{\omega_x} &= \omega_x' \frac{\partial u'}{\partial x} + \omega_y' \frac{\partial}{\partial y}(\bar{u} + u') + (\bar{\omega}_z + \omega_z') \frac{\partial u'}{\partial z} \\ &= \omega_x' \frac{\partial u'}{\partial x} - \left(\frac{\partial w'}{\partial x}\right) \frac{\partial}{\partial y}(\bar{u} + u') + \left(\frac{\partial v'}{\partial x}\right)\left(\frac{\partial u'}{\partial z}\right), \end{aligned} \tag{3.4}$$

$$\begin{aligned} P_{\omega_y} &= \omega_x' \frac{\partial v'}{\partial x} + \omega_y' \frac{\partial v'}{\partial y} + (\bar{\omega}_z + \omega_z') \frac{\partial v'}{\partial z} \\ &= \left(\frac{\partial w'}{\partial y}\right) \frac{\partial v'}{\partial y} + \omega_y' \frac{\partial v'}{\partial y} - \left(\frac{\partial}{\partial y}(\bar{u} + u')\right) \frac{\partial v'}{\partial z}, \end{aligned} \tag{3.5}$$

and

$$\begin{aligned} P_{\omega_z} &= \omega_x' \frac{\partial w'}{\partial x} + \omega_y' \frac{\partial w'}{\partial y} + (\bar{\omega}_z + \omega_z') \frac{\partial w'}{\partial z} \\ &= -\left(\frac{\partial v'}{\partial z}\right) \frac{\partial w'}{\partial x} + \left(\frac{\partial u'}{\partial z}\right) \frac{\partial w'}{\partial y} + (\bar{\omega}_z + \omega_z') \frac{\partial w'}{\partial z}, \end{aligned} \tag{3.6}$$

respectively, since $\omega_i = -\varepsilon_{ijk}\partial u_j/\partial x_k$. As seen from (3.4)–(3.6), the production terms involve stretching, tilting and twisting/turning of the different vorticity components and,

to facilitate their identification, a contribution due to a given action over a certain vorticity component is denoted by $P^{(j)}_{\omega_i}$. For instance, $P^{(x)}_{\omega_x} = \omega'_x \partial u'/\partial x$ represents production of streamwise vorticity due to stretching of the x-vorticity component. Note as well that (3.6) corresponds to production of total lateral vorticity. Production of ω'_z is obtained by subtracting the production terms corresponding to the mean spanwise vorticity, i.e. $P_{\bar{\omega}_z} = \overline{\omega'_j \partial w'/\partial x_j}$.

The root-mean-squared values of $P_{\omega_x}, P_{\omega_y}$ and P_{ω_z}, in wall units, are shown in figure 5(*b–d*). Since our interest primarily lays in the quasi-longitudinal vortices, we will start this part of the discussion considering the production terms corresponding to streamwise vorticity. A straightforward order-of-magnitude analysis is sufficient to show that the leading-order terms always are those involving the mean velocity gradient; as expected since the velocity gradient inevitably attains large values close to the wall in order for the streamwise velocity to satisfy the no-slip condition. Therefore, $P^{(y)}_{\omega_x} = -(\partial w'/\partial x)\partial(\bar{u} + u')/\partial y$ seems to be the leading term in the vicinity of the wall and thus, the importance of ω_y and in particular of $\partial w'/\partial x$ shear layers in the production of streamwise vorticity. Figure 5(*b*) shows that indeed $P^{(y)}_{\omega_x}$ is the dominant term in the very near-wall region and also reveals an overall decrease in the production of ω_x with shear-thinning rheology. Once again, $P^{(z)}_{\omega_y} = -\partial(\bar{u} + u')/\partial y(\partial v'/\partial z)$ is the expected leading-order term in the region close to the wall and, in consequence, the total lateral vorticity, $\bar{\omega}_z + \omega'_z$, can be considered the main source for the production of ω_y. Figure 5(*c*) reveals that $P^{(z)}_{\omega_y}$ is certainly the largest term in the near-wall region and also allows us to see a general decrease in the production of wall-normal vorticity with shear-thinning fluid behaviour.

With respect to the production of spanwise vorticity, as with the production of ω_y, the dominant term in the vicinity to the wall is $P^{(z)}_{\omega_z} = (\bar{\omega}_z + \omega'_z)\partial w'/\partial z$, which implies that, at least on average, production of total lateral vorticity appears to be primarily self-sustained and mainly due to stretching of the mean lateral vorticity $\bar{\omega}_z$ under $\partial w'/\partial z$ shear rates. Figure 5(*d*) shows that, as with P_{ω_x} and P_{ω_y}, there is an overall decrease in the production of ω_z with shear-thinning rheology. Additional insight regarding total production of lateral vorticity can be gained by also considering the transport equation for $\bar{\omega}_z$ by Reynolds averaging equation (3.3) and taking the $i = 3$ component. This results in

$$\begin{aligned} \frac{\partial \bar{\omega}_z}{\partial t} &= -\frac{\partial}{\partial x_j}\overline{(u'_j \omega'_z)} + \overline{\omega'_j \frac{\partial w'}{\partial x_j}} + \overline{\varepsilon_{3jk} \frac{\partial}{\partial x_j}\left(\frac{1}{\rho}\frac{\partial \tau_{klvis}}{\partial x_l}\right)} \\ &= 0, \end{aligned} \tag{3.7}$$

where, in order of appearance, the terms on the right-hand side are the advection of fluctuating lateral vorticity component (also called turbulent force density, see e.g. Tardu & Doche 2009) denoted by $B_{\bar{\omega}_z}$, the total production of $\bar{\omega}_z$ through stretching, turning and lifting (or tilting) by the fluctuating local field and the molecular diffusion of the mean vorticity field due to viscous effects, $MD_{\bar{\omega}_z}$, respectively.

Figure 6 presents $P^+_{\bar{\omega}_z}$ and $B^+_{\bar{\omega}_z}$ being balanced out by $MD^+_{\bar{\omega}_z}$ for both GN fluids confined to the viscous wall region. In the same figure, the rms(ω'^+_z) profiles are also displayed once again. The inhibition of the turbulent force density and in particular of the production term with shear-thinning rheology appears to be related to the very near-wall behaviour observed for the standard deviation of the spanwise vorticity component. Manipulation of the production and advective terms are common in active and passive strategies employed

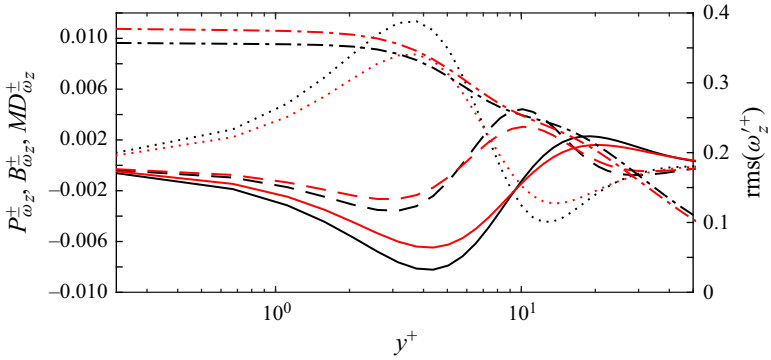

Figure 6. Production, advection and diffusion of mean spanwise vorticity overlapped with the standard deviation of the lateral vorticity for the viscous wall region, $y^+ \leq 50$. Profiles corresponding to $P^+_{\bar{\omega}_z}$, $B^+_{\bar{\omega}_z}$, $MD^+_{\bar{\omega}_z}$ and rms($\omega_z'^+$) are indicated by the line styles '——', '- - -', '· · ·' and '- · -', respectively. Line colours as explained in table 1.

to reduce turbulent drag (Tardu & Doche 2009). In our case, for a common driving pressure gradient, the magnitude of the total lateral vorticity actually increases, as we approach the wall, for the shear-thinning rheology. Recall that $\omega_z|_{y=0} = -\partial(\bar{u} + u')/\partial y|_{y=0}$ and the wall-normal velocity gradient at the wall increases with shear-thinning behaviour to compensate for the appearance of a new non-Newtonian term arising due to fluctuations in viscosity (see e.g. shear stress budget in Arosemena *et al.* 2021 or in Singh *et al.* 2017). The increase in rms($\omega_z'^+$) for case P180, seen as we approach the wall, is expected to be caused by an increase in the difference between production and dissipation of $\overline{\omega_z'\omega_z'}$ for the drag-reducing fluid case.

Regarding interaction between the small-scale eddies and the mean shear, similar to the turbulence-to-mean-shear time scale ratio (see e.g. Appendix A), it is possible to define a parameter with the purpose of analysing such interactions. Figure 7(*a*) presents the ratio of time scale of vorticity to that of the mean shear, given by

$$S^\star = \frac{2\bar{S}_{12}}{\overline{\omega_i'\omega_i'}^{1/2}}, \tag{3.8}$$

where $\overline{\omega_i'\omega_i'}$ is the variance of the vorticity fluctuations, often referred to as the enstrophy. Note that, since the mean shear is equal to the absolute mean vorticity, (3.8) can also be interpreted as the ratio of mean vorticity magnitude (Euclidean norm) to the magnitude of the vorticity fluctuations. As seen from figure 7(*a*), outside the viscous sublayer, there is a small increase in $S^\star$ with shear-thinning rheology and it is expected that the vortical structures will tend to be slightly more oriented along the most extensive strain direction at 45° to the mean-flow direction (Rogers & Moin 1987). In the sublayer region, due to the increase in the spanwise vorticity fluctuation, there is a decrease in $S^\star$ with shear-thinning fluid behaviour. Also, note that, outside the viscous wall region, i.e. $y^+ \gtrsim 50$, for both fluid cases, $S^\star$ is fairly small and the small-scale eddies are likely to behave as in a weakly sheared flow. This tendency is more evident when considering $\eta_c = (c_{ij}c_{ji}/6)^{1/2}$ based on the vorticity anisotropy tensor (Mansour, Kim & Moin 1988; Antonia, Kim & Browne 1991) defined as

$$c_{ij} = \frac{\overline{\omega_i'\omega_j'}}{\overline{\omega_k'\omega_k'}} - \frac{1}{3}\delta_{ij}, \tag{3.9}$$

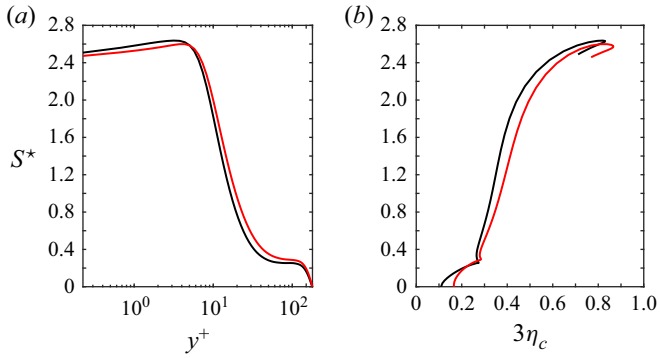

Figure 7. Mean-shear-related properties of the vorticity that resides in the smaller scales: (*a*) vorticity-to-mean-shear time scale ratio, $S^\star$, vs y^+ and (*b*) $S^\star$ vs second invariant of the anisotropy tensor corresponding to the vorticity correlations, i.e. $3\eta_c$. Line colours as explained in table 1.

where δ_{ij} is the Kronecker's delta. Here, the variable $3\eta_c$ varies from unity for vorticity completely aligned in one direction (one-dimensional turbulence) to zero for fully isotropic vorticity fluctuations (three-dimensional isotropic turbulence). Figure 7(*b*) shows $S^\star$ against $3\eta_c$. As can be seen, consistent with the profiles in figure 5(*a*), there is a general increase in the small-scale anisotropy with shear-thinning rheology. Overall, in both GN fluid cases and within the viscous wall region, the small-scale eddies behave as in slightly anisotropic homogeneous shear and as we move towards the log-layer region, the smallest scales start to increasingly decouple from the shear and become more isotropic as y^+ continues to increase.

Finally, some of the aforementioned effects, such as the dampening of quasi-longitudinal vortices, have been reported for several drag-reducing flows including those with solid–spherical particles (Zhao, Andersson & Gillissen 2010), those with polymer additives (Dubief *et al.* 2004) and those in contact with riblet-mounted surfaces (Choi *et al.* 1993). This situation of similar changes in the near-wall structures strongly suggests that the self-sustained cycle in the region close to the wall (Jiménez & Pinelli 1999) has been disrupted, albeit (probably) through different mechanisms.

3.2. *Effects on quasi-streamwise vortices: structures*

3.2.1. *Identification method*

In this work, vortical structures are identified by means of the Q-criterion, i.e. $Q \geq Q_{thresh}$. The inhomogeneity of the channel flow is taken into account through $Q_{thresh} = Q_{thresh}(y)$ depending on the standard deviation of the second invariant of $D_{ij} = \partial u_i/\partial x_j$, which is a more significant statistical indicator of vortical events compared with other quantities. For instance, figure 8(*a*) shows the mean Q-values normalized by their standard deviations and, as can be seen, for both GN fluid cases, in regions with $\bar{Q} > 0$; i.e. regions where on average Q-positive values are slightly more common, $\bar{Q} \ll \mathrm{rms}(Q')$. Figure 8(*a*) also makes apparent that, in the very near-wall region, particularly within the viscous sublayer, the mean Q-values are approximately of the same order of magnitude as the root-mean-squared values of its fluctuations. Other interesting observations regarding the standard deviation of the Q-values as a statistical indicator of vortical structures are noted by considering figure 8(*b*). The figure reveals an apparent inhibition of the intensity corresponding to the fluctuating Q-values with shear-thinning rheology. This result points

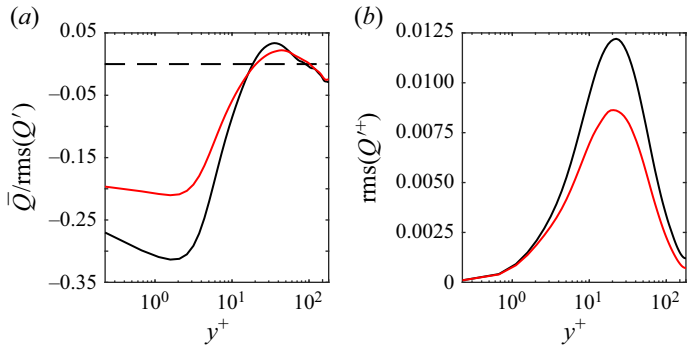

Figure 8. Low-order statistics of Q-values: (*a*) ratio of mean Q-values to their standard deviations, $\bar{Q}/\mathrm{rms}(Q')$, and (*b*) root-mean-squared fluctuating Q-values in inner units, $\mathrm{rms}(Q'^+)$. Line colours as explained in table 1.

to an overall decrease in the population of vortices for the drag-reducing fluid case. Figure 8(*b*), for both fluid cases, also displays a clear peak in the $\mathrm{rms}(Q'^+)$ profiles close to $y^+ \approx 20$ which suggests predominance of vortical structures in and close to that region of the buffer layer.

According to what was discussed in the introduction and in the previous paragraph, non-zero threshold values accounting for variations in the inhomogeneous direction are to be selected in order to deliver proper results but the question about which particular threshold values should be used still remains unanswered. For instance, in the channel flow and at a given wall-normal position, a threshold value, $\mathcal{T}$, is required to be large enough such that it is possible to distinguish individual structures and also to capture as many structures as possible. On the other hand, a too large $\mathcal{T}$-value makes it easier to identify individual structures but only captures the most intense ones. Thus, a common limitation for the Q-criterion and for many other identification methods, is their threshold dependency. The threshold selection remained relatively subjective until Moisy & Jiménez (2004) introduced the percolation analysis to systematically select $\mathcal{T}$-values for proper visualization of the structures. Here, a perceptible transition from a highly clustered region to increasing individual structures, identified according to a particular method (e.g. Q or λ_2-criterion), occurs at a critical threshold value, $\mathcal{T}_c$. Percolation analysis has been successfully used not only for identifying vortex clusters in turbulent channel flows (del Álamo *et al.* 2006) but also for detecting three-dimensional velocity structures (Sillero 2014; Hwang & Sung 2018) and quadrant events in turbulent channels (Lozano-Durán, Flores & Jiménez 2012) and homogeneous shear turbulence (Dong *et al.* 2017) based on a three-dimensional extension of the classical quadrant analysis (Wallace *et al.* 1972; Willmarth & Lu 1972). More recently, the percolation analysis for threshold selection has also been employed by Cheng *et al.* (2020*a*) for the identification of scale-based structures of streamwise wall shear stress fluctuations in turbulent channel flows.

A brief description of the approach used for identifying the three-dimensional vortical structures is given as follows.

(i) For a given instantaneous flow field, the $Q(x, y, z)$-values are computed according to (1.4).
(ii) The vortical structures are identified as fluid connected regions where the criterion

$$Q(x, y, z) \geq Q_{thresh}(y); \quad Q_{thresh}(y) = \mathcal{T}\,\mathrm{rms}(Q') \qquad (3.10a,b)$$

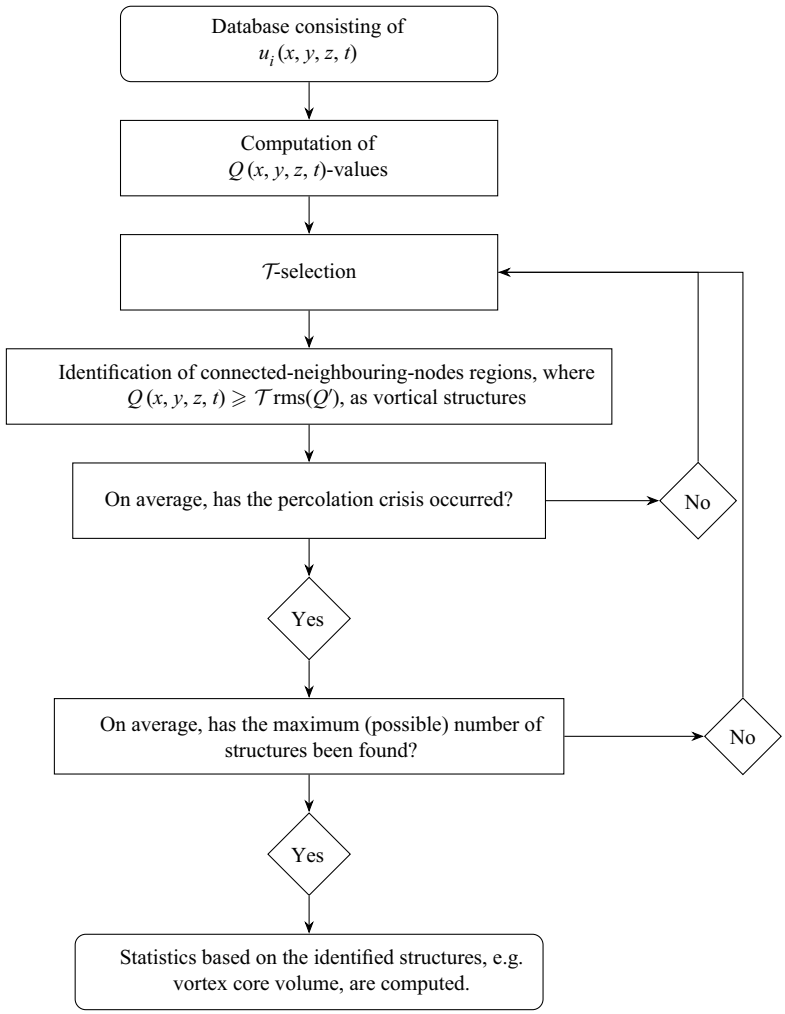

Figure 9. Flowchart of the procedure followed for the identification of three-dimensional vortical structures and computation of related statistics.

is satisfied. Here, percolation analysis is used to determine the value of $\mathcal{T}$ and the standard deviation of the Q-values, for cases P180 and N180, is according to the profiles presented in figure 8(b). Also, the individual structures consist of connected grid point values satisfying (3.10a,b) and connectivity is defined by the six orthogonal nearest neighbours of each grid point. Figure 9 also shows the followed procedure by means of a flowchart.

Figures 10(a) and 10(b) show the time averaged V_{max}/V_{tot}; which is the ratio of the volume corresponding to the largest identified structure V_{max}, at a given $\mathcal{T}$, to the total volume occupied by all structures V_{tot}, and N_{tot}/N_{max}; which is the ratio of the total number of identified objects N_{tot}, at a given $\mathcal{T}$, to the largest number of identified structures over all $\mathcal{T}$-values which is denoted by N_{max}, respectively. In the figure, for both cases, the critical threshold values; where $\mathrm{d}(V_{max}/V_{tot})/\mathrm{d}\mathcal{T}$ is a minimum and the percolation transition occurs, and the threshold value $\mathcal{T}_{max}$ where $N_{tot} = N_{max}$ are marked as well.

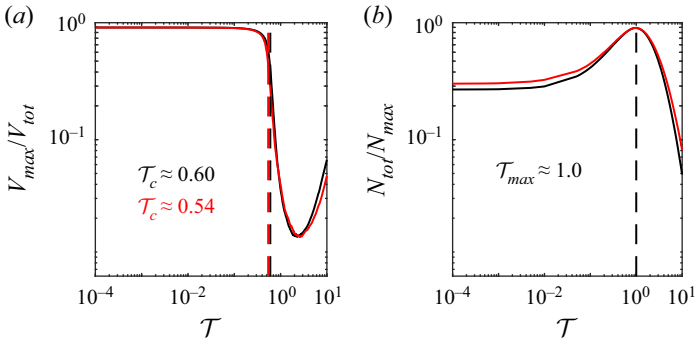

Figure 10. Percolation diagrams: (*a*) V_{max}/V_{tot} and (*b*) N_{tot}/N_{max}. In (*a* and *b*), the line style '- - -' is used to mark the critical threshold value, $\mathcal{T}_c$, and the threshold value resulting in the maximum number of objects, $\mathcal{T}_{max}$, respectively. Line colours as explained in table 1.

Figure 10(*a*) shows that the threshold at which the merging process is more intense, i.e. $\mathcal{T}_c$, slightly decreases with shear-thinning rheology. Note that, for $\mathcal{T} < \mathcal{T}_c$ and as $\mathcal{T}$ keeps decreasing, fewer structures are identified and the existing ones keep merging until a single, large 'sponge-like' object remains, where $V_{tot} = V_{max}$ (del Álamo *et al.* 2006). A tentative explanation for the decrease of $\mathcal{T}_c$ with shear-thinning behaviour may be associated with the overall decrease in the number of identified objects and the intensity of the fluctuating Q-values, as seen in figure 8(*b*) for the shear-thinning case; a cluster of objects leading to a less populated domain is likely to distinctly 'break down' more promptly. From figure 10(*b*) is also apparent that the maximum number of identified objects decreases with shear-thinning fluid behaviour; at low $\mathcal{T}$-values just a few objects are detected and the increase in the ratio N_{tot}/N_{max} with shear-thinning rheology implies that $N_{max,\mathrm{P180}} < N_{max,\mathrm{N180}}$. Figure 10(*b*) also allows us to see that $\mathcal{T}_{max} \approx 1$ for cases P180 and N180. Thus, to facilitate the comparison of the results, the threshold value in (3.10*a*,*b*) is taken equal to the value that maximizes the number of detected objects for both cases, i.e. $\mathcal{T} = \mathcal{T}_{max}$. A short discussion regarding the influence of the threshold value is presented in Appendix B.

Finally, observations regarding the decrease in the total number of identified structures and the slight variations in their orientation (see also discussion of the ratio $S^\star$ in § 3.1) are easily drawn as well from the isosurfaces of the instantaneous Q-values fulfilling (3.10*a*,*b*), which are shown in figures 11(*a*) and 11(*b*). Here, for comparison purposes, a computational box of $12h^+$ in the x-direction and $6h^+$ in the z-direction, corresponding to twice the minimal flow unit up to the logarithmic region (Flores & Jiménez 2010), and centred around the midpoint in the $x - z$ plane is considered. Also, the presented objects are limited to $y^+ \lesssim 50$ and coloured by the streamwise vorticity component.

3.2.2. *Classification: wall-attached and wall-detached structures*

Each object identified with condition (3.10*a*,*b*) is circumscribed within a bounding box aligned with the Cartesian axes, which is used to define both its position and size l_x, l_z and $l_y = y_{max} - y_{min}$; where y_{max} and y_{min} are the maximum and minimum distances of each object to the closer wall, respectively. See figure 12. Figure 13 shows the joint probability density function (j.p.d.f.) of the minimum and maximum wall distances for the vortical structures, $p(y_{min}/h, y_{max}/h)$, for cases P180 and N180. Here, the j.p.d.f.s are approximated via joint probability mass functions (also called discrete density functions).

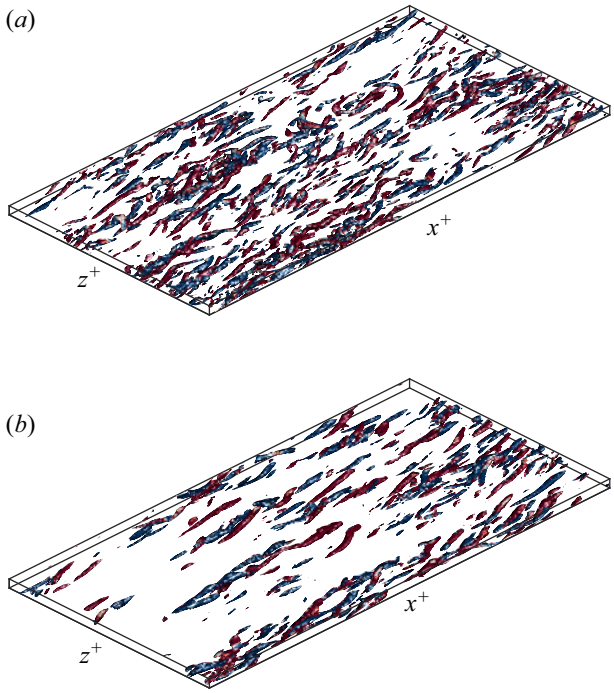

Figure 11. Isosurfaces of instantaneous $Q(x, y, z) \geq \text{rms}(Q')$ coloured by streamwise vorticity, ω_x, for: (*a*) Newtonian and (*b*) shear-thinning fluid cases. Blue and red colours are used to identify values of $\omega_x > 0$ and $\omega_x < 0$, respectively.

As can be seen from figure 13, the objects can be grouped within two families based on their distance to the wall: the first family is the narrow vertical band to the left of $y_{min}/h \lesssim 20/h^+$ which includes some very tall structures reaching almost to the opposite wall, while the second family corresponds to the highly populated inclined band where $y_{min}/h > 20/h^+$, limited by $y_{max} = y_{min}$, and which structures depend little on their distance from the wall and mainly on their vertical height l_y. del Álamo *et al.* (2006) denoted the first and second families as wall-attached and wall-detached vortex clusters, respectively. Comparing figure 13(*b*) with 13(*a*) reveals that both families present taller objects with shear-thinning fluid rheology.

For the following subsections, most of the discussion will focus on the wall-attached structures which are larger but, most importantly, interact with the near-wall flow. Also, regarding possible Reynolds number dependency of the results, it is worth pointing out that del Álamo *et al.* (2006) studied the vortex clusters in turbulent channels of Newtonian fluids for $180 < Re_\tau < 1900$ and showed fairly small Reynolds number dependency in their results. Hence, we therefore anticipate that observed trends with shear-thinning fluid behaviour may hold even at higher Reynolds numbers.

3.2.3. *Length scale self-similarity*

Figures 14(*a*) and 14(*b*) display the p.d.f. of the aspect ratios l_x^+/l_y^+ and l_z^+/l_y^+, respectively, for the wall-attached structures confined to the viscous wall region and for cases P180 and N180. Unsurprisingly, the peaks in the profiles showed in figures 14(*a*) and 14(*b*) suggest self-similarity of the lengths and widths of the wall-attached structures with their heights.

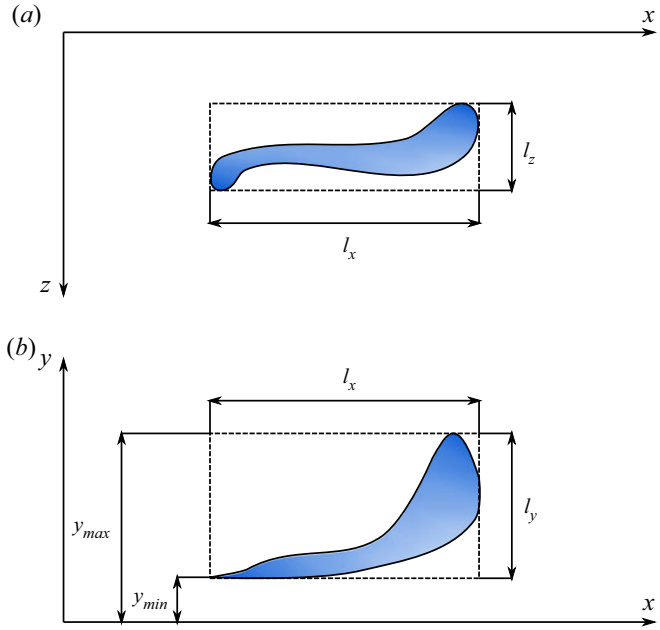

Figure 12. Schematic representation of an identified vortical structure circumscribed in a box of size $l_x \times l_y \times l_z$: (*a*) top view and (*b*) side view.

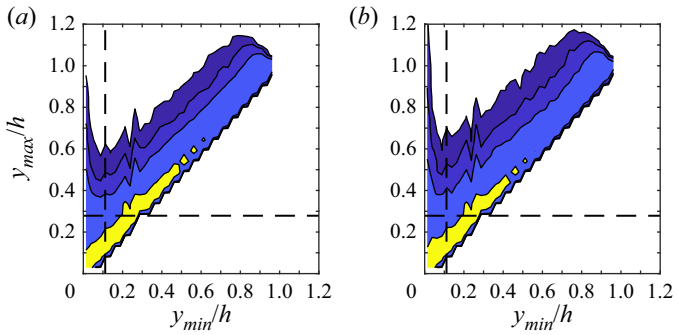

Figure 13. The j.p.d.f. of the maximum and minimum wall distances of the identified structures, $p(y_{min}/h, y_{max}/h)$: (*a*) N180 and (*b*) P180. The contours are 0.25, 0.5, 1 and 5, from darker to lighter blue until yellow. Dashed vertical line at $y_{min}/h \lesssim 20/h^+$ and dashed horizontal line at $y_{max}/h \lesssim 50/h^+$.

For the Newtonian base case, $l_x^+ \approx 3l_y^+$ and $l_z^+ \approx l_y^+$, which are similar to the linear laws reported by del Álamo *et al.* (2006), albeit less wide in comparison since there, $l_z^+ \approx 1.5l_y^+$, for the tall attached structures, i.e. $y_{min}/h \lesssim 20/h^+$ and $y_{max}/h \gtrsim 100/h^+$. With respect to the shear-thinning case, $l_x^+ \approx 4.7l_y^+$ and $l_z^+ \approx 0.9l_y^+$. Thus, it appears that, for a given height, the structures are longer but with approximately the same width for the drag-reducing fluid rheology. With respect to the flow physics, these results show that, unlike what is observed in the streamwise direction, the character of the flow in the cross-stream planes remains unchanged with shear-thinning behaviour.

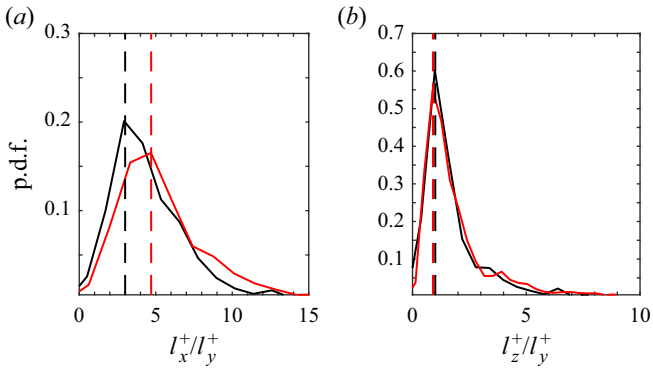

Figure 14. The p.d.f. of the bounding boxes' aspect ratios: (*a*) l_x^+/l_y^+ and (*b*) l_z^+/l_y^+ corresponding to the wall-attached structures, $y_{min}/h \lesssim 20/h^+$, confined to the viscous wall region, $y_{max}/h \lesssim 50/h^+$. Dashed vertical lines mark the approximate peak values of the p.d.f. Line colours as explained in table 1.

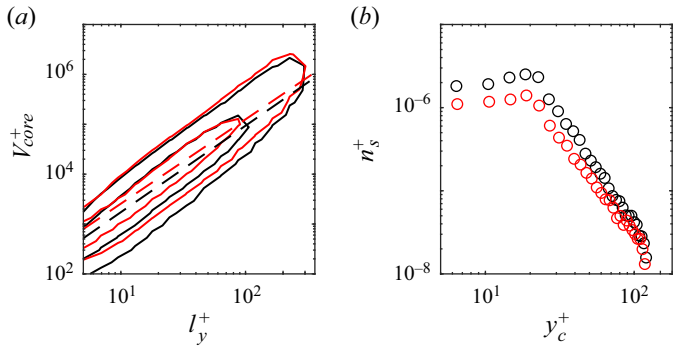

Figure 15. Scale-dependent properties: (*a*) j.p.d.f. of the logarithms of the volumes corresponding to the wall-attached vortical structures and their height, $p(\log(l_y^+), \log(V_{core}^+))$, and (*b*) population density of the wall-attached vortical structures, n_s^+, as function of their wall-normal position, y_c^+. In (*a*), the levels represented contain 70 % and 97 % of the data, respectively, and the dashed lines, found through least-squares fitting, denote $V_{core}^+ \approx 3.5(l_y^+)^{1.7}$ and $V_{core}^+ \approx 4(l_y^+)^{1.7}$ for cases P180 and N180, respectively. Line/marker colours as explained in table 1.

3.2.4. *Scale-dependent properties*

Regarding the actual shape of the identified objects, figure 15(*a*), displaying the j.p.d.f. of the logarithms of volumes corresponding to the wall-attached vortical structures, V_{core}^+, and their heights, i.e. $p(\log(l_y^+), \log(V_{core}^+))$, suggests that the vortex cores grow approximately as $(l_y^+)^{1.7}$ for both GN fluids. This result is consistent with the one reported by del Álamo *et al.* (2006) although, there, the power-law index is slightly larger; $V_{core}^+ \propto (l_y^+)^2$. The growth of the vortex cores contrasts with that of the circumscribing box volume, $l_x l_y l_z$, which grows as $(l_y^+)^3$ for the wall-attached structures within the viscous wall region; see § 3.2.3. Thus, if the exponent found is interpreted as a fractal dimension, it implies that the identified structures are shell-like objects (del Álamo *et al.* 2006). Figure 15(*a*) also reveals that the shear-thinning rheology leads to slightly larger V_{core}^+-values for a given structure height without affecting their crude estimation of their fractal dimension.

Another scale-dependent property of interest is the population density defined as

$$n_s^+ = \frac{N(y_c^+)}{N_f L_x^+ L_z^+}, \tag{3.11}$$

where N is the histogram of the wall-attached structures at a wall-normal position $y_c^+ = y_{min}^+ + l_y^+/2$. Hence, n_s^+ represents the number of wall-attached vortical structures per wall-normal position, number of collected flow fields and wall-normal area. Figure 15(*b*) displays the population density for cases P180 and N180 and consistent with the statistical indicator shown in figure 8(*b*), the densities peak at the buffer layer. Note that, an overall decrease in n_s^+, most noticeable in the buffer layer, and a slight shift towards the channel centre of the wall-normal position at which the population density peaks are also observed with shear-thinning fluid rheology. With respect to the tails of the population density profiles, although not of our main interest, it is worth mentioning that a similar decay for the population density is noticed for both cases. For the tall attached objects, $l_y^+ \approx 2y_c^+$ and $n_s^+ \propto (l_y^+)^{-3}$ (del Álamo *et al.* 2006), which constitutes a faster decay in comparison with the wall-normal decay of the three-dimensional wall-attached quadrant events leading to positive turbulence production (Lozano-Durán *et al.* 2012) and the three-dimensional wall-attached structures based on intense velocity fluctuations (Cheng *et al.* 2020*b*). In consequence, interactions between vortical structures and other types of structures are deemed more likely to occur in regions closer to the wall.

4. Near-wall self-sustaining process

As mentioned in the introduction, a turbulent flow of a GN fluid exhibiting shear-thinning behaviour shows several features common to the LDR regime also seen in flows of polymer solutions with viscoelastic effects. Furthermore, regarding the near-wall structures and aside from the reduction in the spanwise meandering, spacing and the thickening of the velocity streaks (see e.g. Appendix A), Section 3 has provided substantial evidence about the changes of the quasi-streamwise vortices with shear-thinning behaviour; those structures seem to grow in size, depart from the wall, diminish in population and strength in a similar manner as observed when viscoelastic effects are introduced. Recall that, in viscoelastic solutions, the polymers appear to oppose the motion of the vortices (Dubief *et al.* 2005; Kim *et al.* 2007), take energy from them and release it into the streaks through the work arising from the interactions between the corresponding fluctuating velocity and the polymer body force (Dubief *et al.* 2004, 2005). In the case of wall-bounded turbulent flows of a GN fluid, it is known that an analogous force arises due to fluctuations in viscosity (see e.g. Singh *et al.* 2017; Arosemena *et al.* 2021). To gain insight into the potential disruption in the self-sustaining cycle near the wall, in the spirit of De Angelis, Casciola & Piva (2002), the following correlation coefficient is considered:

$$\mathrm{norm}(\overline{u_i' f_i'}) = \frac{\overline{u_i' f_i'}}{\mathrm{rms}(u_i')\,\mathrm{rms}(f_i')}, \tag{4.1}$$

where f_i' is the fluctuating component of the new force $f_i = (1/\rho)\partial(2\mu' S_{ij})/\partial x_j$ arising due to viscosity fluctuations. The summation convention does not apply to subscript i in (4.1). The interaction term $E_i^{(NN)} = \overline{u_i' f_i'}$, appearing in the budget equation of the diagonal components of the Reynolds stress $\overline{u_i' u_k'}$, represents a mechanical work that can enhance ($E_i^{(NN)} > 0$) or diminish ($E_i^{(NN)} < 0$) the energy carried by the velocity component u_i'.

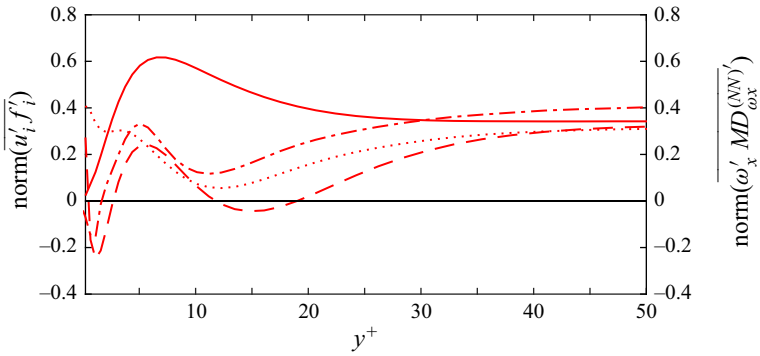

Figure 16. Correlation coefficients potentially related to disruption in the near-wall self-sustaining cycle for the viscous wall region, $y^+ \leq 50$. Profiles corresponding to correlation coefficients of $\overline{u'f'_x}$, $\overline{v'f'_y}$, $\overline{w'f'_z}$ and $\overline{\omega'_x MD^{(NN)'}_{\omega_x}}$ are indicated by the line styles '——', '- - -', '· · ·' and '- · -', respectively. Line colours as explained in table 1.

Figure 16 shows $\mathrm{norm}(\overline{u'_i f'_i})$ confined to the viscous wall region. This correlation coefficient is an indicator of $E_i^{(NN)}$; if the correlation is positive (negative), on average, f'_i has the tendency to increase (decrease) u'_i, which is equivalent to positive (negative) work. In striking contrast to viscoelastic solutions, all velocity fluctuations are, almost everywhere, enhanced by the new force f'_i. In the case of the streamwise velocity fluctuation – related to the near-wall streaks – it is worth to note that, as for polymer solutions showing viscoelastic effects, the major enhancement occurs close to the upper edge of the viscous sublayer, i.e. $y^+ \approx 5$. The wall-normal and spanwise velocity fluctuations – which in a simplified picture of near-wall turbulence are related to the quasi-streamwise vortices – are mostly enhanced by f'_y and f'_z, respectively. This observation indicates that the new forces seem to support rather than to oppose the vortices and contrasts with the findings of e.g. De Angelis *et al.* (2002), Dubief *et al.* (2004), Kim *et al.* (2007) and Li & Graham (2007), where it is reported that the polymer forces oppose and potentially suppress the near-wall vortices. Moreover, figure 16 also displays the profile of $\mathrm{norm}(\overline{\omega'_x MD^{(NN)'}_{\omega_x}})$, which is the correlation coefficient between ω_x and its molecular diffusion due to viscous effects related to fluctuations in viscosity (analogous to the term interpreted as the polymer torque in Kim *et al.* (2007) when considering viscoelastic effects); as seen from the figure, since outside the viscous sublayer the correlation is positive, the effects due to viscosity fluctuations appear to neither act in opposition to the streamwise vorticity component nor reduce the strength of the near-wall quasi-streamwise vortices.

Finally, although the forces arising due to viscosity fluctuations appear to enhance the different turbulent intensities, it is important to consider these effects in conjunction with those resulting from the local increase of mean viscosity with shear-thinning behaviour. Figure 17(*a–c*) presents the total contribution to the budgets of $\overline{u'u'}$, $\overline{v'v'}$ and $\overline{w'w'}$ attributed to viscous effects related to the mean viscosity and its fluctuations, i.e. $2E_i^{(N)}$ and $2E_i^{(NN)}$, respectively. Here, the interaction term $E_i^{(N)} = \overline{u'_i g'_i}$, $g'_i = (1/\rho)\partial(2\bar{\mu}S'_{ij})/\partial x_j$; summation is applied over index j but not over index i. As expected, for the shear-thinning fluid, contributions due to fluctuations in viscosity are fairly small in comparison with those due to the mean viscosity; see the terms related to the budgets of $\overline{v'v'}$ and $\overline{w'w'}$.

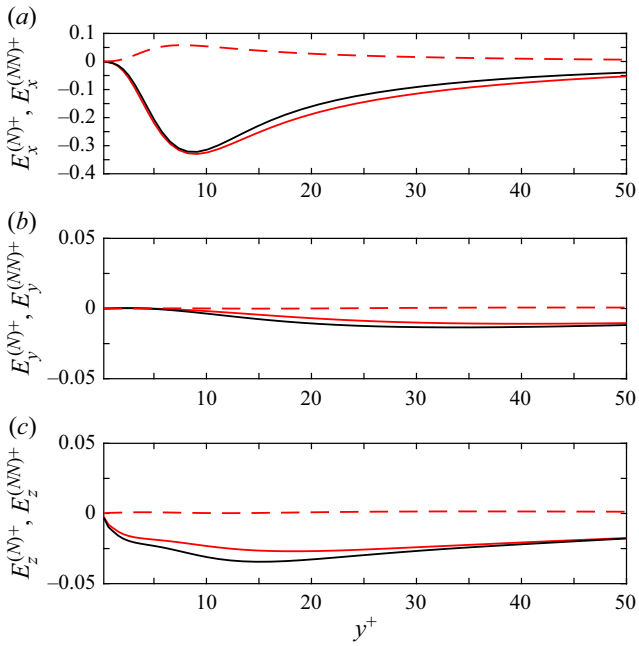

Figure 17. Contributions due to viscous effects, for $y^+ \leq 50$, to the budgets of: (*a*) $\overline{u'u'}$, (*b*) $\overline{v'v'}$ and (*c*) $\overline{w'w'}$. Profiles corresponding to total contributions due to the mean viscosity, $2E_i^{(N)^+}$, and its fluctuations, $2E_i^{(NN)^+}$, are indicated by the line styles '——' and '- - -', respectively. Line colours as explained in table 1.

Nonetheless, as displayed in figure 17(*a*), $2E_x^{(NN)}$ appears to be a source term to the $\overline{u'u'}$-budget that cannot be neglected. An intriguing situation when considering the budget of $\overline{u'u'}$ for a shear-thinning fluid in comparison with a Newtonian base case (see e.g. Arosemena *et al.* 2021), is that, although the production term is decreasing due to the decrease in Reynolds shear stress with shear-thinning behaviour (see figure 1*b*), there is an increase in the streamwise turbulence intensity as reported by several authors (see e.g. Gavrilov & Rudyak 2016; Singh *et al.* 2017; Arosemena *et al.* 2021). In consequence, the interpretation of $2E_x^{(NN)}$ as an additional source term to the $\overline{u'u'}$-budget, explains this well-known observation. The increase in $|2E_x^{(N)}|$ observed in figure 17(*a*) with shear-thinning rheology, required to balance out the overall budget, is also attributed to this new source term. Thus, based on these observations, it is really not surprising that the streaks are thickened and display less meandering/streakiness with shear-thinning behaviour. On the other hand, consistent with the decrease in energy redistribution from the $\overline{u'u'}$-budget through the velocity–pressure gradient term with shear-thinning behaviour (Arosemena *et al.* 2021), there is a decrease in $|2E_y^{(N)}|$ and $|2E_z^{(N)}|$ observed in figures 17(*b*) and 17(*c*), respectively. The fact that less energy is available for the cross-sectional intensities is certainly related to the observed suppression of the quasi-streamwise vortices with shear-thinning rheology.

It is also worth pointing out that the results of this section are in line with our previous remark about the character of the flow which, unlike the streamwise direction, seems to be unaffected in the cross-stream planes with shear-thinning fluid behaviour; see § 3.2.3. In summary, despite the similar flow characteristics between drag-reducing viscoelastic flows and those of (purely viscous) shear-thinning behaviour, the disruption of the near-wall

self-sustaining process does not seem to occur in the same manner. The features of Newtonian near-wall structures remain also for the shear-thinning case; the near-wall vortices cause the streaks and, for instance, their instability or local regions of longitudinal vorticity, that may roll-up, form the coherent quasi-streamwise vortices. The difference is that with shear-thinning rheology, the viscosity – a function of the local properties of the flow – increases as we move away from the wall and a new force arises due to viscosity fluctuations. These two factors appear to be leading to less energetic streamwise-oriented vortical motions and more stable and thicker streaks, respectively.

5. Conclusions

Data of statistically converged turbulent channel flow simulations of GN fluids at $Re_\tau = 180$ (Arosemena *et al.* 2021) are considered to analyse how the near-wall quasi-streamwise vortices change with shear-thinning rheology compared with the Newtonian base case. The shear-dependent rheology leads to drag reduction amounting to approximately 10 % and the study comprises statistics compiled from flow field variables and from identified three-dimensional vortical structures. The following can be inferred from the flow statistics:

(i) On average (in time and in the homogeneous spatial directions), compared with the Newtonian fluid case, the quasi-streamwise vortices appear to grow in size, depart from the wall and decrease in intensity with shear-thinning rheology. In particular, it is found that the different terms involved in production of streamwise vorticity, P_{ω_x}, are suppressed with shear-thinning fluid behaviour.

(ii) Also, with respect to the near-wall small-scale motions and the vorticity field, outside the viscous sublayer, an increase in the time scale of vorticity relative to that of the mean shear, $S^\star$, is noticed for the shear-thinning rheology. Such increase in $S^\star$ suggests that the vortical structures will tend to be slightly more oriented along the most extensive strain direction of the mean flow and also pushes the small-scale eddies towards higher anisotropy states.

Furthermore, considering the identified vortical structures, we reported the following findings:

(i) Tall attached and detached families (del Álamo *et al.* 2006) are also observed with shear-thinning rheology, however, both families appear to be comprised by taller objects in comparison with the Newtonian fluid case.

(ii) Regarding the geometry of the structures confined to the viscous wall region, when they are inscribed into parallelepipedal boxes aligned with the Cartesian axes, the boxes are self-similar, with dimensions $l_x^+ \approx 3l_y^+$, $l_z^+ \approx l_y^+$ and $l_x^+ \approx 4.7l_y^+$, $l_z^+ \approx 0.9l_y^+$ for the Newtonian and shear-thinning fluid cases, respectively. Hence, the vortical structures of a particular height appear to be more elongated but with approximately the same width for the drag-reducing fluid case. This shows that, unlike what is observed in the streamwise direction, the character of the flow in the cross-stream planes remains unchanged with the shear-thinning rheology.

(iii) Also, related to the geometry of the structures, it is found that the actual shape of the vortex cores is still shell like for the shear-thinning fluid case; although, shear-thinning rheology leads to larger volumes, for a given circumscribing box height, their fractal dimension remains the same.

(iv) Finally, a decrease in the population density is observed with the shear-dependent rheology and its peak, at the buffer layer, is significantly suppressed and seen slightly

shifted away from the wall. This observation is consistent with the previous remark, inferred from the flow statistics, about the departure of longitudinal vortices from the vicinity of the wall for the drag-reducing fluid case.

The above findings, by themselves, are useful for the study of certain topics in different fields, for instance, in chemical engineering, information about the aspect ratio and number density of the turbulent vortices are of practical importance when computing the rate of interaction between continuous and dispersed phase in the closure models for fluid particle breakup and coalescence due to turbulence (see e.g. Ghasempour *et al.* 2014; Solsvik & Jakobsen 2016). Furthermore, these results – in conjunction with the observed changes on the near-wall velocity streaks due to the shear-thinning rheology (see e.g. Appendix A) – strongly suggest that the self-sustaining process in the vicinity of the wall has been disrupted.

The study of the interaction between velocity fluctuations and forces related to the viscous effects revealed that, despite the phenomenological similarities with other LDR regime flows, such as those with viscoelastic effects, the qualitative features of the Newtonian near-wall structure remain for the shear-thinning case; quasi-streamwise vortices cause the velocity streaks and either their instability or other parent vortices produce the near-wall rolls. The difference with the shear-thinning rheology is the local increase of viscosity – experienced as we move away from the wall – which seems to lead to less energetic vortices, whereas the streaks are provided with an additional source of energy due to fluctuations in viscosity.

Acknowledgements. The authors are grateful for computer resources provided by NTNU IDUN/EPIC computing cluster (Själander *et al.* 2019).

Funding. This work was supported by the Research Council of Norway (RCN, grant no. 274398).

Declaration of interests. The authors report no conflict of interest.

Author ORCIDs.
Arturo A. Arosemena https://orcid.org/0000-0002-7308-1054;
Ronnie Andersson https://orcid.org/0000-0002-2838-6115;
Helge I. Andersson https://orcid.org/0000-0002-7172-7894;
Jannike Solsvik https://orcid.org/0000-0002-2786-9342.

Appendix A. Effects on the velocity structures

In the shear-dominated viscous and buffer layers, the velocity structures consist of an irregular array of spanwise staggered, alternating regions of low- and high-speed fluid elongated in the streamwise direction and superimposed to the mean flow. In a canonical flow, such as a fully developed channel or a boundary layer of a Newtonian fluid, the streaks are quite long (streamwise length $\lambda_x^+ \approx 10^3$–10^4) with an average spanwise spacing $\lambda_z^+ \approx 100$ (Smith & Metzler 1983).

Information about the effects on the near-wall velocity structures due to shear-thinning rheology can be obtained by analysing the two-point correlation R_{11} for separations in the longitudinal and lateral directions. As seen in figure 18(*a*), $R_{11}(\delta x^+)$ decays more slowly with increasing δx^+ for the shear-thinning fluid than for the Newtonian fluid; indicating that the streaks are coherent over longer streamwise distances. This is more noticeable as the distance from the wall decreases, see the contours of instantaneous u'^+ at the same wall-normal positions in figure 19. Note that for comparison purposes, and since the computational domain for P180 is larger than for case N180, the bounding box for both

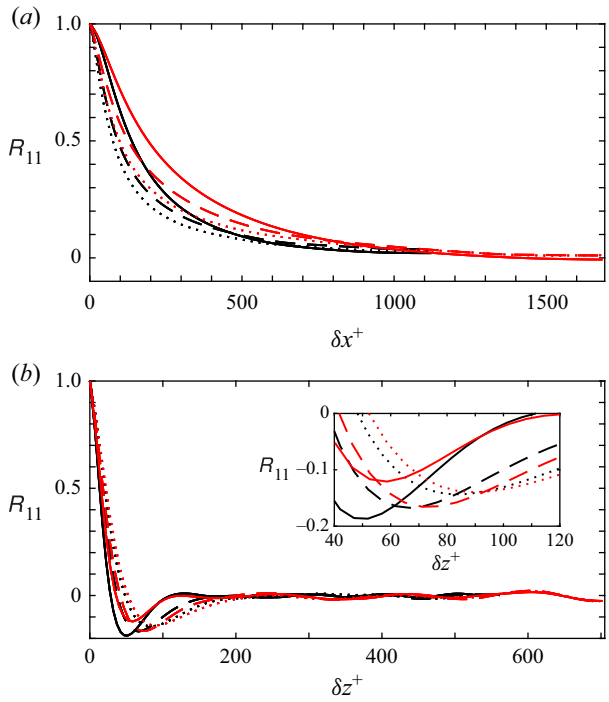

Figure 18. Normalized two-point correlation R_{11} with: (*a*) streamwise separation, δx^+, and (*b*) spanwise separation, δz^+. Line styles '——', '- - -' and '· · ·' are used to identify correlations at $y^+ \approx 5$, 30 and 50, respectively. Line colours as explained in table 1.

GN fluid cases has been set to $12h^+$ in the x-direction and to $6h^+$ in the z-direction centred around the midpoint in the x-z plane. This box constitutes twice the box size containing the minimal flow unit in the logarithmic layer, as discussed by Flores & Jiménez (2010) and thus, it is considered more than enough to observe several streaks within the viscous wall region even for the shear-thinning fluid case.

Figure 18(*b*), on the other hand, shows $R_{11}(\delta z^+)$ decaying rapidly and, at a given y^+, attaining a minimum at a larger spanwise separation with shear-thinning rheology. The location of this minimum is the average distance between a high- and a low-speed streaks and, in consequence, the average streak spacing λ_z^+ is twice such distance (Moser & Moin 1984). Figure 20 shows the average streak spacing for both cases and a distinct increase in λ_z^+ is observed with shear-thinning fluid behaviour. Note that, at $y^+ \approx 5$–10, the attained streak spacing is close to the predicted value based on the expression proposed by Oldaker & Tiederman (1977) for wall-bounded flow of a polymer solution. Also, as for a Newtonian fluid, λ_z^+ increases with increasing distance from the wall. An interesting observation regarding the streak spacing, in the region close to the viscous sublayer, is that its increase is accompanied by an increase in the average lifetime of a streak which is less or equal to the time interval between bursts (Achia & Thompson 1977). The meaning of 'bursting' varies between authors but here it is used to describe the three-stage process of low-speed streak lift-up, oscillation and breakup (Kim, Kline & Reynolds 1971). The increase in the lifetime of a sublayer streak suggests an increase in their stability with shear-thinning rheology and in consequence, less bursting and overall lessening of the turbulent generating events (see for instance the quadrant analysis of Arosemena *et al.* 2021).

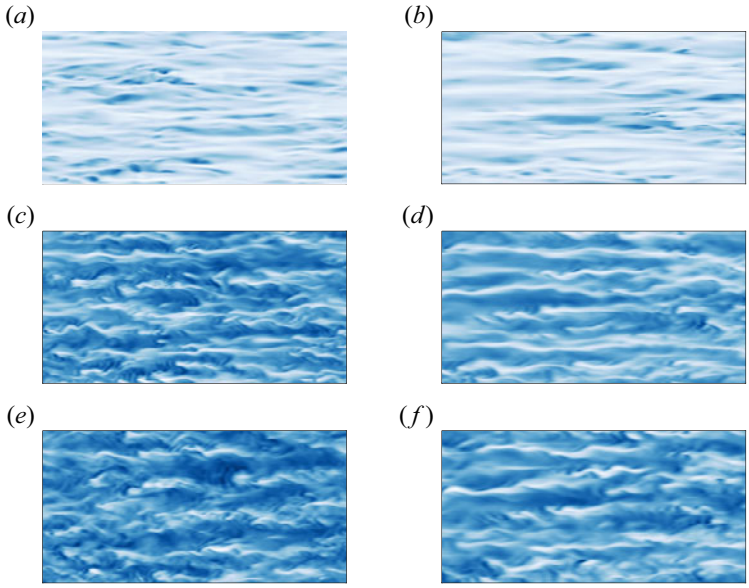

Figure 19. Contours of instantaneous streamwise velocity fluctuations normalized by frictional velocity for Newtonian (left panels) and shear-thinning (right panels) fluid cases at: (*a*,*b*) $y^+ \approx 5$, (*c*,*d*) $y^+ \approx 30$ and (*e*,*f*) $y^+ \approx 50$. White and blue represent negative and positive fluctuations, respectively.

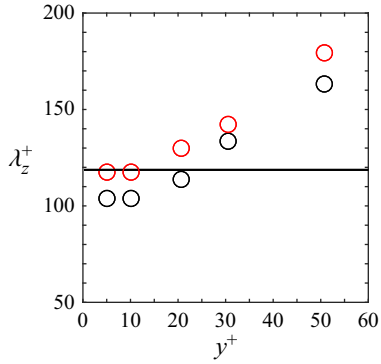

Figure 20. Average spanwise spacing between streaks, λ_z^+. Line style '——' corresponds to correlation $\lambda_z^+ = 1.9\mathrm{DR}\% + 99.7$ proposed by Oldaker & Tiederman (1977) for region close to the viscous sublayer. Marker colours as explained in table 1.

Another important quantity when considering how the energy-containing motions are affected with shear-thinning rheology in a turbulent shear flow, is the turbulent-to-mean-shear time scale ratio (Corrsin 1957) given by

$$S^* = \frac{2\bar{S}_{12}k}{\epsilon_k}, \tag{A1}$$

where $2\bar{S}_{12} = \partial\bar{u}/\partial y$ is the shear rate, $k = \overline{u_i'u_i'}/2$ is the turbulent kinetic energy and ϵ_k is the total mean dissipation rate in the GN fluid flow. Hence, the shear parameter S^* represents a dimensionless measure of the interaction between the mean shear and the large-scale energy-containing, eddies (Jiménez 2013). The shear parameter is presented in

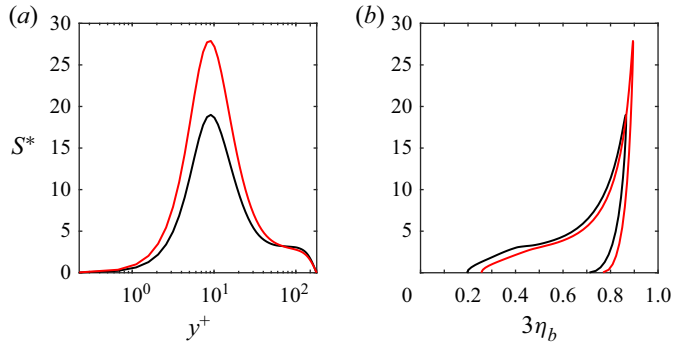

Figure 21. Mean-shear-related properties of the energy-containing scales: (*a*) turbulent-to-mean-shear time scale ratio, S^*, vs y^+ and (*b*) S^* vs second invariant of the Reynolds stress anisotropy tensor, $3\eta_b$. Line colours as explained in table 1.

figure 21(*a*). Within the viscous wall region, for both fluid cases, it is clear that $S^* \gg 1$ and many similarities – in the instantaneous structures and turbulent statistics – with homogeneous shear flow at comparable S^* values and thus with linearized rapid-distortion theory (Lee *et al.* 1990) are expected. Also, with shear-thinning rheology and for $y^+ < 50$, the increase in the ratio of energy-decay time to the time scale of mean deformation implies an increase in the amount that turbulent kinetic energy production exceeds total dissipation. Such increase in S^* for the shear-thinning fluid case implies as well that, compared with the Newtonian base case, mean shear dominates even more the large-scale motions.

A straightforward way to quantify the effect over the energy-containing scales, is to measure their anisotropy. A convenient indicator of turbulence anisotropy at large scales is the variable $\eta_b = (b_{ij}b_{ji}/6)^{1/2}$, see for instance Choi & Lumley (2001), which is based on the second invariant of the Reynolds stress anisotropy tensor (Lumley & Newman 1977) defined as

$$b_{ij} = \frac{\overline{u_i' u_j'}}{\overline{u_k' u_k'}} - \frac{1}{3}\delta_{ij}. \tag{A2}$$

Figure 21(*b*) shows S^* against $3\eta_b$. The variable $3\eta_b$ varies from unity for velocities completely aligned in one direction to zero for fully isotropic ones. As can be seen, the increase in the shear parameter with shear-thinning rheology is accompanied by an overall increase in large-scale anisotropy, which is consistent with the reported enhancement of streamwise turbulence intensity and the inhibition of the other cross-sectional intensities by multiple authors (see, e.g. Gavrilov & Rudyak 2016; Singh *et al.* 2017; Arosemena *et al.* 2021). Furthermore, figure 21(*b*) clearly shows that in the buffer layer, at a y^+ value close to 10, the increase in the maximum value for the shear parameter from $S^*_{max} \approx 19$ to $S^*_{max} \approx 28$ with non-Newtonian rheology pushes the energy-containing eddies towards a one-component turbulent state similar to what it is obtained in the limit when initially isotropic turbulence goes through a hypothetical slip-free asymmetric diffuser (Hanjalić & Launder 2011).

Appendix B. The influence of the selected threshold, $\mathcal{T}$

The influence of the threshold value, in the range $\mathcal{T}_c \leq \mathcal{T} \leq 3\mathcal{T}_c$, is considered. Figures 22(*a*) and 22(*b*) present the p.d.f. of the bounding boxes' aspect ratios and allow

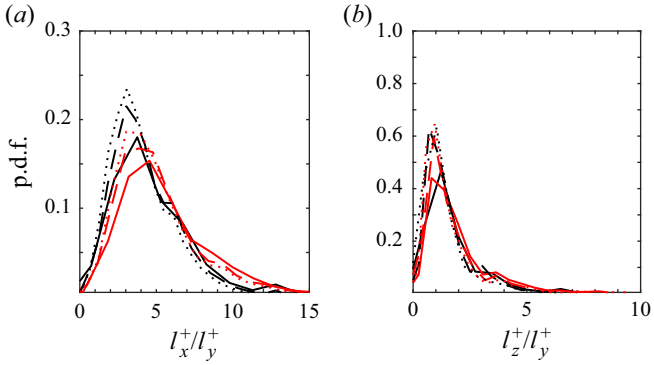

Figure 22. The p.d.f. of the bounding boxes' aspect ratios: (*a*) l_x^+/l_y^+ and (*b*) l_z^+/l_y^+ corresponding to the wall-attached structures, $y_{min}/h \lesssim 20/h^+$, confined to the viscous wall region, $y_{max}/h \lesssim 50/h^+$. The line styles '——', '- - -' and '· · ·' are used to identify the threshold values $\mathcal{T} = \mathcal{T}_c$, $\mathcal{T} = 2\mathcal{T}_c$ and $\mathcal{T} = 3\mathcal{T}_c$, respectively. Line colours as explained in table 1.

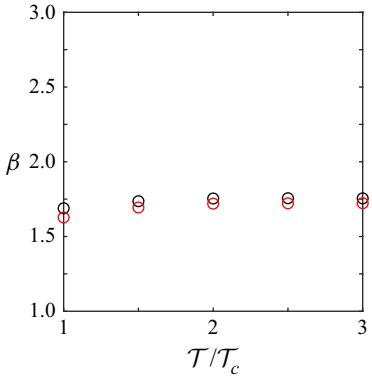

Figure 23. Crude estimate of the fractal dimension of the vortex cores, β, as a function of $\mathcal{T}/\mathcal{T}_c$. Marker colours as explained in table 1.

us to notice an increase in their peak values and a slight shift towards lower aspect ratios with increasing threshold, $\mathcal{T}$, values. However, the overall shape of the distributions and the trend of longer bounding boxes of about the same width, for the shear-thinning case in comparison with the Newtonian one, persists. Note that, in (3.10*a*,*b*), $\mathcal{T}$ is set to $\mathcal{T}_{max} \approx 1$ and thus, $\mathcal{T} \approx 1.67\mathcal{T}_c$ and $\mathcal{T} \approx 1.85\mathcal{T}_c$ for the Newtonian and shear-thinning cases, respectively. In consequence, a slight decrease in the overall number of structures is expected for $\mathcal{T} = 2\mathcal{T}_c$ and $\mathcal{T} = 3\mathcal{T}_c$; this explains the increase in the peaks of the probability distributions with increasing $\mathcal{T}$-values.

Figure 23 displays the effect of the threshold $\mathcal{T}$ on the crude estimate of the fractal dimension of the vortex cores, β; $V_{core}^+ \propto (l_y^+)^\beta$. As seen from this figure, β remains close to 1.7 for both cases and for the considered range of $\mathcal{T}$-values.

References

ACHIA, B.U. & THOMPSON, D.W. 1977 Structure of the turbulent boundary in drag-reducing pipe flow. *J. Fluid Mech.* **81**, 439–464.

DEL ÁLAMO, J.C., JIMÉNEZ, J., ZANDONADE, P. & MOSER, R.D. 2006 Self-similar vortex clusters in the turbulent logarithmic region. *J. Fluid Mech.* **561**, 329–358.

ANTONIA, R.A., KIM, J. & BROWNE, L.W.B. 1991 Some characteristics of small-scale turbulence in a turbulent duct flow. *J. Fluid Mech.* **233**, 369–388.

AROSEMENA, A.A., ANDERSSON, H.I. & SOLSVIK, J. 2021 Turbulent channel flow of generalized Newtonian fluids at a low Reynolds number. *J. Fluid Mech.* **908**, A43.

BAKEWELL, H.P. & LUMLEY, J.L. 1967 Viscous sublayer and adjacent wall region in turbulent pipe flow. *Phys. Fluids* **10**, 1880–1889.

BENCHABANE, A. & BEKKOUR, K. 2008 Rheological properties of carboxymethyl cellulose (CMC) solutions. *Colloid Polym. Sci.* **286**, 1173–1180.

BLACKWELDER, R.F. & ECKELMANN, H. 1979 Streamwise vortices associated with the bursting phenomenon. *J. Fluid Mech.* **94**, 577–594.

BROOKE, J.W. & HANRATTY, T.J. 1993 Origin of turbulence–producing eddies in a channel flow. *Phys. Fluids* A **5**, 1011–1022.

CHAKRABORTY, P., BALACHANDAR, S. & ADRIAN, R.J. 2005 On the relationships between local vortex identification schemes. *J. Fluid Mech.* **535**, 189–214.

CHENG, C., LI, W., LOZANO-DURÁN, A. & LIU, H. 2020*a* On the structure of streamwise wall-shear stress fluctuations in turbulent channel flows. *J. Fluid Mech.* **903**, A29.

CHENG, C., LI, W., LOZANO-DURÁN, A. & LIU, H. 2020*b* Uncovering Townsend's wall-attached eddies in low-Reynolds-number wall turbulence. *J. Fluid Mech.* **889**, A29.

CHOI, H., MOIN, P. & KIM, J. 1993 Direct numerical simulation of turbulent flow over riblets. *J. Fluid Mech.* **255**, 503–539.

CHOI, K-S. & LUMLEY, J.L. 2001 The return to isotropy of homogeneous turbulence. *J. Fluid Mech.* **436**, 59–84.

CHONG, M.S., PERRY, A.E. & CANTWELL, B.J. 1990 A general classification of three-dimensional flow fields. *Phys. Fluids A* **2** (5), 765–777.

CORINO, E.R. & BRODKEY, R.S. 1969 A visual investigation of the wall region in turbulent flow. *J. Fluid Mech.* **37**, 1–30.

CORRSIN, S. 1957 Local isotropy in turbulent shear flow. *NACA Research Memo* 58B11.

COSSU, C., BRANDT, L., BAGHERI, S. & HENNINGSON, D.S. 2011 Secondary threshold amplitudes for sinuous streak breakdown. *Phys. Fluids* **23**, 074103.

DAVIDSON, L. 2020 CALC-LES: a Fortran code for LES and hybrid LES-RANS. *Tech. Rep.* Chalmers University of Technology.

DAVIDSON, L. & PENG, S.-H. 2003 Hybrid LES-RANS: a one-equation SGS model combined with a $k-\omega$ for predicting recirculating flows. *Intl J. Numer. Meth. Fluids* **43** (9), 1003–1018.

DE ANGELIS, E., CASCIOLA, C.M. & PIVA, R. 2002 DNS of wall turbulence: dilute polymers and self-sustaining mechanisms. *Comput. Fluids* **31**, 495–507.

DONG, S., LOZANO-DURÁN, A., SEKIMOTO, A. & JIMÉNEZ, J. 2017 Coherent structures in statistically stationary homogeneous shear turbulence. *J. Fluid Mech.* **816**, 167–208.

DRAAD, A.A., KUIKEN, G.D.C. & NIEUWSTADT, F.T.M. 1998 Laminar-turbulent transition in pipe flow for Newtonian and non-Newtonian fluids. *J. Fluid Mech.* **377**, 267–312.

DUBIEF, Y., TERRAPON, V.E., WHITE, C.M., SHAQFEH, E.S.G., MOIN, P. & LELE, S.K. 2005 New answers on the interaction between polymers and vortices in turbulent flows. *Flow Turbul. Combust.* **74**, 311–329.

DUBIEF, Y., WHITE, C.M., TERRAPON, V.E., SHAQFEH, E.S.G., MOIN, P. & LELE, S.K. 2004 On the coherent drag-reducing and turbulence-enhancing behaviour of polymers in wall flows. *J. Fluid Mech.* **514**, 271–280.

DURÁN, J.D.G., RAMOS-TEJADA, M.M., ARROYO, F.J. & GONZÁLEZ-CABALLERO, F. 2000 Rheological and electrokinetic properties of sodium montmorillonite suspensions: I. Rheological properties and interparticle energy of interaction. *J. Colloid Interface Sci.* **229**, 107–117.

EMVIN, P. 1997 The full multigrid method applied to turbulent flow in ventilated enclosures using structured and unstructured grids. PhD thesis, Chalmers University of Technology, Gothenburg.

EPPS, B.P. 2017 Review of vortex identification methods. AIAA Paper 2017-0989.

ESCUDIER, M.P., GOULDSON, I.W., PEREIRA, A.S., PINHO, F.T. & POOLE, R.J. 2001 On the reproducibility of the rheology of shear-thinning liquids. *J. Non-Newtonian Fluid Mech.* **97**, 94–124.

FLORES, O. & JIMÉNEZ, J. 2010 Hierarchy of minimal flow units in the logarithmic layer. *Phys. Fluids* **22**, 071704.

GARCÍA-MAYORAL, R. & JIMÉNEZ, J. 2011 Hydrodynamic stability and breakdown of the viscous regime over riblets. *J. Fluid Mech.* **678**, 317–347.

GAVRILOV, A.A. & RUDYAK, V.Y.. 2016 Direct numerical simulation of the turbulent flows of power-law fluids in a circular pipe. *Thermophys. Aeromech.* **23**, 473–486.

GHASEMPOUR, F., ANDERSSON, R., ANDERSSON, B. & BERGSTROM, D.J. 2014 Number density of turbulent vortices in the entire energy spectrum. *AIChE J.* **60**, 3989–3995.

GYR, A. & BEWERSDORFF, H.-W. 1995 *Drag Reduction of Turbulent Flows by Additives*. Springer.

HAMILTON, J.M., KIM, J. & WALEFFE, F. 1995 Regeneration mechanisms of near-wall turbulence structures. *J. Fluid Mech.* **287**, 317–348.

HANJALIĆ, K. & LAUNDER, B. 2011 *Modelling Turbulence in Engineering and the Environment: Second-moment Routes to Closure*. Cambridge University Press.

HOEPFFNER, J., BRANDT, L. & HENNINGSON, D.S. 2005 Transient growth on boundary layer streaks. *J. Fluid Mech.* **537**, 91–100.

HUNT, J.C.R., WRAY, A.A. & MOIN, P. 1988 Eddies, streams and convergence zones in turbulent flows. *Rep. No.* CTR-S88. Center for Turbulence Research.

HWANG, J. & SUNG, H.J. 2018 Wall-attached structures of velocity fluctuations in a turbulent boundary layer. *J. Fluid Mech.* **856**, 958–983.

IRGENS, F. 2014 *Rheology and Non-Newtonian Fluids*. Springer.

JEONG, J. & HUSSAIN, F. 1995 On the identification of a vortex. *J. Fluid Mech.* **177**, 69–94.

JEONG, J., HUSSAIN, F., SCHOPPA, W. & KIM, J. 1997 Coherent structures near the wall in a turbulent channel flow. *J. Fluid Mech.* **332**, 185–214.

JIMÉNEZ, J. 1994 On the structure and control of near wall turbulence. *Phys. Fluids* **6**, 944–953.

JIMÉNEZ, J. 2013 Near-wall turbulence. *Phys. Fluids* **25**, 101302.

JIMÉNEZ, J., ÁLAMO, J.C.D. & FLORES, O. 2004 The large-scale dynamics of near-wall turbulence. *J. Fluid Mech.* **505**, 179–199.

JIMÉNEZ, J. & MOIN, P. 1991 The minimal flow unit in near-wall turbulence. *J. Fluid Mech.* **225**, 213–240.

JIMÉNEZ, J. & PINELLI, A. 1999 The autonomous cycle of near-wall turbulence. *J. Fluid Mech.* **389**, 355–359.

KARNIADAKIS, G.E. & CHOI, K. -S. 2003 Mechanisms of transverse motions in turbulent wall flows. *Annu. Rev. Fluid Mech.* **35**, 45–62.

KIM, H.T., KLINE, S.J. & REYNOLDS, W.C. 1971 The production of turbulence near a smooth wall in a turbulent boundary layer. *J. Fluid Mech.* **50**, 133–160.

KIM, K., LI, C.-F., SURESHKUMAR, R., BALACHANDAR, S. & ADRIAN, R.J. 2007 Effects of polymer stresses on eddy structures in drag-reduced turbulent channel flow. *J. Fluid Mech.* **584**, 281–299.

KIM, K. & SURESHKUMAR, R. 2013 Spatiotemporal evolution of hairpin eddies, Reynolds stress, and polymer torque in polymer drag-reduced turbulent channel flows. *Phys. Rev.* E **87**, 063002.

KLINE, S.J., REYNOLDS, W.C., SCHRAUB, F.A. & RUNSTADLER, P.W. 1967 The structure of turbulent boundary layers. *J. Fluid Mech.* **30**, 741–773.

LEE, M.J., KIM, J. & MOIN, P. 1990 Structure of turbulence at high shear rate. *J. Fluid Mech.* **216**, 561–583.

LI, W. & GRAHAM, M.D. 2007 Polymer induced drag reduction in exact coherent structures of plane Poiseuille flow. *Phys. Fluids* **19**, 083101.

LIU, C., WANG, Y., YANG, Y. & DUAN, Z. 2016 New omega vortex identification method. *Sci. China-Phys. Mech. Astron.* **59**, 684711.

LOZANO-DURÁN, A., FLORES, O. & JIMÉNEZ, J. 2012 The three-dimensional structure of momentum transfer in turbulent channels. *J. Fluid Mech.* **694**, 100–130.

LUMLEY, J.L. & NEWMAN, G.R. 1977 The return to isotropy of homogeneous turbulence. *J. Fluid Mech.* **82**, 161–178.

MANSOUR, N.N., KIM, J. & MOIN, P. 1988 Reynolds-stress and dissipation-rate budgets in a turbulent channel flow. *J. Fluid Mech.* **194**, 15–44.

MOISY, F. & JIMÉNEZ, J. 2004 Geometry and clustering of intense structures in isotropic turbulence. *J. Fluid Mech.* **513**, 111–133.

MOSER, R.D. & MOIN, P. 1984 Direct numerical simulation of curved turbulent channel flow. *NASA Tech. Rep.* TM 85974. Stanford University.

NAGAOSA, R. & HANDLER, R.A. 2003 Statistical analysis of coherent vortices near a free surface in a fully developed turbulence. *Phys. Fluids* **15**, 375–394.

OLDAKER, D.K. & TIEDERMAN, W.G. 1977 Spatial structure of the viscous sublayer in drag-reducing channel flows. *Phys. Fluids* **20**, S133.

PARK, J.T., MANNHEIMER, R.J., GRIMLEY, T.A. & MORROW, T.B. 1989 Pipe flow measurements of a transparent non-Newtonian slurry. *Trans. ASME J. Fluids Engng* **11**, 331–336.

PEREIRA, A.S. & PINHO, F.T. 1994 Turbulent pipe flow characteristics of low molecular weight polymer solutions. *J. Non-Newtonian Fluid Mech.* **55**, 321–344.

PINHO, F.T. & WHITELAW, J.H. 1990 Flow of non-Newtonian fluids in a pipe. *J. Non-Newtonian Fluid Mech.* **34**, 129–144.

POPE, S.B. 2000 *Turbulent Flows*. Cambridge University Press.

PTASINSKI, P.K., BOERSMA, B.J., NIEUWSTADT, F.T.M., HULSEN, M.A., VAN DER BRULE, B.H.A.A. & HUNT, J.C.R. 2003 Turbulent channel flow near maximum drag reduction: simulations, experiments and mechanisms. *J. Fluid Mech.* **490**, 251–291.

PTASINSKI, P.K., NIEUWSTADT, F.T.M., VAN DER BRULE, B.H.A.A. & HULSEN, M.A. 2001 Experiments in turbulent pipe flow with polymer additives at maximum drag reduction. *Flow Turbul. Combust.* **66**, 159–182.

ROBINSON, S.K. 1991 Coherent motions in the turbulent boundary layer. *Annu. Rev. Fluid Mech.* **23**, 601–639.

ROGERS, M.M. & MOIN, P. 1987 The structure of the vorticity field in homogeneous turbulent flows. *J. Fluid Mech.* **176**, 33–66.

RUDMAN, M. & BLACKBURN, H.M. 2003 Turbulent pipe flow of non-Newtonian fluids. In *Computational Fluid Dynamics 2002* (ed. S.W. Armfield, P. Morgan & K. Srinivas), pp. 687–692. Springer.

RUDMAN, M. & BLACKBURN, H.M. 2006 Direct numerical simulation of turbulent non-Newtonian flow using a spectral element method. *Appl. Math. Model.* **30**, 1229–1248.

RUDMAN, M., BLACKBURN, H.M., GRAHAM, L.J.W. & PULLUM, L. 2004 Turbulent pipe flow of shear-thinning fluids. *J. Non-Newtonian Fluid Mech.* **118**, 33–48.

SCHOPPA, W. & HUSSAIN, F. 2002 Coherent structure generation in near-wall turbulence. *J. Fluid Mech.* **453**, 57–108.

SILLERO, J. 2014 High Reynolds numbers turbulent boundary layers. PhD thesis, U. Politécnica Madrid.

SINGH, J., RUDMAN, M. & BLACKBURN, H.M. 2016 The rheology dependent region in turbulent pipe flow of a generalised Newtonian fluid. In *Proceedings of the 20th Australasian Fluid Mechanics Conference*. Perth, pp. 1–4. AFMS.

SINGH, J., RUDMAN, M. & BLACKBURN, H.M. 2017 The influence of shear-dependent rheology on turbulent pipe flow. *J. Fluid Mech.* **822**, 848–879.

SINGH, J., RUDMAN, M. & BLACKBURN, H.M. 2018 Reynolds number effects in pipe flow turbulence of generalized Newtonian fluids. *Phys. Rev. Fluids* **3**, 094607.

SJÄLANDER, M., JAHRE, M., TUFTE, G. & REISSMANN, N. 2019 EPIC: an energy-efficient, high-performance GPGPU computing research infrastructure. arXiv:1912.05848

SMITH, C.R. & METZLER, S.P. 1983 The characteristics of low-speed streaks in the near-wall region of a turbulent boundary layer. *J. Fluid Mech.* **129**, 27–54.

SOLSVIK, J. & JAKOBSEN, H.A. 2016 A review of the statistical turbulence theory required extending the population balance closure models to the entire spectrum of turbulence. *AIChE J.* **62**, 1795–1820.

SWEARINGEN, J.D. & BLACKWELDER, R.F. 1987 The growth and breakdown of streamwise vortices in the presence of a wall. *J. Fluid Mech.* **182**, 255–290.

TARDU, S.F. 1995 Active control of near-wall turbulence by local oscillating blowing. *J. Fluid Mech.* **439**, 217–253.

TARDU, S.F. & DOCHE, O. 2009 One-information suboptimal control repercussion on the fine structure of wall turbulence. *Comput. Fluids* **38**, 637–647.

WALLACE, J.M., ECKELMANN, H. & BRODKEY, R.S. 1972 The wall region in turbulent shear flow. *J. Fluid Mech.* **54**, 39–48.

WARHOLIC, M.D., MASSAH, H. & HANRATTY, T.J. 1999 Influence of drag-reducing polymers on turbulence: effects of Reynolds number, concentration and mixing. *Exp. Fluids* **27**, 461–472.

WHITE, C.M. & MUNGAL, M.G. 2008 Mechanics and prediction of turbulent drag reduction with polymer additives. *Annu. Rev. Fluid Mech* **40**, 235–256.

WILLMARTH, W.W. & LU, S.S. 1972 Structure of the Reynolds stress near the wall. *J. Fluid Mech.* **55**, 65–92.

ZHAO, L.H., ANDERSSON, H.I. & GILLISSEN, J.J.J. 2010 Turbulence modulation and drag reduction by spherical particles. *Phys. Fluids* **22**, 081702.

ZHOU, J., ADRIAN, R.J., BALACHANDAR, S. & KENDALL, T.M. 1999 Mechanisms for generating coherent packets of hairpin vortices in channel flow. *J. Fluid Mech.* **387**, 353–396.

Paper III

Velocity–vorticity correlations and the four-layer regime in turbulent channel flow of generalized Newtonian fluids

Arturo A. Arosemena and Jannike Solsvik

Eur. J. Mech. B Fluids **91**, 1–8 (2022)

European Journal of Mechanics / B Fluids 91 (2022) 1–8

Contents lists available at ScienceDirect

European Journal of Mechanics / B Fluids

journal homepage: www.elsevier.com/locate/ejmflu

Velocity–vorticity correlations and the four-layer regime in turbulent channel flow of generalized Newtonian fluids

Arturo A. Arosemena, Jannike Solsvik *

Department of Chemical Engineering, Norwegian University of Science and Technology (NTNU), NO 7491, Trondheim, Norway

ARTICLE INFO

Article history:
Received 9 February 2021
Received in revised form 2 August 2021
Accepted 28 August 2021
Available online 20 September 2021

Keywords:
Turbulence
Wall-bounded flow
Generalized Newtonian fluids
Low Reynolds number
Velocity–vorticity correlations
Four-layer dynamical regime

ABSTRACT

The data of Arosemena et al. (2021), consisting of turbulent channel flow simulations of generalized Newtonian (GN) fluids, are considered to study the effects of shear-dependent rheology on the nonzero velocity–vorticity correlations and the mean dynamics. In the near-wall region and compared to Newtonian channel flow, the velocity–vorticity products contributing to the turbulent inertia term decrease/increase with shear-thinning/thickening fluid behaviour suggesting that with e.g. shear-thinning rheology, the sublayer streaks are more stable, the near-wall vortical motions are dampened and there is a narrower range of turbulent length scales. The mean momentum balance analysis, on the other hand, revealed that the four-layer structure first recognized by Wei et al. (2005a) remains for all GN fluids and that the shear-dependent rheology only seems to influence the location of the layers. For instance, with shear-thinning behaviour, layers II and III are thicker and there is an increase in the importance of the viscous forces in these intermediate layers. The influence of shear-thinning/thickening fluid behaviour on the extent of the layers II and III is found remarkably similar to an increase/decrease of the Reynolds number for Newtonian channel flow. These findings suggest that the shear-dependent rheology should also be taken into account for proper scaling of the intermediate layers. A potential length scale factor is proposed and its suitability is tested.

1. Introduction

Turbulence is ubiquitous in nature and many man-made processes. Wall-bounded shear flows, such as boundary layers and pressure-driven pipes and channels, despite their simplicity in terms of geometrical configuration, are important reference flows for several technological applications. Consider, for instance, drag-related studies for novel designs of vehicles propelled in air and water, or the energy-budget analyses for a new generation of pipelines in the transport of gas and fuel within the petroleum industry.

Control of turbulence in wall-bounded flows for drag reduction, entrainment of particles or mixing purposes has concerned engineers and applied physicists for decades. The time-averaged form of the momentum equation differs from its instantaneous form since it involves a turbulence interaction term consisting of gradients of the net momentum flux $\rho u_i'$ by the macroscopic velocity fluctuations u_j'; here ρ is the density of the fluid. In an incompressible turbulent flow, the gradient of the turbulent or Reynolds stresses, $\partial\left(\overline{u_i'u_j'}\right)/\partial x_j$, can be rewritten as (see e.g. Hinze [1], Tardu [2])

$$\frac{\partial}{\partial x_j}\left(\overline{u_i'u_j'}\right) = \overline{u_j'\frac{\partial u_i'}{\partial x_j}} - \overline{u_j'\frac{\partial u_j'}{\partial x_i}} + \overline{u_j'\frac{\partial u_j'}{\partial x_i}} = -\overline{u_j'\omega_k'}\varepsilon_{ijk} + \frac{\partial}{\partial x_i}\left(\frac{\overline{u_j'u_j'}}{2}\right). \tag{1}$$

In the previous equation, mean and fluctuating variables are identified by $\overline{(\,)}$ and $(\,)'$, respectively, x_i and ω_i denote the spatial-Cartesian coordinates and the vorticity field, respectively, and ε_{ijk} is the alternation or Levi-Civita tensor. Note that, in Eq. (1), $\omega_k' = -\varepsilon_{ijk}\partial u_i'/\partial x_j$. Here, when index notation is used, suffix i (or any other suffix) takes the value 1,2 or 3 to represent the x, y or z component, respectively; i.e. $(x_1, x_2, x_3) = (x, y, z)$, $(u_1, u_2, u_3) = (u_x, u_y, u_z)$ and $(\omega_1, \omega_2, \omega_3) = (\omega_x, \omega_y, \omega_z)$, and a repeated index implies summation from x to z. Also, note that, we have adopted the common approach to denote the velocity correlation $\overline{u_i'u_j'}$ as the Reynolds stress tensor, which is not strictly correct.

For canonical channel flow, the $i = 1$–3 components of Eq. (1) read

$$-\frac{\partial}{\partial y}\left(\overline{u_x'u_y'}\right) = \overline{u_y'\omega_z'} - \overline{u_z'\omega_y'}, \tag{2}$$

* Corresponding author.
E-mail addresses: arturo.arosemena@ntnu.no (A.A. Arosemena), jannike.solsvik@ntnu.no (J. Solsvik).

https://doi.org/10.1016/j.euromechflu.2021.08.006

$$\frac{\partial k}{\partial y} = \overline{u'_z\omega'_x} - \overline{u'_x\omega'_z} + \frac{\partial}{\partial y}\left(\overline{u'_y u'_y}\right), \tag{3}$$

and

$$0 = \overline{u'_y\omega'_x} - \overline{u'_x\omega'_y}, \tag{4}$$

respectively. Here $k = \overline{u'_i u'_i}/2$ is the turbulent kinetic energy. For boundary layer, Eqs. (2)–(4) are approximately valid since the gradients $\partial(\,)/\partial x$ are small but nonzero and become smaller relative to the other terms with increasing Reynolds number (Klewicki [3]). Thus, insight into how the stress gradients are generated can also be gained through the velocity–vorticity correlation terms, i.e., $\overline{u'_j\omega'_k}$.

Experimental and numerical investigations related to the velocity–vorticity products, and to turbulent–vorticity transport in general, are quite scarce (Eyink [4]). The studies by Klewicki and co-workers [3,5–8] are notable exceptions. Klewicki [3] used Eq. (1) and the approximate formulas of Phillips [9] to deduce some unmeasured (at that point) velocity–vorticity correlation profiles from available experimental data. The same study (Klewicki [3]) also showed that contributions to the gradients of the diagonal Reynolds stresses are dominated by the correlations involving the z-vorticity component whilst the contributions to the gradient of the off-diagonal stresses are shared between the correlations involving the z- and y-vorticity components. Klewicki et al. [5] considered zero-pressure-gradient boundary layer measurements to obtain the velocity–vorticity correlations and to investigate the ω'_z motion contributions to the gradients of the turbulent stresses and its possible relation to sweep and ejection events (Willmarth and Lu [10]; Wallace et al. [11]) in connection with important contributions to the turbulent diffusion term in the budget for $\overline{u'_x u'_x}$. Priyadarshana et al. [6] reported a number of statistics, based on laboratory data, related to the velocity–vorticity products including premultiplied cospectra and correlation coefficients and observed their sensitivity to Reynolds number as well to wall roughness. Klewicki et al. [7] pondered Eq. (2) in the context of the mean momentum balance-based layer structure for boundary layer, pipe and channel flows and their scaling behaviour (see Fife et al. [12,13]; Wei et al. [14,15]; Klewicki et al. [16,17]; Chin et al. [18]; White et al. [19], among others).

Afterwards, Morrill-Winter and Klewicki [8] focused on the $\overline{u'_y\omega'_z}$ correlation and its scale separation also in boundary layers, occurring as a function of both the y-coordinate and the Reynolds number, finding that the scaling of motions affiliated with the turbulent inertia term, i.e. $\partial\left(\overline{u'_x u'_y}\right)/\partial y$, is greater than $\mathcal{O}(\mu/(\rho u_\tau))$ in the region $y^+ = y u_\tau/(\mu/\rho) \leq 40$; where μ is the fluid's dynamic viscosity and $u_\tau = \sqrt{\overline{\tau}_w/\rho}$ is the frictional velocity defined in terms of the mean shear stress at the wall, $\overline{\tau}_w$. Aside from Klewicki and co-workers, it is worth mentioning the letter of Yoon et al. [20] who analysed the contributions of the velocity–vorticity correlations to the frictional drag in wall-bounded flows and found them dominant over the other contributions due to viscous and inhomogeneous effects in the x-direction (for boundary layer).

The aforementioned studies, concerning the velocity–vorticity products, are mostly about canonical wall-bounded flows of Newtonian fluids despite that for many industrial applications, the working fluid is non-Newtonian. The purpose of this paper is to explore the effects of shear-dependent rheology on the velocity–vorticity correlations in a turbulent channel flow and the underlying physical implications. As mentioned before, there are but a few studies regarding the velocity–vorticity interaction terms and to the authors' knowledge, none where the effect of having non-constant, nonelastic viscosity is considered. Moreover, our interest not only lays in the changes of the correlations but also in how such changes affect the net mean effect of turbulent inertia and the resulting mean momentum balance in the wall-bounded flow. The study of the redistribution of mean momentum clarifies the influence of shear-dependent rheology over the mean dynamics and potentially leads to a proper scaling of this type of non-Newtonian channel flow.

2. The numerical experiments

Velocity–vorticity correlations and other statistics are computed using data from turbulent channel flow simulations of GN fluids at a frictional Reynolds number, $Re_\tau = \rho u_\tau h/\mu_w = 180$; h being the channel half-width and μ_w the nominal wall viscosity based on $\overline{\tau}_w$ and the considered rheology model (see Draad et al. [21]; Ptasinski et al. [22]). GN fluids are purely viscous, time independent fluids which stress tensor due to viscous effects, $\tau_{ij_{\text{vis}}}$, is given by

$$\tau_{ij_{\text{vis}}} = 2\mu \mathrm{S}_{ij}, \tag{5}$$

where $\mu = \mu(\dot{\gamma})$ is the apparent dynamic viscosity solely depending on the strain rate $\dot{\gamma} = \left(2\mathrm{S}_{ij}\mathrm{S}_{ji}\right)^{1/2}$ and $\mathrm{S}_{ij} = \left(\partial u_i/\partial x_j + \partial u_j/\partial x_i\right)/2$ is the strain rate tensor. The rheology of a GN fluid may be reproduced through different models such as the power-law (PL), Spriggs or Carreau fluid models (see e.g. Irgens [23]) which relate the apparent viscosity to the strain rate through a constitutive equation. The choice of a particular model has little effect on the turbulent flow predictions if high strain rate rheology (typical in turbulent regime near walls) is used in the rheology characterization (Singh et al. [24]).

The direct numerical simulations (DNS) are performed using a FORTRAN 77 code called CALC-LES (Davidson and Peng [25]; Davidson [26]) which solves the incompressible form of the momentum and continuity equations through a finite volume method on a collocated grid, using central differencing approximations in space and the Crank–Nicolson scheme in time. The numerical procedure consists of an implicit, two-time stepping technique where the Poisson's equation for the pressure is solved with an efficient multigrid method (Emvin [27]). Regarding boundary conditions, in the wall-normal direction (y-coordinate) physical (no-slip, impermeable) top and bottom walls are imposed and periodicity is set in the streamwise/longitudinal (x-coordinate) and spanwise/lateral (z-coordinate) directions of the computational box.

In the DNS, to avoid unphysical results at large and low strain rate values which may arise with the simpler PL fluid model, the rheology is incorporated through the Carreau model, i.e.,

$$\mu = \mu_\infty + (\mu_0 - \mu_\infty)\left[1 + (\Lambda\dot{\gamma})^2\right]^{(\alpha-1)/2}, \tag{6}$$

where μ_∞ and μ_0 are the 'infinite' and 'zero' shear rate viscosities, respectively, Λ is a time constant and α is the flow index which for shear-thinning/thickening is to be less/more than unity. Here, the different parameters are adjusted to attain the target Re_τ according to the set nominal wall viscosity. Fig. 1 shows the mean (averaged in time and in the spatially homogeneous directions) viscosity for the considered shear-thinning/pseudoplastic (P180), Newtonian (N180) and shear-thickening/dilatant (D180) fluids cases. As evidenced by Eq. (6), shear-thinning/thickening refers to a fluid exhibiting a decrease/increase in its apparent fluid viscosity with increasing strain rate. It is remarked that at the given flow conditions and within the region where viscous effects are likely dominant, the increase/decrease of local viscosity with shear-thinning/thickening behaviour is (on average) less than 50% of the approximate value at the wall. Such increase/decrease is comparable to what has been reported in previous studies

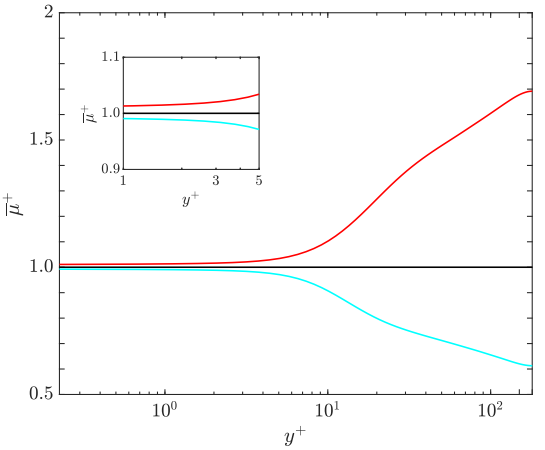

Fig. 1. Mean viscosity profile, $\overline{\mu}^+ = \mu/\mu_w$, vs. y^+. Here, $\mu_\infty/\mu_0 = 1 \times 10^{-3}$, $\mu_0^+ \approx 1.782/0.561$ for fluid case P180/D180, $\Lambda^+ = 0.1$ and α is set to 0.8, 1.0 and 1.2 for fluid cases P180, N180 and D180, respectively. Profiles corresponding to P180, N180 and D180 are identified by red, black and cyan colours, respectively. (For interpretation of the references to colour in this figure legend, the reader is referred to the web version of this article.)

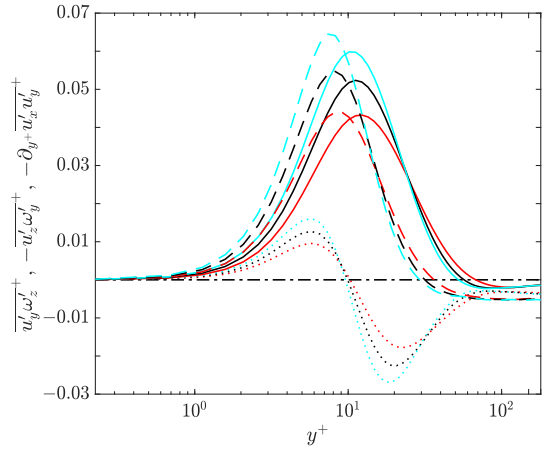

Fig. 2. Contributions to the wall-normal gradient of the Reynolds stress, $-\partial\left(\overline{u_x'u_y'}^+\right)/\partial y^+$, and wall-normal gradient of the Reynolds stress vs. y^+. Line styles "–" and "· · ·" are used to identify contributions from the correlations $-\overline{u_z'\omega_y'}^+$ and $\overline{u_y'\omega_z'}^+$, respectively, whereas line style "- - -" is used for the gradient $-\partial_{y^+}\overline{u_x'u_y'}^+ = -\partial\left(\overline{u_x'u_y'}^+\right)/\partial y^+$ and line style "- · -" for the zero-crossing line. Profiles corresponding to fluid cases P180, N180 and D180 are identified by red, black and cyan colours, respectively. (For interpretation of the references to colour in this figure legend, the reader is referred to the web version of this article.)

(see viscosity rheograms in e.g. Rudman et al. [28]; Gavrilov and Rudyak [29]; Singh et al. [30]). Note as well that, the channel flow is pressure-driven and that all turbulent scales have been properly resolved for the simulations of the three considered GN fluid cases. For further details regarding the computational set-up and the used database, we refer to Arosemena et al. [31].

In the following sections, most statistics are given in 'wall' units, $(\,)^+$, using $\mu_w, u_\tau, (\mu_w/\rho)/u_\tau, (\mu_w/\rho)/u_\tau^2$ and ρu_τ^2 as characteristic viscosity, velocity, length, time and stress, respectively.

3. Velocity–vorticity correlations

Figs. 2 and 3 show the contributions to the wall-normal gradient of the nonzero Reynolds stresses, i.e., terms on the right-hand side of Eqs. (2) and (3), respectively. As it can be seen from Fig. 2, for the considered GN fluid cases, contributions to the gradient of the off-diagonal component, $\partial\left(\overline{u_x'u_y'}^+\right)/\partial y^+$, are shared by correlations involving both ω_z' and ω_y'; the interaction term $-\overline{u_z'\omega_y'}$, in particular, appears to dominate the most within the region $y^+ \lesssim 30$. The relative contributions of these correlations to the turbulent inertia term are clarified by taking their ratio; see Fig. 4. The figure also displays the wall-normal position, y_m^+, at which a maximum is attained for the Reynolds shear stress, i.e., the zero-crossing point of its wall-normal gradient. As seen from Fig. 4, at y_m^+ the ratio $\overline{u_y'\omega_z'}/\overline{u_z'\omega_y'} \approx 1$ whereas prior/beyond y_m^+, the correlation $\overline{u_y'\omega_z'}$ becomes smaller/larger than the $-\overline{u_z'\omega_y'}$ term. On the other hand, Fig. 3 reveals that, for all considered GN fluid cases, contributions to the gradient of the diagonal stresses are dominated by the correlation involving ω_z'. The interaction terms appearing in Eq. (4), found to be several orders of magnitude less than $\overline{u_z'\omega_x'}$ which is the smallest velocity–vorticity product studied so far (see Fig. 3), are considered approximately zero. Thus, for all cases, the wall-normal and streamwise velocity components appear to be uncorrelated to the longitudinal and wall-normal vorticity components, respectively.

The velocity–vorticity correlations presented in Fig. 2 are particularly important since their difference not only expresses the

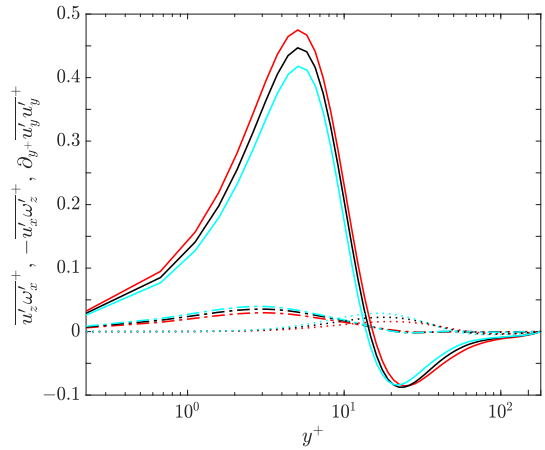

Fig. 3. Contributions to the wall-normal gradient of the turbulent kinetic energy, $\partial k^+/\partial y^+$, vs. y^+. Line styles "–", "- · -" and "· · ·" are used to identify contributions from the correlations $-\overline{u_x'\omega_z'}^+$, $\overline{u_z'\omega_x'}^+$ and the gradient $\partial_{y^+}\overline{u_y'u_y'}^+ = \partial\left(\overline{u_y'u_y'}^+\right)/\partial y^+$, respectively. Profiles corresponding to fluid cases P180, N180 and D180 are identified by red, black and cyan colours, respectively. (For interpretation of the references to colour in this figure legend, the reader is referred to the web version of this article.)

mean effect of turbulent inertia in the differential statement of mean dynamics (Morrill-Winter and Klewicki [8]) but also, their cross-stream gradients are the source or sink for the mean vorticity (Tennekes and Lumley [32]). The correlation $\overline{u_y'\omega_z'}$ is related to the advective transport, central to Taylor's mixing-length theory of vorticity transfer [33], and it has been shown to be particularly relevant for the development of the logarithmic

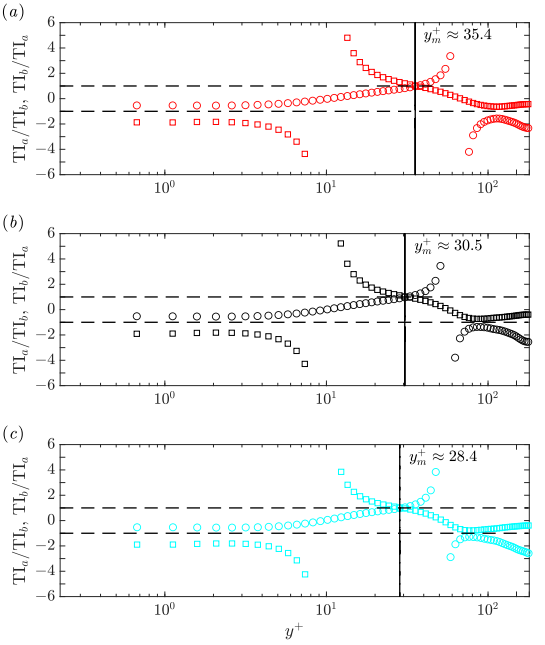

Fig. 4. Ratios of the velocity–vorticity correlations, $\mathrm{Tl}_a/\mathrm{Tl}_b$ and $\mathrm{Tl}_b/\mathrm{Tl}_a$, vs. y^+; here $\mathrm{Tl}_a = \overline{u_y'\omega_z'}$ and $\mathrm{Tl}_b = \overline{u_z'\omega_y'}$. In (*a*)-(*c*), profiles corresponding to fluid cases P180, N180 and D180 are identified by red, black and cyan coloured markers, respectively. The marker 'o' is used for the $\mathrm{Tl}_a/\mathrm{Tl}_b$ ratio whilst the marker '□' is used for the $\mathrm{Tl}_b/\mathrm{Tl}_a$ ratio. (For interpretation of the references to colour in this figure legend, the reader is referred to the web version of this article.)

mean velocity profile (Klewicki et al. [16]) once the leading order terms in the mean dynamics are purely inertial (Wei et al. [14]). On the other hand, the correlation $\overline{u_z'\omega_y'}$ is related to change-of-scale effects (Tennekes and Lumley [32]), constitute a gain (or loss) of mean vorticity in the channel flow—note that total production of $\overline{\omega}_z$ is given by $\overline{\omega_j'\partial u_z'/\partial x_j} = \partial\left(\overline{\omega_j' u_z'}\right)/\partial x_j$ since ω_j' is divergenceless— and when it is not negligible implies that the mixing-length theory is not an appropriate approximation. In Fig. 2, the peaks in the correlations occur near $y^+ \approx 5-10$ where the wall-normal gradients of $-\overline{u_x'u_y'}^+$ are the largest. Also, close to the peak values and with shear-thinning/thickening fluid rheology, the absolute value of the correlations decrease/increase which is consistent with the overall decrease/increase of turbulent shear stress and its wall-normal gradient with shear-thinning/thickening fluid behaviour (see the mean shear stress budget in e.g. Singh et al. [30]). Here, an interesting observation is that both velocity–vorticity products are affected by the shear-dependent rheology. This is in contrast with the observed changes due to Reynolds number for Newtonian wall-bounded flow where only the correlation $\overline{u_z'\omega_y'}$ appears to be Reynolds-number-dependent (Chin et al. [18]). Meanwhile, unsurprisingly and as shown in Fig. 3, the principal contribution to $\partial k^+/\partial y^+$ also attains its maximum close to the edge of the viscous sublayer, $y^+ \approx 5$, and increases/decreases with shear-thinning/thickening fluid behaviour. This interaction term involves u_x'—largest velocity fluctuation— and ω_z'—important source for the sustainment of turbulence—which intensities are known to increase/decrease with shear-thinning/thickening fluid rheology in the very near-wall region (see e.g. Arosemena et al. [31]).

At this point, we would like to highlight the (potential) physical implications of changes observed with shear-dependent rheology in the velocity–vorticity correlations contributing to the turbulent inertia term. The region of positive $\overline{u_y'\omega_z'}$, seen up to $y^+ \approx 10$ (compared to the Newtonian case, actual zero-crossing point slightly increases/decreases with shear-thinning/thickening behaviour as displayed in Fig. 2), is believed to be related to the outward motion of sublayer streaks (Klewicki et al. [5]) whereas the region of negative $\overline{u_y'\omega_z'}$, after $y^+ \approx 10$, is believed to be due to the vertical advection of detached hairpin-like vortex heads; likely important for the near-wall self-sustaining process of vortical motion (Falco et al. [34]; Klewicki et al. [5]). In consequence, compared to a Newtonian fluid and with e.g. shear-thinning fluid behaviour, the suppression of $\overline{u_y'\omega_z'}$ across the channel seems to imply that the sublayer streaks are more stable, i.e., less prone to be lifted-up, oscillate and eventually break-up during a 'bursting' process (Kim et al. [35]; Offen and Kline [36]) and that the strength of the near-wall vortical motions is reduced. See contours of instantaneous streamwise velocity fluctuations, u_x', in e.g. Singh et al. [37]; Arosemena et al. [31], where coarser structures with less 'streakiness', more streamwise coherence and larger spanwise separation are observed with shear-thinning rheology and Arosemena et al. [31], where the intensity of the streamwise vorticity component is reported to decrease—for the shear-thinning fluid— when compared to the Newtonian base case.

Related to one of the previous remarks, it is worth comparing the changes experienced by the near-wall streaks in Newtonian channel flow due to a decrease in Reynolds number with those attributed to shear-thinning rheology. In Newtonian fluids where the flow is wall-bounded, the streaks are known to keep a relatively constant spanwise spacing (see e.g. Klewicki et al. [38]; Cossu and Hwang [39]) but the bursting periods are longer (see e.g. Jímenez et al. [40]). The fact that, for a Newtonian fluid, the bursting period seems to increase with decreasing Re_τ does not imply an increase in stability in the same sense as for shear-thinning behaviour, i.e. structures less prone to be lifted-up, but that perhaps due to the lessened turbulence intensity (see e.g. Lee and Moser [41]), the streaks are likely to persist over longer periods of time. Furthermore, as aforementioned, the correlation associated with the outward motion of the streaks ($\overline{u_y'\omega_z'}$) appears nearly invariant to changes of Reynolds number. On the other hand, with respect to the term $-\overline{u_z'\omega_y'}$ associated with the modulation (change-of-scale effect) of near-wall motions, its overall attenuation—for the shear-thinning fluid case— is a clear indicative of a decrease in the range of length scales in the turbulent channel flow. See the previously mentioned contours of u_x' in Singh et al. [37]; Arosemena et al. [31], where a narrower range of turbulent eddy sizes is observed for the shear-thinning fluid compared to the Newtonian fluid and also, Section 4.1; about the hierarchy of length scales.

Finally, it would be wise to discuss the possible Reynolds number dependency of the velocity–vorticity correlations and related statistics. At least up to moderate frictional Reynolds numbers ($Re_\tau = 750$), contribution of viscosity fluctuations (in e.g. the mean shear budget or the turbulent kinetic energy budget) are known to remain relatively small and consistent trends in the different statistics (including the Reynolds shear stress which wall-normal gradient is directly related to the terms $\overline{u_y'\omega_z'}$ and $-\overline{u_z'\omega_y'}$) are seen when comparing Newtonian and shear-dependent fluid cases (Singh et al. [37]). In consequence, at least up to moderate Reynolds numbers, a similar Re_τ dependency (for the different statistics) is deem probable for all GN fluid cases. In other words, it is likely that for a particular GN fluid, an increase in Reynolds number would lead to an invariant $\overline{u_y'\omega_z'}$-profile whereas the correlation $-\overline{u_z'\omega_y'}$ is expected to display a

similar Reynolds number dependency to the turbulent inertia term as reported by Chin et al. [18] for Newtonian wall-bounded flow. It is emphasized that this last statement elucidates what the authors find probable and should be taken with caution. Definite evidence about the Reynolds number dependency of the velocity–vorticity products for GN fluids in wall-bounded turbulent flows requires actual computation of these profiles for a wide range of Reynolds numbers and it is proposed as further work.

4. Streamwise mean momentum balance and the four-layer structure

Based on the properties of the mean velocity profile and the mean shear stress field, turbulent boundary layer, channel and pipe flows are commonly scaled according to identified regions consisting of different layers (see e.g. Tennekes and Lumley [32]; Pope [42]): there is an inner layer region; comprised by a viscous sublayer $\left(y^+ \lesssim 5\right)$, a buffer layer region $\left(5 \lesssim y^+ \lesssim 30\right)$, a log-law region $\left(30 \lesssim y^+ \lesssim 0.15h^+\right)$, and a remaining outer region. There is some discrepancy in the location of the layers reported by different authors and in general, the logarithmic-law layer, overlapping the inner and outer regions, is more distinct as the Reynolds number increases (see e.g. Smits et al. [43]; Marusic et al. [44]). Wei et al. [14] remarked that it is the gradients of the stresses and not the stresses themselves that are the relevant dynamical quantities and proposed an alternative layer structure directly based on the mean dynamics described by the time-averaged momentum balance. As a framework, before discussing the mean dynamics for the shear-dependent cases, we briefly outline the mean momentum equation analysis for turbulent channel flow of GN fluids which (as presented) is indistinct to the one of Newtonian channel and pipe flows and fairly similar to the one of zero-pressure-gradient turbulent boundary layer; see for instance Fife et al. [12]; Wei et al. [14]; Klewicki et al. [17]; Chin et al. [18], among others.

For a statistically converged, pressure-driven, turbulent channel flow of a GN fluid, the streamwise mean momentum equation reads

$$\frac{\partial}{\partial y^+}\left(\overline{u_x'u_y'}\right)^+ = \frac{1}{Re_\tau} + \frac{\partial}{\partial y^+}\left(\overline{\tau}_{xy_{\text{vis}}}^+\right), \tag{7}$$

since the mean continuity equation and the y-component of the mean momentum equation lead to $-\partial\overline{p}^+/\partial x^+ = -\mathrm{d}\overline{p}_w^+/\mathrm{d}x^+ = \overline{\tau}_w^+/h^+$ which by definition is equivalent to $1/Re_\tau$. Here p denotes pressure and the subscript 'w' refers to values at the bottom wall of the channel. In general, for a GN fluid, the total mean viscous shear stress is given by $\overline{\tau}_{xy_{\text{vis}}}^+ = 2\left[\overline{\mu}^+\overline{S}_{xy}^+ + \left(\overline{\mu' S_{xy}'}\right)^+\right]$; i.e., $\overline{\tau}_{xy_{\text{vis}}}^+$ may also include a contribution arising due to viscosity fluctuations. In terms of simpler notation, Eq. (7) can be rewritten as

$$\text{TI} = \text{PG} + \text{VF}. \tag{8}$$

Hence, for the channel flow, the mean statement of dynamics indicates that the net effect of turbulent inertia (TI) is balanced by the sum of the mean pressure gradient (PG) and net viscous force (VF). Based on Eq. (8), for $Re_\tau \geq 180$, Wei et al. [14] noted that indeed the three effects must all be in balance, or have at least two non-negligible terms in balance, and recognized that the mean dynamical balance can be described by a four-layer structure: layer I, $|\text{PG}| \approx |\text{VF}| \gg |\text{TI}|$; layer II, $|\text{VF}| \approx |\text{TI}| \gg |\text{PG}|$; layer III, $|\text{PG}| \approx |\text{VF}| \approx |\text{TI}|$; layer IV, $|\text{PG}| \approx |\text{TI}| \gg |\text{VF}|$.

Fig. 5, displaying the terms appearing in Eq. (8), reveals the mean dynamics for turbulent channel flow of the considered GN fluid cases. In the figure, the net mean viscous force is split into $\text{VF}^{(\text{N})} = 2\left(\overline{\mu}^+\overline{S}_{xy}^+\right)$ and $\text{VF}^{(\text{NN})} = 2\left(\overline{\mu' S_{xy}'}\right)^+$, being the last term non-zero only for the shear-dependent cases since it arises due to fluctuations in viscosity. As seen from Fig. 5, in the near-wall region and for all cases, the turbulent inertia term is balanced out by $\text{VF}^{(\text{N})}$ with an error $\text{VF}^{(\text{NN})} + \text{PG}$. Furthermore, as mentioned while discussing Fig. 2, with shear-thinning/thickening fluid behaviour the peak value in $-\text{TI}$ is suppressed/enhanced and moves slightly to the right/left in comparison with the Newtonian case. Also, as already seen from Fig. 4, the zero-crossing point of the turbulent inertia term (y_m^+) appears to be affected by the shear-dependent rheology; with shear-thinning/thickening, the wall-normal position at which $\text{TI} = 0$ occurs further/nearer the wall in comparison with the Newtonian fluid case. On the other hand, the term arising due to fluctuation in viscosity $\left(\text{VF}^{(\text{NN})}\right)$ peaks in magnitude near the upper edge of the traditional viscous sublayer, i.e. $y^+ \approx 5$, and seems to be in favour/against $-\text{TI}$ for shear-thinning/thickening fluid rheology. Nonetheless, $\text{VF}^{(\text{NN})}$ approaches zero as we move further away from the wall and, across the channel, its magnitude is always smaller than the magnitude of the normalized, constant, driving pressure gradient. In summary, the inherent character of the mean dynamics seems to remain the same for all GN fluids and the shear-dependent rheology appears to only influence the location of the regions depending on the leading-order balance between the terms in Eq. (8).

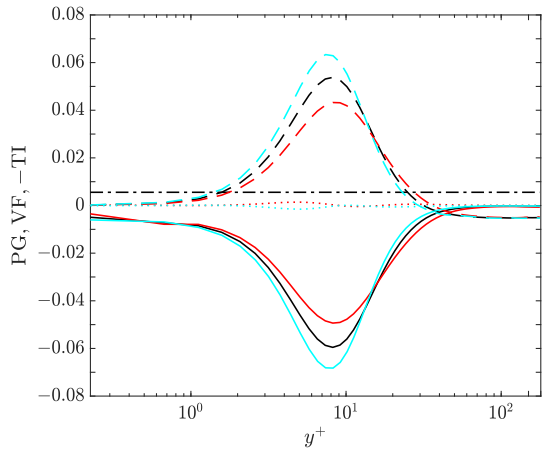

Fig. 5. Distribution of stress gradients in the Reynolds-averaged streamwise momentum equation vs. y^+. Line styles "- · -" , "—", "· · ·" and "- - -" are used to identify PG, $\text{VF}^{(\text{N})}$, $\text{VF}^{(\text{NN})}$ and −TI, respectively. Profiles corresponding to fluid cases P180, N180 and D180 are identified by red, black and cyan colours, respectively. (For interpretation of the references to colour in this figure legend, the reader is referred to the web version of this article.)

Following Wei et al. [14], the regions corresponding to the four-layer structure are revealed through the $-\text{VF}/\text{TI}$ ratio shown in Fig. 6. The inner viscous/pressure-gradient balance layer (layer I), extending from the wall up to $y^+ \approx 3$, does not differ in a significant manner from the traditional viscous sublayer and appears to be unaffected by the shear-dependent rheology in terms of its physical extent but does display a larger $|\text{VF}/\text{TI}|$ ratio with shear-thinning fluid behaviour. At the outer edge of layer I, the ratio $-\text{VF}/\text{TI}$ approaches -1 and marks the beginning of the stress-gradient balance layer (layer II). Note that, at low Reynolds numbers for pressure-driven channel flow, the ratio of -1 is approached asymptotically, probably, due to a net diminishing effect of the associate surface flux of vorticity (Wei et al. [14]). Layer II extends up to a wall-normal position where the ratio $-\text{VF}/\text{TI}$ is less than -2 (Wei et al. [14]) and marks the start of

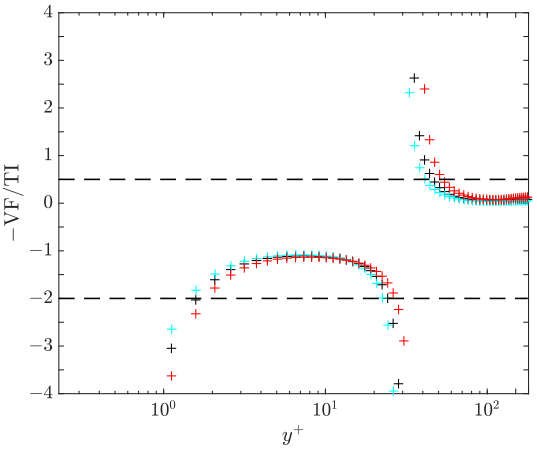

Fig. 6. Ratio of the mean viscous force to the mean effect of turbulent inertia, −VF/TI, vs. y^+. Profiles corresponding to fluid cases P180, N180 and D180 are identified by red, black and cyan coloured markers, respectively. (For interpretation of the references to colour in this figure legend, the reader is referred to the web version of this article.)

the viscous/pressure-gradient/inertial balance layer (layer III). In layer III, TI changes sign at y_m^+ and Eq. (8) undergoes a balance breaking and exchange of terms (Klewicki et al. [7]); i.e., in the mean force balance, the turbulent inertia starts to be of leading order instead of the mean viscous force (Morrill-Winter and Klewicki [8]). Finally, the inertial/pressure-gradient balance layer (layer IV) is attained when the ratio −VF/TI decreases to 0.5 (Wei et al. [14]) and marks the beginning of an inertial subrange where viscous forces can be neglected. As seen from Fig. 6, layers II and III appear to be thicker/thinner with shear-thinning/thickening fluid behaviour in comparison to the Newtonian case and thus, the influence of VF appears to increase/decrease up to wall-normal positions further away from/closer to the wall with shear-thinning/thickening rheology. Moreover, such behaviour is probably due to the local increase/decrease of viscosity as y^+ increases for the shear-thinning/thickening cases; see Fig. 1. This clearly contrasts with the results reported for viscoelastic channel flow (White et al. [19]); where, even for the low drag reduction regime (Warholic et al. [45]), the increase of importance in the viscous effects—compared to Newtonian channel flow and as we move further away from the wall— is attributed not to an increase in viscosity but to a diminishing importance of the inertial effects.

It is also worth remarking that the effect of shear-thinning/thickening rheology in the −VF/TI profile seems to be similar to an increase/decrease of the Reynolds number in the Newtonian case (see e.g. Klewicki et al. [17]) which suggests that proper scaling of the intermediate layers in turbulent channel flow of GN fluids should account for their shear-dependency. In Section 4.1, scaling concepts are applied to identify the (potential) appropriate length scales in the different regions and to gain further insight into the four-layer structure once the shear-dependent rheology is introduced. The analysis follows the conceptual framework used by Fife et al. [12,13] in which the stress gradient balance layers have a mathematical structure composed of a hierarchy of length scales and, where, the traditional inner and outer scales are simply the two extremes in a continuum of length scales.

4.1. The hierarchy of length scales

Consider Eq. (7) in the following convenient form

$$\frac{\mathrm{dV}}{\mathrm{dy}^+} + \frac{\mathrm{dT}}{\mathrm{dy}^+} + \epsilon^2 = 0, \tag{9}$$

where $\mathrm{V}\left(y^+\right) = \overline{\tau}_{xy_{\mathrm{vis}}}^+$, $\mathrm{T}\left(y^+\right) = -\overline{u_x' u_y'}$ and $\epsilon^2 = 1/Re_\tau$. Also, consider a mathematical construct, based on the Reynolds shear stress, defined as

$$\mathrm{T}^\beta\left(y^+\right) = \mathrm{T}\left(y^+\right) + \epsilon^2 y^+ - \beta y^+. \tag{10}$$

Here T^β is an adjusted Reynolds stress (in T^β, β is a superscript not an exponent) and β is a small positive number restricted to $\beta \leq \left[\max\left(\mathrm{dT}/\mathrm{dy}^+\right) + \epsilon^2\right]/C$; where the coefficient C is a number in the interval 5 to 20 (Fife et al. [12]). Note that, the function T^β satisfies

$$\frac{\mathrm{dT}^\beta}{\mathrm{dy}^+} = \frac{\mathrm{dT}}{\mathrm{dy}^+} + \epsilon^2 - \beta, \tag{11}$$

and thus, Eq. (9) can be rewritten as

$$\frac{\mathrm{dV}}{\mathrm{dy}^+} + \frac{\mathrm{dT}^\beta}{\mathrm{dy}^+} + \beta = 0. \tag{12}$$

As will be seen shortly, the introduction of T^β allow us to have an exact differential equation in rescaled variables with no explicit dependency on any parameter. Moreover, T^β has led to Eq. (12) expressing an approximate balance between its first two terms for an arbitrary (small) β-parameter. Such balance must be (eventually) broken, at a given y^+, and changes to another kind of balance where the three terms in Eq. (12) have the same order of magnitude (Fife et al. [12]; Fife [46]).

Proper scaling of Eq. (12)—in a given region—requires that the two derivatives are bounded and at least one of them cannot be too small. Through a transformation of differentials, such as

$$\mathrm{dy}^+ = \ell \mathrm{d}\hat{y}, \quad \mathrm{dV} = \phi \mathrm{d}\hat{\mathrm{V}}, \quad \mathrm{dT}^\beta = \delta \mathrm{d}\hat{\mathrm{T}}^{\hat{\beta}}, \tag{13}$$

it is possible to rescale the original variables into the new variables $\hat{y}$, $\hat{\mathrm{V}}$ and $\hat{\mathrm{T}}^{\hat{\beta}}$ which (potentially) represent most clearly and naturally the momentum balance within a certain subdomain of interest. The coefficients ℓ, ϕ and δ in the linear transformations are β-dependent. In consequence, with the use of the differential transformations (13), Eq. (12) is recast as

$$\left(\frac{\phi}{\ell}\right)\frac{\mathrm{d}\hat{\mathrm{V}}}{\mathrm{d}\hat{y}} + \left(\frac{\delta}{\ell}\right)\frac{\mathrm{d}\hat{\mathrm{T}}^{\hat{\beta}}}{\mathrm{d}\hat{y}} + \beta = 0. \tag{14}$$

A suitable scaling would render the previous differential equation (14) into a parameterless equation. This requires matching, in formal order of magnitude, between the two terms involving derivatives in Eq. (14) and the third term, β. Therefore, one can specify

$$\ell = \frac{\phi}{\beta}, \quad \delta = \phi. \tag{15}$$

As seen from Eq. (15), the criterion of equal order of magnitude, by itself, does not define uniquely the three scaling factors since, for a given β, one of them is still undetermined. A possible closure is found assuming that e.g. $\phi(\beta) = \beta^{-\sigma}$; where the parameter σ is an exponent (Fife [46]). Hence

$$\ell = \beta^{-(\sigma+1)}, \quad \delta = \phi = \beta^{-\sigma}. \tag{16}$$

If $\beta = \epsilon^2$, inner and outer length scaling are recovered for $\sigma = -1$ and $\sigma = 0$, respectively. The continuum of scales is between these two extreme cases, i.e., $\sigma \in [-1, 0]$ when $\beta = \epsilon^2$.

The intermediate or 'meso' layer III in Wei et al. [14] corresponds to $\sigma = -1/2$ and $\beta = \epsilon^2$. However, this mesolayer III is

Table 1
Scaling behaviour of the intermediate layer III for turbulent channel flow of GN fluids. Here, $\Delta y^+_{\mathrm{III}} = y^+_3 - y^+_2$; where y^+_2 and y^+_3 denote the beginning and end of mesolayer III.

Case	$\Delta y^+_{\mathrm{III}}$	$\mu^+\left(y^+_m\right)$	$\Delta y^+_{\mathrm{III}}/\sqrt{Re_\tau \mu^+\left(y^+_m\right)}$
D180	18.6	0.75	1.60
N180	22.1	1	1.65
P180	26.2	1.41	1.64

just one among many, in the sense that, different adjusted mesolayers can be constructed by replacing T by T^β and mesolayer III is just a particular case, where $\mathrm{T}^\beta = \mathrm{T}$, and which approximate centre is at the location $y^+ = y^+_m$ where the balance breaking and exchange of leading-order terms in the streamwise mean momentum equation occurs (Fife et al. [12]). Note as well that, when $\beta = \epsilon^4$, $\sigma = -1/2$ and $\mathrm{T}^\beta \neq \mathrm{T}$ also corresponds to the outer length scaling case.

At this point, it is worth mentioning that the previous observations are valid for all GN fluids however, the fact that local variations of viscosity take place for the shear-dependent cases, and in the light of results presented in Fig. 6— where the extension of the intermediate layers seems to be affected by the shear-dependent rheology—make us ponder if the choice $\sigma = -1/2$ and $\beta = \epsilon^2$ is the most suitable for layer III. Considering that the balance breaking in Eq. (8) happens at $y^+ = y^+_m$, where $\mathrm{TI} = 0$ (see Fig. 4), another reasonable candidate for the parameter of interest, β, would be $\epsilon^2/\overline{\mu}^+\left(y^+_m\right)$; i.e., a rescaling factor which takes into account the increase/decrease of the mean viscosity (with respect to nominal μ_w) at $y^+ = y^+_m$ for the shear-thinning/thickening fluid case. For the Newtonian case, as remarked earlier, the intermediate layer is centred in the vicinity of y^+_m since $\mathrm{dT}/\mathrm{d}y^+ = \mathrm{dT}^\beta/\mathrm{d}y^+ = 0$. In contrast, for the shear-thinning and shear-thickening fluid cases is centred around $y^+ = y^+_\beta$ where $\mathrm{dT}^\beta/\mathrm{d}y^+ = 0$. This wall-normal position, for the considered cases, is nearby y^+_m. In comparison with y^+_m, y^+_β is slightly closer to/further away from the wall for the shear-thickening/thinning case since the location of the maximum for T^β decreases as β increases. In consequence, for the shear-dependent cases, $\overline{\mu}^+\left(y^+_\beta\right)$ is expected to be slightly larger than $\overline{\mu}^+\left(y^+_m\right)$ but not to significantly affect the proposed scaling, in particular, as $\epsilon^2 \to 0$, i.e., as the frictional Reynolds number increases.

The suitability of the choice $\beta = \epsilon^2/\overline{\mu}^+\left(y^+_m\right)$ for turbulent channel flow of GN fluids can be checked in a quantitative manner. Based on the transformations (13), we obtain $y^+_3 - y^+_2 = \beta^{-1/2}\left(\hat{y}_3 - \hat{y}_2\right)$; where y^+_2 and y^+_3 denote the beginning and end of mesolayer III, respectively, and $\hat{y}_2$ and $\hat{y}_3$ the same wall-normal positions but now in the rescaled variable. Here, $\Delta\hat{y} = \hat{y}_3 - \hat{y}_2 = \mathcal{O}(1)$ and thus, $\Delta y^+ = y^+_3 - y^+_2 = \mathcal{O}\left(\beta^{-1/2}\right)$. As seen from Table 1, the ratio $\Delta y^+/\sqrt{Re_\tau \mu^+\left(y^+_m\right)}$ appears to bounded for all GN fluid cases, and, it is expected that will tend to 1 as Re_τ increases, i.e., as $\epsilon^2 \to 0$. Note as well that this decrease/increase in the overall range of length scales with shear-thinning/thickening fluid behaviour is in line with the showed trends for $-\overline{u'_z\omega'_y}$ in Section 3.

5. Summary

Turbulent channel flow simulations of GN fluids, consisting of weakly shear-thinning, Newtonian, and weakly shear-thickening fluid cases, at $Re_\tau = 180$ (Arosemena et al. [31]) are considered to compute the nonzero velocity–vorticity correlations and some statistics related to the mean dynamics.

Regarding the velocity–vorticity products, for all considered GN fluid cases, contributions to the wall-normal gradient of $-\overline{u'_x u'_y}$ are shared between the vortex-stretching and advective transport terms, i.e., $-\overline{u'_z\omega'_y}$ and $\overline{u'_y\omega'_z}$, respectively. On the other hand, contributions to the wall-normal gradient of the turbulent kinetic energy are dominated by the correlation $-\overline{u'_x\omega'_z}$ which, in the near-wall region, seemingly increases/decreases in magnitude with shear-thinning/thickening fluid behaviour. The opposite trend is noted for the velocity–vorticity products related to the turbulent inertia term, suggesting that with e.g. shear-thinning rheology, the sublayer streaks are more stable, the near-wall vortical motions are dampened, and there is a narrower range of turbulent eddy sizes.

In the context of mean momentum balance analysis, for the shear-dependent cases, the contributions $\mathrm{VF}^{(\mathrm{NN})}$ (arising due to fluctuations in viscosity) are found to peak in the vicinity of the wall but, across the channel, are always smaller than PG and overall are deemed negligible. The study of the terms contributing to the mean momentum balance revealed that the four-layer structure, first recognized by (Wei et al. [14]), remains for all GN fluids and that the shear-dependent rheology appears to only influence the location of the layers. Compared to Newtonian channel flow, with shear-thinning/thickening fluid behaviour, the upper bound for layers II and III are located further away/closer to the wall and with e.g. shear-thinning rheology, the balance breaking and exchange of mean forces at y^+_m also moves further away from the channel wall. The results imply an increase/decrease in the importance of the viscous forces in the intermediate layers with shear-thinning/thickening behaviour.

We remark that the effect of shear-dependent rheology on the thickness of layer II and III is strikingly similar to a change of Reynolds number for Newtonian channel flow (see e.g. Klewicki et al. [17]; Chin et al. [18]) which strongly suggests that the shear-dependency should be taken into account for proper scaling of the intermediate layers in wall-bounded flows of GN fluids. The mean momentum balance-based layers have a mathematical structure composed of a hierarchy of length scales (Fife et al. [12]) and for the intermediate layer III, in case of shear-dependent rheology, it is proposed that a suitable length scale should account for the local variation in the mean viscosity (with respect to its nominal wall value) at y^+_m. Quantitative evidence (see Table 1) revealed that the width of the mesolayer III, $\Delta y^+_{\mathrm{III}}$, seems to scale with $\sqrt{Re_\tau \mu^+\left(y^+_m\right)}$ which is in line with the previous observation about the overall decrease/increase in the range of turbulent length scales with shear-thinning/thickening rheology in the channel flow.

Declaration of competing interests

The authors declare that they have no known competing financial interests or personal relationships that could have appeared to influence the work reported in this paper.

Acknowledgements

This work was supported by the Research Council of Norway (RCN, Grant No. 274398). The authors are grateful for computer resources provided by NTNU IDUN/EPIC computing cluster (Själander et al. [47]).

References

[1] J. Hinze, Turbulence, McGraw-Hill, 1975.
[2] S. Tardu, Statistical Approach to Wall Turbulence, Wiley-ISTE, 2011.
[3] J.C. Klewicki, Velocity–vorticity correlations related to the gradients of the Reynolds stress in parallel turbulent wall flows, Phys. Fluids A 1 (1989) 1285–1289, http://dx.doi.org/10.1063/1.857354.

[4] G.L. Eyink, Turbulent flow in pipes and channels as cross-stream "inverse cascades" of vorticity, Phys. Fluids 20 (2008) 125101, http://dx.doi.org/10.1063/1.3013635.
[5] J.C. Klewicki, J. Murray, R.E. Falco, Vortical motion contributions to stress transport in turbulent boundary layers, Phys. Fluids 6 (1994) 277–286, http://dx.doi.org/10.1063/1.868082.
[6] P.A. Priyadarshana, J.C. Klewicki, S. Treat, J.F. Foss, Statistical structure of turbulent-boundary layer velocity-vorticity products at high and low Reynolds numbers, J. Fluid Mech. 570 (2007) 307–346, http://dx.doi.org/10.1017/S0022112006002771.
[7] J. Klewicki, P. Fife, T. Wei, P. McMurty, A physical model of the turbulent boundary layer consonant with mean momentum balance structure, Phil. Trans. R. Soc. A 365 (2007) 823–839, http://dx.doi.org/10.1098/rsta.2006.1944.
[8] C. Morrill-Winter, J. Klewicki, Influences of boundary layer scale separation on the vorticity transport contribution to turbulent inertia, Phys. Fluids 25 (2013) 015108, http://dx.doi.org/10.1063/1.4775361.
[9] W.R.C. Phillips, The wall region of a turbulent boundary layer, Phys. Fluids 30 (1987) 2354–2361, http://dx.doi.org/10.1063/1.866125.
[10] W.W. Willmarth, S.S. Lu, Structure of the Reynolds stress near the wall, J. Fluid Mech. 55 (1972) 65–92, http://dx.doi.org/10.1017/S002211207200165X.
[11] J.M. Wallace, H. Eckelmann, R.S. Brodkey, The wall region in turbulent shear flow, J. Fluid Mech. 54 (1972) 39–48, http://dx.doi.org/10.1017/S0022112072000515.
[12] P. Fife, T.W.J. Klewicki, P. McMurty, Stress gradient balance layers and scale hierarchies in wall bounded turbulent flows, J. Fluid Mech. 532 (2005) 165–189, http://dx.doi.org/10.1017/S0022112005003988.
[13] P. Fife, J. Klewicki, P. McMurty, T. Wei, Multiscaling in the presence of indeterminacy: wall-induced turbulence, Multiscale Model. Simul. 4 (2005) 936–959, http://dx.doi.org/10.1137/040611173.
[14] T. Wei, P. Fife, J. Klewicki, P. McMurty, Properties of the mean momentum balance in turbulent boundary layer, pipe and channel flows, J. Fluid Mech. 522 (2005) 303–327, http://dx.doi.org/10.1017/S0022112004001958.
[15] T. Wei, P. McMurty, J. Klewicki, P. Fife, Meso scaling of the Reynolds shear stress in turbulent channel and pipe flows, AIAA J. 43 (2005) 2350–2353, http://dx.doi.org/10.2514/1.15617.
[16] J. Klewicki, P. Fife, T. Wei, On the logarithmic mean profile, J. Fluid Mech. 638 (2009) 73–93, http://dx.doi.org/10.1017/S002211200999084X.
[17] J. Klewicki, C. Chin, H.M. Blackburn, A. Ooi, I. Marusic, Emergence of the four layer dynamical regime in turbulent pipe flow, Phys. Fluids 24 (2012) 045107, http://dx.doi.org/10.1063/1.3702897.
[18] C. Chin, J. Philip, J. Klewicki, A. Ooi, I. Marusic, Reynolds-number-dependent turbulent inertia and onset of log region in pipe flows, J. Fluid Mech. 757 (2014) 747–769, http://dx.doi.org/10.1017/jfm.2014.486.
[19] C.M. White, Y. Dubief, J. Klewicki, Properties of the mean momentum balance in polymer drag-reduced channel flow, J. Fluid Mech. 834 (2018) 409–433, http://dx.doi.org/10.1017/jfm.2017.721.
[20] M. Yoon, J. Ahn, J. Hwang, H.J. Sung, Contribution of velocity–vorticity correlations to the frictional drag in wall-bounded turbulent flows, Phys. Fluids 28 (2016) 081702, http://dx.doi.org/10.1063/1.4961331.
[21] A.A. Draad, G.D.C. Kuiken, F.T.M. Nieuwstadt, Laminar-turbulent transition in pipe flow for Newtonian and non-Newtonian fluids, J. Fluid Mech. 377 (1998) 267–312, http://dx.doi.org/10.1017/S0022112098003139.
[22] P.K. Ptasinski, F.T.M. Nieuwstadt, B.H.A.A. Van Der Brule, M.A. Hulsen, Experiments in turbulent pipe flow with polymer additives at maximum drag reduction, Flow Turbul. Combust. 66 (2001) 159–182, http://dx.doi.org/10.1023/A:1017985826227.
[23] F. Irgens, Rheology and Non-Newtonian Fluids, Springer, 2014, http://dx.doi.org/10.1007/978-3-319-01053-3.
[24] J. Singh, M. Rudman, H.M. Blackburn, A. Chryss, L. Pullum, L.J.W. Graham, The importance of rheology characterization in predicting turbulent pipe flow of generalized Newtonian fluids, J. Non-Newton. Fluid Mech. 232 (2016) 11–21, http://dx.doi.org/10.1016/j.jnnfm.2016.03.013.
[25] L. Davidson, S.-H. Peng, Hybrid LES-RANS: A one-equation SGS model combined with a k-ω for predicting recirculating flows, Internat. J. Numer. Methods Fluids 43 (9) (2003) 1003–1018, http://dx.doi.org/10.1002/fld.512.
[26] L. Davidson, CALC-LES: A Fortran code for LES and hybrid LES-RANS, Technical Report, Chalmers University of Technology, 2020, URL http://www.tfd.chalmers.se/~lada/postscript_files/calc-les.pdf.
[27] P. Emvin, The Full Multigrid Method Applied to Turbulent Flow in Ventilated Enclosures Using Structured and Unstructured Grids (Ph.D. thesis), Chalmers University of Technology, Gothenburg, 1997.
[28] M. Rudman, H.M. Blackburn, L.J.W. Graham, L. Pullum, Turbulent pipe flow of shear-thinning fluids, J. Non-Newton. Fluid Mech. 118 (2004) 33–48, http://dx.doi.org/10.1016/j.jnnfm.2004.02.006.
[29] A.A. Gavrilov, V.Y. Rudyak, Direct numerical simulation of the turbulent flows of power-law fluids in a circular pipe, Thermophys. Aeromech. 23 (2016) 473–486, http://dx.doi.org/10.1134/S0869864316040016.
[30] J. Singh, M. Rudman, H.M. Blackburn, The influence of shear-dependent rheology on turbulent pipe flow, J. Fluid Mech. 822 (2017) 848–879, http://dx.doi.org/10.1017/jfm.2017.296.
[31] A.A. Arosemena, H.I. Andersson, J. Solsvik, Turbulent channel flow of generalized Newtonian fluids at a low Reynolds number, J. Fluid Mech. 908 (2021) A43, http://dx.doi.org/10.1017/jfm.2020.903.
[32] H. Tennekes, J.L. Lumley, A First Course in Turbulence, MIT Press, 1972.
[33] G.I. Taylor, The transport of vorticity and heat through fluids in turbulent motion, Proc. R. Soc. Lond. Ser. A Math. Phys. Eng. Sci. 135 (1932) 685–701, http://dx.doi.org/10.1098/rspa.1932.0061.
[34] R.E. Falco, J.C. Klewicki, K. Pan, Production of turbulence in boundary layers and potential for modification of the near-wall region, in: A. Gyr (Ed.), Structure of Turbulence and Drag Reduction, Springer-Verlag, Berlin Heidelberg, 1990, pp. 59–67, http://dx.doi.org/10.1007/978-3-642-50971-1_4.
[35] H.T. Kim, S.J. Kline, W.C. Reynolds, The production of turbulence near a smooth wall in a turbulent boundary layer, J. Fluid Mech. 50 (1971) 133–160, http://dx.doi.org/10.1017/S0022112071002490.
[36] G.R. Offen, S.J. Kline, A comparison and analysis of detection methods for the measurement of production in a boundary layer, in: Proc. 3rd Biennial Symposium of Turbulence in Liquids, University of Missouri-Rolla, 1973, pp. 289–320, URL http://scholarsmine.mst.edu/sotil/119.
[37] J. Singh, M. Rudman, H.M. Blackburn, Reynolds Number effects in pipe flow turbulence of generalized Newtonian fluids, Phys. Rev. Fluids 3 (2018) 094607, http://dx.doi.org/10.1103/PhysRevFluids.3.094607.
[38] J. Klewicki, M.M. Metzger, E. Kelner, E.M. Thurlow, Viscous sublayer flow visualizations at $R_\theta \approx 150\,000$, Phys. Fluids 7 (1995) 857–863, http://dx.doi.org/10.1063/1.868763.
[39] C. Cossu, Y. Hwang, Self-sustaining processes at all scales in wall-bounded turbulent shear flows, Phil. Trans. R. Soc. A 375 (2017) 20160088, http://dx.doi.org/10.1098/rsta.2016.0088.
[40] J. Jímenez, G. Kawahara, M.P. Simens, M. Nagata, M. Shiba, Characterization of near-wall turbulence in terms of equilibrium and "burstin" solutions, Phys. Fluids 17 (2005) 015105, http://dx.doi.org/10.1063/1.1825451.
[41] M. Lee, R.D. Moser, Direct numerical simulation of turbulent channel flow up to $Re_\tau \approx 5200$, J. Fluid Mech. 774 (2015) 395–415, http://dx.doi.org/10.1017/jfm.2015.268.
[42] S.B. Pope, Turbulent Flows, Cambridge University Press, 2000, http://dx.doi.org/10.1017/CBO9780511840531.
[43] A.J. Smits, B.J. McKeon, I. Marusic, High-Reynolds number wall turbulence, Annu. Rev. Fluid Mech. 43 (2011) 353–375, http://dx.doi.org/10.1146/annurev-fluid-122109-160753.
[44] I. Marusic, J.P. Monty, M. Hultmark, A.J. Smits, On the logarithmic region in wall turbulence, J. Fluid Mech. 716 (2013) R3, http://dx.doi.org/10.1017/jfm.2012.511.
[45] M.D. Warholic, H. Massah, T.J. Hanratty, Influence of drag-reducing polymers on turbulence: effects of Reynolds number, concentration and mixing, Exp. Fluids 27 (1999) 461–472, http://dx.doi.org/10.1007/s003480050371.
[46] P. Fife, Scaling Approaches to Steady Wall-Induced Turbulence, Technical Report, The University of Utah, 2006, URL: http://www.math.utah.edu/~fife/revarticle.pdf.
[47] M. Själander, M. Jahre, G. Tufte, N. Reissmann, EPIC: An energy-efficient, high-performance GPGPU computing research infrastructure, 2019, arXiv:1912.05848.

Paper IV

Characterization of vortical structures in a stirred tank

Arturo A. Arosemena, Haider Ali, and Jannike Solsvik

Phys. Fluids **34**, 5.0083843 (2022)

Physics of Fluids

Characterization of vortical structures in a stirred tank

Cite as: Phys. Fluids **34**, 025127 (2022); https://doi.org/10.1063/5.0083843
Submitted: 30 December 2021 • Accepted: 02 February 2022 • Published Online: 23 February 2022

A. A. Arosemena, H. Ali and J. Solsvik

Physics of Fluids ARTICLE scitation.org/journal/phf

Characterization of vortical structures in a stirred tank

Cite as: Phys. Fluids **34**, 025127 (2022); doi: 10.1063/5.0083843
Submitted: 30 December 2021 · Accepted: 2 February 2022 ·
Published Online: 23 February 2022

A. A. Arosemena, H. Ali, and J. Solsvik[a)]

AFFILIATIONS

Department of Chemical Engineering, Norwegian University of Science and Technology (NTNU), NO-7491 Trondheim, Norway

[a)]Author to whom correspondence should be addressed: jannike.solsvik@ntnu.no

ABSTRACT

Data obtained from large eddy simulations of single-phase, turbulent flow of Newtonian and shear-thinning fluids in a baffled stirred tank reactor are considered to identify and characterize vortical structures. The identification proceeds through an objectivized Eulerian method, accounting for the inhomogeneities in the flow, which palliates some shortcomings of previous implementations. The characterization focuses on turbulent vortices larger than the dissipative scales and, to a lesser extent, on trailing and macro-instability vortices. The characterization performed through different statistical analyses includes aspects such as size, number density, shape, distribution and organization in space, and correlation with the kinetic energy due to turbulence and the periodic passage of the blades. To the authors' knowledge, some of these representative aspects have been rarely investigated or have not been addressed at all for the turbulent flow in a stirred vessel. The influence of changing the rotational speed of the tank and the rheology of the working fluid are explored as well. Finally, considering one-way coupling, some potential and practical implications for liquid–liquid and gas–liquid dispersed systems are briefly discussed.

I. INTRODUCTION

Mechanically agitated tanks are widely used in numerous industries for chemical and biochemical processes. A stirred tank has three essential components: (i) a cylindrical vessel containing the working fluid, (ii) a propeller (typically a shafted six-bladed disk/Rushton turbine) generating the swirling motion, and (iii) baffles (commonly four in an equally-spaced configuration) fitted to the walls of the vessel to prevent gross vortexing.[1] A sketch of the typical flow pattern produced in a baffled vessel by a flat-bladed turbine is shown in Fig. 1. The Rushton turbine generates a strong radial discharge, pushing the fluid until reaching the tank walls and thereby creating circulation zones on top and bottom of the propeller region. In stirred tanks, depending upon aspects such as the desired products, the operation may take place under turbulent or locally transitional regimes. Furthermore, the working fluids may be Newtonian but more often than not present more complex rheology. See, e.g., Nouri and Whitelaw,[2] Soos *et al.*,[3] Fernandes del Pozo *et al.*,[4] and Hara *et al.*[5]

Over the last decades, stirred tank reactors have received significant attention and substantial effort has been made to improve our understanding of flow phenomena in these vessels. Broadly speaking, stirred tank studies can be grouped into two categories: experimental investigations and numerical simulations. Experimentally, different visualization techniques, such as particle image velocimetry (PIV), hot-wire anemometry, and laser Doppler velocimetry (LDV), are largely used to investigate flow patterns and acquire instantaneous velocity measurements in stirred vessels (see e.g., Schäfer *et al.*,[6] Sharp and Adrian,[7] Venneker *et al.*,[8] and de Lamotte *et al.*;[9] also, see Mavros[10] for a concise review of different employed experimental techniques). On the other hand, nearly all well-known numerical approaches for turbulent flows in computational fluid dynamics (CFD) have been considered for stirred tank modeling. These include attempted direct numerical simulations (DNS; see Sbrizzai *et al.*,[11] Derksen and den Akker,[12] and Tamburini *et al.*[13]), scale resolving simulations (SRS; see Eggels,[14] Derksen and Van den Akker,[15] Hartmann *et al.*,[16] and Sungkorn *et al.*[17]), and Reynolds-averaged Navier–Stokes simulations (RANS; see Hartmann *et al.*,[16] Singh *et al.*,[18] and Tamburini *et al.*,[19] among many others).

Previous studies (either experimental or numerical), for the most part, have focused on flow patterns, turbulence intensities, turbulent kinetic energy, and dissipation rates. Changes due to different types of impellers, vessel configurations, Reynolds numbers, and working fluid rheology have been explored as well. These properties, geometrical features, and operational aspects are of interest due to their relevance in mixing and transport phenomena within the agitated tank. For instance, flow patterns are known to influence mixing performance at the largest scales (macromixing), while the turbulent dissipation rate is

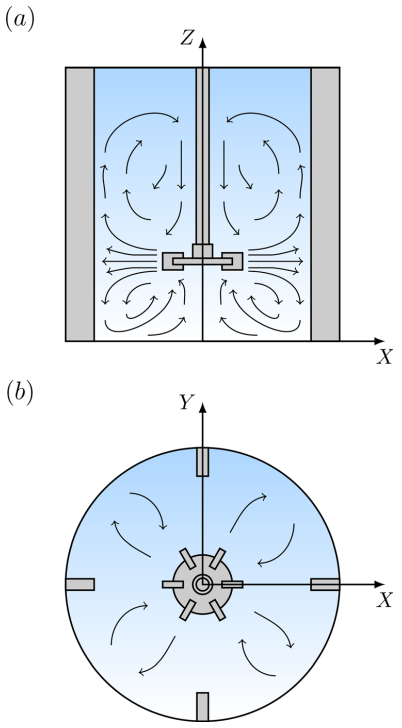

FIG. 1. Illustration of the flow pattern produced by a Rushton-type impeller in a baffled tank: (a) cross-sectional view and (b) top view.

important for both dispersion of fluid particles (drops and bubbles) and mass transfer in multiphase systems; see Garcia–Ochoa and Gomez[20] for a review about gas–liquid mass transfer in a bioprocess where the dissipation rate is identified as one of the main factors affecting the oxygen transfer rate. In addition, topics such as turbulence anisotropy for modeling of realizable states of turbulence,[21] local shear-rate quantification,[22] and identification of coherent vortical structures (starting with the tomographic observations of Takashima and Mochizuki[23]) have also been addressed in studies about stirred tanks, albeit perhaps to a lesser extent.

Vortices are swirling-like structures, which play a major role in turbulence. The popular quote by Richardson,[24] broadly describing the direct energy cascade process, constitutes a memorable illustration of such a role. In a mechanically agitated vessel, these structures are clearly important not only for the cascade process but also for actual mixing (at the molecular level) and particle dispersion and coalescence; many models for fluid particle breakup and coalescence in dispersed turbulent flow systems are based on particle–eddy interaction mechanisms (see Liao and Lucas[25,26] and Solsvik *et al.*[27] for reviews of these models). As illustration, in the context of deformation and breakup of fluid particles, consider Kresta and Brodkey[28] who presented different particle responses depending on the size and intensity of the surrounding eddies. A droplet may be simply advected when interacting with a much larger eddy, whereas it may deform or even breakup in daughter particles when the interacting eddies are of comparable size or much smaller than the size of the original droplet. It is worth mentioning that despite vortices of different sizes being encountered in stirred tanks, trailing/tip vortices at an intermediate scale and those related to flow macroinstabilities (MIs) are the most studied.

Trailing vortices are counter-rotating vortex pairs generated behind the upper and lower edges of each impeller blade due to their periodic passage.[29–31] Trailing vortices have been subject of extensive research because of the seemly strong correlation between them and regions of high vorticity, strain rate, turbulent dissipation, and Reynolds stresses; see e.g., Yianneskis *et al.*,[32] Stoots and Calabrese,[33] Lee and Yianneskis,[34] Derksen *et al.*,[35] Sharp and Adrian,[7] Escudié and Liné,[36] Escudié *et al.*,[37] Bouremel *et al.*,[38] Sharp *et al.*,[39] Chara *et al.*,[40] among others. Aside reporting turbulent quantities in the near-impeller region, some of these authors have also attempted to characterize the trailing vortices by identifying their cores and corresponding mean trajectories, surface area (indicative of vortex size), and velocity circulation (indicative of vortex strength). Meanwhile, MIs are temporal mean flow variations affecting the flow patterns and stemming from changes of impeller off-bottom clearance, changes in Reynolds numbers, and/or precessional motion of a vortex (or vortices) around the impeller shaft.[41,42] MIs vortices were first identified by Yianneskis *et al.*[32] as low-frequency, "whirlpool"-like type of vortex precessing around the shaft in which characterization started with their frequency at different impeller designs, impeller clearances,[41] and Reynolds numbers.[42] Further information, such as the trajectory of these structures[43] and their interaction with trailing vortices,[44] has also been reported for mixing enhancement purposes.

The present work aims to identify and characterize vortical structures. The input flow fields are obtained from large eddy simulations of single-phase, turbulent flow of Generalized Newtonian (GN) fluids[45] in a baffled stirred tank reactor. Different from previous investigations, the identification is performed using a fully frame invariant version of an Eulerian local region-type method, which takes into account that the stirred flow is inhomogeneous in all spatial directions. The characterization includes representative aspects of the identified structures that have been rarely investigated or have not been addressed at all in the context of stirred tanks and focuses on turbulent vortices larger than the dissipative scales and, to a lesser extent, on trailing and MI vortices. The effects of having different rotational speeds and shear-thinning rheology (in comparison with Newtonian fluids) are also explored. Some potential and practical implications for liquid–liquid and gas–liquid dispersed systems, where the local fraction of the dispersed phase (holdup) is always sufficiently small, are briefly discussed as well.

This paper is organized as follows. The used numerical approach, the considered fluid flow cases, and other computational details, such as impeller motion treatment or employed grid, are described in Sec. II. Eulerian methods that are commonly used for the identification of vortical structures and their main weaknesses when considering flows due to induced swirling motion are outlined in Sec. III. Section III also describes the considered vortex identification method, which is not only Galilean invariant but also observer-independent, and different regions of potential interest in the stirred vessel. The characterization of the identified structures, including aspects such as size, number

TABLE I. Physical properties, Carreau model parameters, and Reynolds number of the fluid flow cases under study. Here, W600 and C600 denote the cases where the stirred vessel is operated at 600 rpm, whereas W800 and C800 denote the cases where it is operated at 800 rpm. *Re* is the Reynolds number based on the impeller rotational speed N(rev s^{-1}), its diameter D; see Subsection II D, and μ_a for an average strain rate according to the Metzner–Otto correlation for a Rushton-type stirrer,[50] i.e., $k_s N \approx 11.5N$. k_s is the Metzner constant.

Case	Fluid	Line/marker color	$\rho \times 10^3$ (kg m^{-3})	$\mu_0 \times 10^{-3}$ (Pa s)	$\mu_\infty \times 10^{-3}$ (Pa s)	λ (s)	α $(\cdots)$	$Re = \rho N D^2/\mu_a$ $(\cdots)$
W600	Water	Black	1.00	1.00	⋯	⋯	1.000 0	49 000
W800	Water	Black	1.00	1.00	⋯	⋯	1.000 0	65 333
C600	CMC 0.2%	Red	1.00	97.40	14.80	0.281 5	0.689 2	1144
C800	CMC 0.2%	Red	1.00	97.40	14.80	0.281 5	0.689 2	1616

density, shape, distribution and organization in space, and the correlation between the vortex indicator and the kinetic energy due to turbulence and the periodic passage of the blades, is addressed in Sec. IV. Finally, a summary of our main findings, some possible implications in terms of multiphase systems, and further work are presented in Sec. V.

II. NUMERICAL PROCEDURE

A. Large-eddy simulations (LES)

In the LES approach, large grid scales are resolved while the smallest, subgrid-scales (SGS) are modeled. The smallest scales are supposed to be more isotropic and more in equilibrium than the large scales. Moreover, the smallest scales only contain a minor fraction of the total turbulent kinetic energy. The governing equations in LES are obtained by spatially filtering the governing equations for mass and momentum conservation. For incompressible GN fluids, in the absence of external forces, the filtered equations read as

$$\frac{\partial \widetilde{u}_i}{\partial x_i} = 0, \tag{1}$$

$$\frac{\partial \widetilde{u}_i}{\partial t} + \frac{\partial (\widetilde{u}_i \widetilde{u}_j)}{\partial x_j} = -\frac{1}{\rho}\frac{\partial \widetilde{p}}{\partial x_i} + \frac{1}{\rho}\frac{\partial}{\partial x_j}\left(2\widetilde{\mu_a \mathrm{S}_{ij}}\right) - \frac{\partial \tau_{ij}}{\partial x_j}, \tag{2}$$

where $\widetilde{(\,)}$ indicates a grid-filtered variable, x_i and u_i denote the spatial-Cartesian coordinates and the instantaneous velocity field, respectively, and t represents time while ρ is the fluid density and p is the pressure field. In Eq. (2), μ_a is the apparent dynamic viscosity, which, for a GN fluid, solely depends on the strain rate $\dot{\gamma} = (2\mathrm{S}_{ij}\mathrm{S}_{ij})^{1/2}$, and $\mathrm{S}_{ij} = (\partial u_i/\partial x_j + \partial u_j/\partial x_i)/2$ is the strain rate tensor. In this paper, when index notation is used, subscript i (or any other subscript) takes the value 1, 2, or 3 to represent the X, Y, or Z component, respectively. In the stirred vessel, the Cartesian coordinate system is as shown in Fig. 1.

The SGS- or residual stress tensor τ_{ij}, introduced after filtering the momentum equation, is defined as

$$\tau_{ij} = \widetilde{u_i u_j} - \widetilde{u}_i \widetilde{u}_j, \tag{3}$$

which is to be modeled. The SGS-stress tensor for a shear-dependent GN fluid is treated in the same manner as for a Newtonian fluid[17] and modeled through the Smagorinsky–Lilly model[46,47] as

$$\tau_{ij} - \frac{1}{3}\delta_{ij}\tau_{kk} = -2\nu_{sgs}\widetilde{\mathrm{S}}_{ij} = -2\left[\ell_{sgs}^2\left(2\widetilde{\mathrm{S}}_{ij}\widetilde{\mathrm{S}}_{ij}\right)^{1/2}\right]\widetilde{\mathrm{S}}_{ij}. \tag{4}$$

In SGS-kinematic viscosity ν_{sgs}, SGS-length ℓ_{sgs} is given by

$$\ell_{sgs} = \min(C_s\Delta, \kappa d). \tag{5}$$

Here, C_s is the flow-dependent Smagorinsky "constant," Δ is the local grid size based on the volume of the corresponding computational cell, $\kappa \approx 0.4$ is the von Kármán constant, and d is the distance to the nearest wall. For stirred tank flow, the optimal value for C_s has yet to be determined.[12] In this work, as in Fan *et al.*[48] and Devi and Kumar,[49] C_s is set as 0.1.

B. Fluid rheology

In simulations, shear-dependent rheology is incorporated through the Carreau fluid model (see, e.g., Irgens[15]) i.e.,

$$\mu_a = \mu_\infty + (\mu_0 - \mu_\infty)\left[1 + (\lambda\dot{\gamma})^2\right]^{(\alpha-1)/2}, \tag{6}$$

where μ_∞ and μ_0 are the "infinite" and "zero" shear rate viscosities, respectively, λ is a time constant, and α is the flow index, which, for shear-thinning, is to be less than unity. Newtonian fluid behavior is recovered for $\alpha = 1$. The values for different physical properties and Carreau model parameters of the fluids under study, water and 0.2 wt. % carboxymethyl cellulose (CMC) solution, are presented in Table I. The corresponding viscosity rheogram for the shear-thinning fluid case (CMC 0.2%) is shown in Fig. 2.

C. Impeller motion treatment

The rotational motion of the impeller adds complexity to the simulations. For baffled stirred tanks, the contradiction between the rotating impeller and the stationary baffles requires specific numerical treatment.[51] Modeling is typically performed using either the multiple

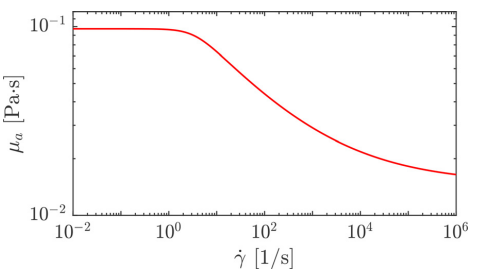

FIG. 2. Apparent viscosity as a function of the strain rate, μ_a vs $\dot{\gamma}$, for 0.2 wt. % CMC solution.

reference frame (MRF, Luo *et al.*[52]) or the sliding mesh (SM, Murthy *et al.*[53]) approach. The MRF approach is a steady-state approximation for stirred tanks having a weak impeller-baffle interaction. In the MRF method, the computational mesh is fixed at the beginning of simulation and the domain is divided into an impeller zone (using a rotating reference frame) and a stationary zone (using a stationary reference frame). On the other hand, the SM technique is a fully transient approach where the rotational motion of the impeller is explicitly taken into account.[54] In the SM approach, the computational domain is also divided into two non-overlapping submeshes, one rotating with the impeller while the other is fixed as in the MRF method. However, the SM method allows the adjacent meshes to slide relative to one another and the coupling along the sliding interface is accounted for by re-establishing the cell connectivity each time when sliding occurs.[51] In other words, as the computation proceeds and the impeller moves in a periodic manner, the computational mesh is adjusted accordingly. The SM approach is considered as a more accurate method for unsteady state simulations in stirred tanks, and it is used in this work.

D. Computational aspects

Simulations were performed for a laboratory-scale, 11 L stirred tank. Table I summarizes the considered flow cases, and Fig. 3 shows the stirred vessel configuration. The corresponding geometrical details are as follows: tank diameter $T = 24$ cm, fluid column height $H = T$, baffles width $w_{bf} = T/9.6$, baffles thickness $t_{bf} = T/24$, off-bottom clearance $C = 7$ cm, impeller diameter $D = C$, impeller diameter without blades $D_i = 5.2$ cm, blades height $h_b = 1.5$ cm, blades width $w_b = 1.8$ cm, blades thickness $t_b = 0.2$ cm, outer diameter of shaft $DS_o = 1.2$ cm, and inner diameter of shaft $DS_i = 1$ cm.

The computational domain was enclosed between two main parts: an inner rotating cylinder, consisting of the shaft and impeller, and an outer stationary cylinder containing the baffles and rest of the tank. The domain was discretized with structured hexahedral elements using Ansys ICEM (version 19.1, Ansys, Inc., Canonsburg, PA). The inner rotating cylinder region and regions near wall boundaries and edges were discretized using finer cells than those used in other regions of the tank. Boundary layers were specified to resolve the flow effects near to the walls of the stirred tank. The boundary layers were defined using a first layer thickness approach. The total number of boundary layers was five, and the first layer thickness was set to 0.2 mm. This is the minimum grid size while the maximum size goes up to 4 mm. The grid quality was checked by computing the determinant of hexahedral elements. The determinant test computes the deformation of the elements by calculating the Jacobian of each hexahedron and then normalizing the determinant of the matrix. Determinant values above 0.3 are acceptable for most commercial solvers and, in this work, the minimum and maximum values of the determinant were 0.764 and 1, respectively. It is worth commenting that the mesh size was selected after performing a grid sensitivity analysis. In the tests, the grid size of the stirred tank was scaled by a factor of 2 (see Table II). For different axial positions and for a radial coordinate close to the edge of the impeller blades, the radial, axial, and tangential velocity components for water and CMC 0.2% cases were computed and compared for all grid sizes as shown in Table II. A slight difference (1%–3%) between the computed values of the velocity components using grid sizes G2 and G3 was found, and thus, G2 was selected for conducting all the simulations. Table II also shows the near-wall resolution, y^+, for different grids and when water is the working fluid. To the best of the authors' knowledge, in most rotation flow problems, the grid is generally considered well resolved with $y^+ < 40$. See Fig. 4 for an illustration of the employed grid distribution, G2. With respect to the boundary conditions, the inner rotating cylinder containing the impeller and shaft was specified with rotational speed (rpm). The contact boundary between the inner rotating cylinder and outer stationary cylinder was set as interface. The top surface of the tank was set to no-slip boundary condition to mimic the placement of a lid at the top

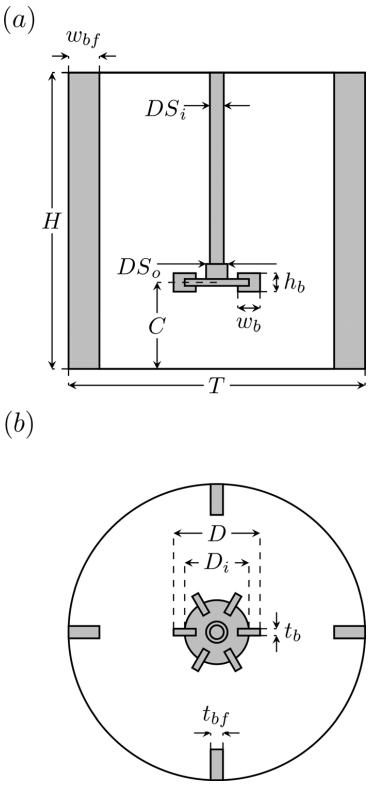

FIG. 3. Stirred tank configuration: (a) cross-sectional view and (b) top view.

TABLE II. Grids considered during sensitivity analysis.

Grid label	Number of cells (10^6)	Number of nodes (10^6)	y^+
G1	0.845	0.891	23.8
G2	1.570	1.631	19.5
G3	3.146	3.249	12.5

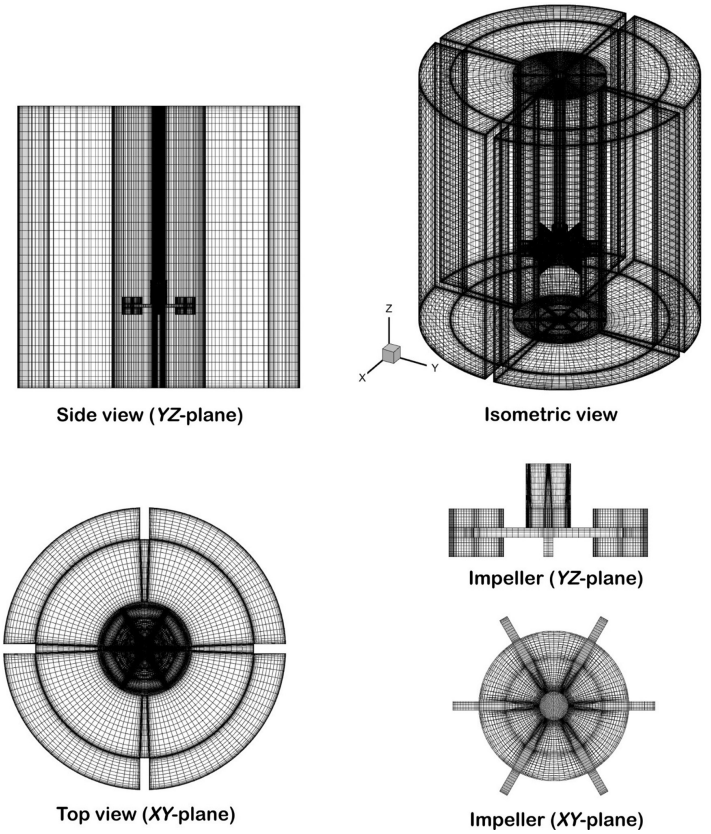

FIG. 4. Illustration of the computational mesh used for large eddy simulations of the baffled stirred tank.

surface in experiments to avoid the formation of air bubbles in the liquid. All other remaining boundaries were specified with no-slip and impermeability boundary conditions.

LES were performed using a finite volume based-method through the commercial package, Ansys FLUENT (version 19.1, Ansys, Inc., Canonsburg, PA). In this software, the term in parentheses, appearing on the right-hand side of Eq. (2), is approximated as $\mu_a \widetilde{S}_{ij}$. Also, μ_a is calculated considering a strain rate based on the resolved flow field. The discretized governing equations were solved using the algebraic multigrid method. The bounded central differencing scheme was used for the spatial discretization of the cell-face values of the transported field in the momentum equation. Meanwhile, Green–Gauss node-based and second-order schemes were used for the evaluation of gradients and for interpolating the pressure values at the cell–faces, respectively. A second order implicit scheme was used for the temporal formulation. Coupling between the continuity and momentum equations was done using the pressure-based SIMPLEC segregated algorithm.

Computations were initialized with the results obtained from steady RANS (realizable version of $k-\varepsilon$ eddy-viscosity model; Launder and Spalding[55]) simulations. These simulations were conducted with a time step of 0.2 ms (corresponding to 1° of impeller rotation). The number of iterations per time step was set to 50 for ensuring that every residual parameter reached the set absolute convergence criteria of 1×10^{-5}. A total number of 27 000 time steps were performed, corresponding to at least 35 impeller revolutions. The volume-averaged torque and turbulent kinetic energy were monitored during LES and after 10–13 impeller revolutions, the system reached quasi-steady state. Afterward, for each fluid flow case, instantaneous realizations of the grid-resolved velocity field in the Cartesian coordinate system, i.e., $\widetilde{u}_i = \widetilde{u}_i(x_i, t)$, were exported and a total of 1700 flow fields were collected for post-processing into our own in-house FORTRAN scripts. For simplicity, hereafter the tilde is dropped and, unless otherwise stated, a variable without tilde should be interpreted as a grid-resolved one, $u_i \equiv \widetilde{u}_i$. All simulations were performed on Fram, a Norwegian national high-performance computing (HPC) system, and each simulation case consumed about 50 000 CPU hours. Post-processing consisting of the identification of vortical structures

and computation of other relevant statistics was carried out on the Idun cluster, a local NTNU HPC-facility.

III. VORTEX IDENTIFICATION METHOD

As remarked in the Introduction, the identification and consequent understanding of vortices is of paramount importance for mixing in stirred tanks. Our intuition associates vortical structures with circular patterns seen in a flow; however, until today, there is no formal (mathematical) definition of a "vortex," which is unanimously recognized by the fluid dynamics community. For instance, when looking at a vortex as a finite structure, it is difficult to agree on its extension, i.e., where the vortex ends.[56] This lack of an accepted definition hinders their identification and explains the emergence of multiple criteria for vortex detection during the last decades. Vortex identification methods can be broadly classified as Lagrangian and Eulerian (see Epps[57] for a recent comprehensive review). The most popular vortex identification methods such as the Q-criterion,[58] the Δ-criterion[59] or the λ_2-criterion[60] are region-type methods, where vortex cores are defined within regions where a scalar field based on e.g., local or point-wise values of the velocity gradient tensor, $D_{ij} = \partial u_i/\partial x_j$, exceeds or not a certain threshold.

The aforementioned Eulerian local region-type methods are conceptually easy to explain in the sense that a vortex exists if the considered criterion is met and typically have clear physical meaning such as a vortex represents regions of coherent swirling motion (swirling-strength criterion, Zhou *et al.*[61]) or a vortex is a local region where there is an excess of rotation rate relative to strain rate (Q-criterion; see Chakraborty *et al.*[62]). Moreover, since these methods can be computed in a point-wise manner and only depend on the instantaneous velocity field, their computation can be parallelized and they adapt instantaneously to an evolving unsteady flow field.[57] Nevertheless, these identification methods have also several shortcomings (see, e.g., Kolář[63]) such as their inability to provide the same results in different rotation frames (i.e., material objectivity or frame invariance, see Haller[64]) or their sensitivity to the selected threshold value; that is, different vortical structures are visualized at different thresholds (see, e.g., Liu *et al.*[65]).

For industrial equipment where swirling motion is induced by rotating mechanical parts, such as turbomachines or stirred-tank reactors, material objectivity is particularly desirable; unless rotational invariance is fulfilled, different observers applying these methods (e.g., Q and Δ criteria) in their own frame of reference will identify different regions as vortical structures.[66] In this regard, recently, Haller[67] remarked that in the available objectivization procedures for these local vortex criteria, only the replacement of the spin/rotation rate tensor by a spin-deviation tensor defines compatible local observers for arbitrary fluid flows. Here, the idea is to compute the spin-deviation tensor as the difference between the original rotation rate tensor and its instantaneous spatially averaged value obtained from the instantaneous spatially averaged vorticity field; see Haller *et al.*[68] The procedure was proposed and implemented by Liu *et al.*[69] and Liu *et al.*[70] to objectivize the Rortex criterion[71–73] and the omega method.[65]

The other issue, about the threshold sensitivity of these Eulerian methods, comprises (i) the (potential) spatial dependency of the threshold in the case of inhomogeneous flows and, perhaps more importantly, (ii) the absence of a general procedure that removes the user-subjective approach in the selection of threshold values. The first aspect can be addressed considering a non-uniform threshold based on a statistical indicator of the criterion used for the vortex detection. Nagaosa and Handler[74] proposed a threshold varying in the wall-direction with the standard deviation of the Q-values for (canonical) turbulent channel flow. Thereupon, the idea of using the standard deviation of the considered Eulerian criterion to take into account inhomogeneities in the flow has been successfully employed by multiple authors (see, e.g., del Álamo *et al.*,[75] Lozano-Durán *et al.*,[76] and Cheng *et al.*[77]). The second aspect, about the arbitrary selection of thresholds, can be palliated considering the percolation crisis analysis introduced by Moisy and Jiménez[78] (see, e.g., del Álamo *et al.*,[75] Lozano-Durán *et al.*,[76] Dong *et al.*,[79] Hwang and Sung,[80] Osawa and Jiménez,[81] and Cheng *et al.*[77]). In this procedure, different thresholds are evaluated to examine where a perceptible transition from a highly clustered region to increasing individual structures identified according to a particular method (e.g., Q or Δ-criterion) occurs. The threshold at which the percolation transition/crisis takes place is considered a critical one, and the threshold for proper visualization of the structures lies above it. Nonetheless, it is still up to the researcher to decide how large the selected threshold should be with respect to the critical one. For this reason, the clustering methodology is often accompanied by a sensitivity analysis where the influence of the selected threshold is briefly studied.

In the case of stirred-tank devices, previous studies have mostly implemented nonobjective and threshold sensitive vortex identification methods. Escudié *et al.*[37] used the λ_2-criterion to identify vortex cores of trailing vortices, and Escudié *et al.*[37] and Escudié and Liné[82] remarked that earlier investigations localize trailing vortices either (i) from the phase-averaged velocity fields, where for a given angular position of the measurement plane compared to the blade, the vortex center is defined by the location where the vertical velocity is zero or (ii) from a dimensionless vorticity calculated in a vertical plane of measurement relative to the blade position, which had to exceed an arbitrary threshold value for the detection of a vortex core. Afterward, the λ_2-criterion gained significant popularity and has been used for the identification of both trailing and MI-vortices; see e.g., Ducci and Yianneskis,[43] Chara *et al.*,[40] and Başbuğ *et al.*[83] In recent years, aside the λ_2-criterion, other methods such as the swirling-strength criterion (see Sharp *et al.*[39] and Singh *et al.*[18]) or the standard Q-criterion (see Zamiri and Chung[84]) have been implemented as well. Nevertheless, these methods present the same shortcomings. In this work, vortical structures are identified using an Eulerian local region-type method, which should be fully frame invariant, take into account that the flow is inhomogeneous in all spatial directions and also lead to consistent results even if slightly different threshold values are used. Subsection III A describes the procedure employed to identify the vortical structures.

A. An objectivized version of the Q-criterion

The previously mentioned velocity-gradient-based vortex identification criteria (see Sec. III) are Galilean invariant, i.e., invariant under translation of frames but not material objective since the angular rotation rates in the spin tensor are (implicitly) measured relative to the reference frame of the observer.[57] Eulerian methods based on instantaneous point-wise values of D_{ij} can be objectivized by replacing the velocity gradient tensor with a net version of it, defined as[67,69]

$$D_{ij\star} = S_{ij} + \left(\Omega_{ij} - \langle\Omega_{ij}\rangle\right), \tag{7}$$

where $D_{ij\star}$ is a net velocity gradient tensor, $\Omega_{ij} = (\partial u_i/\partial x_j - \partial u_j/\partial x_i)/2$ is the spin/rotation rate tensor, and $\langle\Omega_{ij}\rangle = -\varepsilon_{ijk}\langle\omega_k\rangle/2$ is a spatially averaged spin tensor based on a spatially averaged vorticity, $\langle\omega_k\rangle$. Here, ε_{ijk} is the alternation or Levi–Civita tensor. Haller *et al.*[68] defines this instantaneous spatially averaged vorticity as

$$\langle\omega_k\rangle = \frac{1}{\mathcal{V}}\int_{\mathcal{V}} \omega_k \mathrm{d}\mathcal{V}, \tag{8}$$

where $\mathcal{V}$ is the volume of the flow domain. From Eq. (7), we can easily define objective versions of the different well-known vortex identification criteria.

The objectivized version of the Q-criterion,[58] in the context of incompressible flows, can be expressed as

$$Q_\star = -\frac{1}{2}\left(D_{ij\star}D_{ji\star}\right) = \frac{1}{2}\left(\Omega_{ij\star}\Omega_{ij\star} - S_{ij}S_{ij}\right) > 0, \tag{9}$$

where $Q_\star$ denotes the considered objective version of the Q-criterion and $\Omega_{ij\star} = \Omega_{ij} - \langle\Omega_{ij}\rangle$ is the corresponding net spin tensor. In this work, we have decided to use the $Q_\star$-criterion to identify vortical structures in the stirred tank considering that the classical Q-criterion is one of the most commonly used vortex identification methods (see, e.g., Mihalić *et al.*[85] for an application in turbomachinery or Wang *et al.*[86] for an application in design of marine propellers). Conceptually, $Q_\star > 0$ defines a vortex as a connected fluid region where there is more net rotation than stretching; however, similar to the original criterion, a non-zero threshold value is required for the identification of (distinct) individual structures. Moreover, this threshold should account for the fact that the swirling flow in the stirred tank is inhomogeneous in all spatial directions and its selection should not be arbitrary.

Following the arguments presented above, at a given instant, we consider that a grid point in the spatial domain belongs to a vortex if

$$Q_\star \geq \mathcal{T}\,\mathrm{stv}(Q_\star), \tag{10}$$

where $\mathcal{T}$ is the thresholding parameter and $\mathrm{stv}(Q_\star)$ is the standard deviation of the $Q_\star$-values and the selected statistical indicator to take into account inhomogeneities in the flow. Here, for a given $\mathcal{T}$, neighboring grid points satisfying Eq. (10) are connected, merged, and classified as individual structures. Connectivity is defined by the six orthogonal nearest neighbors of each grid point, and the $\mathcal{T}$-parameter is chosen following a percolation crisis analysis. In a percolation analysis, the ratio between the volume of the largest structure, V_{max}, and the total volume occupied by all the structures, V_{tot}, is computed for different values of $\mathcal{T}$. Here, as mentioned in Sec. III, the idea is to set a threshold larger than that of the critical one for proper visualization. The critical threshold corresponds to the $\mathcal{T}$-value where the percolation transition occurs, i.e., where the change of the ratio with respect to $\mathcal{T}$ attains a minimum. Before the critical threshold, most of the domain is occupied by large objects, and in practice, it is not possible to distinguish individual structures. In percolation analysis, aside the V_{max}/V_{tot}-ratio, the ratio between the total number of identified objects at a given $\mathcal{T}$, N_{tot}, to the largest number of identified structures' overall $\mathcal{T}$-values, N_{max}, is often studied as well.

For a wide range of $\mathcal{T}$-values, Fig. 5(a) displays the time average of the V_{max}/V_{tot}-ratio, whereas Fig. 5(b) shows the time average of the

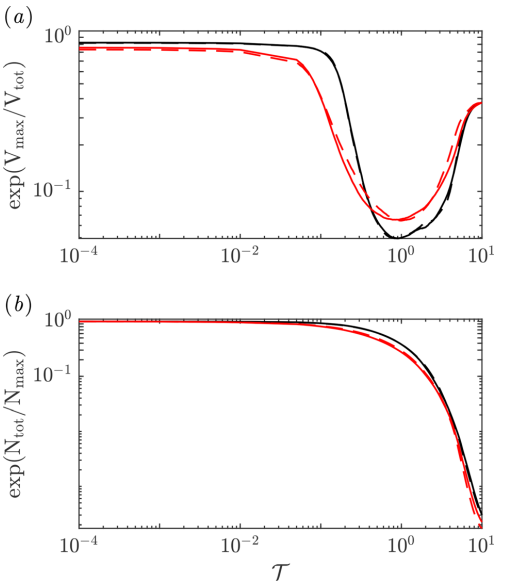

FIG. 5. Percolation diagrams: (a) $\exp(V_{max}/V_{tot})$ and (b) $\exp(N_{tot}/N_{max})$. Here, $\exp(\,)$ denotes an expectation or time-averaged quantity. Cases where the impeller operates at 800 and 600 rpm are identified by the line styles "——" and "- - -," respectively. Colors as explained in Table I.

N_{tot}/N_{max}-ratio. Considering these percolation diagrams, we observe the following:

(i) Before the percolation transition takes place, the largest identified object occupies most of the domain. Moreover, the maximum (possible) number of structures is detected as well.

(ii) The percolation transition starts at the critical threshold and goes up to $\mathcal{T} \approx 1$. For cases C600, C800, W600, and W800, the critical threshold is about 0.073, 0.077, 0.177, and 0.179, respectively.

(iii) The percolation transition appears to delay (slightly) with an increase of Reynolds number, *Re*, but this fact alone is not deemed sufficient to explain the difference between the profiles corresponding to Newtonian and shear-thinning fluid cases for a given impeller rotational speed, *N*. The overall decrease in the number of structures with shear-thinning behavior is probably the main reason for the difference in the percolation transition. A cluster of objects leading to a less populated domain is likely to fall apart more promptly.

In summary, the clustering methodology allows us to recognize the lowest practical threshold for which the vortices can still be identified individually, i.e., the critical one. Here, for comparison purposes and for more easily distinguish the individual structures, $\mathcal{T}$ is set to 1 for all fluid flow cases. At such a threshold, between 30% and 40% of

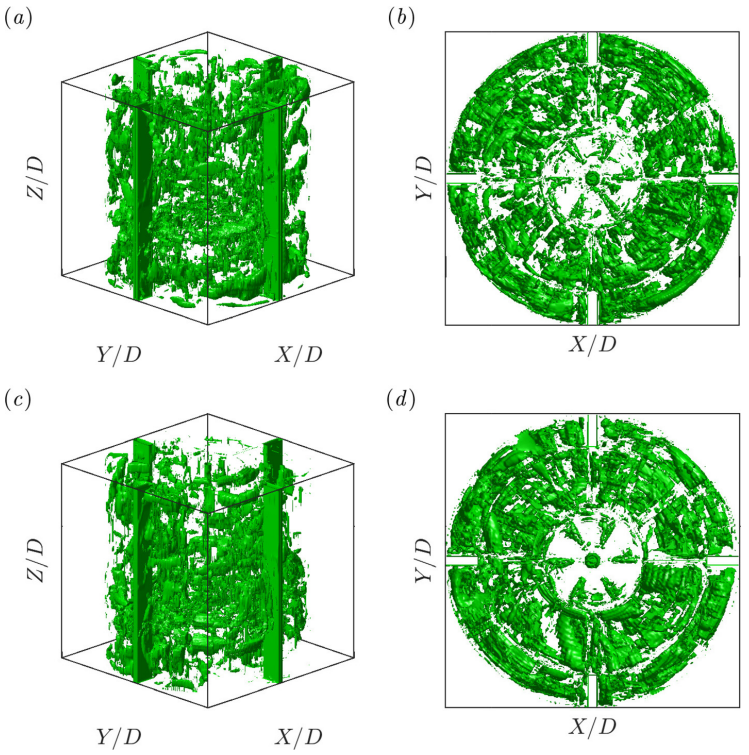

FIG. 6. Instantaneous vortical structures identified by the isosurfaces of $Q_*/\mathrm{stv}(Q_*) = 1$ for (a), (b) W800 and (c), (d) C800. 3D view displayed in (a), (c) and top view in (b), (d). Fluid flow cases as described in Table I.

the maximum (possible) number of structures are identified and the largest object does not occupy most of the domain. Due to the computational cost, a sensitivity analysis of the results to the selected threshold is not performed. Nonetheless, considering previous works (see, e.g., Cheng *et al.*[77] and Arosemena *et al.*[87]) and for threshold values larger than the that of the critical one, it is deemed probable that consistent trends in the results will be observed when the threshold value is changed to another one differing by less than an order-of-magnitude.

Figure 6 shows the vortical structures identified by criterion (10) with $\mathcal{T} = 1$ for the Newtonian and shear-thinning fluid cases when the stirred tank operates at 800 rpm. Here, despite using a threshold value close to the end of the percolation transition, it is still challenging to interpret the results. Nevertheless, from the figure, we note an apparent increase in the size of the objects and an overall decrease in the number of detected structures for the shear-thinning fluid case. Furthermore, for both the cases, some regions in the tank seem more populated than others and the range of scales of the vortices probably varies as well.

B. Regions of potential interest in a stirred tank

Regardless of the fluid flow case, the identified vortical structures in the stirred tank appear to be complex, being highly three-dimensional and presenting a wide range of scales. Considering Fig. 6, as we move in a circular manner from the tank's center toward its wall, the following three distinct regions are seen:

(i) $r = \sqrt{X^2 + Y^2} \in [0, 0.5D]$, i.e., up to the impeller. This region in comparison with the others does not seem as highly populated. Moreover, the size of the structures appears more moderated and the range of scales narrower.

(ii) $r \in (0.5D, 0.396T]$, i.e., approximately up to the baffles. Here, a larger range of scales is seen and, compared to (i), this region is more populated.

(iii) $r \in (0.396T, 0.5T]$, i.e., up to the tank's wall. In this region, compared to (i) and (ii), sizable structures are mostly seen. Visually, this also make it difficult to determine if region (iii) is more populated than (i) and (ii).

Likewise, distinct features are expected in the axial direction, as we move from bottom of the tank up to its top. However, based on Fig. 6, it is not evident which regions are the most populated or which ones present a wider range of spatial scales. Having said that, it is also well-known that the trailing vortices are generated behind the upper and lower edges of each blade, which makes the impeller region and those right next to it, compelling targets for investigation.

TABLE III. Subdomains of potential interest in a stirred tank.

Label	Regions covered	Resulting volume
SUB-A	(i)-(a)	$\pi(0.5D)^2(C-0.5h_b)$
SUB-B	(i)-(b)	$[\pi((0.5D)^2-(0.5D_i)^2)-6t_b(0.5w_b)]h_b$
SUB-C	(i)-(c)	$\pi[(0.5D)^2-(0.5DS_i)^2](T-C-0.5h_b)$
SUB-D	(ii)-(a)	$\pi[(0.396T)^2-(0.5D)^2](C-0.5h_b)$
SUB-E	(ii)-(b)	$\pi[(0.396T)^2-(0.5D)^2]h_b$
SUB-F	(ii)-(c)	$\pi[(0.396T)^2-(0.5D)^2](T-C-0.5h_b)$

In consequence, there are (at least) three regions of potential interest in the axial direction:

(a) $Z \in [0, C-0.5h_b]$, i.e., up to the lower edge of each impeller blade. This is the lower circulation loop region (see illustration in Fig. 1).
(b) $Z \in (C-0.5h_b, C+0.5h_b]$, i.e., up to the upper edge of each impeller blade. This is the impeller region.
(c) $Z \in (C+0.5h_b, T]$ constituting the remaining part of the tank where the upper circulation loop is observed (see illustration in Fig. 1). It is worth remarking that the upper circulation loop does not extend to the top of the tank and there is a badly mixed region occupying 14%–18% of the total tank volume.[16] In the case of shear-thinning fluid rheology, such a badly mixed region is probably larger.

The regions of potential interest in the stirred tank lead to certain subdomains and, most of them, are summarized in Table III. Here, six different subdomains consisting of either cylindrical or tube-like volumes are considered (see Fig. 7). It is noted that the seemingly clustered region of structures between baffles and tank wall is not explored. The characterization of the identified vortices in these subdomains of potential interest is presented in Sec. IV. Here, a vortical structure is included in the analysis of a particular subdomain if the centroid of such a structure, (X_c, Y_c, Z_c), is encountered in that subdomain. Further details about spatial distribution of the detected vortices are discussed in Subsection IV C.

IV. CHARACTERIZATION OF VORTICAL STRUCTURES

Before continuing with Subsections IV A–IV D, we would like to stress that although the presented results correspond to single-phase flow simulations, their discussion is vastly motivated by the possible implications in multiphase flow systems. This is particularly the case for systems in which the local fraction of the dispersed phase is always small enough such that the influence of the dispersed phase over the continuous one is negligible. Hence, the reason for introducing different representative aspects in the context of interactions with fluid particles in the following.

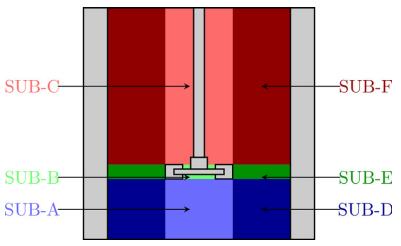

FIG. 7. Schematic representation of subdomains of potential interest as described in Table III. Subdomains A, B, C, D, E, and F colored in light blue, light green, light red, dark blue, dark green, and dark red, respectively.

A. Size and number density

Information about the size of the structures is relevant for understanding and modeling the interaction between turbulent vortices and fluid particles. For instance, in several models,[27] particle breakup is presumed to take place when the particles interact with vortices of comparable size. In this work, particular attention is paid to structures with an equivalent diameter $d_{eq} = (6V_{core}/\pi)^{1/3}$, where V_{core} is the vortex core volume, which is equal to 2, 5, and 8 mm since such structures are representative of those likely to interact with mother particles of typical size used in laboratory setups, see, e.g., Solsvik and Jakobsen[88] where the injected mother bubble diameters were in the range of 2.5–3.4 mm or Vejražka *et al.*[89] where the bubbles where in the range of 1.8–5 mm.

For different cases, Fig. 8(a) shows the resulting d_{eq} normalized by the equivalent diameter of the largest detected structure, $\max(d_{eq})$,

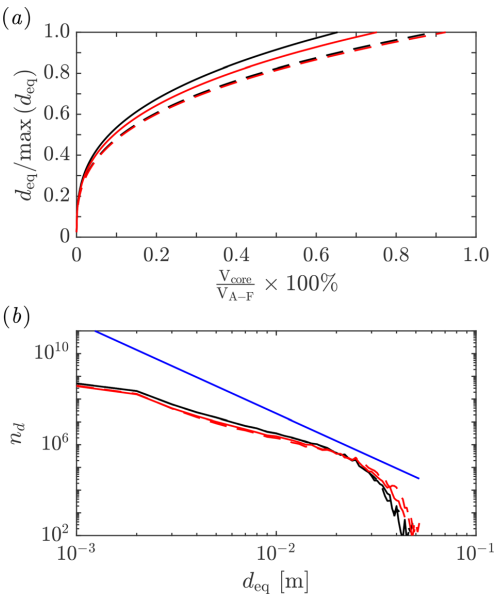

FIG. 8. Normalized size indicator and number density of the identified structures: (a) $d_{eq}/\max(d_{eq})$ vs $(V_{core}/V_{A-F}) \times 100\%$ and (b) n_d vs d_{eq}. Cases where the impeller operates at 800 and 600 rpm are identified by the line styles "——" and "- - -," respectively. Colors as explained in Table I. In (b), the blue line denotes $n_d = 24\mathcal{A}/[(2\pi)^{5/3}\mathcal{B}d_{eq}^4]$, which is the theoretical limit corresponding to the inertial subrange considering $\mathcal{A} = 1.5$[91] and $\mathcal{B} = 4.82\mathcal{A}$.[92]

as a function of the percentage volume fraction occupied by the corresponding structure, $V_{core}/V_{A-F} \times 100\%$. Here, V_{A-F} is the volume of the fluid in the subdomains A–F (see Table III). The plot includes all possible d_{eq} based on V_{core} of the structures detected in the subdomains A–F. As seen from Fig. 8(a), for a given type of fluid, an increase in N is leading to finer structures and to a decrease in the range of length scales, which is to be expected since Re is increasing as well. On the other hand, when comparing Newtonian and shear-thinning fluid cases at the same N, more sizable structures are found but not within a narrow range of length scales. This increase in size with the shear-thinning behavior is consistent with previous findings for the simpler turbulent channel flow of GN fluids (see Arosemena *et al.*[87]). Regarding the range of length scales, also for the turbulent channel flow of GN fluids, it is known that both the fluid rheology and the Reynolds number have an influence in the velocity–vorticity correlation associated with change-of-scale-effects.[90] In this case, when comparing the Newtonian and shear-thinning fluid cases at the same N, Re is probably playing a major role over the range of length scales. From a practical point of view, it is worth commenting that the size indicator, d_{eq}, appears to be in the range of $\approx$ 1 mm to 52, 47, 53, and 49 mm for cases W600, W800, C600, and C800, respectively.

Another important feature when considering the interaction with fluid particles, it is the number of structures of a given size in the stirred vessel. In the aforementioned example about particle breakup, the likelihood of the breakup event will possibly increase if the number of structures of comparable size to the mother particle is large rather than small. A quantitative indicator of the amount of vortical structures is the number density n_d defined as

$$n_d = \frac{n}{n_f V_{\text{fluid}} \Delta d_{\text{eq}}}, \tag{11}$$

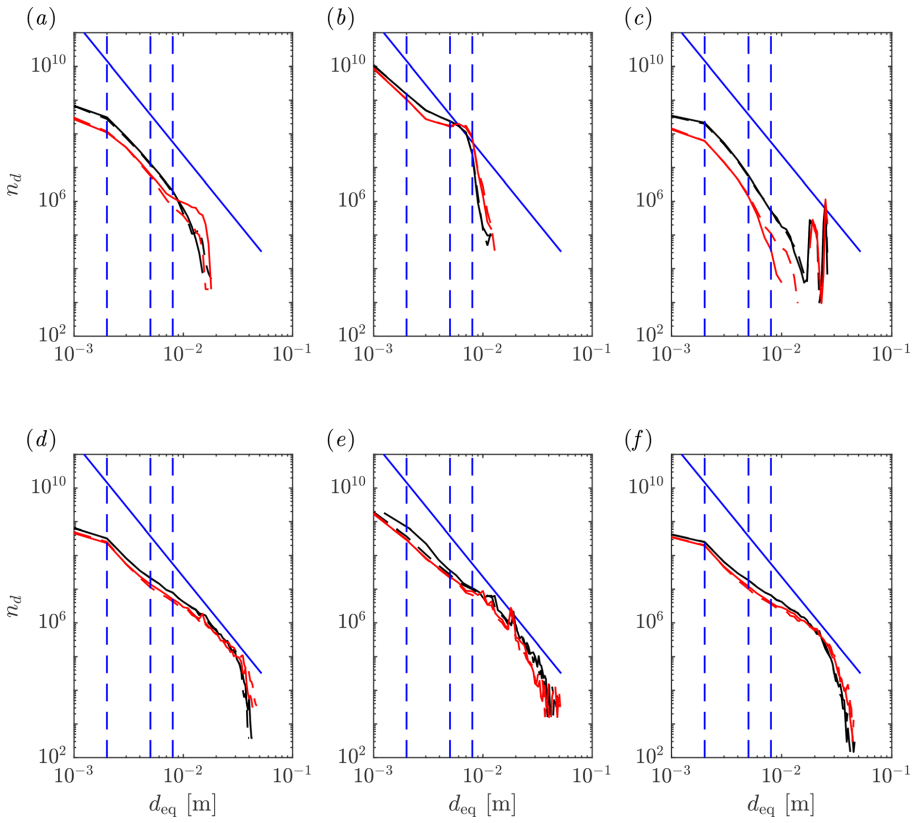

FIG. 9. Number density, n_d, as the function of the size indicator, d_{eq}, for (a) SUB-A, (b) SUB-B, (c) SUB-C, (d) SUB-D, (e) SUB-E, and (f) SUB-F. Cases where the impeller operates at 800 and 600 rpm are identified by the line styles "——" and "- - -," respectively. Colors as explained in Table I. In (a)–(f), the blue, straight line denotes $n_d = 24\mathcal{A}/[(2\pi)^{5/3}\mathcal{B}d_{eq}^4]$, which is the theoretical limit corresponding to the inertial subrange, considering $\mathcal{A} = 1.5$[91] and $\mathcal{B} = 4.82\mathcal{A}$,[92] whereas the blue, dashed lines mark values of constant d_{eq} of interest; i.e., $d_{eq} = 2$, 5, and 8 mm, respectively.

where n is the number of identified vortices of size between d_{eq} and $d_{eq} + \Delta d_{eq}$ for the collected realizations, n_f is the number of collected flow fields, V_{fluid} is the considered fluid volume within the stirred tank, i.e., $V_{fluid} = V_{A-F}$ for a number density defined in the subdomains A–F, and Δd_{eq} is the bin width for n. In other word, n_d is the time-averaged number of identified vortices of size between d_{eq} and $d_{eq} + \Delta d_{eq}$ per bin width in the considered fluid volume. Figure 8(b) displaying the number density allows us to note a monotonic decrease in n_d with increasing d_{eq} for all cases. Moreover, keeping in mind the models for n_d proposed for the whole energy spectrum,[93] we observe that the profiles appear to depict only the energy containing and inertial subranges. This is in line with the fact that large eddy simulations have been carried out. With respect to trends with fluid rheology and impeller speed, at small d_{eq} values, there is an overall decrease in the number density with shear-thinning behavior when compared to the Newtonian cases, whereas there is almost no difference in the profiles of the same fluid at different N values. Therefore, under the premise that the interaction with particles of typical size found in laboratory setups (leading to their breakup and actual mixing) is probably occurring with structures of comparable size, i.e., those having small d_{eq}, a decrease in particle breakage and dispersed–continuum phases mass transfer are expected for shear-thinning behavior in comparison with a Newtonian fluid flow operating at the same N. Recent experimental studies of bubble–liquid mass transfer[94,95] have revealed that indeed there is a decrease in bubble breakage and volumetric mass transfer coefficient with shear-thinning rheology. See trends for the bubble size distributions and the volumetric mass transfer coefficient in, e.g., Ali and Solsvik[94] for water compared to the CMC cases at the same operational conditions and axial liquid height. On the other hand, at large d_{eq}, the rapid decrease in n_d is seemingly delayed both with decreasing N and shear-thinning fluid behavior; consistently with what it is expected as the Reynolds number decreases.

Additional insight into the interaction with fluid particles, in particular regions of the tank, can be gained by considering the n_d profile in the subdomains A–F as shown in Fig. 9. Here, aside the already noted decrease in n_d with shear-thinning behavior for $d_{eq} \lesssim 10^{-2}$ m, the following particularities are observed: (i) a wider range in d_{eq} is seen for subdomains D–F, (ii) larger n_d values for structures with $d_{eq} = 2$, 5, and 8 mm are perceived in subdomains B, D, and E, (iii) a conspicuous n_d value is noticed for $d_{eq} \approx 18$ mm in subdomain E, and (iv) for $d_{eq} \gtrsim 10^{-2}$ m, n_d appears to peak twice in subdomain C; first between 18 mm $\lesssim d_{eq} \lesssim$ 20 mm and then at $d_{eq} \approx 25$ mm. These particularities have the following (potential) implications: (i) greater range of turbulent scales for subdomains D–F, (ii) improved likelihood of particle breakage and overall mixing in subdomains B (impeller region), D and E, (iii) evidence of trailing vortices and/or remnant of them at an intermediate scale, and (iv) existence of sizable structures

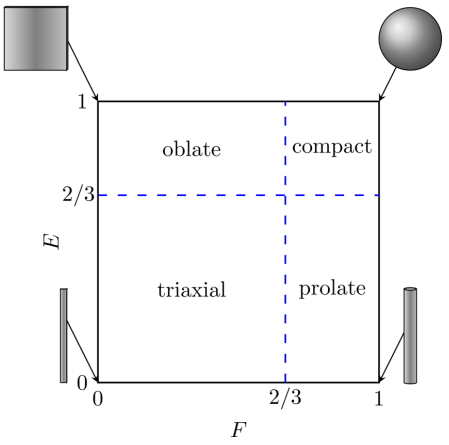

FIG. 10. Elongation, E, against flatness, F, diagram for classifying structures based on Zingg's categories.[97] The corners also illustrate the extreme cases:[78] ribbons (0,0), tubes (1,0), sheets (0,1), and spheres (1,1).

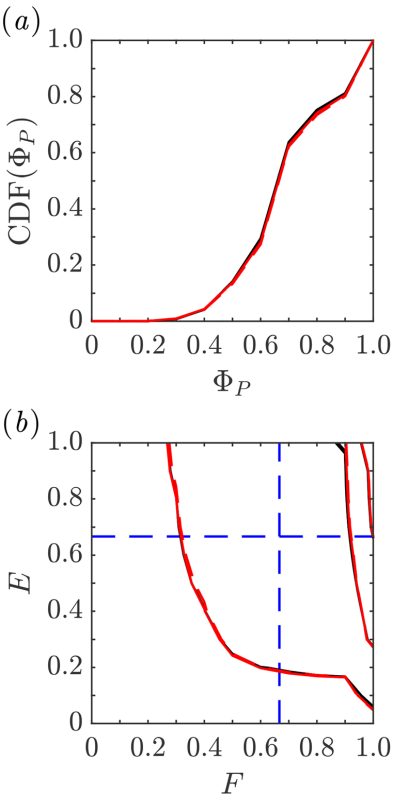

FIG. 11. Shape indicators of the identified structures across the stirred tank: (a) CDF of the maximum projection sphericity, Φ_P, and (b) JCDF of E and F, respectively. Cases where the impeller operates at 800 and 600 rpm are identified by the line styles "——" and "- - -," respectively. Colors as explained in Table I. In (b), the levels represented contain 99%, 70%, and 30% of the data. Also, the blue lines mark values of constant E and F, where E and F are equal to 2/3.

above the impeller region, probably very large structures toward the stagnation region of the tank and MI-vortex, respectively.

B. Shape

In theoretical models for breakup and coalescence of fluid particles, it is common to represent the turbulent vortices interacting with the drops or bubbles as spherical structures. Thus, the reason for using an equivalent diameter based on a spherical geometry for quantifying the size of the structures in Subsection IV A. Nonetheless, this assumption is rather questionable even for representing the largest, energy containing eddies, considering that the turbulent flow in a stirred tank is highly complex, showing different degrees of anisotropy across the vessel.[21]

Morphological analyses, typical for solid particles, include properties such as roughness, roundness (measure of the sharpness of the edges and corners of an object), and sphericity (degree to which an object approximates the shape of a sphere and measure of equidimensionality). Analogously, we can consider the sphericity and other length measurements to study the overall shape of the detected vortices. Here, the shape of the identified vortical structures is determined considering their maximum projection sphericity[96] defined as

$$\Phi_P = \left(\frac{d_S^2}{d_L d_I}\right)^{1/3}, \tag{12}$$

and their flatness and elongation parameters[97] are given by

$$F = \frac{d_S}{d_I}, \tag{13a}$$

$$E = \frac{d_I}{d_L}, \tag{13b}$$

respectively. In Eqs. (12) and (13), d_S, d_I, and d_L denote the shortest, intermediate, and largest dimensions of the oriented bounding-box (OBB) of the corresponding structure. The OBB was computed by principal component analysis (PCA), see e.g., Jolliffie.[98] The sphericity index (12) represents the ratio between the maximum projection area of a sphere of the same volume as the structure to the maximum projection area of the structure and has a maximum value of 1 for structures with the perfect spherical shape. On the other hand, the ratios F and E can be used to broadly classify the structures into four categories:[97] oblate if $F < 2/3$ and $E > 2/3$, compact if $F > 2/3$ and $E > 2/3$, triaxial if $F < 2/3$ and $E < 2/3$, and prolate if $F > 2/3$ and $E < 2/3$ (see Fig. 10). It is worth mentioning that compared to the so-called true sphericity,[99] Φ, the maximum projection sphericity is higher and lower for prolate and oblate structures, respectively. For compact and triaxial structures, $\Phi_P \approx \Phi$. Also, it is relevant to remark that in the context of turbulent structures, Moisy and Jiménez[78] proposed a similar approach to characterize the geometry of the structures. In the study, a different methodology is used to compute the lengths, d_S, d_I, and d_L, but the characterization is based on the same two dimensionless aspect ratios, F and E. In the case of ideal ribbons, tubes, sheets and spheres, these parameters are of the order of (0,0), (1,0), (0,1), and (1,1), respectively[78] (see Fig. 10).

Figure 11(a) shows the cumulative distribution function, CDF, of Φ_P across the stirred vessel for the cases described in Table I. As seen from this figure, the probability of the identified vortices being non-spherical is close to 80%, i.e., $\mathrm{CDF}(\Phi_P \leq 0.9) \approx 0.8$ for all cases. Moreover, there are two ranges in Φ_P where the probability is fairly high; one is seen for $0.6 < \Phi_P \leq 0.7$ where the probability is close to 35% and the other is seen for $0.9 < \Phi_P \leq 1.0$ corresponding to perfect spherical structures and those approaching them. With respect to the length-related parameters, Fig. 11(b) displaying the joint cumulative distribution function, JCDF, of F and E across the tank allows us to note that about 70% of the data is likely to fall into the compact and prolate categories, whereas only 30% falls into the compact category alone. The fact that $\mathrm{CDF}(\Phi_P)$ and $\mathrm{JCDF}(F, E)$ are similar for different tank rotational speeds and working fluid rheology implies that the corresponding probability density and joint probability density functions, $\mathrm{PDF}(\Phi_P)$ and $\mathrm{JPDF}(F, E)$, are also similar and, thus, suggest that the cases are statistically identical regardless of Re and fluid behavior. In other words, at least for the considered cases, the effects of shear-thinning rheology and Reynolds number over the shape of the identified structures in the whole tank appear negligible. In addition, Fig. 12 displaying the isocontours of $\mathrm{JPDF}(F, E)$ for case W800 allows us to observe two clear peaks; one for $0.9 < F \leq 1.0$, $0.2 < E \leq 0.3$ and another for $0.9 < F \leq 1.0$, $0.9 < E \leq 1.0$. These peaks correspond to the two aforementioned regions of high probability in Fig. 11(a). It is also worth mentioning that the expectation (mean value) for Φ_P, F, and E is 0.68, 0.83, and 0.5, respectively. To summarize, considering the information revealed by Figs. 11 and 12, although a substantial number of the detected vortices in the stirred tank present sphere-like shape, the majority do not. Furthermore, tube-like vortical structures are as likely to appear as the spherical blobs if not more so.

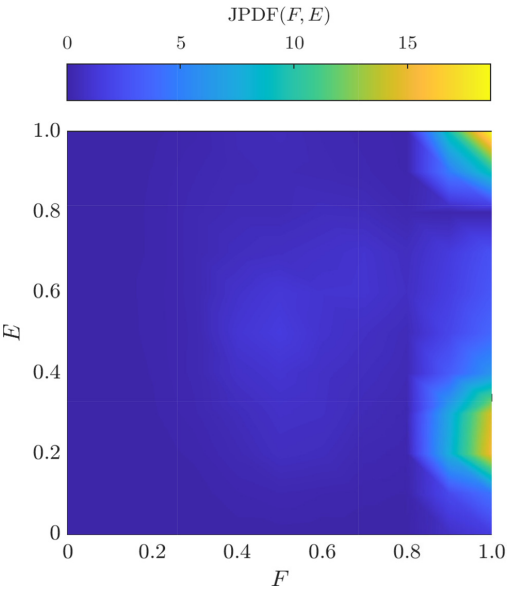

FIG. 12. Isocontours of the JPDF of E and F across the stirred tank for case W800 (see Table I).

Aside considering the form of the structures in the whole vessel, it is also reasonable to ponder which shapes are more likely to be observed locally and for those structures within a d_{eq}-range of interest. Figures 13(a)–13(f) present the JCDF(F, E) for cases W800 and C800 in different subdomains. Even though similar profiles were found when comparing Newtonian and shear-thinning cases in the entire tank, it is judged possible that these differences will arise in different subdomains and/or when considering structures of a given size in these subdomains. As seen from the figure, the probability of having compact and prolate structures remains high for all considered subdomains albeit compact structures are deemed more likely to be observed for subdomains B and E where most of the energy is contained. With respect to the influence of the shear-dependent rheology, the same figure reveals a slight increase in the likelihood of seeing more ribbon-like structures with shear-thinning rheology in the different subdomains; see consistent movement to the left and bottom of curve covering 99% of all data in subdomains A–F for case C800. Figures 13(a)–13(f) also display the peaks values of the JPDF(F, E) for a particular d_{eq}-range of interest in the subdomains A–F. In subdomain C, with independence of the fluid rheology, those structures considered to be very large and the MI-vortex appear almost and fully tubular, respectively, whereas in subdomain E, those structures hypothesized as trailing vortices seem fairly triaxial. The influence of the shear-thinning rheology over the remaining smaller structures of interest seems more complicated. On a first impression, at least to a moderate extent, it appears that structures of comparable size with $d_{eq} \lesssim 10^{-2}$ m present a different shape-related probability distribution if the fluid rheology is non-Newtonian. Nonetheless, in general, the peak of JPDF(F, E) for the considered d_{eq}-ranges in the cases W800 and C800 suggests a higher probability of the structures being more similar to ribbons and tubes than to sheets and spheres.

C. Distribution and organization in space

Under the premise that mixing is enhanced with a larger probability of interaction between vortical structures and fluid particles, a matter of practical importance is the spatial distribution of the vortices in the tank. Although it has been showed that the largest number density of vortical structures is found within subdomains B, D, and E (see Subsection IV A), information is still pending about the positioning in space where there are higher probabilities of encountering those structures. Figures 14(a)–14(f) show the marginal JCDF($r_c/D, Z_c/D$), i.e., for all possible angular positions of the centroids and where $r_c = \sqrt{X_c^2 + Y_c^2}$, in different subdomains. The figure also presents the $(r_c/D, Z_c/D)$ coordinates corresponding to peaks in the marginal JPDF($r_c/D, Z_c/D$) for a particular d_{eq}-range of interest only for cases

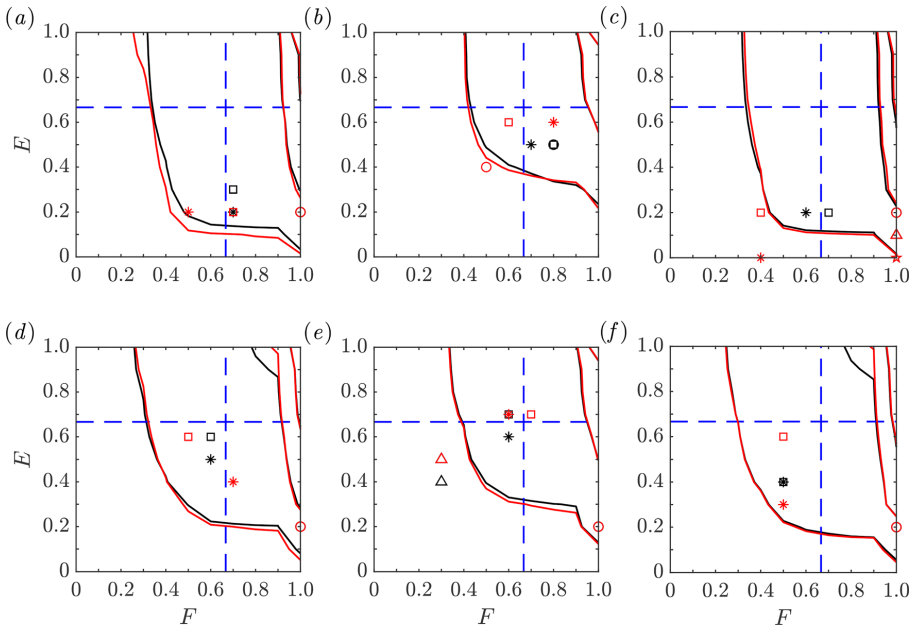

FIG. 13. JCDF of *E* and *F* for (a) SUB-A, (b) SUB-B, (c) SUB-C, (d) SUB-D, (e) SUB-E, and (f) SUB-F. The levels represented contain 99%, 70%, and 30% of the data, respectively, for cases W800 and C800. The blue lines mark values of constant *E* and *F*, where *E* and *F* are equal to 2/3. Other colors as explained in Table I. Also, the markers "○," "∗," "□," and "⋆" are used to identify the (*E*, *F*)-values where the JPDF(F, E) peaks for d_{eq} = 2–3, 5–6, 8–9, and 25–26 mm, respectively, for cases W800 and C800. In addition and for the same cases, the "△"-marker used in (c) and (e) represents the values where the joint probability peaks for d_{eq} = 18–21 and 18–19 mm, respectively.

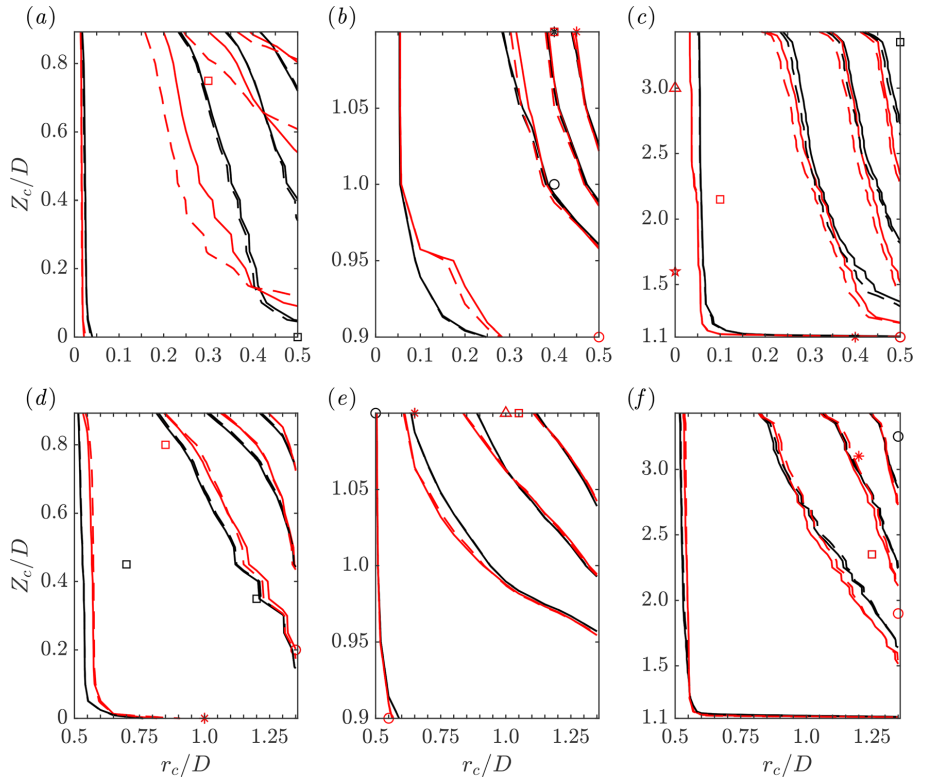

FIG. 14. Marginal JCDF of the normalized centroids in the radial and axial direction, r_c/D and Z_c/D, for (a) SUB-A, (b) SUB-B, (c) SUB-C, (d) SUB-D, (e) SUB-E, and (f) SUB-F. Cases where the impeller operates at 800 and 600 rpm are identified by the line styles "——" and "- - -," respectively. The levels represented contain 99%, 70%, 50%, and 30% of the data. Colors as explained in Table I. Also, the markers "○," "∗," "□," and "⋆" are used to identify the $(r_c/D, Z_c/D)$-values where the marginal JPDF$(r_c/D, Z_c/D)$ peaks for $d_{eq} = 2$–3, 5–6, 8–9, and 25–26 mm, respectively, for cases W800 and C800. In addition and for the same cases, the "△"-marker used in (c) and (e) represents the values where the marginal joint probability peaks for $d_{eq} = 18$–21 and 18–19, respectively.

W800 and C800. As seen from Fig. 14, in comparison with changes in rotational speed for a given working fluid, changes in rheology for the tank operating at a specified N seem to impact the distributions in a more significant manner. Compared to the Newtonian cases for subdomains A and C, the curves covering 99% of the data move toward positions closer to the center of the tank with shear-thinning rheology, whereas the opposite behavior is observed for subdomains D and F. These trends are likely due to pronounced differences in the local flow since the changes are more evident as we approach the top and bottom walls of the stirred vessel, i.e., $Z/D \approx 3.43$ and $Z/D = 0$, respectively. On the other hand, with respect to the subdomains with the largest number density and for all cases, it is remarked that at least 70% of the data falls into $0.25 < r_c/D \leq 0.5, 0.95 < Z_c/D \leq 1.11$; $0.8 < r_c/D \leq 1.36, 0.15 < Z_c/D \leq 0.89$; and $0.6 < r_c/D \leq 1.36, 0.95 < Z_c/D \leq 1.11$ for subdomains B, D, and E, respectively. Regarding the most probable $(r_c/D, Z_c/D)$ coordinates for the considered d_{eq}-range, as with the shape indicators in Subsection IV A, a rather hectic behavior is observed. Nonetheless, for the impeller region (SUB-B), it does appear that structures with $d_{eq} \lesssim 10^{-2}$ m are likely to be detected with centroids at radial positions larger than $0.4D$. Finally, from Figs. 14(c) and 14(e) and with independence of the fluid rheology, it is remarked that structures considered to be very large and the MI-vortex appear around the center of the tank with $Z_c/D \approx 3$ and 1.6, respectively, while those structures associated with trailing vortices are probably observed with $r_c/D \approx 1$ and $Z_c/D \approx 1.1$.

Another interesting aspect, particularly when considering that high deformation and eventual breakup of fluid particles may occur due to interactions with pairing of eddies,[100] it is the organization in space of nearby structures sharing similar size. Here, the nearest structure (j) to a vortex (i) is determined by considering the minimum, absolute distance between (i), and all other detected structures (k). Thus,

$$d^{(i,j)} = \min\left(\sqrt{\left(X_c^{(k)} - X_c^{(i)}\right)^2 + \left(Y_c^{(k)} - Y_c^{(i)}\right)^2 + \left(Z_c^{(k)} - Z_c^{(i)}\right)^2}\right) = \sqrt{\left(X_c^{(j)} - X_c^{(i)}\right)^2 + \left(Y_c^{(j)} - Y_c^{(i)}\right)^2 + \left(Z_c^{(j)} - Z_c^{(i)}\right)^2}, \quad (14)$$

where $d^{(i,j)}$ is the absolute distance between an structure (i) and the nearest one to it (j). In addition, following the works of Lozano-Durán *et al.*,[76] Dong *et al.*,[79] Osawa and Jiménez,[81] and Cheng *et al.*,[77] we consider that two structures, (i) and (j), are of similar size if their size indicator differs by less than a factor of 2, i.e., if $0.5 < d_{eq}^{(i)}/d_{eq}^{(j)} < 2$. To evaluate the likelihood of the nearest structure to vortex (i), i.e., the structure at $d^{(i,j)}$, being of similar size, we consider the PDF($d_{eq}^{(i)}/d_{eq}^{(j)}$) in the different subdomains and for all cases, see Figs. 15(a)–15(f). As seen from this figure, PDF($d_{eq}^{(i)}/d_{eq}^{(j)}$) peaks at $d_{eq}^{(i)}/d_{eq}^{(j)} \approx 1$ regardless of the case and considered subdomain in the tank. Moreover, when considering a particular subdomain, this PDF appears fairly similar for the different cases described in Table I. From Fig. 15, we also note that the probability of having the nearest structure of similar size is, at least, of 80% for SUB-A–F. As for the PDF($d_{eq}^{(i)}/d_{eq}^{(j)}$) corresponding to a given d_{eq}-range of interest, Fig. 15 also displays the peaks for $d_{eq} = 2$–3, $d_{eq} = 5$–6, and $d_{eq} = 8$–9 mm, respectively, for cases W800 and C800. As observed from the figure, irrespective of the subdomain and for both the cases, the probability distribution peaks within $0.5 < d_{eq}^{(i)}/d_{eq}^{(j)} < 2$ only for the lowest d_{eq}-range of interest.

Subsequently, to gain insight into the spatial organization of nearby structures sharing similar size, we will discuss their relative position with respect to the Cartesian coordinate system. The normalized relative separation between structures (i) and (j) in the X-, Y-, and Z-directions are defined as

$$dX = \frac{X_c^{(j)} - X_c^{(i)}}{d^{(i,j)}}, \quad (15a)$$

$$dY = \frac{Y_c^{(j)} - Y_c^{(i)}}{d^{(i,j)}}, \quad (15b)$$

$$dZ = \frac{Z_c^{(j)} - Z_c^{(i)}}{d^{(i,j)}}, \quad (15c)$$

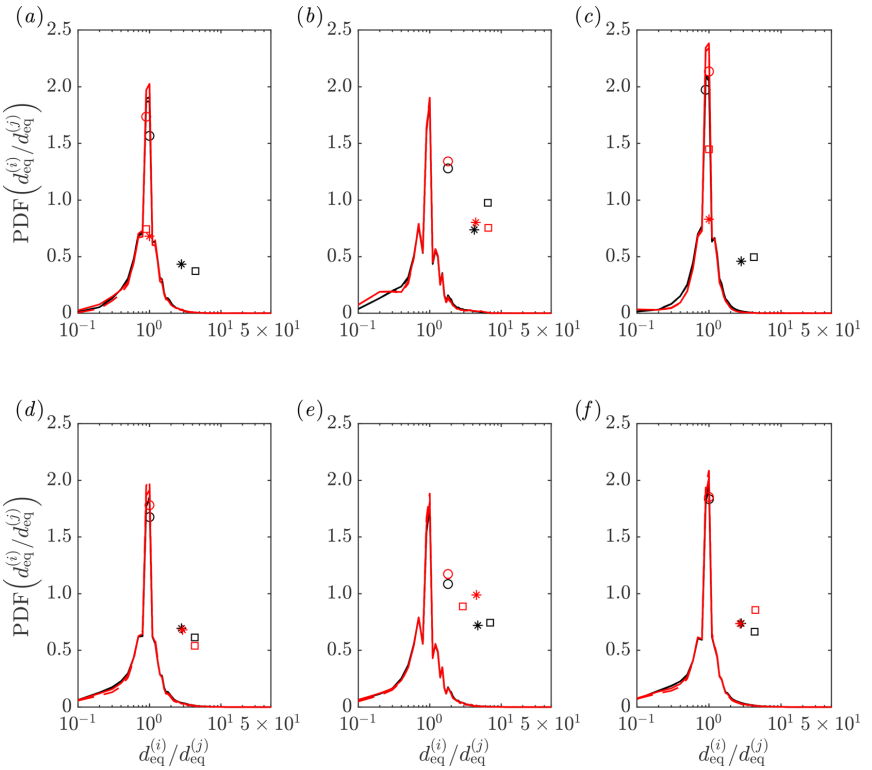

FIG. 15. PDF of ratio between the size indicator of a vortex "i" to the nearest vortex "j" to it, $d_{eq}^{(i)}/d_{eq}^{(j)}$, for (a) SUB-A, (b) SUB-B, (c) SUB-C, (d) SUB-D, (e) SUB-E, and (f) SUB-F. Cases where the impeller operates at 800 and 600 rpm are identified by the line styles "—" and "- - -," respectively. Colors as explained in Table I. Also, the markers "○," "∗," and "□" are used to identify the $d_{eq}^{(i)}/d_{eq}^{(j)}$-values where the PDF($d_{eq}^{(i)}/d_{eq}^{(j)}$) peaks for $d_{eq} = 2$–3, 5–6, and 8–9 mm in cases W800 and C800.

respectively. From the perspective of analytic geometry, relationships (15) represent the direction cosines of a straight line joining the centroids of structures (i) and (j). As a consequence, these relationships range from –1 to 1 for corresponding direction angles ranging from π to 0. For SUB-A–F, Fig. 16 shows the marginal probabilities, PDF(dX), PDF(dY), and PDF(dZ). We remark that the figure only displays the marginal probabilities for case W800 since similar distributions were found for cases W600, C600, and C800 (not shown here). As seen from the figure, for all subdomains, PDF(dX) and PDF(dY) seem statistically identical and the largest values in these marginal probabilities are observed for dX and dY equal to $-\sqrt{2}/2, 0$, and $\sqrt{2}/2$. In contrast and with respect to PDF(dZ), the marginal probability always peaks at $dZ = 0$ and, only for subdomains B and E, peaks at $dZ = \pm\sqrt{2}/2$ are moderately discernible. We emphasize that these finding about the marginal probabilities only indicate which direction cosine is more probable when considering all possible values for the two remaining direction cosines. Nonetheless, the consistent peaks at dX and dY equal to $\pm\sqrt{2}/2$ and the fact that, in the Z-direction, the most likely outcome appears to be a right angle with the nearest structures of similar size, it is already conveying. Figure 17 shows the marginal JPDF(dX, dZ) for case W800 and the subdomains with the largest number density, SUB-B, -D, and -E. As displayed by this figure, the global maxima of the marginal joint distributions for these subdomains are the same and occur at $dX \approx \pm\sqrt{2}/2, dZ = 0$. Likewise, for subdomain E, additional local maxima is clearly observed at $dX = 0, dZ \approx \pm\sqrt{2}/2$. Recalling that only two of the three direction cosines are independent, it is expected that $dY = \pm dX$ for the global maxima and $dY = \pm dZ$ for the additional maxima in SUB-E. These findings imply a high probability of encountering the nearest structures having similar size, side-by-side in the radial direction. Furthermore, these pairs of nearest structures having similar size are unlikely to overlap and seem organized both in the X and Y directions with separation of about $d^{(i,j)}$. It is worth mentioning that based on the other found maxima, at least for SUB-E, it is probable to encounter nearest structures having similar size on top of each other without perfect alignment of their centroids. Also, considering the similarities between the marginal distributions for subdomains A, C, D, and

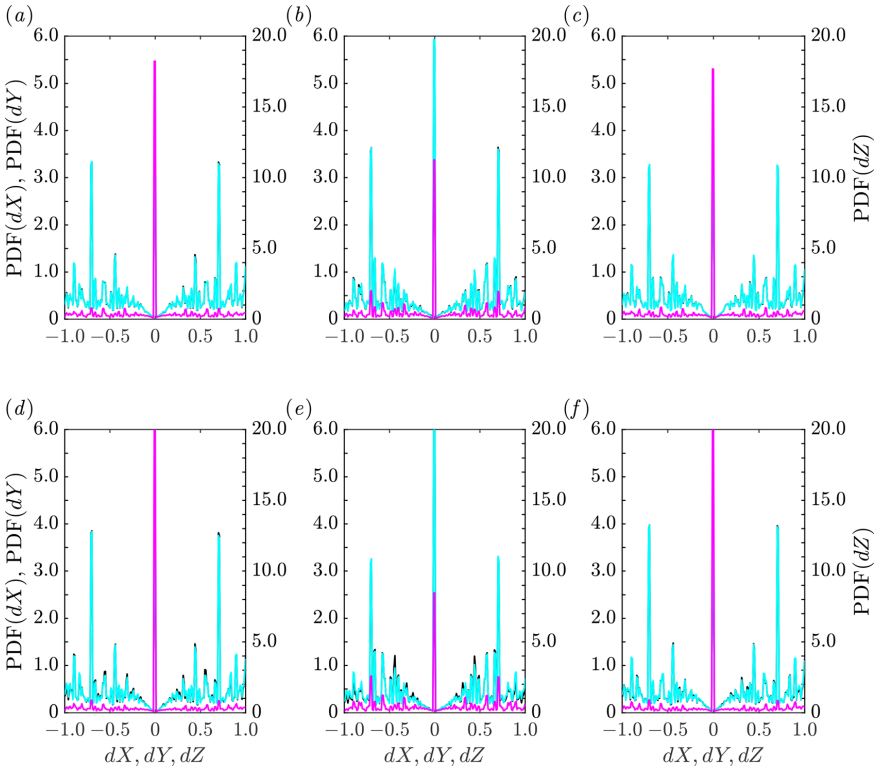

FIG. 16. Marginal PDF of the normalized relative separation between nearest structures of similar size, dX, dY, and dZ, for case W800 as described in Table I and for (a) SUB-A, (b) SUB-B, (c) SUB-C, (d) SUB-D, (e) SUB-E, and (f) SUB-F. Black, cyan, and magenta colors are used to represent the profiles corresponding to the marginal probabilities of dX, dY, and dZ, respectively.

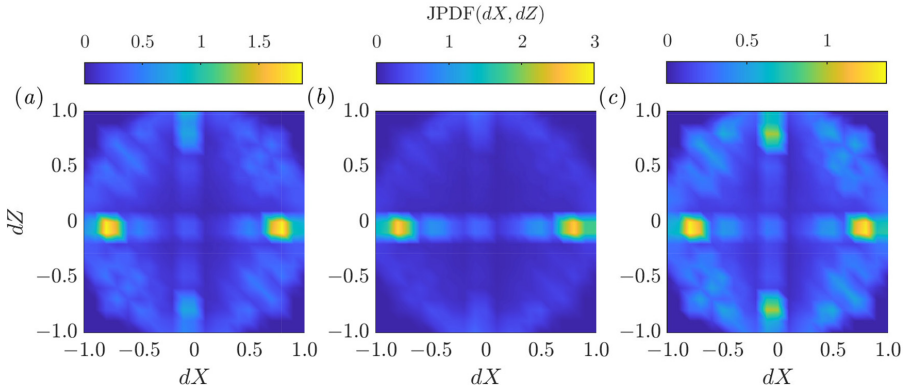

FIG. 17. Isocontours of the marginal JPDF of *dX* and *dZ* for case W800 as described in Table I and for (a) SUB-B, (b) SUB-D, and (c) SUB-E.

F (see Fig. 16), a similar organization as the one observed for SUB-D is expected for SUB-A, -C, and -F.

D. Correlation with kinetic energy

Finally, when thinking about dispersion of fluid particles and actual mixing in a stirred vessel, it is important to explore whether the identified structures are positioned in regions with high energy contents or not. Many criteria for deformation and eventual breakup of drops and bubbles are based on energy balances between the fluid particles and the surrounding eddies, see e.g., Liao and Lucas[25] and Solsvik *et al.*[27] In this work, to address the degree of correlation between the identified vortices and the kinetic energy due to turbulence and the periodic blade passage (associated with the trailing vortices), we consider the following correlation coefficient:

$$\mathcal{C}_{\mathrm{Q}_\star,k} = \frac{\mathrm{cov}(\mathrm{Q}_\star, k)}{\mathrm{stv}(\mathrm{Q}_\star)\mathrm{stv}(k)}, \tag{16}$$

where $\mathrm{cov}(\mathrm{Q}_\star, k)$ is the covariance or mixed second moment of $\mathrm{Q}_\star$ subject to condition (10) and $k = (u_i - \exp(u_i))^2/2$, i.e., the instantaneous kinetic energy due to turbulent fluctuations and the periodic component imposed by the frequency of the blade passages. Here, $\mathrm{stv}(k)$ is the standard deviation of k and $\exp(u_i)$ is the expectation or time-averaged value for u_i. The correlation coefficient is a statistical indicator about the degree of (linear) correlation between two stochastic variables. If the coefficient is zero, the variables are entirely irrelevant (in a linear sense), whereas if it is 1, they are perfectly correlated. In the case where the coefficient is -1, the variables are perfectly negatively correlated and the increase in one leads to the (linear) decrease in the other. As a consequence, $\mathcal{C}_{\mathrm{Q}_\star,k}$ is a practical tool to determine how closely related is the vortex indicator, $\mathrm{Q}_\star$, to k.

For the regions exhibiting the largest number density of structures, the circumferential averages $\langle\,\rangle_\theta$, i.e., averages over the angular direction θ, corresponding to $\mathcal{C}_{\mathrm{Q}_\star,k}$ and k are presented in Figs. 18–20 for cases W600, W800, and C800. In these figures, $\langle k\rangle_\theta$ is normalized by its local maximum, $\max_{SUB}\langle k\rangle_\theta$, in that particular subdomain. As displayed by the figures, the isocontours corresponding to cases W600 and W800 seem quite similar, whereas case C800 presents some differences. For the shear-thinning case, more discernible patches of moderate correlation values are observed at larger radial distances and the regions of high kinetic energy seem more localized. Nonetheless, regardless of the case and for $r/D \gtrsim 0.25$, positive and fairly high correlation values are noted in the subdomain occupied by the impeller. Moreover, such a region, where the passage of the blades takes place, appears as the most energetic in SUB-B, see Figs. 18(d)–20(d). With respect to subdomains D and E, the largest correlation values are also seen in the vicinity of the most energetic regions for the three cases, see Figs. 18(b)–20(b), 18(c)–20(c), 18(e)–20(e), and 18(f)–20(f). In addition, also for subdomains D and E, it is observed that low correlation regions corresponds to those with low energy contents but a high distribution of vortical structures (see Subsection IV C). Overall, these findings suggest that strong vortices in the sense of how much their rotation rate exceeds their strain rate are detected in regions with a significant amount of k, and in such regions, a linear approximation between $\mathrm{Q}_\star$ and k may be reasonable to some extent. Conversely, as one moves from the impeller region and k solely represents turbulent kinetic energy, its correlation with the vortex indicator is rather poor. Of course, this does not imply that $\mathrm{Q}_\star$ and k are independent but just that the relationship between them is nonlinear, which is in chord with our understanding of the direct cascade process.

V. FINAL REMARKS

Instantaneous flow fields have been considered to identify and characterize vortical structures. The flow fields, collected after quasi-steady state conditions are achieved, correspond to large eddy simulations of a laboratory-scale, baffled, stirred tank with a Rushton-type impeller. In simulations, the tank operates under turbulent flow conditions (at least in the region near the impeller) either at 600 or 800 rpm and with water or 0.2 wt. % CMC solution as the working fluid. Thus, changes in the detected structures arising due to variations of the tank rotational speed and the fluid rheology are explored as well.

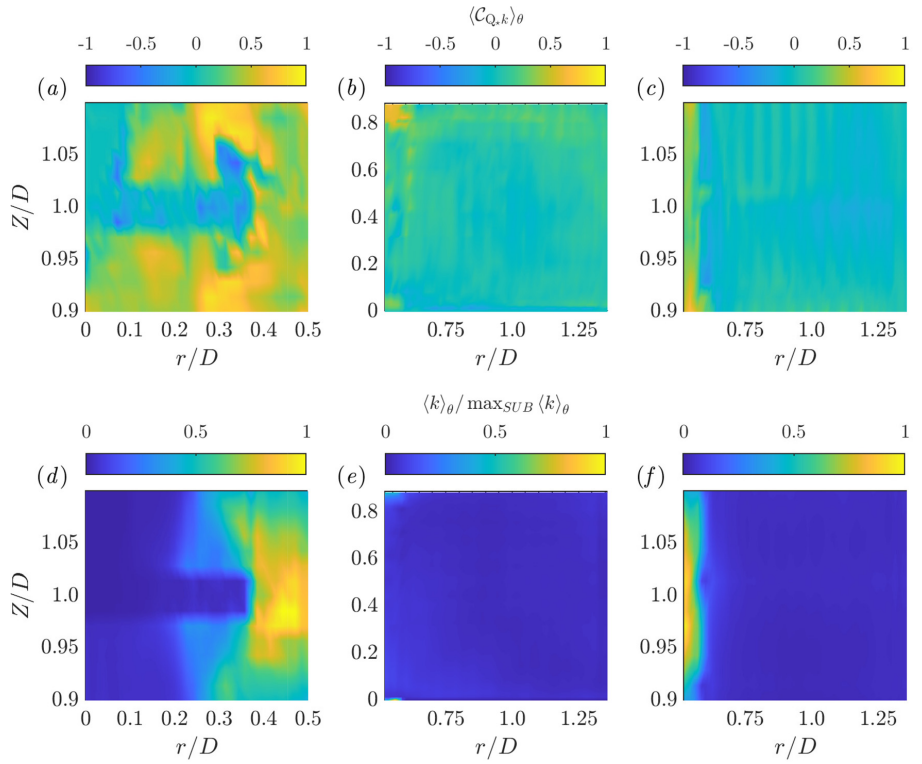

FIG. 18. Isocontours of the circumferential average, $\langle\,\rangle_\theta$, corresponding to the correlation coefficient between the considered vortex criterion, $Q_\star$, and the kinetic energy due to turbulence and the periodic passage of the blades, k, and normalized k: (a)–(c) $\langle \mathcal{C}_{Q_\star k} \rangle_\theta$ and (d)–(f) $\langle k \rangle_\theta / \max_{SUB} \langle k \rangle_\theta$. (a) and (d), (b) and (e), and (c) and (f) correspond to SUB-B, -D, and -E, respectively. Case W600 as described in Table I. In (a), for visualization purposes, 3D undefined positions; i.e., those in regions occupied by the shaft and disk of the impeller, have been set to 0 before taking the circumferential average.

The identification of the structures is performed using an objectivized version of the traditional Q-criterion,[58] which also takes into account that the flow in a stirred tank is inhomogeneous in all spatial directions. The implemented method is believed to yield consistent results even if slightly different threshold values are used. The characterization of the detected structures, involving aspects such as size, number density, shape, spatial organization, and correlation with kinetic energy, is done through different statistical analyses. Our main findings can be summarized as follows:

(i) Considering a size indicator based on the equivalent diameter of a sphere, the largest detected structures seem to be about the same order of magnitude as the impeller diameter, whereas the smallest identified structures appear to be about one order of magnitude less than D. Moreover, finer structures within a narrower range of length scales are observed with an increase of the impeller rotational speed for the same working fluid. Regarding the effect of shear-thinning rheology respect to a Newtonian case operating at the same N, more sizable structures are detected but not within a narrower range of length scales. This latter observation is explained in terms of the Reynolds number playing a more important role than the fluid rheology when compared to Newtonian and shear-thinning cases operating at the same N.

(ii) The profiles obtained for the number density as a function of the size indicator, covering different subdomains under study in the stirred tank, appear to depict only the energy containing and inertial subranges. This observation is in line with the fact that LES are performed. For the smallest detected scales, the effect of changing N for the same working fluid seems negligible while a change from Newtonian to shear-thinning rheology for the tank operating at the same N leads to an overall decrease in n_d. On the other

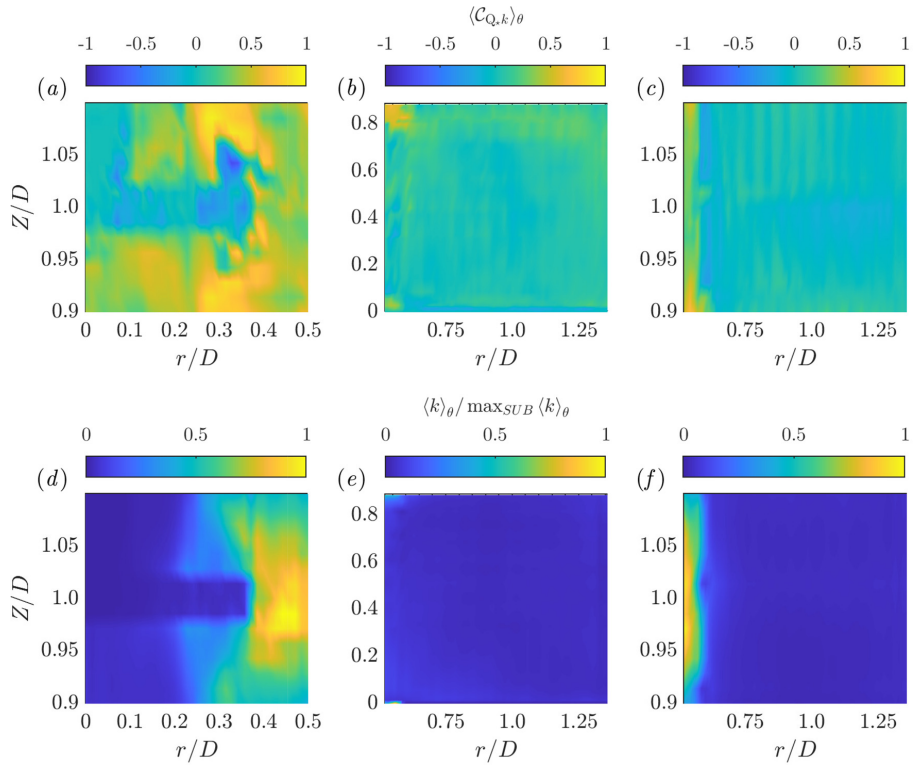

FIG. 19. Isocontours of the circumferential average, $\langle\,\rangle_\theta$, corresponding to the correlation coefficient between the considered vortex criterion, Q_*, and the kinetic energy due to turbulence and the periodic passage of blades, k, and normalized k: (a)–(c) $\langle \mathcal{C}_{Q_*,k} \rangle_\theta$ and (d)–(f) $\langle k \rangle_\theta / \max_{SUB} \langle k \rangle_\theta$. (a) and (d), (b) and (e), and (c) and (f) correspond to SUB-B, -D, and -E, respectively. Case W800 as described in Table I. In (a), for visualization purposes, 3D undefined positions, i.e., those in regions occupied by the shaft and disk of the impeller, have been set to 0 before taking the circumferential average.

hand, at large values of d_{eq}, the rapid decrease in n_d is seemingly delayed both with decreasing N and shear-thinning fluid behavior. This observation is consistent with what we expect as the Reynolds number decreases.

(iii) Also, with respect to n_d but for particular regions of the tank, the largest values in n_d are observed in subdomains B, D, and E (see Table III) for structures having d_{eq} of about one order of magnitude less than D. n_d profile is also given for a wider range of d_{eq} in subdomains D–F, and conspicuous values of n_d are achieved in subdomains C and E, which are hypothesized to be related to MI and trailing vortices, respectively (see Fig. 9).

(iv) In regard to the shape of the detected structures based on the flatness and elongation parameters (see Subsection IV B), tube-like vortical structures are as likely to appear as spherical blobs if not more so. Furthermore, when considering particular subdomains in the tank, only for subdomains B and E—where most of the energy is contained—it is found that sphere-like structures are more likely to be observed. It is also worth remarking that the structures considered MI and trailing vortices appear fully tubular and fairly triaxial, respectively [see Figs. 13(c) and 13(e)]. On the other hand, the effect of shear-thinning rheology as compared to a Newtonian case operating at the same N seems to lead to more ribbon-like structures in different subdomains of the tank.

(v) Respecting the spatial distribution of structures within subdomains having largest n_d, it is remarked that at least 70% of the data covering all angular positions fall into $0.25 < r_c/D \leq 0.5, 0.95 < Z_c/D \leq 1.11$; $0.8 < r_c/D \leq 1.36$, $0.15 < Z_c/D \leq 0.89$; and $0.6 < r_c/D \leq 1.36, 0.95 < Z_c/D \leq 1.11$ for subdomains B, D, and E, respectively. Moreover, in comparison with changes in rotational speed for a given working fluid, changes in rheology for the tank operating at

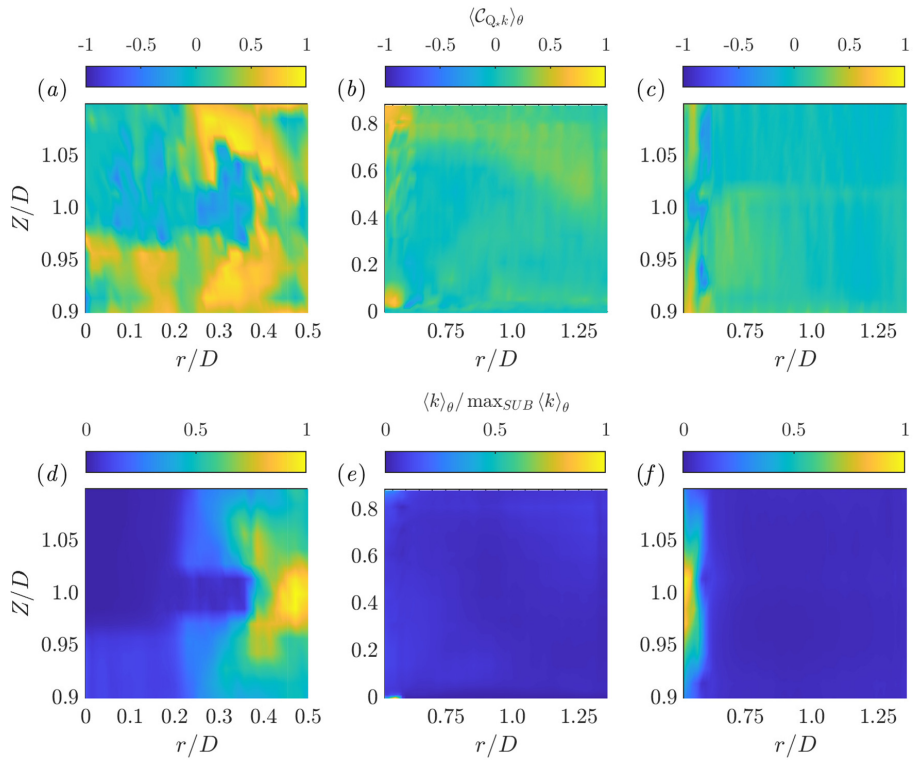

FIG. 20. Isocontours of the circumferential average, $\langle\,\rangle_\theta$, corresponding to the correlation coefficient between the considered vortex criterion, $Q_\star$, and the kinetic energy due to turbulence and the periodic passage of blades, k, and normalized k: (a)–(c) $\langle \mathcal{C}_{Q,k} \rangle_\theta$ and (d)–(f) $\langle k \rangle_\theta / \max_{SUB} \langle k \rangle_\theta$. (a) and (d), (b) and (e), and (c) and (f) correspond to SUB-B, -D, and -E, respectively. Case C800 as described in Table I. In (a), for visualization purposes, 3D undefined positions, i.e., those in regions occupied by the shaft and disk of the impeller, have been set to 0 before taking the circumferential average.

a specified N appear to impact the distributions in a more significant manner (see Subsection IV C).

(vi) In term of spatial organization, it is found that the nearest structure to another detected one shares the same size and are likely to be side-by-side in the radial direction. Furthermore, these pairs of nearest structures having similar size are unlikely to overlap and seem organized both in the X and Y directions with a separation of about the minimum absolute distance between a pair [see Eq. (14)]. Additionally, it is worth commenting that for subdomain E, the probability of encountering nearest structures having similar size on top of each other but without perfect alignment of their centroids is high as well.

(vii) With respect to the correlation between the vortex indicator and the kinetic energy due to turbulence and the periodic component, positive and fairly high correlation values are observed in regions with high energy contents for subdomains B, D, and E, i.e., the subdomains having largest n_d. These results suggest that, at least to some extent and for regions with the local high energy content, a linear relationship between the vortex indicator and this kinetic energy may be reasonable.

Although the above findings correspond to simulations of the single-phase, turbulent flow of the Newtonian and shear-thinning fluids in a baffled stirred tank reactor, the potential implications for liquid–liquid and gas–liquid dispersed systems are worth pondering. This is particularly the case when considering one-way coupling in which the influence of the dispersed phase over the continuous one is negligible, i.e., for multiphase systems where the local fraction of the dispersed phase (holdup) is always sufficiently small. Hence, in the case of one-way coupling, some of the aforementioned findings possibly imply the following:

(i) There is a higher probability of fluid particle breakage in subdomains B, D, and E where the number density is the largest for the smallest detected structures, i.e., those having

a size indicator of about one order of magnitude less than D. This statement, of course, is only valid under the premise that the interaction with particles of typical size found in laboratory setups (leading to their deformation and eventual breakup) is indeed occurring with structures of comparable size.

(ii) It is questionable to assume that vortical structures interacting with fluid particles present spherical shape. Perhaps such assumption, common in some phenomenological models used to predict fluid particle breakage rate and size distributions (consider, e.g., Luo and Svendsen[101]) should be limited to regions of high energy content in the stirred vessel such as subdomains B and E. Moreover, breakage models where turbulent vortices would be described as tube-like structures instead of spherical ones are also worth exploring when considering the energy containing scales and when moving beyond them. A reasonable starting point would be to consider non-spherical vortex models for isotropic turbulence, see, e.g., Saffman.[102]

(iii) The probability of pairs of vortices sharing similar size and interacting with fluid particles seems fairly high. Moreover, the spatial organization of these pairing is such that the odds of encountering several pairs in the vicinity of a fluid particle is also high. These are aspects that should be accounted for in models for breakup of bubbles and droplets in turbulent flows.

(iv) Optimal feeding points for fluids particles would be those where the probability of detecting the structures—of a similar size to the particles under consideration—is fairly large but more so where the correlation between the vortex indicator and the energy content is high as well. Such tentative feeding points can be found by cross-referencing the results presented Subsections IV C and IV D.

Finally, we would like to highlight some natural extensions of the present work. On one side, since the input flow fields are obtained from LES and not DNS, the smallest structures at the dissipative scales are yet to be analyzed. In addition, in light of recent studies about reconstruction of 3D flow fields in stirred vessels using proper orthogonal decomposition (POD),[103–105] it would be interesting to explore the identification and characterization of vortical structures based on reconstructed DNS flow fields corresponding to different POD modes (not just the first and most energetic ones). Conversely, the previous implications are just potential outcomes and require corroboration by means of experimentation and/or proper simulations of turbulent dispersions in stirred tank reactors. Moreover, even though recent DNS of single inertial drops in isotropic turbulence have shown that local patches of swirling fluid provide the main source for particle deformation, see plausible reinterpretation of the arrival/bombarding eddies of Luo and Svendsen[101] as "outer" eddies by Vela-Martín and Avila,[106] vortices or swirling-like structures are not necessarily the only type of flow structure that plays an active role in the deformation and breakup of fluid particles.

ACKNOWLEDGMENTS

This work was supported by the Research Council of Norway (RCN, Grant No. 274398). The authors are grateful for computer resources provided by Sigma2 (Grant No. NN9771K) and by local cluster, Idun,[107] at NTNU. The authors would like to thank Professor C. Liu and his group at the University of Texas at Arlington for providing the FORTRAN code, "Objective-OmegaUTA". Although the code was not used, it allowed better understanding the procedure to objectivize any Eulerian vortex identification method.

AUTHOR DECLARATIONS

Conflict of Interest

The authors have no conflicts to disclose.

DATA AVAILABILITY

The data that support the findings of this study are available from the corresponding author upon reasonable request.

NOMENCLATURE

Abbreviations

CDF	Cumulative distribution function
CMC	Carboxymethyl cellulose
cov	Covariance
DNS	Direct numerical simulations
exp	Expectation/mean
GN	Generalized Newtonian
JCDF	Joint cumulative distribution function
JPDF	Joint probability density function
LES	Large-eddy simulations
MI/MIs	Macroinstability/macroinstabilities
MRF	Multiple reference frame
PDF	Probability density function
RANS	Reynolds-averaged Navier–Stokes simulations
SGS	Subgrid-scales
SM	Sliding mesh
stv	Standard deviation
SUB	Subdomain

Greek letters

$\dot{\gamma} = (2S_{ij}S_{ij})^{1/2}$	Strain rate (1/s)
μ_a	Fluid apparent dynamic viscosity (Pa s), see Eq. (6)
ρ	Fluid density (kg/m^3)
Φ_P	Maximum projection sphericity, see Eq. (12)

Other symbols

C	Off-bottom clearance (cm)
$\mathcal{C}_{Q_\star k}$	Correlation coefficient between $Q_\star$ and k, see Eq. (16)
C600,C800	CMC flow cases under study, see Table I
D	Impeller diameter (cm)
D_i	Impeller diameter (cm) without blades
D_{ij}	Velocity gradient tensor (1/s)
$d_{eq} = (6V_{core}/\pi)^{1/3}$	Equivalent diameter (m) of a vortical structures.

$d_{eq}^{(i)}, d_{eq}^{(j)}$	d_{eq} of a vortex (i) and d_{eq} of the nearest vortex to it (j)
$d^{(i,j)}$	Absolute distance (m) between a vortex (i) and the nearest one to it (j), see Eq. (14)
DS_i	Shaft inner diameter (cm)
dX, dY, dZ	Normalized relative separation between a vortex (i) and the nearest one to it (j), see Eq. (15)
F, E	Flatness and elongation parameters, see Eq. (13)
h_b	Blades height (cm)
k	In Subsection IV D, kinetic energy (m/s) due to turbulence and the periodic blade passage
N	Impeller rotational speed (rev/s)
n_d	Number density per number of temporal realizations (per m^4 s) of vortical structures
$Q_\star$	Objective version of Q-criterion of Hunt *et al.*[58] (1/s), see Eq. (9). Also, vortex indicator when inequality (10) is fulfilled
$r = \sqrt{X^2 + Y^2}$	Radial coordinate (m)
$r_c = \sqrt{X_c^2 + Y_c^2}$	Radial coordinate (m) of the centroid of a vortical structure
Re	Reynolds number, see Table I
S_{ij}	Strain rate tensor (1/s), symmetric part of D_{ij}
T	Stirred tank diameter (cm)
$\mathcal{T}$	Threshold parameter, see inequality (10)
t_b	Blades thickness (cm)
u_i	Instantaneous velocity field (m/s). After Subsection II D, $u_i \equiv \widetilde{u}_i$
V_{A-F}	Volume of fluid (m^3) within subdomains A–F, see Table III
V_{core}	Vortex core volume (m^3)
w_b	Blades width (cm)
W600,W800	Water flow cases under study, see Table I
X, Y, Z	Cartesian coordinates (m), see Fig. 1
X_c, Y_c, Z_c	Centroid (m) of a vortical structure in Cartesian coordinates
$\theta = \tan^{-1}(Y/X)$	Angular coordinate (rad)
$\widetilde{\ }$	Grid filtering operator in the context of LES

REFERENCES

[1]R. P. Chhabra and J. F. Richardson, "Liquid mixing," in *Non-Newtonian Flow and Applied Rheology* (Butterworth-Heinemann, 2008), pp. 376–461.
[2]J. M. Nouri and J. H. Whitelaw, "Particle velocity characteristics of dilute to moderately dense suspension flows in stirred reactors," Int. J. Multiphase Flow **18**, 21–33 (1992).
[3]M. Soos, R. Kaufmann, R. Winteler, M. Kroupa, and B. Lüthi, "Determination of maximum turbulent energy dissipation rate generated by a Rushton impeller through large eddy simulation," AIChE J. **59**, 3642–3658 (2013).
[4]D. Fernandes del Pozo, A. Liné, K. M. Van Geem, C. L. Men, and I. Nopens, "Hydrodynamic analysis of an axial impeller in a non-Newtonian fluid through particle image velocimetry," AIChE J. **66**, e16939 (2020).
[5]S. Hara, S. Ebihara, and Y. Kawaguchi, "Influence of viscoelasticity on mixing performance of primary and secondary circulation flows in stirred vessels," Phys. Fluids **32**, 075102 (2020).
[6]M. Schäfer, M. Höfken, and F. Durst, "Detailed LDV measurements for visualization of the flow field within a stirred-tank reactor equipped with a Rushton turbine," Chem. Eng. Res. Des. **75**, 729–736 (1997).
[7]K. V. Sharp and R. J. Adrian, "PIV study of small-scale flow structure around a Rushton turbine," AIChE J. **47**, 766–778 (2001).
[8]B. C. H. Venneker, J. J. Derksen, and H. E. A. Van den Akker, "Turbulent flow of shear-thinning liquids in stirred tanks—The effects of Reynolds number and flow index," Chem. Eng. Res. Des. **88**, 827–843 (2010).
[9]A. de Lamotte, A. Delafosse, S. Calvo, and D. Toye, "Analysis of PIV measurements using modal decomposition techniques, POD and DMD, to study flow structures and their dynamics within a stirred-tank reactor," Chem. Eng. Sci. **178**, 348–366 (2018).
[10]P. Mavros, "Flow visualization in stirred vessels: A review of experimental techniques," Chem. Eng. Res. Des. **79**, 113–127 (2001).
[11]F. Sbrizzai, V. Lavezzo, R. Verzicco, M. Campolo, and A. Soldati, "Direct numerical simulation of turbulent particle dispersion in an unbaffled stirred-tank reactor," Chem. Eng. Sci. **61**, 2843–2851 (2006).
[12]J. J. J. Derksen and H. E. A. Van den Akker, "Direct numerical simulation of the turbulent flow in a baffled tank driven by a Rushton turbine," AIChE J. **58**, 3878–3890 (2012).
[13]A. Tamburini, G. Gagliano, G. Micale, A. Brucato, F. Scargiali, and M. Ciofalo, "Direct numerical simulations of creeping to early turbulent flow in unbaffled and baffled stirred tanks," Chem. Eng. Sci. **192**, 161–175 (2018).
[14]J. G. M. Eggels, "Direct and large-eddy simulation of turbulent fluid flow using the lattice-Boltzmann scheme," Int. J. Heat Fluid Flow **17**, 303–323 (1996).
[15]J. Derksen and H. E. A. Van den Akker, "Large eddy simulations on the flow driven by a Rushton turbine," AIChE J. **45**, 209–221 (1999).
[16]H. Hartmann, J. J. Derksen, C. Montavon, J. Pearson, I. S. Hamill, and H. E. A. van den Akker, "Assessment of large eddy and rans stirred tank simulations by means of LDA," Chem. Eng. Sci. **59**, 2419–2432 (2004).
[17]R. Sungkorn, J. J. Derksen, and J. G. Khinast, "Modeling of aerated stirred tanks with shear-thinning power law liquids," Int. J. Heat Fluid **36**, 153–166 (2012).
[18]H. Singh, D. F. Fletcher, and J. J. Nijdam, "An assessment of different turbulence models for predicting flow in a baffled tank stirred with a Rushton turbine," Chem. Eng. Sci. **66**, 5976–5988 (2011).
[19]A. Tamburini, A. Brucato, M. Ciofalo, G. Gagliano, G. Micale, and F. Scargiali, "CFD simulations of early- to fully-turbulent conditions in unbaffled and baffled vessels stirred by a Rushton turbine," Chem. Eng. Res. Des. **171**, 36–47 (2021).
[20]F. Garcia-Ochoa and E. Gomez, "Bioreactor scale-up and oxygen transfer rate in microbial processes: An overview," Biotechnol. Adv. **27**, 153–176 (2009).
[21]R. Escudié and A. Liné, "Analysis of turbulence anisotropy in a mixing tank," Chem. Eng. Sci. **61**, 2771–2779 (2006).
[22]J.-C. Gabelle, J. Morchain, D. Anne-Archard, F. Augier, and A. Liné, "Experimental determination of the shear rate in a stirred tank with a non-Newtonian fluid: Carbopol," AIChE J. **59**, 2251–2266 (2013).
[23]I. Takashima and M. Mochizuki, "Tomographic observations of the flow around agitator impeller," J. Chem. Eng. Jpn. **4**, 66–72 (1971).
[24]L. F. Richardson, "The fundamental equations: The effects of eddy motion," in *Weather Prediction by Numerical Process* (Cambridge University Press, 1922), p. 66.
[25]Y. Liao and D. Lucas, "A literature review of theoretical models for drop and bubble breakup in turbulent dispersions," Chem. Eng. Sci. **64**, 3389–3406 (2009).
[26]Y. Liao and D. Lucas, "A literature review on mechanisms and models for the coalescence process of fluid particles," Chem. Eng. Sci. **65**, 2851–2864 (2010).
[27]J. Solsvik, S. Tangen, and H. A. Jakobsen, "On the constitutive equations for fluid particle breakage," Rev. Chem. Eng. **29**, 241–356 (2013).
[28]S. M. Kresta and R. S. Brodkey, "Turbulence in mixing applications," in *Handbook of Industrial Mixing: Science and Practice*, edited by E. L. Paul, V. A. Atiemo-Obeng, and S. M. Kresta (John Wiley & Sons, 2004), pp. 44–45.
[29]K. Van't Riet and J. M. Smith, "The behaviour of gas–liquid mixtures near Rushton turbine blades," Chem. Eng. Sci. **28**, 1031–1037 (1973).
[30]K. Van't Riet and J. M. Smith, "The trailing vortex system produced by Rushton turbine agitator," Chem. Eng. Sci. **30**, 1093–1105 (1975).

[31]K. Van't Riet, W. Bruijn, and J. M. Smith, "Real and pseudo-turbulence in the discharge stream from a Rushton turbine," Chem. Eng. Sci. **31**, 407–412 (1976).
[32]M. Yianneskis, Z. Popiolek, and J. H. Whitelaw, "An experimental study of the steady and unsteady flow characteristics of stirred reactors," J. Fluid Mech. **175**, 537–555 (1987).
[33]C. M. Stoots and R. V. Calabrese, "Mean velocity field relative to a Rushton turbine blade," AIChE J. **41**, 1–11 (1995).
[34]K. C. Lee and M. Yianneskis, "Turbulence properties of the impeller stream of a Rushton turbine," AIChE J. **44**, 13–24 (1998).
[35]J. J. Derksen, M. S. Doelman, and H. E. A. Van den Akker, "Three-dimensional LDA measurements in the impeller region of a turbulently stirred tank," Exp. Fluids **27**, 522–532 (1999).
[36]R. Escudié and A. Liné, "Experimental analysis of hydrodynamics in a radially agitated tank," AIChE J. **49**, 585–603 (2003).
[37]R. Escudié, D. Bouyer, and A. Liné, "Characterization of trailing vortices generated by a Rushton turbine," AIChE J. **50**, 75–85 (2004).
[38]Y. Bouremel, M. Yianneskis, and A. Ducci, "On the utilisation of vorticity and strain dynamics for improved analysis of stirred processes," Chem. Eng. Res. Des. **87**, 377–385 (2009).
[39]K. V. Sharp, D. Hill, D. Troolin, G. Walters, and W. Lai, "Volumetric three-component velocimetry measurements of the turbulent flow around a Rushton turbine," Exp. Fluids **48**, 167–183 (2010).
[40]Z. Chara, B. Kysela, J. Konfrst, and I. Fort, "Study of fluid flow in baffled vessels stirred by a Rushton standard impeller," Appl. Math. Comput. **272**, 614–628 (2016).
[41]L. Nikiforaki, G. Montante, K. C. Lee, and M. Yianneskis, "On the origin, frequency and magnitude of macro-instabilities of the flows in stirred vessels," Chem. Eng. Sci. **58**, 2937–2949 (2003).
[42]C. Galletti, A. Paglianti, K. C. Lee, and M. Yianneskis, "Reynolds number and impeller diameter effects on instabilities in stirred vessels," AIChE J. **50**, 2050–2063 (2004).
[43]A. Ducci and M. Yianneskis, "Vortex tracking and mixing enhancement in stirred processes," AIChE J. **53**, 305–315 (2007).
[44]Z. Doulgerakis, M. Yianneskis, and A. Ducci, "On the interaction of trailing and macro-instability vortices in a stirred vessel-enhanced energy levels and improved mixing potential," Chem. Eng. Res. Des. **87**, 412–420 (2009).
[45]F. Irgens, "Generalized Newtonian fluids," In *Rheology and non-Newtonian Fluids* (Springer, 2014), pp. 113–125.
[46]J. Smagorinsky, "General circulation experiments with the primitive equations. I: The basic experiment," Mon. Weather Rev. **91**, 99–165 (1963).
[47]D. K. Lilly, "On the application of the eddy viscosity concept in the inertial subrange of turbulence," Technical Report No. NCAR MS 123 (National Centre for Atmospheric Research, Boulder, CO, 1966).
[48]J. Fan, Y. Wang, and W. Fei, "Large eddy simulations of flow instabilities in a stirred tank generate by a Rushton turbine," Chin. J. Chem. Eng. **15**, 200–208 (2007).
[49]T. T. Devi and B. Kumar, "Large-eddy simulation of turbulent flow in stirred tank with a curved blade impeller," J. Eng. Thermophys. **24**, 152–168 (2015).
[50]A. B. Metzner and R. E. Otto, "Agitation of non-Newtonian fluids," AIChE J. **3**, 3–10 (1957).
[51]C. Yang and Z.-S. Mao, "Multiphase stirred reactors," in *Numerical Simulation of Multiphase Reactors with Continuous Liquid Phase* (Academic Press, 2014), pp. 75–151.
[52]J. Y. Luo, R. I. Issa, and A. D. Gosman, "Prediction of impeller induced flows in mixing vessels using multiple frames of reference," in *Proceedings of 8th European Conference on Mixing* (InTech, 1994), pp. 549–556.
[53]J. Y. Murthy, S. R. Mathur, and D. Choudhury, "CFD simulation of flows in stirred tank reactors using a sliding mesh technique," in *Proceedings of 8th European Conference on Mixing* (InTech, 1994), pp. 341–348.
[54]M. Moštěk, A. Kukuková, M. Jahoda, and V. Machoň, "Comparison of different techniques for modelling of flow field and homogenization in stirred vessels," Chem. Pap. **59**, 380–385 (2005), see https://www.chempap.org/?id=7&paper=13.
[55]B. E. Launder and D. B. Spalding, "The numerical computation of turbulent flows," Comput. Methods Appl. Mech. Eng. **3**, 269–289 (1974).
[56]V. Holmén, "Methods for vortex identification," Master's thesis (Lund University, 2012).
[57]B. P. Epps, "Review of vortex identification methods," in 55th AIAA Aerospace Sciences Meeting, 2017.
[58]J. C. R. Hunt, A. A. Wray, and P. Moin, "Eddies, streams and convergence zones in turbulent flows," in *Center for Turbulence Research, Proceedings of the Summer Program* (NASA Ames Research Center, 1988), pp. 193–208.
[59]M. S. Chong, A. E. Perry, and B. J. Cantwell, "A general classification of three–dimensional flow fields," Phys. Fluids A **2**(5), 765–777 (1990).
[60]J. Jeong and F. Hussain, "On the identification of a vortex," J. Fluid Mech. **285**, 69–94 (1995).
[61]J. Zhou, R. J. Adrian, S. Balachandar, and T. M. Kendall, "Mechanisms for generating coherent packets of hairpin vortices in channel flow," J. Fluid Mech. **387**, 353–396 (1999).
[62]P. Chakraborty, S. Balachandar, and R. J. Adrian, "On the relationships between local vortex identification schemes," J. Fluid Mech. **535**, 189–214 (2005).
[63]V. Kolář, "Vortex identification: New requirements and limitations," Int. J. Heat Fluid Flow **28**, 638–652 (2007).
[64]G. Haller, "An objective definition of a vortex," J. Fluid Mech. **525**, 1–26 (2005).
[65]C. Liu, Y. Wang, Y. Yang, and Z. Duan, "New omega vortex identification method," Sci. China–Phys. Mech. Astron. **59**, 684711 (2016).
[66]T. Günther, M. Schulze, and H. Theisel, "Rotation invariant vortices for flow visualization," IEEE Trans. Visual Comput. Graphics **22**, 817–826 (2016).
[67]G. Haller, "Can vortex criteria be objectivized?," J. Fluid Mech. **908**, A25 (2021).
[68]G. Haller, A. Hadjighasem, M. Farazmand, and F. Huhn, "Defining coherent vortices objectively from the vorticity," J. Fluid Mech. **795**, 136–173 (2016).
[69]J. Liu, Y. Gao, and C. Liu, "An objective version of the vortex vector for vortex identification," Phys. Fluids **31**, 065112 (2019).
[70]J. Liu, Y. Gao, Y. Wang, and C. Liu, "Objective omega vortex identification method," J. Hydrodyn. **31**, 455–463 (2019).
[71]C. Liu, Y. Gao, S. Tian, and X. Dong, "Rortex—A new vortex vector definition and vorticity tensor and vector decompositions," Phys. Fluids **30**, 035103 (2018).
[72]S. Tian, Y. Gao, X. Dong, and C. Liu, "Definitions of vortex vector and vortex," J. Fluid Mech. **849**, 312–103 (2018).
[73]Y. Gao and C. Liu, "Rortex and comparison with eigenvalue based vortex identification criteria," Phys. Fluids **30**, 085107 (2018).
[74]R. Nagaosa and R. A. Handler, "Statistical analysis of coherent vortices near a free surface in a fully developed turbulence," Phys. Fluids **15**, 375–394 (2003).
[75]J. C. del Álamo, J. Jiménez, P. Zandonade, and R. D. Moser, "Self-similar vortex clusters in the turbulent logarithmic region," J. Fluid Mech. **561**, 329–358 (2006).
[76]A. Lozano-Durán, O. Flores, and J. Jiménez, "The three-dimensional structure of momentum transfer in turbulent channels," J. Fluid Mech. **694**, 100–130 (2012).
[77]C. Cheng, W. Li, A. Lozano-Durán, and H. Liu, "On the structure of streamwise wall-shear stress fluctuations in turbulent channel flows," J. Fluid Mech. **903**, A29 (2020).
[78]F. Moisy and J. Jiménez, "Geometry and clustering of intense structures in isotropic turbulence," J. Fluid Mech. **513**, 111–133 (2004).
[79]S. Dong, A. Lozano-Durán, A. Sekimoto, and J. Jiménez, "Coherent structures in statistically stationary homogeneous shear turbulence," J. Fluid Mech. **816**, 167–208 (2017).
[80]J. Hwang and H. J. Sung, "Wall-attached structures of velocity fluctuations in a turbulent boundary layer," J. Fluid Mech. **856**, 958–983 (2018).
[81]K. Osawa and J. Jiménez, "Intense structures of different momentum fluxes in turbulent channels," Phys. Rev. Fluids **3**, 084603 (2018).
[82]R. Escudié and A. Liné, "A simplified procedure to identify trailing vortices generated by a Rushton turbine," AIChE J. **53**, 523–526 (2007).
[83]S. Başbuğ, G. Papadakis, and J. C. Vassilicos, "DNS investigation of the dynamical behaviour of trailing vortices in unbaffled stirred vessels at transitional Reynolds numbers," Phys. Fluids **29**, 064101 (2017).
[84]A. Zamiri and J. T. Chung, "Numerical evaluation of turbulent flow structures in a stirred tank with a Rushton turbine based on scale-adaptive simulation," Comput. Fluids **170**, 236–248 (2018).

[85]T. Mihalić, Z. Guzović, and A. Predin, "Performances and flow analysis in the centrifugal vortex pump," J. Fluids Eng. **135**, 011107 (2013).
[86]L. Wang, C. Guo, Y. Su, and T. Wu, "A numerical study on the correlation between the evolution of propeller trailing vortex wake and skew of propellers," Int. J. Nav. Archit. Ocean Eng. **10**, 212–214 (2018).
[87]A. A. Arosemena, R. Andersson, H. I. Andersson, and J. Solsvik, "Effects of shear-thinning rheology on near-wall turbulent structures," J. Fluid Mech. **925**, A37 (2021).
[88]J. Solsvik and H. A. Jakobsen, "Single air bubble breakup experiments in stirred water tank," Int. J. Chem. React. **13**, 477–491 (2015).
[89]J. Vejražka, M. Zedníková, and P. Stanovský, "Experiments on breakup of bubbles in a turbulent flow," AIChE J. **64**, 740–757 (2018).
[90]A. A. Arosemena and J. Solsvik, "Velocity–vorticity correlations and the four-layer regime in turbulent channel flow of generalized Newtonian fluids," Eur. J. Mech. B **91**, 1–8 (2022).
[91]H. Tennekes and J. L. Lumley, *A First Course in Turbulence* (MIT Press, 1972).
[92]G. K. Batchelor, *The Theory of Homogeneous Turbulence* (CUP, 1982).
[93]J. Solsvik and H. A. Jakobsen, "A review of the statistical turbulence theory required extending the population balance closure models to the entire spectrum of turbulence," AIChE J. **62**, 1795–1820 (2016).
[94]H. Ali and J. Solsvik, "Axial distributions of bubble–liquid mass transfer coefficient in laboratory-scale stirred tank with viscous Newtonian and non-Newtonian fluids," Phys. Fluids **32**, 123308 (2020).
[95]H. Ali and J. Solsvik, "Bubble hydrodynamics and mass transfer in stirred tank with non-Newtonian fluids: Scale-up from laboratory to pilot-scale," Phys. Fluids **33**, 033319 (2021).
[96]E. D. Sneed and R. L. Folk. Pebbles in the lower Colorado river, Texas: A study in particle morphogenesis. J. Geol. **66**, 114–150 (1958).
[97]T. Zingg, "Beitrag zur schotteranalyse," PhD thesis (ETH, Zurich, 1935).
[98]I. T. Jolliffe, *Principal Component Analysis* (Springer, 2002).
[99]H. Wadell, "Volume, shape, and roundness of rock particles," J. Geol. **40**, 443–451 (1932).
[100]R. Andersson and B. Andersson, "Modeling the breakup of fluid particles in turbulent flows," AIChE J. **52**, 2031–2038 (2006).
[101]H. Luo and H. F. Svendsen, "Theoretical model for drop and bubble breakup in turbulent dispersions," AIChE J. **42**, 1225–1233 (1996).
[102]P. G. Saffman, "Vortex models of isotropic turbulence," Philos. Trans. R. Soc., London A **355**, 1949–1956 (1997).
[103]G. Janiga, "Large-eddy simulation and 3D proper orthogonal decomposition of the hydrodynamics in a stirred tank," Chem. Eng. Sci. **201**, 132–144 (2019).
[104]K. Mikhaylov, S. Rigopoulos, and G. Papadakis, "Reconstruction of large-scale flow structures in a stirred tank from limited sensor data," AIChE J. **67**, e17348 (2021).
[105]C. Mayorga, J. Morchain, and A. Liné, "Reconstruction of the 3D hydrodynamics in a baffled stirred tank using proper orthogonal decomposition," Chem. Eng. Sci. **248**, 117220 (2022).
[106]A. Vela-Martín and M. Avila, "Deformation of drops by outer eddies in turbulence," J. Fluid Mech. **929**, A38 (2021).
[107]M. Själander, M. Jahre, G. Tufte, and N. Reissmann, "EPIC: An energy-efficient, high-performance GPGPU computing research infrastructure," arXiv:1912.05848.

ISBN 978-82-326-6412-2 (printed ver.)
ISBN 978-82-326-6781-9 (electronic ver.)
ISSN 1503-8181 (printed ver.)
ISSN 2703-8084 (online ver.)

NTNU
Norwegian University of
Science and Technology